

# Unravelling the Indian Ocean Dipole from the Oceanic Perspective

by

**Ankit Kavi**

*Thesis  
Submitted to Flinders University  
for the degree of*

**DOCTOR OF PHILOSOPHY**

College of Science and Engineering  
May 2020

---

# CONTENTS

<b>LIST OF FIGURES.....</b>	<b>III</b>
<b>LIST OF TABLES .....</b>	<b>IX</b>
<b>ABSTRACT .....</b>	<b>X</b>
<b>DECLARATION .....</b>	<b>XII</b>
<b>ACKNOWLEDGEMENTS.....</b>	<b>XIII</b>
<b>Chapter 1 Introduction.....</b>	<b>1</b>
1.1 Background and relevance .....	1
1.2 Literature review.....	5
1.3 Aims and Objectives .....	21
<b>CHAPTER 2 METHODOLOGY .....</b>	<b>24</b>
2.1 Overview .....	24
2.2 Data sources.....	24
2.3 Theories .....	25
2.4 Statistical Methods.....	28
<b>CHAPTER 3 RESULTS AND DISCUSSION .....</b>	<b>30</b>
3.1 Dipole Mode Index and SST .....	30
3.2 SST variability in south eastern tropical Indian Ocean .....	36
3.3 Statistical analysis of surface winds.....	46
3.3.1 Climatological cycle .....	46
3.3.2 Interannual variability of the equatorial winds .....	54
3.3.3 Interannual variability of southern coastal Java and Sumatra winds ....	64
Section Summary .....	70

3.4 High frequency convective events and anomalous atmospheric circulation..	72
3.4.1 Tropical convection over the Indian Ocean.....	72
3.4.2 Temporal characterisation of the convective events.....	78
3.4.3 Synoptic structure of the convective event and anomalous atmospheric circulation .....	85
Section Summary .....	103
3.5 Event analysis of cyclonic circulation in the IOD perspective.....	105
3.5.1 Cyclonic events of individual years.....	105
3.5.2 Ocean Response to the cyclonic events.....	133
3.5.3 Westerly wind bursts and sea level anomalies.....	157
3.5.4 Suppressed convection is a precursor and not an aftermath.....	170
3.5.3 Composite view of all the SETIO cyclones .....	177
<b>CHAPTER 4 SUMMARY AND CONCLUSION.....</b>	<b>186</b>
<b>REFERENCES.....</b>	<b>193</b>
<b>APPENDIX A .....</b>	<b>200</b>
<b>APPENDIX B .....</b>	<b>203</b>
<b>Appendix B .....</b>	<b>205</b>
<b>Appendix B .....</b>	<b>208</b>

## LIST OF FIGURES

**N Figure 1.2.1:** Definition of the surface areas used to calculate the DMI. The western region is defined by (50°E-70°E, 10°S-0°N) and the eastern region by (90°E-110°E, 10°S-0°S).

**Figure 1.3.1:** Panel (a) displays the time-longitude plots of monthly climatology of sea surface temperature at equator of the Indo-Pacific basin, from NOAA OI PSD data over period of 1981-2016, and panel (b) represents the long-term climatological values of the NOAA PSD OLR (outgoing long wave radiation in W/m<sup>2</sup>) from 1980 to 2016. NOAA High Resolution SST and OLR data provided by the NOAA/OAR/ESRL PSD, Boulder, Colorado, USA, from their Web site at <https://www.esrl.noaa.gov/psd/>.

**Figure 1.3.2:** Panel (a) displays the schematics of the Walker circulation over the Pacific and Indian Ocean (Ref: NOAA Climate.gov) and panel (b) displays time-longitude plots of monthly climatology of surface zonal winds at equator of the Indo-Pacific basin, from CCMP V2 data over period of 1988-2016

**Figure 2.3.1:** Panel (a) displays the schematic of the coastal upwelling process along a coast of finite extent ( $L_o$ ) in the southern hemisphere. Full upwelling occurs within a distance of  $L$ , where  $L_o$  is the length of entire coastline. Panel (b) displays the schematic of individual and cumulative changes of the depth of the surface mixed layer along the finite length coastline (Kämpf and Kavi, 2018).

**Figure 3.1.1:** Maps shows sea surface temperature (SST, °C) distribution over the tropical Indian Ocean during June to September, where panel (a) displays long term (1988-2016) average conditions, panel (b) displays long term (1988-2016) average minus long term (1988-2016) minimum values and panel (c) displays long term (1988-2016) maximum values minus long term (1988-2016) minimum values. Marked boxes in all panels displays IOD events eastern and western box.

**Figure 3.1.2:** Line plot in panel (a) displays dipole mode index (DMI) with sea surface temperature anomaly values over the eastern and western boxes of the IOD events. Panel (b) indicates NIÑO 3.4 sea surface temperature anomaly values.

**Figure 3.2.1:** Maps shows sea surface temperature distribution over the south eastern tropical Indian Ocean, where panel (a) displays the average SST values during three positive IOD events (1994, 1997 and 2006), panel (b) displays the average SST values during all other 26 years from the period 1988-2016. Contour Interval in each panel is 0.2°C. Panel (c) displays the differences of values shown in (a) and (b). SST values are derived from NOAA-OI data set during boreal summer-fall season (July to November). The rectangle in both panels shows the eastern area used for calculation of the DMI.

**Figure 3.2.2:** Map displays the schematics of south eastern tropical Indian Ocean, where large rectangle indicates eastern box of the DMI. Black dotted rectangles: regions are used to calculate area average the classical Bakun upwelling index based on the orientation of the adjacent coastline.

**Figure 3.2.3:** Panel (a) displays time series of seasonally averaged (June to September) Upwelling Index (UI) of Sumatra box 1, box 2, box 3 and Java box (of **figure 3.1.4**) using monthly CCMP V2 data. Black arrows indicate years of pronounced upwelling along the southern Sumatra-Java coastline. Panel (b) displays time series of area average monthly sea surface temperature anomalies (SSTA, °C) over the similar box regions of **figure 3.1.4**, derived from monthly NOAA OI data.

**Figure 3.2.4:** All line plots display area average SST anomaly (°C), panel (a) for 1998, panel (b) for 2001 and panel (c) for 2004. The area over which SSTA is averaged is displayed in legends. Blue horizontal arrow indicates season of interest.

**Figure 3.2.5:** All line plots display area average SST anomaly (°C), panel (a) for 1994, panel (b) for 1997 and panel (c) for 2006. The area over which SSTA is averaged is displayed in legends. Blue horizontal arrow indicates season of interest.

**Figure 3.2.6:** All line plots display area average SST anomaly (°C), panel (a) for 2003, panel (b) for 2008 and panel (c) for 2009. The area over which SSTA is averaged is displayed in legends. Blue horizontal arrow indicates season of interest.

**Figure 3.3.1:** Schematic of the study region highlighting the SETIO region (80E to 110E and EQ to 10S).

**Figure 3.3.2:** Schematic of tropical IO with east & west basins

**Figure 3.3.3:** Time-longitude plots (Hovmoller diagram) along the equator of Indian the Ocean. Panel a) displays SST data from NOAA OI data over period of 1981-2016. Two horizontal thick arrows display the timing of spring and fall Wyrтки Jets. Panel b) represents values of thermocline depth from ARGO data over period of 2005-2016. Panel c) displays values of outgoing longwave radiation (OLR) from NOAA OLR data over period of 1975-2016. Panel d) shows values of zonal wind speed (m/s) from CCMP data over 1988-2015 period. All data are monthly climatological averages.

**Figure 3.3.4:** Seasonal averages of monthly climatological zonal wind velocity (m/s) along the equator of the Indian Ocean (40°-100°E) over the 1988-2015 period. Shown are the periods April-May, June-September, and October-November.

**Figure 3.3.5:** Climatological cycle of the coast parallel winds averaged for the regions shown in the right panel.

**Figure 3.3.6:** Schematic of tropical IO. Marked boxes represents the equatorial zones.

**Figure 3.3.7:** Seasonal average (June to September) and STD from seasonal average of zonal wind speed derived from daily wind fields of CCMP satellite data. Averaged over the marked regions shown in **figure 3.3.6**, where Panel a) displays values for Eq Box1 (90°E to 100°E), b) displays values for Eq Box 2 (70°E to 90°E), c) displays values for Eq Box 3 (50°E to 70°E) and (d) displays values for Eq Box 4 (40°E to 50°E).

**Figure 3.3.8:** Histogram of area average daily zonal wind speed from CCMP satellite data over the boxed regions shown in **figure 3.3.6**, in boreal summer (June to September) of 1988 to 2016. Panel a) for Eq Box1 (90°E to 100°E), (b) for Eq Box 2 (70°E to 90°E), (c) for Eq Box 3 (50°E to 70°E) and (d) for Eq Box 4 (40°E to 50°E).

**Figure 3.3.9:** Histogram of area average daily zonal wind speed from CCMP satellite data over the boxed regions shown in **figure 3.3.6**, in boreal summer (June to September) of 1994. Panel a) for Eq Box1 (90°E to 100°E), (b) for Eq Box 2 (70°E to 90°E), (c) for Eq Box 3 (50°E to 70°E) and (d) for Eq Box 4 (40°E to 50°E).

**Figure 3.3.10:** Histogram of area average daily zonal wind speed from CCMP satellite data over the boxed regions shown in **figure 3.3.6**, in boreal summer (June to September) of 1997. Panel a) for Eq Box1 (90°E to 100°E), (b) for Eq Box 2 (70°E to 90°E), (c) for Eq Box 3 (50°E to 70°E) and (d) for Eq Box 4 (40°E to 50°E).

**Figure 3.3.11:** Histogram of area average daily zonal wind speed from CCMP satellite data over the boxed regions shown in **figure 3.3.6**, in boreal summer (June to September) of 2006. Panel a) for Eq Box1 (90°E to 100°E), (b) for Eq Box 2 (70°E to 90°E), (c) for Eq Box 3 (50°E to 70°E) and (d) for Eq Box 4 (40°E to 50°E).

**Figure 3.3.12:** Seasonal average (June to September) and STD from seasonal of coast parallel stress average over the regions shown in **figure 3.3.5b** derived from daily wind fields of CCMP V2 satellite data for 1988 to 2016. Panel a) displays values along the coasts of Java and panel b) displays values along the southern coastal Sumatra.

**Figure 3.3.13:** Histogram of area average daily coast parallel stress derived from satellite CCMP V2 data and averaged over the coastal Java region shown in **figure 3.3.5b**. Panel a) displays histogram for June September 1988-2016, b) for June to September of 1994, c) for June to September 1997 and d) for June to September 2006.

**Figure 3.3.14:** Histogram of area average daily coast parallel stress derived from satellite CCMP V2 data and averaged over the coastal Java region shown in **figure 3.3.5b**. Panel a) displays histogram for June September 1988-2016, b) for June to September of 1994, c) for June to September 1997 and d) for June to September 2006.

**Figure 3.4.1:** OLR values (OLR,  $W/m^2$ ) as seasonal average in the climatological year (1975-2016) derived from daily satellite data (NOAA PSD data) over the tropical Indian Ocean and the Pacific Ocean. Panel (a) displays monthly climatological values averaged over Jan-Mar, (b) same as (a) but averaged over April-May, panel (c) same as (a) but averaged over Jun-Sep, panel (d) same as (a) but averaged over Oct-Dec.

**Figure 3.4.2:** The maps display seasonal average climatological values (1975-2016) of Outgoing Longwave Radiation (OLR,  $W/m^2$ , as a proxy of tropical convection) in boreal summer-fall (from June to September) derived from daily satellite data (NOAA PSD data) over the tropical Indian ocean. Marked box region indicates the region of interest: SETIO (80°E to 110°E and EQ to 10°S).

**Figure 3.4.3:** (a) Standard deviation of daily OLR values ( $W/m^2$ , NOAA OLR PSD data) over the period Jun-Sep of 1988-2016 (b) Standard deviation of zonal wind speed (m/s, CCMP V2 data) over the period Jun-Sep of 1988-2016.

**Figure 3.4.4:** Panel (a) displays the power spectral density plot for the OLR values average over the study region and panel (b) displays the power spectral density plot for the zonal winds speed values average over the eastern equatorial Indian Ocean.

**Figure 3.4.5:** (a) Normalised wavelet spectrum daily time series of the area average zonal wind speed from June to September of 1988 to 2016 and (b) OLR anomalies daily time series from June to September of 1988 to 2016 in the SETIO region using Morse Wavelet. Colour shading indicates the region of 95% confidence and a dashed line indicates area under edge effect.

**Figure 3.4.6:** (a) Bandpass filtered OLR anomaly over the study region in 2000 (b) Variance of 1 to 8 days, 8 to 20 days (QBWO) and 20 to 60 days (MJO) bandpass filtered time series of OLR anomaly displayed in (a). Variance displayed is for the entire study period of 1988 to 2016.

**Figure 3.4.7:** Autocorrelation of 8-20-day filtered OLR anomaly over the study region.

**Figure 3.4.8:** Maps display anomaly values (from daily 1988-2016 climatology) of composite 157 atmospheric convective events captured during boreal summer-fall of the study period (198—2016) over the study region. Panel (a) shows OLR (W/m<sup>2</sup>) anomaly, (b) displays wind speed anomaly (m/s) and 1000 Mb wind vectors (m/s), (c) displays anomaly of wind stream function at 0.995 sigma.

**Figure 3.4.9:** The 8-20 days filtered time series from June to September 2000 of (a) OLR anomaly over the study region, (b) zonal wind speed over the eastern equatorial Indian Ocean and (c) is (a) + (b).

**Figure 3.4.10:** The composite maps of six convective events triggered during boreal summer-fall of 2000 displayed in **figure 3.4.9**. Left panels display OLR anomalies, middle panels display surface wind vectors, and right panels display surface wind divergence with wind streamlines (right).

**Figure 3.4.11:** Schematics of anomalous cyclonic circulation over the study region under the influence of Rossby wave response from convective heating. Solid arrows indicate seasonal wind directions, dashed arrows indicate anomalous winds from cyclonic circulation and red box displays study region.

**Figure 3.5.1:** Each panel displays time series of OLRA anomaly averaged over 80°-110°E, Eq-10°S (black line and blue shading) and zonal wind speed averaged over 70°-90°E, 5°N-5°S (red line, orange shading). The values of OLR anomaly below -10 W/m<sup>2</sup> and values of zonal wind speed above 5 m/s are shaded, and arrows indicate deep convective event.

**Figure 3.5.2a:** Each map displays the surface circulation with the streamlines and wind vectors over the study region during the mature phase of atmospheric convective phase of 1998.

**Figure 3.5.3:** Schematics of Java and Sumatra coastal region. Red box area is used to calculate area average coast parallel stress and pinpoint locations with number are used to prepare wind roll plot. Black arrows indicate ideal coast parallel direction along respective coastline.

**Figure 3.5.4:** Top panel in each **figure** displays line plot of OLR anomaly  $W/m^2$  (blue shading, thin black line), coast parallel stress in southern coastal Sumatra region (thick black line) and coast parallel stress in coastal Java region (dashed red line). Bottom panels displays wind roll time series at six different location at Sumatra coastline of **fig 3.5.3**, ideal coast parallel direction along southern Sumatra coastline is displayed in black arrow with direction axis in each **figure** with unit length of arrow is 0.01 Pa. Plot (a) displays wind conditions during boreal summer-fall of 1998 , plot (b) for 2001 and plot (c) for 2004

**Figure 3.5.5:** Time sires of OLRA anomaly averaged over  $80^{\circ}$ - $110^{\circ}$ E,  $Eq-10^{\circ}$ S (black line and blue shading) and zonal wind speed averaged over  $70^{\circ}$ - $90^{\circ}$ E,  $5^{\circ}$ N- $5^{\circ}$ S (red line, orange shading). The values of OLR anomaly below  $-10 W/m^2$  and values of zonal wind speed above 5 m/s are shaded, and arrows indicate deep atmospheric convective event.

**Figure 3.5.6:** Maps display the surface circulation with the streamlines and wind vectors of the study region during the peak convective phase of 1994, 1997 and 2006.

**Figure 3.5.7:** Similar to **figure 3.5.4**, for (a) 1994, (b) 1997 and (c) 2006.

**Figure 3.5.8:** Time sires of OLRA anomaly averaged over  $80^{\circ}$ - $110^{\circ}$ E,  $Eq-10^{\circ}$ S (black line and blue shading) and zonal wind speed averaged over  $70^{\circ}$ - $90^{\circ}$ E,  $5^{\circ}$ N- $5^{\circ}$ S (red line, orange shading). The values of OLR anomaly below  $-10 W/m^2$  and values of zonal wind speed above 5 m/s are shaded, and arrows indicate deep convective event.

**Figure 3.5.9:** Maps display the surface circulation with the streamlines and wind vectors of the study region during the peak convective phase of 2003, 2008 and 2012.

**Figure 3.5.10:** Similar to **figure 3.5.4**, for (a) 2003, (b) 2008 and (c) 2012.

**Figure 3.5.11:** Schematics of study region, where red box regions are used to calculate area average MLD (m),  $\Delta\rho$  ( $kg/m^3$ ) and SST ( $^{\circ}$ C). Pinpoint location with number are used to calculate coastal upwelling index where number of each location indicates southern geographical latitude as well.

**Figure 3.5.12:** Monthly time series of area average values in red box regions of **figure 3.5.11**. Panel (a) displays mixed layer depth and panel (b) displays density difference between mixed layer density to density at 100 m depth. The values written on each

plot (right-side) indicates boreal summer-fall long term average (2005-2016) and STD (2005-2016).

**Figure 3.5.13:** Panels (a) to (c) represents daily time series of  $\Delta h_i$  (m) at locations 3S, 6S and 9S marked in **figure 3.5.8**, black line indicates long term mixed layer value and two-sided arrows indicates deep convective events adopted from **figure 3.5.1**. Panels (d) to (e) represents SST anomalies ( $^{\circ}\text{C}$ ) over boxed region of **figure 3.5.8**.

**Figure 3.5.14:** Panels (a) to (c) represents daily time series of  $\Delta h_i$  (m) at locations 3S, 6S and 9S marked in **figure 3.5.8**, black line indicates long term mixed layer value and two-sided arrows indicates deep convective events adopted from **figure 3.5.1**. Panels (d) to (e) represents SST anomalies over boxed region of **figure 3.5.8**.

**Figure 3.5.15:** Panels (a) to (c) represents daily time series of  $\Delta h_i$  (m) at locations 3S, 6S and 9S marked in **figure 3.5.8**, black line indicates long term mixed layer value and two-sided arrows indicates deep convective events adopted from **figure 3.5.1**. Panels (d) to (e) represents SST anomalies ( $^{\circ}\text{C}$ ) over boxed region of **figure 3.5.8**.

**Figure 3.5.16:** Panels (a), (c), (e), (g), (i), (k), (m), (o) and (q) displays Hovmoller plot of zonal wind speed (m/s) at the equator of the Indian Ocean. Panels (b), (d), (f), (h), (j), (l), (n), (p) and (r) displays the Hovmoller plot of sea level anomalies (m) at the equator of the Indian ocean. Line plot adjacent to each sea level anomaly plot displays sea level anomalies at four pinpoint locations ( $1^{\circ}\text{S}$ ,  $3^{\circ}\text{S}$ ,  $6^{\circ}\text{S}$  and  $9^{\circ}\text{S}$ ) along the southern Java and Sumatra coasts marked in **figure 3.5.11**.

**Figure 3.5.17:** Panels (a) to (c) represents OLR difference (black line,  $\text{W}/\text{m}^2$ ) between DMI east box and west box along with Dipole mode index (red dashed line, DMI). Panels (d) to (f) indicates OLR values ( $\text{W}/\text{m}^2$ ) of east box of DMI (black line) and west box of DMI (red line) individually.

**Figure 3.5.18:** Red line in each plot displays SST anomaly of east box of DMI, and black line displays SST anomaly of west box of DMI.

**Figure 3.5.19:** Panels (a) to (c) represents OLR difference (black line,  $\text{W}/\text{m}^2$ ) between DMI east box and west box along with Dipole mode index (red dashed line, DMI). Panels (d) to (f) indicates OLR values ( $\text{W}/\text{m}^2$ ) of east box of DMI (black line) and west box of DMI (red line) individually.

**Figure 3.5.20:** Panels (a) to (c) represents OLR difference (black line,  $\text{W}/\text{m}^2$ ) between DMI east box and west box along with Dipole mode index (red dashed line, DMI). Panels (d) to (f) indicates OLR values ( $\text{W}/\text{m}^2$ ) of east box of DMI (black line) and west box of DMI (red line) individually.

**Figure 3.5.21:** Season averaged OLR values for boreal summer-fall over tropical Indian Ocean. Panel (a) displays OLR values for June to September of neutral 25 years and (b) displays OLR values for June to September of three strong pIOD years.

**Figure 3.5.22:** Location of cyclonic circulation triggered from atmospheric Rossby waves during “bi-weekly” convective event in the study region during June to September of study period (1988-2016). Panel (a) displays locations all event of 1988 to 2016 (b) displays locations of events during pIOD years 1994, 1997 and 2006.

**Figure 3.5.23:** Number of “SETIO cyclones” recorded during the boreal summer-fall of each year (data adopted from table 3.5.2). Red arrows indicate positive Indian Ocean Dipole event years.

**Figure 3.5.24:** Seasonal presence of different values in percentage from June to September. Panel (a) displays presence of OLR anomaly values below  $-10$  ( $W/m^2$ ) averaged over  $80^{\circ}$ - $100^{\circ}$ E and  $2^{\circ}$ N- $10^{\circ}$ S, (b) displays presence of zonal wind speed values above 5 (m/s) averaged over  $70^{\circ}$ - $90^{\circ}$ E and  $1^{\circ}$ N- $1^{\circ}$ S, (c) displays presence of northerly with values above 3 (m/s) averaged over  $97^{\circ}$ - $102^{\circ}$ E and  $00^{\circ}$ N- $3^{\circ}$ S (blue bars) and  $100^{\circ}$ - $104^{\circ}$ E and  $4^{\circ}$ S- $6^{\circ}$ S (orange bars). Blue arrow indicates positive Indian Ocean Dipole events years.

## LIST OF TABLES

**Table 3.1.1:** Table displays DMI value statistics during three strong positive IOD events and three weak/aborted IOD events.

**Table 3.1.2:** Table displays standard deviation of DMI values during different periods and its correlation with the SST anomalies of eastern and western IOD boxes.

**Table 3.3.1:** Percentage values from Histogram of **figure 8** to **figure 11**. The heading in the table can be read as HEW: high energy westerly, W: westerly, HE: high energy easterly, E: easterly, Weak: weak easterly or westerly.

**Table 3.3.2:** Values displayed in Histogram of **figure 14** to **figure 16** in table format for ease of comparison. The heading in the table can be read as HEW: high energy westerly, W: westerly, HE: high energy easterly, E: easterly, Weak: weak easterly or westerly, HES: high energy southerly, S: southerly, HN: high energy northerly, N: northerly, Weak: weak southerly or northerly. Brown shading indicates upwelling favourable component for the particular region.

**Table 3.5.1:** Displays summary of **figure 3.5.18**, **3.5.19** and **3.5.20**.

**Table 3.5.2:** Displays detected cyclonic circulation in lower atmosphere in daily wind fields maps triggered from Rossby wave response during the convective events within the SETIO.

**Table 3.5.3:** Displays summary of values of table 1 and **figure 4**.

## ABSTRACT

This dissertation investigates the physical oceanographic processes related to Indian Ocean dipole mode events, specifically focusing on wind-driven ocean surface circulation and sea level anomalies. The atmospheric and oceanic physical properties are investigated to reveal the dominant processes. Highly unstable nature of tropical climatic conditions attracts the attention of researcher from many years and number of studies have been performed worldwide. Surface wind variability in a tropical climate is one of the most complex phenomena which drive the surface circulation as well. The role of synoptic-scale tropical atmospheric processes triggered from tropical convection is examined which are erratic.

Although, the variability of winds as ocean surface forcing was analysed previously in several studies though the source of its variability and related processes is still unexplored particularly within the eastern tropical Indian Ocean region. Multitemporal and multiresolution satellite data of atmospheric and oceanic properties at the interface is analysed for as long as 30 years of period to precisely disclose the processes involved in the regional wind variability and subsequently the variability of the ocean surface circulation and the ocean surface temperature variability. The in-situ subsurface database arrived later from 2005 for the tropical Indian Ocean regime; hence, subsurface physical properties are incorporated from that year.

The primary results indicate the high interannual and intraseasonal variability of winds along the southern Sumatra coastline along with zonal wind variability over the eastern equatorial Indian Ocean during boreal summer-fall of each year in the study period (1980-2016), where intraseasonal variations are captured using wavelet spectrum for higher precision. The intraseasonal zonal wind variability at eastern equatorial Indian Ocean is known in previous studies though no previous study claimed a precise process which triggers these wind events. This study reveals that high frequency intraseasonal convective oscillations over the southeastern tropical Indian Ocean (SETIO) triggers low latitude synoptic-scale cyclonic circulation in the lower atmosphere which consecutively trigger zonal wind events at the eastern equatorial Indian Ocean. This study is also discovered the intraseasonal wind reversal

along the southern Sumatra coastline during boreal summer-fall under the influence of synoptic-scale low pressure cyclones which I called “SETIO cyclone”.

Simplified coastal upwelling theory along the coast of a finite horizontal length is developed under the direction my supervisor, to explain the coastal upwelling process precisely under the highly varying wind field conditions along the southern Sumatra coastline. This theory requires subsurface stratification and mixing scheme of the subsurface water in the region precisely, though as mentioned above due to the lack of subsurface data in the last century in the study region; hence, a decadal seasonal average values from ARGO data of 2005 to 2016 are used to define mixing depths of the study region. The theory of coastal upwelling defined here discloses why the southern coastal Java upwelling has a more frequent signature in surface oceanic cooling and on the other hand the adjacent southern Sumatra coastline has a rare appearance in surface cooling.

Moreover, I proposed a convective dipole over the same region of IOD boxes, eastern IOD box and western IOD box, and suggest that reversal in the convective dipole is a precursor and not the aftermath of the Indian Ocean Dipole events.

# DECLARATION

I certify that this thesis does not incorporate without acknowledgment any material previously submitted for a degree or diploma in any university and that to the best of my knowledge and belief it does not contain any material previously published or written by another person except where due reference is made in the text.

Signed Ankit Kavi

Date 8<sup>th</sup> August 2019

## ACKNOWLEDGEMENTS

It is impossible to eloquently and succinctly summarize a journey that has taken the last five years and to adequately acknowledge all the people who have supported and guided me through this process. Nevertheless, here is an attempt.

First, would like to offer my profound gratitude to my principal supervisor, A/Prof Jochen Kaempf, for his work in training me to think like an oceanographer and giving me the opportunities and tools to succeed in academia. I sincerely appreciate not only his scientific brilliance when discussing perplexing questions, but also his loyalty and care for me as a person. I am very grateful for his dedication to mentoring me with unconventional in the field, and for supporting me through this process. Jochen Kaempf has been an incredible mentor in modelling and life.

Secondly, I would like to thank and pay the tribute to Late emeritus Professor Matthias Tomczak, who had been very influential in my time here at Flinders University, and I sincerely appreciate the opportunities he has given me to understand fundamentals of Oceanography. Matthias Tomczak has been influential in training me in physical oceanography and helping me analysing deep-sea data.

I am very grateful to be a part of the wonderful community of Stanford EFML; I certainly, could not have completed this journey without all of them. I am grateful to the Flinders University Science and Engineering scholarship for funding me for the first three years. I was also funded by a grant from the Flinders University for the conference travel and teaching support.

On a personal level, this journey has been the most difficult five years of my life. There were many times I did not know if I would be able to complete my degree and I could see a dark ahead. I am grateful to have been surrounded by many colleagues, and a community of friends and family who encouraged me to keep pushing forward and pursue my passion even in the face of difficulty and at times outright despair. A few people who have been especially influential to me include my wife Krupa, my parents, local friends. Finally, my son Hasya continues to provide such joy, inspiration and fun to live; as his birth was in the middle of my candidature which makes all this worthwhile.

I would like to dedicate this dissertation to my beloved parents and grandparents, who always valued education.

As I grow older, I appreciate more and more the people in my life who take the time to look outside themselves and help another. I hope that I have learned to do the same. While this PhD journey has been difficult, I love the work I do. I am so glad I decided to pursue this field of climate and ocean science and am thankful for all the people who have helped me on the way. I am excited to see what the future brings!

Ankit Kavi

Flinders University, Adelaide.

# CHAPTER 1: INTRODUCTION

Weather defines the present condition of atmosphere for example precipitation, temperature, winds etc. at certain place and time. Change is inevitable in nature and weather is the best example as it has tendency to change at each moment. Climate is typical behaviour of weather around a certain place at multiple time scales. "Climate is what you expect, the weather is what you get" (Heinlein, 1974).

## 1.1 Background and relevance

### 1.1.1 Global climate

Variability in climate at millennium scale (1000 years) has caused changes in flora and fauna at large scale throughout the globe. Decadal climate variability has seen dramatic changes in fish catches, diversified vegetation cover and has altered tree species composition. These changes may be attributed to two super El Niño events and several more "normal" El Niño and La Nina in the last century. Which in turn triggers the events like major droughts, severe storms, floods, sea-level rise in the tropical of the globe and have significantly affected species diversity and sustainability.

Coastal sites have measured rise in sea level along with Antarctic sites have documented the decrease of some penguin populations and a rise in other populations as a result of enhanced climatic warming over last 50 or more years. Climate variability has constantly been on investigators' minds. It is little wonder that ecologists recognize climate as a driver of biotic systems (Greenland, Goodin & Smith; 2003). Over the past 30 years, there has been a pattern of increasingly higher average temperatures for the whole world.

Our perception of climate change is as changes in atmospheric variables, like, temperature variation or change in rainfall pattern. The atmosphere is not a standalone system, it interacts with the other component of the Earth system – the oceans, for example. The ocean stores heat and carbon dioxide and redistribute them via its large-scale circulation. Hence, the world's oceans are one of the most important elements in the global climate system. The oceans cover around 70 per cent of the Earth's Surface. In the Northern Hemisphere, about 60% of the surface is the ocean and 40% is the land. In the Southern Hemisphere, the ocean surface is much more dominant

with about 80% being the ocean. This hemispheric asymmetry in land-sea contrast is important to understanding the differences in the ocean circulation and its effect on climate in both hemispheres.

The idea of coupled ocean-atmosphere system is recognised with the discovery of El-Niño which is a coupled system. The questions which drive attention of meteorologist, oceanographer, climate scientist and ecologist, is “What causes climate variability or which component is dominant in climate variability ocean or atmosphere?” El Niño is one of the renowned ocean-atmosphere coupled phenomena that fluctuates the climate and weather patterns which disrupts normal weather patterns, bringing heavy rains and drought to different parts of the world. It is a complex and naturally occurring weather pattern that results when ocean temperatures in the Pacific Ocean near the equator vary from the normal conditions and causes a shift in atmospheric circulation which attracts the scientific community to investigate a climate as a coupled system.

Once the El Niño stage is over, the atmospheric/oceanic conditions swing back to normal state, during this reversal process it is possible that the ocean-atmospheric conditions may (at some instances) reach the intensified conditions of normal state. The intensified state of normal conditions resembles a La Niña stage. Which means a La Niña stage a La Niña stage is an amplification of the normal climatic conditions. Together, the cycling of El Niño and La Niña is called El Niño Southern Oscillation (ENSO). Though El Niño’s strongest impacts are felt around the equatorial Pacific, they can affect weather around the world by influencing high- and low-pressure systems, winds and precipitation. Up to now, typhoons in the Pacific, wildfires in Indonesia and bushfire in Australia, heavy rains and floods in south-eastern India, and flooding of the Mississippi River have been attributed to El Niño.

### **1.1.2 The Indian Ocean**

The global ocean consists of three interconnected ocean basins: The Pacific Ocean, the Atlantic Ocean and the Indian Ocean. The largest connection between these oceans is in the Southern Hemisphere; where the oceans are unblocked by continents. In the tropics a much smaller connection between the Pacific and the Indian Ocean exists through the Indonesian Straits. A connection also exists in the Northern Hemisphere between the Pacific and the Atlantic through the shallow Bering

Strait. The Indian Ocean is the third largest of the world's oceanic divisions, covering about 20 per cent of the Earth's water surface.

The Indian Ocean is in several aspects very different from other Oceans, with the most striking feature is the seasonally changing wind patterns in the northern Indian Ocean region known as monsoons (Tomczak & Godfrey, 2003) which also reverses the ocean surface currents of the region. Moreover, the Indian Ocean is confined with landmasses to its north; hence, it does not reach to the cold region of the northern hemisphere, this situation blocks the northern heat sink of the Indian Ocean. Other features which separate the Indian Ocean from other two big oceans are absent of trade winds at the equator with no equatorial upwelling, lack of any year-round large upwelling system (equatorial or coastal), climatological winds at the equator are westerlies (Schott, Xie, & McCreary, 2009; Tomczak & Godfrey, 2003).

Until the end of last century, it was believed widely that the Indian Ocean and its regional climate has a passive nature in global climate and its influence on global climate was not substantial. The variability of oceanic processes of the Indian Ocean and climatic fluctuations of the region was considered merely from the remote forcings, for example, El Niño. This view has been changed profoundly, particularly since 1997, with new evidence indicating an important climatic role of the Indian Ocean.

By many measures, 1997 was an extraordinary year for the Indian Ocean and the countries on its rim. The highest on record rainfall was received over East Africa during October and November of 1997; causing severe flooding in Somalia, Ethiopia, Kenya, Sudan, and Uganda; leaving large scale devastating effects on flora/fauna and displaced hundreds of thousands of people. On the other side of the Indian Ocean, Indonesia suffered severe droughts at the same time and out of control wildfires broke on several of its islands. Not all these natural calamities were due to the El Niño of the century, but the unusual regional climatic conditions in the tropical IO made them worse. Efforts to determine the physical cause of the extraordinary 1997 event led to rapid progress in understanding the Indian Ocean coupled air-sea systems as an independent mode of climate variability.

The Indian Ocean Dipole (IOD) is a phenomenon that demonstrates the independent mode of climate variability in coupled air-sea systems of the regime,

which explains the inter-annual climate variability of the tropical Indian Ocean region (Saji *et al.*, 1999; Webster *et al.*, 1999). Previous studies; based on the historical observational data (Saji *et al.* 1999; Webster *et al.* 1999; Vinayachandran *et al.* 2002; Saji and Yamagata 2003; Krishnamurthy and Kirtman 2003), modelling (Li *et al.* 2002; Shinoda *et al.* 2004; Lau and Nath 2004; Zhong *et al.* 2005; Cai *et al.* 2005; Behera *et al.* 2008) and theoretical arguments (Li *et al.* 2003; Zhong *et al.* 2005); confirms that the IOD events are a seasonally dependent mode whose phase is locked into the annual cycle of the Asian monsoon system. The IOD events grow rapidly during northern summer, reaches to a mature phase in northern fall, and decays and transforms into a normal SST conditions in subsequent northern winter and spring. The peak strength of the IOD index normally exhibits during boreal fall September/October (Hong *et al.* 2008a; Burns *et al.* 2016).

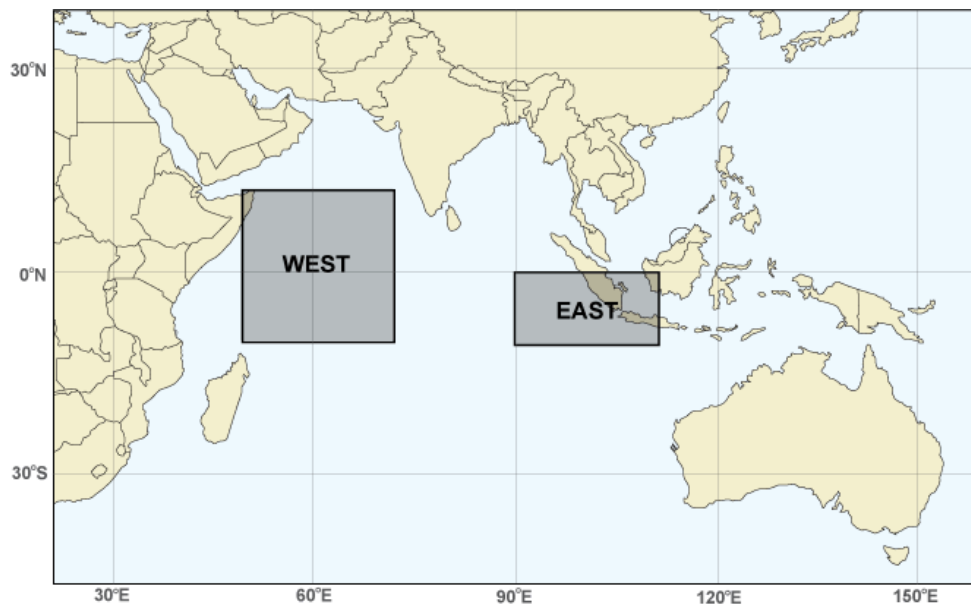


**Figure 1.1.1:** Definition of the surface areas used to calculate the DMI. The western region is defined by (50°E-70°E, 10°S-0°N) and the eastern region by (90°E-110°E, 10°S-0°S).

The Indian Ocean Dipole events are monitored and described by two boxed regions displayed in **figure 1.1.1** where area average SST anomalies (over these boxes) are derived to calculate Dipole mode Index (DMI) (Saji *et al.* 1999; Vinayachandran *et al.* 2002). The positive IOD (pIOD) event is described with cooler sea surface temperature anomalies, lower sea level, and shallower thermocline in the eastern box of the IOD index and warmer SST anomaly, higher sea level, and deeper thermocline in the western box of it compare to normal conditions (Annamalai and

Murtugudde 2003; Vinayachandran *et al.* 2002/2009). The negative IOD (nIOD) event is the opposite, characterized by warmer SST anomalies in the east and cooler SST anomalies in the west (Saji *et al.* 1999; Webster *et al.* 1999; Vinayachandran *et al.* 2002).

The region of a western box of IOD events (**figure** 1.1.1) comprises two distinguished large-scale oceanic features; one is the thermocline Ridge of Indian Ocean (TRIO) and the other is the Somali Upwelling system. Though, most previous studies agree on the fact that SST anomalies of the western box (of the IOD) and related variability of the oceanographic processes are the consequences and not a trigger of the IOD events. Hence, the western box region of the IOD has comparatively passive role in the index. On the other hand, the eastern box regime has comparatively active characteristics, where the eastern equatorial wind reversal and variability of physical oceanographic processes of Java-Sumatra upwelling region are considered as the trigger of the IOD events.

The coastal upwelling of the Java-Sumatra upwelling region is forced by seasonal local alongshore winds associated with prevailing south-easterlies during boreal summer-fall which drives offshore Ekman transport (Susanto *et al.*, 2001). During the rest of the year, reversed wind conditions linked to the boreal winter circulation do not allow upwelling to develop in the region. While, the eastern equatorial upwelling is absent in the Indian Ocean as normal equatorial winds are westerlies. Though, the eastern equatorial Indian Ocean winds suffers reversal during certain boreal summer which develops equatorial upwelling and act as trigger of the pIOD event (Cai *et al.*, 2009 & 2001; Vinayachandran *et al.*, 2009).



## 1.2 Literature review

### 1.2.1 The Indo-Pacific basin

Tropical climate experiences complex fluctuations at interdecadal timescale for example the Pacific Decadal Oscillation (Mantua *et al.*, 2002; Power *et al.*, 1999; Newman *et al.*, 2016; Henley *et al.*, 2015), at interannual timescale for example ENSO and IOD and at intraseasonal time scales for example MJO (Madden and Julian, 1994). The ENSO and IOD have long been recognized as a dominant mode of interannual variability, which strongly influences global and regional climate. ENSO is the typical feature of the tropical Pacific Ocean and IOD is a typical feature of the Indian Ocean tropics. Though, teleconnection between the two systems (ENSO and IOD) through the atmospheric bridge is also part of the ongoing debate.

The Pacific Ocean is the largest ocean on the Earth and dominates the global climate systems through various climatic and physical oceanographic processes; hence, it is also studied the most. The most distinguishable property of the Pacific Ocean is SST distribution in the tropics, where the eastern equatorial Pacific exhibits cold tongue (Hayes *et al.*, 1989) and the warm pool in the west. Moreover, the presence of equatorial trade winds is well known with the persistent westward winds in the equatorial Pacific Ocean. Together with trade winds and south-easterlies along the Peru-Chile coastline the role of upwelling favourable winds and upwelling system in the region is well explored. Under the influence of strongest upwelling favourable conditions, the coastal ocean off Chile and Peru is characterized by the upwelling of cold and nutrient-rich waters (Carr 2001, 2002 & 2003). -The upwelling is induced by the southerlies which drives coastal upwelling at Chile and Peru coasts, and further in the equatorial region it is induced by the equatorial trade winds which drive equatorial upwelling through Ekman divergence (Kämpf, J., & Chapman, P. (2016).

Long-term (1988 – 2016) monthly averages of SST and OLR data of the Indo-Pacific basin is retrieved from NOAA PSD data sets and displayed as Hovmoller plot in **figure 1.2.1** along the equator of both the basins for a typical climatological year. The Pacific Ocean has longitudinal coverage of 120°E to 80°W at the equator, likewise the Maritime Continent has coverage from 100°E to 120°E and the Indian Ocean has the coverage of 40°E to 100°E (**figure 1.2.1**). **Figure 1.3.1a**, confirms the location of the warm pool over the wester tropics of the Pacific Ocean and the cold tongue over

the eastern tropics of the Pacific Ocean. The seasonal climatological cycle of SST over the equatorial Pacific (**figure 1.2.1a**) indicates, the cold tongue weakens in February and March and strengthens from July to November. Conversely, the warm pool weakens in August and September and strengthen from January to April (**figure 1.2.1a**). Over the western Pacific tropical convection (over the warm pool) weakens at the same time from August to November (increased OLR in **figure 1.2.1b**) and strengthen from January to April (**figure 1.2.1b**). Although, the intraseasonal variability of tropical convection may have more dominance in climatic fluctuations.

Atmospheric convection is one of the major factors contributing in the intraseasonal atmospheric variability. The warm pool of the western tropical Pacific causes the evaporation and build deep atmospheric convection, as a result the centre of deep atmospheric convection of the tropical Pacific is located above the western warm pool. Outgoing Longwave Radiation (OLR) data retrieved from satellites can indirectly confirm the location of centre deep tropical convection over the western Pacific warm pool. The OLR data collected by NOAA satellites have been used in this study as a proxy of tropical atmospheric convection. Lower values of satellite derived OLR values in the tropics indicate colder and thicker clouds, which are assumed to be associated with deep convection (Hartgen, 1996).

As a consequence of east west SST gradient of the tropical Pacific Ocean surface winds around the equatorial Pacific is easterly, widely known as trade winds which supports the trading ships in the history. The longitude-time plot of climatological mean (1988 – 2016) of zonal wind speed data (satellite CCMP V2) at the equator of the Pacific Ocean and the Indian Ocean is represented in **figure 1.2.2b**, which confirms the presence of strong surface easterlies over the eastern Pacific and weak easterlies over the Pacific western warm pool.

The large-scale zonal mode circulation of the tropical Pacific Ocean is characterised by surfaces easterlies (“trade winds”) blowing from over the colder eastern Pacific (**figure 1.2.2a**) toward the Western Pacific warm pool (**figure 1.2.2a**). Subsequently, the warm air rises over the warm pool along with updraft of tropical convection (**figure 1.2.1b**). The rising warm air further moves eastward in the upper atmosphere and descends in the eastern Pacific. The closed zonal circulation of

equatorial wind cell is known as the “Walker circulation” (Bjerknes 1969) and schematics of the same is shown in **figure 1.2a**.

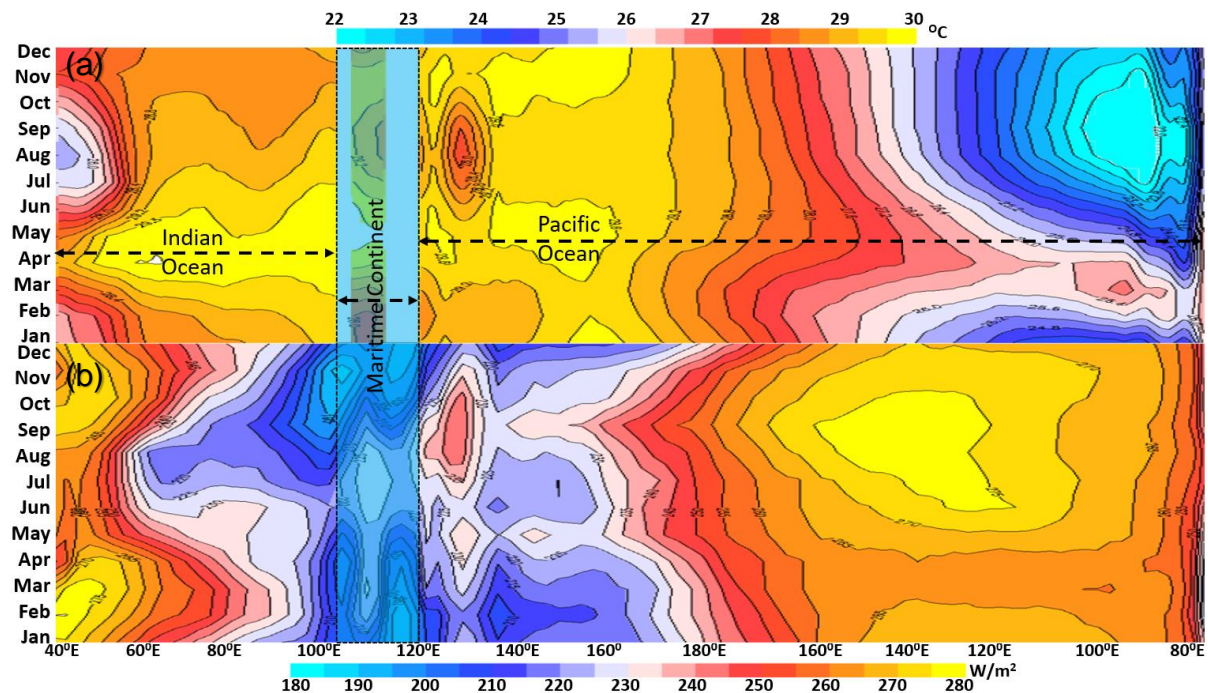


**Figure 1.2.1:** Panel (a) displays the time-longitude plots of monthly climatology of sea surface temperature (SST) at the equator of the Indo-Pacific basin derived from NOAA OI PSD data (1981-2016), and panel (b) represents the long-term climatological values of outgoing long wave radiation (OLR,  $W/m^2$ ) from the NOAA PSD (1980-2016). NOAA High Resolution SST and OLR data can be accessed at the NOAA/OAR/ESRL PSD, Boulder, Colorado, USA, web site at <https://www.esrl.noaa.gov/psd/>.

From the very early era of the physical oceanographic studies, researchers realised the potential of surface equatorial winds in physical oceanographic processes and its impact on climate. The unique ability of zonal component of surface equatorial winds is to trigger the equatorial Kelvin waves, which has vital effects on ocean dynamics and function of global climate. The Kelvin waves modify the heat budget of the thermocline and air-sea interaction. Major tropical climatic fluctuation modes like ENSO, IOD and MJO events can be characterised by variation in the zonal wind, sea surface temperature (SST) and fluctuation of atmospheric convection. Previous studies confirmed the crucial role of abrupt variability of equatorial zonal winds and subsequently triggered the Kelvin waves in all these climatic fluctuations.

The El-Niño Southern Oscillation (ENSO) is the primary mode of interannual variability of the coupled ocean-atmosphere system of the Pacific Ocean. It has two modes El-Niño and La-Nina, during El-Niño surface easterlies weaken and exhibit

reversal from easterlies to westerlies over the western equatorial Pacific, while during La-Nina surface easterlies are intensified. Consequently, the Walker Circulation weakens or reverses during El Niño events and strengthens during a La Niña events.

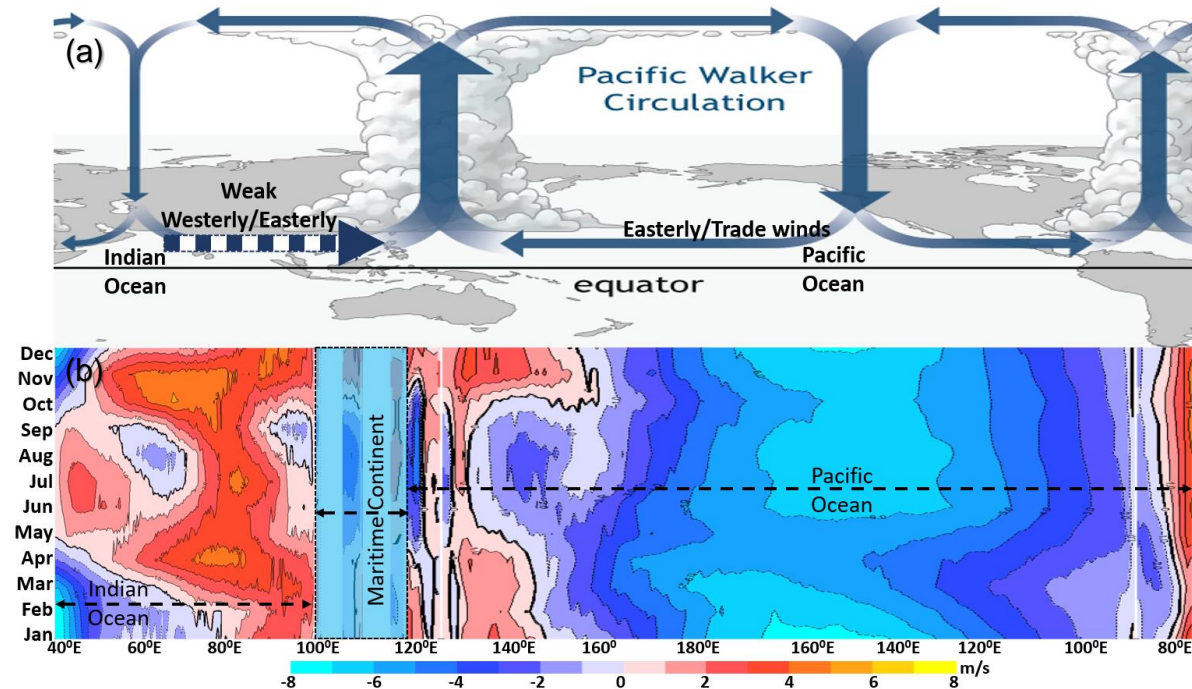


**Figure 1.2.2:** Panel (a) displays the schematics of the Walker circulation over the Pacific and Indian Ocean (Ref: NOAA Climate.gov) and panel (b) displays time-longitude plots of monthly climatology of surface zonal winds at equator of the Indo-Pacific basin, from CCMP V2 data of 1988-2016

Reversal of the equatorial easterlies in the Pacific Ocean to erratic westerlies in the western Pacific is well explored in the context of the El-Niño trigger in several studies. Early studies of Bjerknes (1969) and Wyrtki (1975, 1985) laid the foundation of our current conceptual understanding of the ENSO. It was claimed in previous studies that an increase in central Pacific Warm Water Volume (WWV) or shift of the western tropical Pacific warm pool to the central Pacific leads to a reversal of surface zonal winds (Wyrtki 1975, 1985). Increases in the central Pacific WWV is considered as the important precursors to ENSO events (Cane and Zebiak 1985; Santoso *et al.*, 2019; Holmes *et al.*, 2018; Neske *et al.*, 2018). Bjerknes (1969) suggests that development of a positive SST anomaly over the central equatorial Pacific during an El Niño growth phase induces westerly wind anomalies, which consecutively trigger the equatorial downwelling Kelvin waves and push western warm water to the east and deepen the thermocline in the east. Thereby reinforcing the positive SST anomaly

in the eastern tropical Pacific, and this is closed cyclic process continues up to the El Niño peak phase.

Later in 1997, Jin summarised all the early work performed on the ENSO events by suggesting recharge-discharge oscillator (RDO) theory and proposed ENSO as a self-sustained cycle. As per RDO, during El Niño (La Niña) events, equatorial westerly (easterly) wind anomalies and the eastern tropical Pacific positive (negative) SST anomalies reinforce each other (Bjerknes feedback, 1969). At the same time, as the oceanic adjustment to these altered wind conditions, the ocean acts to discharge (recharge) equatorial upper ocean heat content and leads to a change in the phase of ENSO. The theoretical arguments proposed in the RDO theory have been confirmed later in observational studies by Bosc & Delcroix (2008), McPhaden (2012), Meinen & McPhaden (2000), Meinen & McPhaden (2001). They confirmed that rise in upper ocean heat content (or WWV) of the central equatorial Pacific region (120°E–80°W and 5°N–5°S) leads the ENSO state (SST anomalies) by 1 to 3 seasons. Further in agreement, McPhaden (*et al.*, 2009) suggested the role of heat content as a precursor of ENSO, based on the relation between WWV and ENSO SST explained in RDO.

Despite the existence of the RDO theory, which links the Pacific WWV and ENSO through long-term oceanic adjustments and self-sustained cycle, some aspects of this relationship remain unclear. In the second decade of 21st century Bunge & Clarke, 2014; Horii *et al.*, 2012; McPhaden, 2012; noted that lead time between the Pacific WWV and ENSO SST reduced in the first decade of the 21st century (during 2000 to 2010). Moreover, this change in lead time has also been accompanied by an apparent reduction in the predictive skill of ENSO in the post-2000 period (e.g., Wang *et al.*, 2010; Kumar *et al.*, 2015; Barnston *et al.*, 2012). Furthermore, Kessler (2002) noted that the Pacific climate system can pause for up to two years in a weakly recharged, weak La Niña state, prior to El Niño events, which is far longer than the ocean's dynamic memory of the region. All these studies suggest doubts over the cyclic nature (RDO) of ENSO system and long-term reversible adjusted nature.

In parallel to these studies, Luther *et al.* (1984), Luther and Harrison (1984), Keen (1988), Sui and Lau (1992), Harrison and Giese (1991) suggested that weak easterlies over the western Pacific can episodically reverse and become westerlies. Such abrupt episodes of westerlies can be characterised by a distinct shift in wind

direction and wind speeds with exceeding wind speed magnitude compare to the prevailing easterlies, with variable duration of 2 – 15 days. Later in 2003, Boulanger (*et al.*) demonstrated that 80% of the Kelvin wave signal at 175°E (between 1993–2001) is wind induced rather than being the adjusted contribution of the Rossby wave reflection (as previously claimed in the RDO). Hence, all these studies increased the attention towards abrupt episodes of westerly winds as possible precursors to or triggering mechanism of El Niño/Southern Oscillation (ENSO) (Keen, 1982; Harrison and Giese, 1988). The episodes of westerly winds apply a sudden strong westerly stress over the western equatorial Pacific Ocean. This sudden stress can trigger equatorial Kelvin waves which propagate eastward across the equatorial Pacific (according to equatorial ocean dynamics) and modify SST and depth of thermocline of the eastern equatorial Pacific remotely (Harrison and Giese, 1988; McPhadene *et al.*, 1988).

Though, the fundamental question arises here is, what causes the WWV recharge (discharge) prior to an El Niño (La Niña) events as if the westerly wind events are not part of a self-sustained cycle? In 2016, McGregor (*et al.*, 2016) proposed from his modelling efforts that series of bursts of anomalous westerly winds produce near instantaneous WWV response. Moreover, Neske (*et al.*, 2018) noted from his modelling efforts, anomalous change in WWV is induced from a series of synoptic wind events with specific triggers, rather than cyclic nature and the adjusted response of Rossby waves. Later this situation can be phase locked as reversed Bjerknes feedback and can evolve further. Hence, increase in equatorial Pacific warm water volume (WWV) prior to ENSO events along with westerly wind events (WWE) are now believed to be the primary precursors to the ENSO events (Santoso *et al.*, 2019; Holmes *et al.*, 2018; Neske *et al.*, 2018).

Previous studies have different opinions on the trigger of westerly wind events (WWE) events itself. Keen (1988), Hartten (1996) and McBride (*et al.* 1995) suggested that WWBs can be triggered by tropical cyclones. While many other studies demonstrated that, the convective episodes associated with the passage of the active phase of the Madden–Julian oscillation might be the trigger of WWBs (Zhang 1996; Lin and Johnson 1996; Chen *et al.*, 1996; Zhang 2005, Seiki *et al.*, 2007; Chiodi and Harrison, 2014). They suggested that, during the westerly phase of intraseasonal

oscillation like MJO (Madden–Julian Oscillation), events like WWE can be triggered. Recent studies widely consider these WWBs as the primary trigger of ENSO and related climatic fluctuations.

In the summary the climate of the Pacific Ocean regime can be characterised by a coupled Ocean-Atmosphere system. Where, higher SST, warm pool (WWV), deep convection and surface zonal winds are coupled together and can be described as the Walker Circulation. Intraseasonal oscillation like MJO can disturb this regular setting and trigger abrupt wind events. The purpose of this brief introductory remarks is, though all the ENSO related facts are well known, to understand the tropical climatic processes of the Indian Ocean by relating analogous tropical climate characteristics of the Pacific and to identify the undiscovered secrets of the tropical climate of the Indian Ocean.

### **1.2.2 The voyage from El Niño Southern Oscillation to IOD**

The unique characteristics of the Indian Ocean and surrounding landmass is Monsoons system with unique annual wind reversal system and it dominate the climate of the Indian Ocean and the surrounding countries, which drive annual reversal of surface circulation of the ocean in the region as well (Schott and McCreary, 2001; Shankar *et al.*, 2002, Vinayachandran *et al.*, 2009; Schott *et al.*, 2009). During boreal winter-spring (November-February) winds are north-easterly and during boreal summer-fall (May-September) winds are south-westerly in the tropical Indian Ocean.

Moreover, the tropical warm pool of the Indian Ocean is anchored at the eastern coast, in contrast to the other two oceans, the Pacific and the Atlantic Ocean. The Somali upwelling along the African coast and the absence of significant equatorial upwelling on the eastern side may be the primary reason for this reversed appearance. The warm pool of Indian Ocean has a maximum surface area in April-May and minimum in September (fig 1.3.1a; Vinayachandran *et al.*, 1991; Zhang *et al.*, 2008; Kim *et al.*, 2012; Saji *et al.*, 2015). This single-mode annual cycle of the warm pool is the response of annual northern hemispheric summer heating (Saji *et al.*, 2015).

Annual average winds in the equatorial Indian Ocean is westerly with strong semi-annual westerly component (Wyrtki, 1973). The strong westerly component dominates the equatorial IO in the inter-monsoon period of boreal spring (April-May)

and fall (October-November) (fig 1.3.2b; Wyrтки 1973; Vinaychandran *et al.*, 2009; Schott *et al.*, 2009) which drives strong eastward current along the equator of the IO (Wyrтки 1973; Vinaychandran *et al.*, 2009). Equatorial Indian Ocean is characterised by surface warmer in the east along with a deeper thermocline in the east, which supports a more convective atmosphere than in the west. During certain years, surface water of the eastern Indian Ocean exhibit unusually cold characteristics under the influence of anomalous reversed equatorial “easterly” winds and stronger than normal “south easterly” winds along the southern coast of Sumatra. As a result, the thermocline rises in the region and the atmospheric convection gets suppressed. Simultaneously, the western Indian Ocean exhibits warmer than normal surface water which enhances the atmospheric convection. This coupled see-saw air-sea coupled phenomenon is known as the Indian Ocean Dipole (IOD).

The Indian Ocean dipole (IOD) mode (IOD; Saji *et al.* 1999; Webster *et al.* 1999, Vinayachandran *et al.*, 1999) is one of the most important interannual climate mode and it is defined by basin-scale pattern of surface and subsurface temperature anomalies that seriously affects the interannual climate of the region. The IOD has devastating effects on the regional climate of many nations around the Indian Ocean rim, as well as the global climate system (Yamagata *et al.* 2004). It is a coupled ocean-atmosphere phenomenon in the tropical Indian Ocean (Saji *et al.*, 1999; Rao *et al.*, 2002; Yamagata *et al.*, 2002) with vast impact on the climate of areas around the Indian Ocean (Ashok *et al.*, 2001; Zubair *et al.*, 2003; Behera and Yamagata, 2003; Saji and Yamagata, 2003, Cai *et al.* 2009, Du *et al.*, 2012, 2013). It has been the subject of thorough study and sometimes of scientific debate concerning its dependence/independence on/from the El Niño–Southern Oscillation since it was first clearly revealed (Saji *et al.*, 1999; Meyers *et al.*, 2007). Our understanding of the dynamics of the IOD has improved rapidly during the past two decades and has been thoroughly summarized by Yamagata *et al.* (2004) and Vinaychandran *et al.* (2009). There has been an increase in the IOD frequency and strength in recent decades (Abram *et al.* 2008; Cai *et al.* 2009; Xie *et al.* 2010; Zheng *et al.* 2010; Du *et al.*, 2013).

There is a wider perception of the IOD events that they are co-occurring with ENSO events. Though studies suggest that some (but not all) positive IOD events occur during the same year as El Niño, and the same can be said about negative IOD

events and La Niña (Yamagata *et al.* 2004). The previous studies and modelling results suggest that at least fifty per cent of IOD events triggered in last century were co-occurred with the ENSO (Yamagata *et al.*, 2004; Meyers *et al.*, 2007; Vinaychandran *et al.*, 2009; Du *et al.*, 2013) and the trigger of these IOD events are from the altered climatic condition due to the ENSO. Though, the trigger mechanism of the other fifty per cent events is still ambiguous. Meyers *et al.* (2007) noted that the positive mode of the IOD event can be triggered by either an anomalous shallow thermocline from remote forcing and/or an anomalous strong easterly wind along the Java coast which results in stronger than normal upwelling flowed by regional cooler SSTs. Similar growth and maintenance mechanisms of the IOD are described in coupled modelling studies of Gualdi *et al.* 2003; Annamalai *et al.* 2003; Yamagata *et al.* 2004; and Cai, Hendon and Meyers 2005.

A positive IOD event is associated with anomalously cool SST in the southeastern Indian Ocean and relatively warm SST in the central or western equatorial Indian Ocean. An IOD event normally triggers during boreal summer (May/June), peaks in fall (October) and terminates in early winter (December) (Saji *et al.*, 1999; Yamagata, 2007; Meyers *et al.*, 2007, Vinaychandran *et al.*, 2009). Unlike the El Niño events, all IOD events do not follow the seasonal cycle identically as previously they displayed late mature stage and early termination number of times (Rao and Yamagata, 2004, Meyers *et al.*, 2007, Rao *et al.*, 2007; Du *et al.*, 2013). The easterly wind anomalies are also developed in the eastern equatorial Indian Ocean along with upwelling-favourable alongshore wind anomalies off Sumatra during positive IOD conditions (Vinayachandran *et al.*, 2002, 2009; Feng and Meyer 2003).

Du *et al.*, (2008) noted that the most significant negative SST anomaly developed in the eastern basin of Indian Ocean in positive IOD event years, near the coast of Java and Sumatra consecutively the SST anomaly values may drop below -3°C in the coastal region and below -1°C for entire eastern IOD box (fig 1.2.1). Hence, the positive phase of Indian Ocean Dipole (IOD) events, which is characterised by a cold SST anomaly in the eastern box of the IOD, depends on this infrequent southern Sumatra coastal upwelling. They also noted that during the 1994 and 1997 positive IOD events, cold wedge formed in the eastern equatorial Indian Ocean and extending to the west of 90°E.

The eastward equatorial jets over central equatorial Indian Ocean at intermonsoon periods (Wyrtki, 1973) pile up warm saline water in the eastern equatorial Indian Ocean and create the equatorial warm pool of the tropical Indian Ocean. With the presence of the warm pool, the eastern equatorial Indian Ocean characterised by higher sea surface temperature (SST) and a deep thermocline. Vinayachandran *et al.* (2009) suggested that the presence of warm surface water and deep thermocline in the region eastern equatorial upwelling cannot develop in the Indian Ocean.

However, seasonal coastal upwelling can develop along the southern Sumatra and Java coastline and can extend up to the equator in certain years (Susanto *et al.*, 2000; Delman *et al.*, 2016). Climatological winds at off Java and Sumatra exhibit seasonal reversal following unique Indian Ocean monsoon system. Driven by seasonal south-easterly winds during boreal summer, seasonal coastal upwelling tends to occur along the southern Java, and southern Sumatra coastline from June to October (Susanto *et al.*, 2000) and is eventually terminated by the reversal of winds associated with the onset of the northwest monsoon in October. Though, later studies identified that coastal upwelling along the southern Sumatra coastline is not a regular feature, it appears rare during strong pIOD event (Chen *et al.*, 2016; Delman *et al.*, 2016).

The strong upwelling and cooler SSTA developed in the south-eastern tropical Indian Ocean (SETIO), in 1994, 1997 and 2006 pIOD events (Saji *et al.*, 1999; Webster *et al.*, 1999; Murtugudde *et al.*, 2000; Vinaychandran *et al.*, 2009) evidently influenced the climate of many adjacent and remote regions to the Indian Ocean, including Indonesia, East Africa, Australia, East Asia, Europe, and South America (Ashok *et al.*, 2003; Black *et al.*, 2003; Clark *et al.*, 2003; Saji and Yamagata, 2003; Yuan *et al.*, 2008; Chan *et al.*, 2008; Ummenhofer *et al.*, 2009; Kripalani *et al.*, 2010; Cai *et al.*, 2011). These studies indicate that rarely developed stronger seasonal upwelling along the southern Sumatra coastline is coupled with the prominent Java upwelling during boreal summer-fall and can significantly drop the SST values of the eastern equatorial warm pool. Though, the climatic and physical oceanographic processes and the trigger of IOD events are under speculations.

The weaker or aborted pIOD events with weaker SSTA and smaller temporal extent in the southeastern tropical Indian Ocean were also recorded in years 2003 (Senan *et al.*, 2003), 2007, 2008 (Cai *et al.*, 2009; Luo *et al.*, 2008), 2011 and 2012 and they are characterised as the weaker seasonal coastal upwelling along the southern Sumatra coastline. During the weaker pIOD events, negative SST anomalies cannot expand within the entire eastern IOD region (Du *et al.*, 2012, 2013, Delman *et al.*, 2016).

Chen *et al.* (2016) and Delman *et al.* (2016) noted seasonal upwelling along the southern Java and southern Sumatra exhibit strong interannual variability. The driving factor or processes behind this interannual variability of seasonal coastal upwelling in the region is still unclear, and the mechanism which governs the different spatial extent of negative SST anomalies during each event in the region is also ambiguous.

The variation of subsurface temperature within the thermocline depth plays an important role in the growth and maintenance of positive and negative SST anomaly patterns during the IOD events. Yamagata *et al.* (2004) suggested from coupled numerical models that the IOD can grow by ocean-atmosphere interaction with the involvement of the thermocline temperature anomalies (Yamagata *et al.* 2004). Subsurface observational studies of the depth of the thermocline always suffer scarcity of data in the region; nevertheless, observations studies have shown that the thermocline experiences large vertical displacements beneath both poles of the dipole and the displacements are correlated to the local SST anomalies (Meyers 1996; Rao *et al.* 2002; Xie *et al.* 2002; Feng and Meyers 2003). Feng and Meyers 2003 suggested that both remote forcing and the local wind are factors in the generation of the negative SST anomalies of the eastern pole during the pIOD events. Hence, negative SST anomalies can develop in the region when the wind is favourable for upwelling along the coast of southern Java and Sumatra along with the shallower thermocline due to remote forcing.

Modelling studies explored the role of Wyrтки Jets in thermocline variability of the SETIO in the year 2002 (Masson *et al.*, 2002), and suggested that inter-monsoon Wyrтки jets inject high saline surface water of western tropical Indian Ocean into the eastern tropical Indian Ocean. They also noted (Masson *et al.*, 2002) that, the pumped high saline water can subduct up to the pycnocline which creates intermittent “barrier

layer in the region (Sprintall and Tomczak, 1992; Masson *et al.*, 2002, Qu and Meyers, 2005) and can deepen thermocline in the eastern equatorial Indian Ocean region. Furthermore, the SETIO region is influenced by a large amount of freshwater flux from the Bay of Bengal and the Indonesian throughflow (Sprintall and Tomczak, 1992; Sengupta *et al.*, 2006). Potemra *et al.* 2016, using sea surface salinity data of satellite observations (Aquarius), suggested a seasonal existence of freshwater flow from Sunda Strait to the SETIO region.

The year-round freshwater flux into the SETIO region and saline water flux from inter-monsoon Wyrki jets, develop strong vertical haline stratification with subsurface salinity maximum in the region. This scenario causes density mixed layer (ML) shallower than surface isothermal layer (IL) (Sprintall and Tomczak, 1992). The intermediate high saline water layer, between ML and IL, is referred to as the barrier layer (BL), a unique characteristic of SETIO (Godfrey and Lindstrom, 1989). Previous modelling studies suggested that the barrier layer can behave as a blockade to turbulent entrainment of the cold thermocline water into the ML in upwelling scenario; hence its presence can have a significant impact on upwelling feedback to SST (Masson *et al.*, 2002; Du *et al.*, 2005). A recent subsurface analysis in the SETIO region, from ARGO float profiles, suggested, that presence of barrier layer and its variability affect air-sea interactions during the mature phase of IOD events (September-November) (Qiu *et al.*, 2012). Though, it is unclear still unclear that up to how much extent (remnant) barrier layer can influence the progress of upwelling in the SETIO and resultant pIOD events.

### **1.2.3 Upwelling**

The California Current System, running along the North American West Coast, hosts a rich and diverse marine ecosystem that provides considerable socioeconomic benefit. The process underlying this exceptional biological productivity is wind-driven coastal upwelling, which delivers deep, nutrient-rich water to the sunlit surface layer and stimulates growth of phytoplankton that form the base of the marine food web.

Winds blow across the ocean surface and push the top layer of the ocean water away which develops surface ocean currents. Around coastal region, when the ocean surface layer is pushed away by the local winds it needs to be replaced, then water rises up from beneath the surface layer to replace the surface water that was pushed

away. This process is known as “upwelling.” Sustained winds in a consistent direction over the ocean move the top layer (about 100 meters depth) of seawater. Coastal upwelling produces about half the World’s fish supply. Major coastal upwelling regions (e.g. the Peruvian) are located at the eastern margins of subtropical ocean gyres and are governed by classical wind-driven upwelling dynamics (Mann and Lazier, 1996; Kämpf et al., 2004).

In 1902, Ekman first theorized this phenomenon in accordance with earth’s rotational effects known as Coriolis effect and water layers frictional effects. When surface water molecules move away by the force of the wind, they, in turn, drag deeper layers of water molecules below them. Each layer of water molecules is moved by friction from the shallower layer, and each deeper layer moves more slowly than the layer above it, until the movement ceases (approximately at a depth of about 30-100 meters), which depends of strength of surface wind and density of the ocean surface layer.

Unlike the surface water, the deeper water is deflected by the Coriolis effect to the right in the Northern Hemisphere and to the left in the Southern Hemisphere. As a result, each successively deeper layer of water moves more slowly to the right (or left, according to hemispheric location) creating a spiral effect and entire swirl movement of the surface ocean layer is known as Ekman Spiral (**figure 1.2.3**). Because the deeper layers of water move more slowly than the shallower layers, they tend to “twist around” and flow opposite to the surface current.

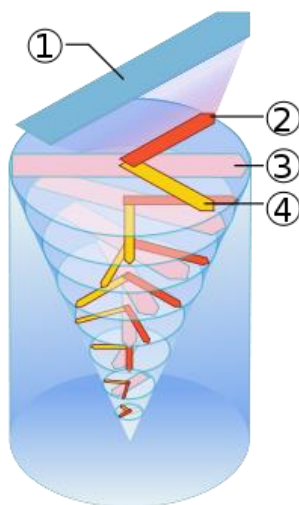


**Figure 1.2.3:** Schematics of Ekman spiral effect, where (1) displays surface wind direction, (2) net wind force direction from above, (3) effective (net) direction of the surface current and (4) direction of Coriolis effect.

Net horizontal transport of upper ocean layer that occurs under certain wind conditions is known as Ekman transport. It is named after Swedish oceanographer Vagn Walfrid Ekman, who first described the phenomenon in 1902. Along the coastal area where Ekman transport moves surface waters away from the coast, surface waters are replaced by water that wells up from below and the process known as “**coastal upwelling**”. An example of typical coastal upwelling process in the Northern Hemisphere is shown in **figure 1.2.4**, where the surface ocean layer moves to the right of the wind direction. In the southern hemisphere, the seawater layer moves to the left of the wind direction, under the influence of the reversed Coriolis effect.

Water that rises to the surface as a result of upwelling is typically colder and is rich in nutrients. These nutrients “fertilize” surface waters, meaning that these surface waters often have high biological productivity. Therefore, good fishing grounds typically are found where upwelling is common (Kämpf, J., & Chapman, P., 2016).

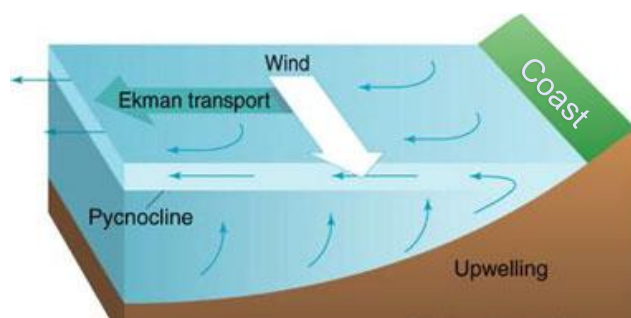


**Figure 1.2.4:** Schematics of typical coastal upwelling system in northern hemisphere.

If the coastline is to the right of the wind direction, and the winds persist for more than a day, a 'coastal upwelling' process draws up colder and more nutrient-rich water from the depths of the ocean to the surface. The longer the winds persist, and the longer the stretch of coastline that experiences a similar wind direction, the colder water brought to the surface. This upwelled water can last for days (or longer) until wind conditions change and the seawater mixes. The reverse process (downwelling) can also occur, bringing warmer water towards the coast from boundary currents such as the East Australian Current or Leeuwin Current (Smith et al. 1991).

Given the ecological importance of upwelling, indices designed to monitor its intensity were introduced during early era of physical oceanographic research. The strength of an upwelling process can be calculated based on estimates of wind speed. Using such data, Andy Bakun (1973) developed the coastal Upwelling index. The

Upwelling Index is, as its name implies, a measure of the volume of water that upwells along the coast; it identifies the amount of offshore transport of surface waters due to geostrophic wind fields. More details and mathematical formula of the Upwelling Index is displayed and discussed in section 2.3.1.

### **Ekman Divergence/convergence (for open ocean)**

In open ocean wind-induced currents are among the strongest currents in the oceanic surface layer. Furthermore, the depth-integrated Ekman transports is among the most important causes of flow in the deeper layers as well, within the upper 500-1000 meters of the ocean. The reason behind this situation is the Ekman transports converge in some regions and diverge in others, and vertical flow develops at the bottom of the surface boundary layer to replace or remove the converging water masses. This process of generation of flow below the surface layer through vertical movement into and out of it is known as Ekman pumping/suction (Tomczak, M., & Godfrey, J. S., 2013; Kämpf, J., & Chapman, P., 2016). This process has strong rank for the distribution of hydrographic properties below the surface layer. Variations of Ekman layer transport can result from two factors, the change of the Coriolis parameter with latitude and the structure of the wind stress field. In most situations the variation of Coriolis parameter is small and Ekman pumping/suction is dominated by spatial variations of wind stress strength and direction.

#### **1.2.4 The equatorial Indian Ocean winds**

The eastern equatorial Indian Ocean regime is characterised by the warm pool of the Indian Ocean. The warm pool of the Pacific Ocean displays highly variable tropical convective activities and zonal wind events over the region. Such high-frequency convective events and consecutively triggered zonal wind variations are not discussed in detail over the Indian Ocean warm pool region, particularly during boreal summer-fall.

The surface equatorial winds are considered weak easterly or westerly in most previous studies especially over the eastern equatorial Indian Ocean (EEIO) (Schott *et al.*, 2009; Vianaychandra. P. *et al.*, 2009; Delman *et al.*, 2016; Chen *et al.*, 2016). The zonal winds during the Wyrcki jets period are exempted from this consideration in the previous studies. The principal argument behind this consideration is to explain

the ocean-atmospheric processes related to the positive mode of Indian Ocean Dipole events. In positive phase of IOD (pIOD) eastern pole Indian Ocean experience surface cooling from coastal and equatorial upwelling (Saji *et al.*, 1999; Webster *et al.*, 1999; Murtugudde *et al.*, 2000; Susanto *et al.* 2000). They also suggest that the surface cooling of the eastern equatorial Indian ocean shifts tropical convection to western equatorial Indian Ocean region which consecutively triggers surface easterlies to further support the rare equatorial upwelling (Webster and Lukas, 1992; Izumo *et al.*, 2010; Kim *et al.*, 2012; Chen *et al.*, 2015).

The southeastern tropical Indian Ocean (SETIO) region is located at the eastern end of the Indian Ocean equatorial waveguide, hence vulnerable to equatorial Kelvin Waves related activities from remote forcing. The Kelvin waves propagate eastward (if triggered by abrupt easterlies/westerlies) on the equator and later towards the coasts of Sumatra and Java as coastal Kelvin waves. The Kelvin wave activities at the equatorial Indian Ocean are documented widely (Qiu *et al.*, 1999; Murtugudde *et al.*, 2000; Iskandar *et al.*, 2005, 2006; Sengupta *et al.*, 2007; Chen *et al.*, 2015; Delman *et al.*, 2016), and is also considered as the dominant forcing of variability of sea level and thermocline depth of the SETIO region (Sprintall *et al.*, 2000; Susanto *et al.*, 2001; Murtugudde *et al.*, 2000; Iskandar *et al.*, 2005; Chen *et al.*, 2015; Delman *et al.*, 2016). Sprintall *et al.* (2000) analysed the equatorial and subsequently coastal Kelvin wave activities of the Indian Ocean triggered from the equatorial zonal wind events with the measurements of the pressure gauges of the Indonesian seas and offshore moorings.

Later studies have documented this kind of abruptly stronger wind events in the equatorial IO. Senan (*et al.*, 2003) noted the presence of high-frequency westerly wind bursts (WWBs, 10 – 40 days longer) at equatorial IO in the early stage of northern summer monsoon season, from 2000 to 2002. They named it “monsoon jets” and noted that this WWBs were associated with the intraseasonal oscillations (ISO) of the northern summer monsoon. With the advent of high frequency (in the temporal domain) satellite data later studies (after Senan *et al.*, 2003) reveal that the eastern equatorial Indian Ocean is vulnerable zonal wind events during boreal summer-fall. Abrupt zonal wind events can trigger equatorial Kelvin waves and it was reported in many previous studies of the equatorial Indian Ocean from correlation statistics

between sea level anomalies (SLA) of the eastern equatorial Indian Ocean and zonal wind fields of the same region (Rao and Yamagata, 2004; Iskandar *et al.*, 2005, 2006; Sengupta *et al.*, 2007; Chen *et al.*, 2015; Delman *et al.*, 2016).

Once the region of wind variability is identified the temporal characteristics of the eastern equatorial zonal wind events were explored. Rao and Yamagata (2004) proposed the longer duration of strong westerlies with temporal coverage of 64 days and suggested the intraseasonal disturbance (ISD) as trigger mechanism and proposed that the ISD is the reason of the early termination of developing pIOD event of the year 2003. Iskandar (*et al.* 2005) performed the investigation of the equatorial Indian Ocean winds using wavelet analysis and noted that intraseasonal atmospheric disturbances over the eastern Indian Ocean during the boreal summer can trigger equatorial and coastal Kelvin waves. They noted that high-frequency zonal wind events with a life span of 20 – 40 days are triggered between 70°E to 90°E on the equatorial Indian Ocean which is responsible for the sea level variation along the southern Java and Sumatra Coast. Later Chen *et al.*, 2015, 2016 and Delman *et al.*, 2016 attempted the intraseasonal and interannual variability of the zonal wind over the eastern equatorial Indian Ocean for a decadal length. They performed the statistical correlation of zonal wind of the eastern equatorial Indian Ocean and the sea level anomalies (SLA) of the eastern Indian Ocean and the SETIO region, which indicates the notable correlation between SLA and the zonal wind events of the eastern equatorial Indian Ocean.

### **1.2.5 Tropical convection and MJO**

The tropical convective activity is the fundamental phenomena with high variability at intraseasonal time scale with erratic nature. Previous studies noted that the fundamental forcing behind the atmospheric ISVs is associated with atmospheric intraseasonal oscillations (ISOs) known as the Madden–Julian Oscillation (MJO) as the dominated mode (Madden and Julian 1971; Hendon and Glick 1997; Webster *et al.* 2002; Shinoda *et al.* 2013). The MJO is the dominant mode of tropical climate fluctuations with 30-60-day time scale. The MJO can be characterised as the westward propagation of convective activity and related surface wind over the Indian Ocean and consecutively over the Pacific Ocean and several times a year the MJO is a strong contributor to various extreme events throughout the globe.

The MJO is recognised as the symbol of abrupt intraseasonal tropical instabilities over the Pacific Ocean and the Indian Ocean. According to the mechanism of MJO, it evolves in eastern tropical IO, and progresses eastward over the tropical IO, though related abrupt westerly or easterly wind events, as evident in the Pacific, were never discussed widely. Many studies discussed Indo-Pacific teleconnection through an atmospheric bridge, but there is a lack of discussion about abrupt wind events like wind bursts over tropical IO. The abrupt, short-lived wind events are long known in Pacific as the primary predictor of ENSO, though these events were received very little attention over the Indian Ocean regime.

On the other hand, some studies suggested that in boreal summer, particularly during June to September period, MJO (Madden–Julian Oscillation) is weaker or non-active (Madden and Julian, 1971; Webster *et al.*, 2002; Wheeler and Hendon, 2004; Chen *et al.*, 2015). Kikuchi and Wang (2009), Shukla (2014) and Adams (*et al.*, 2016) noted that mean atmospheric columnar moisture content shifts towards summer hemisphere in boreal summer particularly over the tropical Indian Ocean; hence, consecutively triggered dominant convective intraseasonal oscillation exists over the northern hemisphere of Indian Ocean.

Though, Rao and Yamagata (2004) noted, from wavelet analysis, that the zonal wind variability in the eastern equatorial Indian Ocean is directly linked to the convective activities over the same region. Other studies claimed the intraseasonal convective fluctuations over the eastern equatorial Indian Ocean during the boreal summer as the forcing of the wind events (Iskandar 2005; Duan *et al.*, 2013; Chen *et al.*, 2015, 2016, 2017). They claimed that the fluctuations of tropical convective activity over the warm pool of the Indian Ocean is the forcing of the atmospheric intraseasonal variation (ISV) though no studies provide clear evidence on this forcing.

Moreover, some of the previous efforts on analysis of spectral structure of the zonal winds and convective activity over the tropics of the Indian Ocean and the western Pacific Ocean reveals the dominant presence of 10–20-day oscillation mode during boreal summer-fall around the equatorial region (Murakami and Frydrych 1974; Murakami 1975; Zangvil 1975; Krishnamurti and Bhalme 1976; Krishnamurti and Ardanuy 1980; Chen and Chen 1993; Kiladis and Wheeler 1995; Numaguti 1995; Wen and Zhang, 2007).

Further, Vinaychandran *et al.* (2009) noted that convection over the eastern and western Indian Ocean during the monsoon behaves like a seesaw; enhancement of one is associated with the suppression of the other. Hence, there is a need to understand the variability pattern of atmospheric convection in this region, particularly during the summer monsoon and its probable role in taking IOD events to maturity through the ocean-atmosphere coupling in this region.

In the 1970s and 1980s high-frequency mode of intraseasonal oscillation was explored in the tropical IO during the northern summer monsoon, known as 10-20-day mode of Indian Monsoon (Chen and Chen, 1993). Wen and Zhang (2007) and Chatterjee and Goswami (2004) also confirms the presence of high frequency convective coupled zonal wind oscillation mode over the eastern equatorial Indian Ocean during boreal spring and summer (March to May). Though, none of the previous studies discussed the existence of this convective coupled any mode of zonal wind oscillation in the southeastern tropical Indian Ocean (SETIO) particularly during boreal summer-fall (June to September) which can claim the zonal wind events exclusively.

### 1.3 Aims and objectives

There is a wider perception the IOD events are co-occurring with ENSO events from the previous studies and modelling results which suggest that at least fifty per cent of IOD events triggered in last century were co-occurred with the ENSO (Vinaychandran *et al.*, 2009) and the trigger of these IOD events are from the altered climatic condition due to the ENSO. Though, the trigger mechanism of the other fifty per cent events is still ambiguous.

The inclusive objective of this study is to characterise of ocean-atmosphere coupled system in the tropical Indian Ocean from the statistical analysis of physical parameters and explore the undiscovered processes related to Indian Ocean Dipole (IOD) events from oceanic perspective. As the starting point, I characterise the physical oceanographic processes in the eastern box of the IOD events which dominate during a neutral phase of the Indian Ocean and other processes which dominates the positive phase of the Dipole mode events. Likewise, the atmospheric conditions and surface wind circulation are also explored during the neutral and positive phase of the dipole mode.

Investigation of sea-surface temperature and surface winds are performed to reveal the dominating physical parameter which governs the climatic processes during different mode of climatic conditions, neutral or positive mode dipole. Role of tropical convective variability in wind variability is known for a long time and investigated thoroughly for the tropical Pacific though this relationship is unexplored over the southeastern tropical Indian Ocean during boreal summer-fall. This study investigates the intraseasonal convective phases over the southeastern tropical Indian Ocean during the boreal summer-fall and establishes its relationship with regional wind events. The entire results and discussion are covered in a single chapter, chapter three, comprising five individual sections.

The primary purpose of section 3.1 is to characterise the different climatic conditions during the neutral and positive IOD phases using sea surface temperature anomalies of the tropical Indian Ocean at interannual and intraseasonal time scale.

In section 3.2 focusses on the climatic conditions of the eastern tropical Indian Ocean to define its role in the dipole mode conditions by analysing the regional sea

surface temperature anomalies and surface wind conditions and identify the knowledge gaps in the regional climatic processes which can explain the different climatic modes in the Dipole mode outlook.

The aim of section 3.3 is the statistical analysis of surface winds of the eastern tropical Indian Ocean at interannual and intraseasonal time scale as forcing parameter of coastal and equatorial upwelling. The multiplatform cross calibrated daily satellite wind data (CCMP V2) provided by REMSS from 1988 to 2016 are used to analyse the interannual and intraseasonal characteristics of zonal winds over the eastern equatorial Indian Ocean during the boreal summer-fall season. Similar satellite wind data is used to explore the interannual and intraseasonal behaviour of surface winds along the southern Java and southern Sumatra coastline during the boreal summer-fall season.

The aim of section 3.4 is to identify the processes and parameters which governs the intraseasonal and interannual surface wind variability of the study region. The relation of tropical convection wind regional wind variability is known for a long time. The outgoing longwave radiation (OLR) data from multiplatform satellites provided by NOAA atmospheric science division are used to analyse the convective events of the region and to establish its relationship with regional wind variability. Daily OLR data for the period of 1988 to 2016 are analysed to characterise the convective events over the study region during boreal summer-fall and to analyse its role regional surface wind variability at intraseasonal time scale.

The aim of section 3.5 is to reveal the role of synoptic-scale anomalous cyclonic circulation triggered by convective events in upwelling processes of the region and relation to the dipole mode conditions. The event analysis approach is followed in the section to explain the ocean response to the different mode of atmospheric circulation. A simple theory of coastal upwelling at the coast with finite horizontal length, developed in collaboration with my supervisor, is used to explain the physical oceanographic processes in the region. The southern Java-Sumatra coastal upwelling region is analysed using the simplified coastal upwelling theory to explain the surface and sub-surface physical oceanographic processes and the irregular ocean response at interannual time scale is explored which contributes largely in the positive Dipole

mode index (DMI). The prime objective here is to investigate the triggers of the rare appearance of the coastal upwelling along southern Sumatra coastline.

The section is concluded with a composite view of all the cyclonic events triggered from convective episodes during the study period (1988-2016) with the presence of the events at interannual time scale is analysed, and its relationship with the dipole mode conditions are explored. The data sets and methodology used in the study are elucidated in the next chapter 2.

# CHAPTER 2: METHODOLOGY

## 2.1 Overview

The advent of high-resolution satellite era from 1980 changes the long-term scarcity of high-quality data in the physical oceanographic and climatic research. From early 2000, the dawn of ARGO profile networks puts the subsurface observation also in the category of high-quality data network, though they suffer from spatial coverage till the first decade of this century. This study performer the physical oceanographic research with thorough use of the multi-temporal satellite and in-situ subsurface data sets. The high-quality sea surface temperature data is available from 1982 and surface wind data is available from 1988 over the tropical Indian Ocean; hence, this study performs the analysis covering the period from 1988 to 2016.

## 2.2 Data sources

The surface wind analysis is performed in this study using daily cross-calibrated multiplatform (CCMP) satellite ocean surface wind vectors version V2 derived from CCMP Version-2.0 vector wind analyses, produced by Remote Sensing Systems (Atlas *et al.*, 2011). CCMP results and satellite data used in this study are available freely from Remote Sensing Systems via our website ([www.remss.com](http://www.remss.com)).

The Cross-Calibrated Multiplatform (CCMP) ocean surface wind data set was originally developed by Atlas (and coworkers) to blend cross-calibrated satellite winds, in situ data, and wind analyses from numerical weather prediction. CCMP uses a variational method to blend information from satellite wind retrievals, in situ wind measurements, and a background wind field from a numerical weather analysis to produce a gap-free estimate of vector winds over the world's oceans. CCMP Version 1.1 was originally developed in the late 2000s using a combination of the ERA-40 reanalysis and the European Center for Medium Range Weather Forecasting operational analysis as the background wind vector field and a variety of satellite wind speed/vector data sets (Atlas *et al.*, 2011).

CCMP Version 2.0 is an upgraded version that uses accurately intercalibrated winds from Remote Sensing Systems (Wentz, 2013, 2015) and exclusively uses a background field from the ERA-Interim reanalysis (Dee *et al.*, 2011) and included

several newer satellites that were not used for V1.1. These two changes lead to an improvement in long-term stability, though significant problems remain even in the improved product (McGregor et al., 2017). The details quality of the wind product and minor problems with accuracy of the CCMP V2 data set is discussed in detail in studies of McGregor et al. (2017) and Mears et al. (2019). In this study we used CCMP V2.0 (NO BUOY) version to avoid discrepancies in sensitive details as per the suggestion of Mears et al. (2019).

The sea surface temperature analysis of this study is based on NOAA OI SST V2 High Resolution SST data provided (NOAA/OAR/ESRL PSD) (Reynolds et la., 2007). Data are available at <https://www.esrl.noaa.gov/psd/>.

Interpolated OLR data provided by the NOAA/OAR/ESRL PSD (Boulder, Colorado, USA) are used to investigate tropical convective activity in this study (Lee, H.-T., 2014). Data are available at <https://www.esrl.noaa.gov/psd/>. The weekly SSH anomalies (SSHAs) available since October 1992 from AVISO (Archiving, Validation, and Interpretation of Satellite Oceanographic) from multi-platform satellite altimeter, and they are used form 1993-2016 in this study. (<https://www.aviso.altimetry.fr/en/my-aviso.html>). The grid resolution of surface winds, SST and OLR is  $0.25^{\circ}$  and for SSHA it is nearly  $1/3^{\circ}$ .

## 2.3 Theories

The classical coastal upwelling index and the theory of coastal upwelling along a finite horizontal length of coastline is systematically applied in this study to understand the response of the upper layer of the ocean in the study region to the local and remote wind variability. It precisely demonstrates the mixed layer depth variability of each particular segment of the coastline under the influence of changing winds at that particular segment and other segments of the coastline as a cumulative effect.

### 2.3.1 Upwelling index

The classical Bakun upwelling index (Bakun, 1973) is used in this study, which can be defined by,

$$UI = |\tau|/(\rho_0|f|) \cos(\alpha^*) \quad (2.1.1)$$

where  $|\tau|$  is wind-stress magnitude,  $\rho_0 = 1026 \text{ kg/m}^3$  is a typical seawater density,  $f$  is the Coriolis parameter, and  $\alpha^*$  is the relative angle between the wind direction and the coastline orientation (Kämpf and Chapman, 2016). This index is equivalent to the offshore Ekman volume transport per unit width of the coastline. Hereby it is important to note that Ekman layers develop on time scales of the inertia period that increases with proximity to the equator.

### 2.3.2 Coastal upwelling along a coast of finite horizontal extent

The theoretical consideration of the simple theory of coastal upwelling along a coast of finite horizontal extent is adopted from the original paper of Kämpf and Kavi (2018). The theory is developed on the fact that all the coastlines in the real world have a finite horizontal extent. **Figure 2.3.1a** displays the schematics of coastal upwelling along a finite length coast, where  $L_0$  is the total length of the coast,  $h_0$  is the surface mixed layer depth and  $L$  is the distance at which full upwelling conditions is developed under the influence of coastal upwelling favourable winds. Which means, the hypothetical coastline (of this theoretical consideration in fig 3.2.1) can reach at full upwelling conditions beyond the distance  $L$ , which is represented by green shading in figure 3.2.1(a). Hence, the expression of the distance  $L$  (pole ward) within the

coastline over which full upwelling conditions develops along the coastline can be described by,

$$L = \Delta\rho g h_0^2 / \overline{\tau \cos(\alpha^*)} \quad (2.1.2)$$

Where,  $\Delta\rho$  is the difference between the density of surface mixed layer water and thermocline water density,  $|\tau|$  is wind-stress magnitude,  $h_0$  is the surface mixed layer depth at initial state considered constant along the coastline and  $\alpha$  is the relative angle between the wind direction and the coastline orientation.  $h_0$  is considered at constant value of 50m at initial state. The detailed derivation of this equation can be found in the original paper of Kämpf and Kavi (2018).

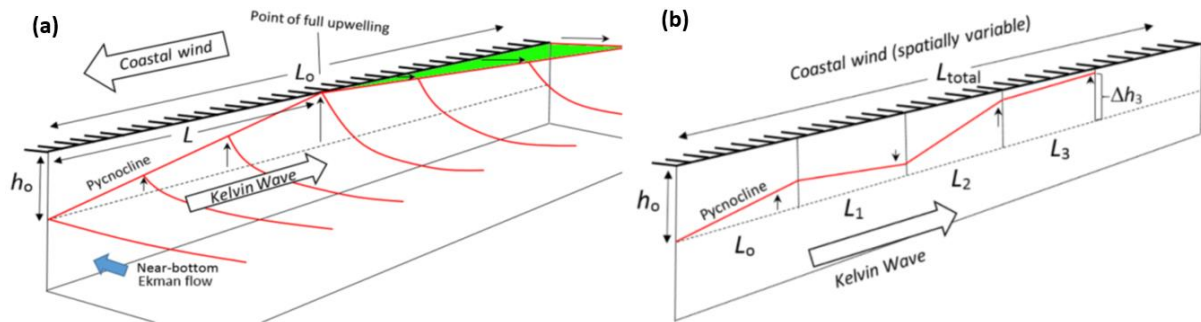


**Figure 2.3.1:** Panel (a) displays the schematic of the coastal upwelling process along a coast of finite extent ( $L_0$ ) in the southern hemisphere. Full upwelling occurs after a distance of  $L$  (green shading) and  $L_0$  is the length of entire coastline. Green shading in (a) represents full upwelling condition reached theoretically. Panel (b) displays the schematic of individual and cumulative changes of the depth of the surface mixed layer along the finite length coastline (Kämpf and Kavi, 2018).

The original theory (Kämpf and Kavi, 2018). also suggested that the extended coastline can be divided into smaller segments of length  $L_1$ ,  $L_2$  up to  $L_i$ ; to precisely examine the response of the local wind variability to the surface mixed layer depth of each segment. Hence; the contribution of each segment to the total change of the thermocline can be calculated from,

$$\delta h_i = h_o L_i / L \quad (2.1.3)$$

where  $L_i$  is the length of the  $i^{\text{th}}$  segment of the coastline,  $L$  is the length after which full upwelling conditions developed where  $h_o$  is the depth of surface mixed layer at initial state. The detailed derivation and conditions under which this equation is developed can be found in the original paper of Kämpf and Kavi (2018). The cumulative change in the depth of mixed layer at each segment, adding with the change of precursor segments, can be expressed as,

$$\Delta h_i = \sum_{j=1}^l \delta h_j \quad (2.1.4)$$

The theoretical consideration expressed by equation 2.1.4 can identify the segments along a coastline where the full upwelling conditions is developed by achieving the criteria  $\Delta h_i > h_o$ . This equation precisely incorporates the wind variability at the precursor segments. For example, the downwelling favourable wind at the precursor locations can offset the full upwelling conditions at a particular segment. It should be noted here that, the theory presented above exclusively considers regional wind effects, and it does not capture the effects due to regional air-sea heat flux anomalies, lateral heat flux anomalies induced by variations in oceanic currents. It also does not capture alongshore variability of the mixed layer depth under the influence of the coastal Kelvin waves (triggered from remote forcing) which may also modify SST anomalies in the regional ocean. The enhanced localised upwelling effects which might be triggered by the bathymetric irregularities of the region such as shelf-break canyons are ignored in this study (Kämpf, 2012).

## **2.4 Statistical methods**

### **2.4.1 Wavelet analysis**

Wavelet analysis is a unique tool for analysing a time series with the expansion of a function in the frequency domain, the data can be represented by frequency (or period) vs time instead of conventional amplitude v/s time. The wavelets are localized in time and frequency and connect the function being represented by their coefficients. The Continuous Wavelet Transform (CWT) is a consecutive series of band-pass filters applied to a time series, where a number of waves with particular width is applied to the entire time series to capture frequency response. It constructs a time-frequency representation of a signal that offers excellent time and frequency localization. Moreover, the inverse continuous wavelet transforms (ICWT) can reconstruct the signal by summing the scaled CWT coefficients over all scales. An approximation to the original signal can be obtained by summing the scaled CWT coefficients from defined scales. Hence, the ICWT can play a crucial role, when the study is interested over particular localised scale. The 'Morse Wavelet' has been used as the mother wavelet in CWT.

Two tier wavelet treatment is applied to the time series of the zonal winds, as CWT capture the entire range of frequencies. To remove the dominance of the low frequency (or higher period, unwanted) signals ICWT is applied to the extracted CWT. The inverse continuous wavelet transforms (ICWT) is applied to the signal of each year (time series of every year), with the 'Morse Wavelet' as the mother wavelet. This study is interested in the variability of the zonal wind time series at the frequency range of 2 days to 40 days. Hence, the ICWT is applied to created CWT, to reconstruct an approximation of daily zonal wind data based on 2 to 40 days of the period.

### **2.4.2 Power spectral density**

A Power Spectral Density (PSD) is the measure of signal's power content versus frequency. A PSD is typically used to characterize broadband random signals. The amplitude of the PSD is normalized by the spectral resolution employed to digitize the signal.

The power spectral density (PSD) of the OLR data is computed using a standard approach (Kikuchi and Wang 2009). The seasonal and the mean and linear

trends were removed from the time series for a given season (boreal summer-fall, June-September) of a given year. After applying a 5% cosine taper to the time series to reduce end effects and sidelobe leakage, the PSD for a given season and year was obtained by means of a fast Fourier transform (FFT). The final computed PSDs is the time average over the 28 years, from individual PSDs of each season and year of 28 years (1988-2016) in the region.

### **2.4.3 Band pass filtering**

The atmospheric variability related to wind and convection occurs at various frequencies ranging from intra-day to intraseasonal to interannual. To extract high frequency convective oscillation over the study region associated with “bi-weekly” frequency mode, a temporal band pass filter is applied to wind and OLR data set. The 8–20-day Lanczos bandpass filter is applied in this study to OLR data and zonal wind of the study region to identify the presence of “bi-weekly” mode oscillations in the region.

## CHAPTER 3: RESULTS AND DISCUSSION

### 3.1 Dipole Mode Index and SST

The Indian Ocean Dipole (IOD) events are initially described by Saji *et al.* (1999) and suggested significant fluctuation of SST anomalies in the eastern and western part of the tropical Indian Ocean are triggered anomalously. Saji *et al.* (1990) also described the two independent regions of tropical Indian Ocean as an eastern box of the IOD and western box of the IOD, which can be selected as the areas to statistically calculate the SST anomalies and the relation between the anomalies of two boxes can be established. They called it the dipole mode Index (DMI), which monitors the abruptly triggered seesaw conditions between SST anomalies of the two ends of the tropical Indian Ocean. The region of the eastern box and western box are selected from the EOF analysis of the Saji *et al.* (1999) in which the IOD is the second mode of EOF for the SST variability in the tropical Indian Ocean. The coverage of the selected boxes is marked in **figure 3.1.1**, where the western box has coverage of 50°-70°E and 10°N-10°S while the eastern box has coverage of 90°-110°E and Eq-10°S.

The distribution of the average SST values clearly marks the presence of equatorial warm pool as displayed in **figure 3.1.1a**, while the difference between average and minimum values marked the region of rarely developed Java-Sumatra upwelling system in the eastern box of the DMI as displayed in **figure 3.1.1b** (red shading). The Somali upwelling region can be visualised in **figure 3.1.1c** (red shading), which displays the difference between the maximum and minimum values of the SST.

According to previous studies, normally the IOD events are seasonally phase locked with the boreal summer-fall season; hence, in this study the focus is on this season which is defined by 1st June to 30th September every year. The availability of high-quality data over the tropical Indian Ocean is from the advent of the high-resolution Satellite observations from 1988; this study performs the analysis covering this entire period from 1988 to 2016. Simple statistics are applied to the long-term daily data set of the seas surface temperature (1988-2016) derived from the NOAA OI data set to visualise the IOD related interannual changes. The long-term average values of the SST are derived for the boreal summer-fall of 28 years (1988-2016) from daily SST

values of NOAA OI data, likewise long-term minimum (min values for 28 years period) and maximum (max values in 28 years period) values of the SST are also derived. The maps of the results are displayed in **figure 3.1.1**, where **figure 3.1.1a** displays the long-term average of the SST data ( $SST_{avg}$ ) over the tropical Indian Ocean, **figure 3.1.1b** indicates the difference between long-term average and long term minimum values of SST ( $SST_{avg} - SST_{min}$ ) and **figure 3.1.1c** displays the difference between long-term maximum value long-term minimum values of SST ( $SST_{avg} - SST_{min}$ ).

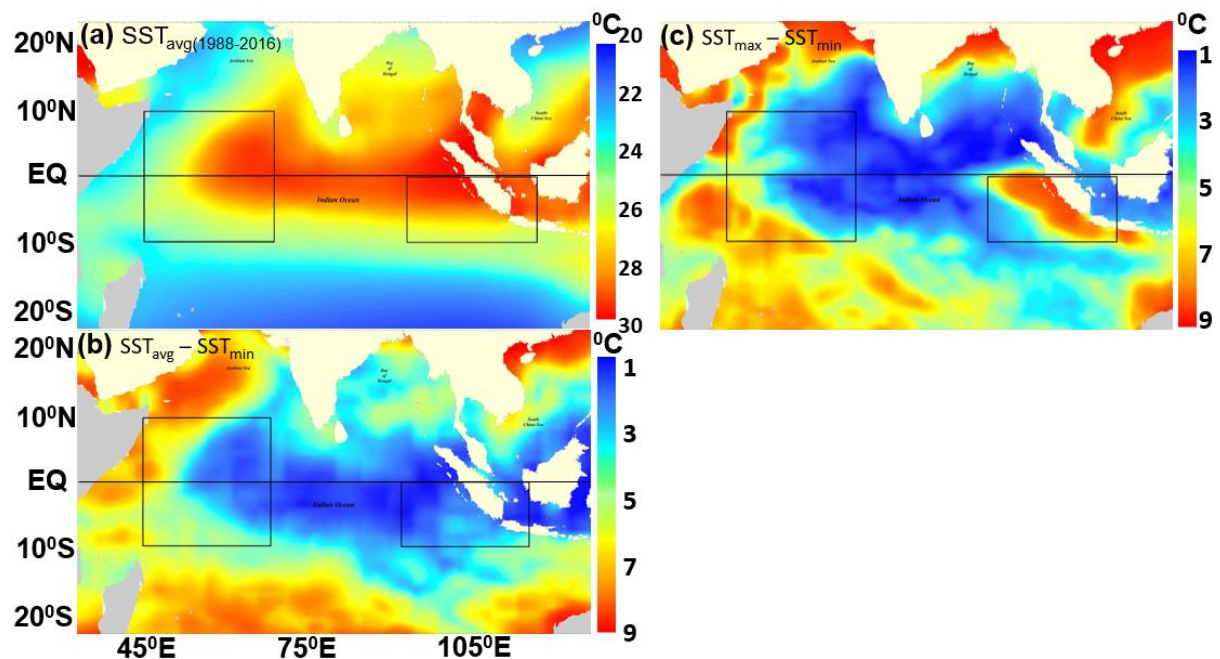


**Figure 3.1.1:** Maps shows sea surface temperature (SST, °C) distribution over the tropical Indian Ocean during June to September, where panel (a) displays long term (1988-2016) average conditions, panel (b) displays long term (1988-2016) average minus long term (1988-2016) minimum values and panel (c) displays long term (1988-2016) maximum values minus long term (1988-2016) minimum values. Marked boxes in all panels displays IOD events eastern and western box.

Strength of the IOD event can be defined by DMI index, where positive values of DMI indicates positive mode of the IOD and negative values of DMI displays negative mode. The line plot of **figure 3.1.2a** displays the weekly time series of the SST anomaly of the eastern box and western box along with the DMI index itself during the entire study period of 1988 to 2016. The positive values of DMI dominate the entire time series of **figure 3.1.2a** (blue line), in which it crosses the value of +1°C at many occasions and stays beyond this value for the substantial time for example during 1994, 1997 and 2006. While the negative mode is not so frequent and strong, it shows irregular inconsistent peaks.

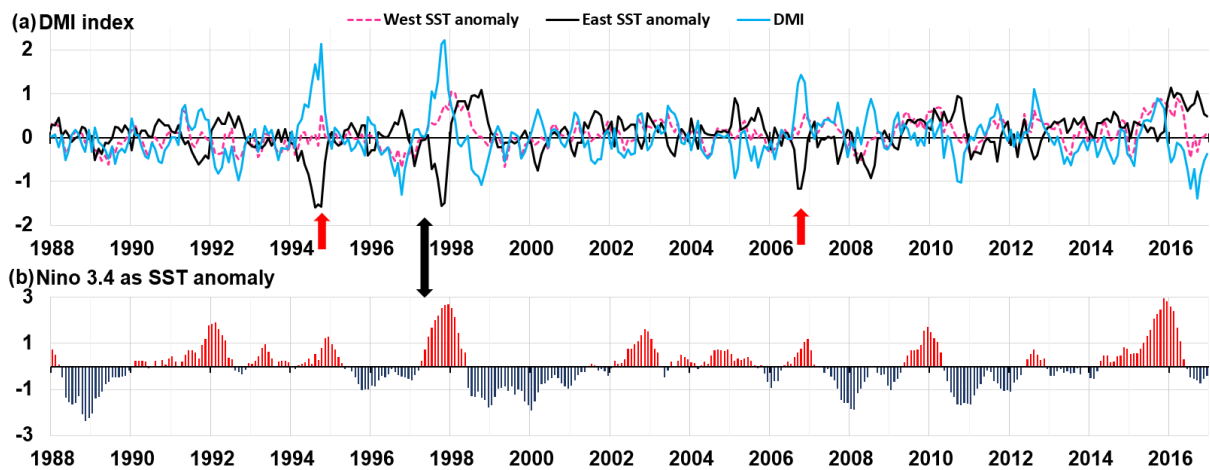


**Figure 3.1.2:** Line plot in panel (a) displays dipole mode index (DMI) with sea surface temperature anomaly values over the eastern and western boxes of the IOD events. Panel (b) indicates NIÑO 3.4 sea surface temperature anomaly values. All values on y-axis in both plots (line a and bar b) are in °C and x-axis represents time in years.

Previous studies claimed dependence of IOD on ENSO mode and doubted the independent status of the Indian Ocean coupled mode. Though recent studies believed the independently sustainable nature of the IOD, as only 50% of the IOD events of the past century are co-occurred with the ENSO (Vinayachandran *et al.*, 2009). The line plot of DMI index displayed in **figure 3.1.2a** and bar plot of NIÑO 3.4 SSTA displayed in 3.5.2b also supports the independent nature of the IOD events, where out of three strong positive IOD events (**figure 3.1.2a**; marked arrows; 1994, 1997 and 2006) only one event of 1997 was co-occurred with the ENSO event (**figure 3.1.2a**; marked black arrow). A detailed study on the relationship between the ENSO and the Indian Ocean dipole had been performed by Ashok *et al.* 2003.

The focus of this study is on the sea surface temperature (SST) variability of the tropical Indian Ocean in the perspective of the Indian Ocean Dipole (IOD) events. According to previous studies, to consider the strong positive or negative phase of the IOD event, the DMI index is expected to cross the 1 STD value and it should stay beyond this value for 10-12 weeks. Though, the negative phase of the IOD is believed to be the intensification of normal conditions over the tropical Indian Ocean, this study will exclusively focus on the positive mode of the IOD event which has devastating effects on the climate of the surroundings (Webster *et al.*, 1999; Kinter, 2002; Saji & Yamagata, 2003, Vinayachandran *et al.*, 2009). The correlation statistics of SST

anomalies of individual boxes (of DMI) with DMI itself were carried out in previous studies such as Ashok *et al.* (2003) and Saji and Yamagata (2003).

The principle motive of this study is the characterisation of the positive mode of IOD events of the past three decades, and it uncovers the physical oceanographic processes which are triggered from local climatic variation of the region. To begin with, the study identifies the dominating area of the tropical Indian Ocean, out of eastern box and western box of DMI, which fundamentally triggers strong SST anomalies and performs a crucial role in the development of the positive mode of IOD events. Then, it focuses on the investigation of the behaviour of the air-sea coupling, surface wind conditions and ocean response to the surface winds within the dominating areas.

**Table 3.1.1:** Table displays DMI value statistics during three strong positive IOD events and three weak/aborted IOD events.

Year	Above 1 STD	Peak value	Peak value month
1994	17 weeks	2.57	oct
1997	18 weeks	2.49	Nov
2006	12 weeks	1.6	Nov
<b>2003</b>	3 weeks	1	July
<b>2008</b>	2 weeks	0.9	July
<b>2012</b>	3 weeks	1.4	Sep

The detailed statistics of the IOD events are derived from DMI plot of **figure 3.1.2a**, where the weeks in the study period (1988-2016) with the DMI value above 1 STD are derived and occasions when two or more consecutive weeks fulfilling this condition are identified and displayed in table 3.1.1. The strongest positive values the DMI witnesses during boreal summer-fall of 1994, 1997 and 2006 according to **figure 3.1.2a** (marked arrows) and the statistics of these events are displayed in table 3.1.1. During the strong positive IOD (pIOD) event of 1994 DMI value stays above 1STD value for consecutive 17 weeks, during pIOD event of 1997 it stays above 1 STD value for consecutive 18 weeks and during event of 2006 it stays above 1 STD value for consecutive 12 weeks (table 3.1.1). The DMI reaches to the peak value of 2.57 in October 1994 during the event of 1994, at 2.49 in November 1997 during the event of 1997 and 1.6 in November 2006 during the event of 2006 (table 3.1.1). Certain other

years in the study period (1988-2016) exhibits moderated strength positive values of DMI, they are 2003, 2008 and 2012. According to table 3.1.1, the DMI values stays above 1 STD value, for three consecutive weeks during event of 2003, for two consecutive weeks during event of 2008 and for three consecutive weeks during event of 2012. The DMI reaches to peak value of 1, 0.9 and 1.4 during the event of 2003, 2008 and 2012 respectively.

**Table 3.1.2:** Table displays standard deviation of DMI values during different periods and its correlation with the SST anomalies of eastern and western IOD boxes.

From 1988 to 2016		During positive IOD event years	
STD of DMI	0.5314	STD of DMI	0.71926
STD of SST Anomaly East	0.45228	STD of SST Anomaly East	0.6076
STD of SST Anomaly West	0.34246	STD of SST Anomaly West	0.36175
DMI Correl with SST Anomaly East	-0.76913	DMI Correl with SST Anomaly East	-0.86471
DMI Correl with SST Anomaly West	0.53606	DMI Correl with SST Anomaly West	0.53624

The visual inspection of **figure** 3.1.2a indicates that negative SST anomaly of the eastern box of the DMI (black line) dominates the positive DMI values (blue line). To confirm this claim, the correlation statistics of SSTA of eastern box of DMI and DMI itself are derived and displayed in table 3.1.2 along with STD of both the time series during natural conditions and positive mode of IOD independently. The STD of the DMI of the entire study period (198—2016) displays value of 0.5314, while the STD of the SSTA of eastern box displays value of 0.45228 and the STD of the SSTA of the western box of DMI displays value of SSTA 0.34246 for the same period (1988-2016) (table 3.1.2). Moreover, During the entire study period (1988-2016) the DMI has higher correlation with eastern box with value -0.77 and it has lower correlation with western box with value 0.536 (table 3.1.2).

During positive phase of the IOD events; the STD of the DMI displays value of 0.72, while the STD of the SSTA of eastern box displays value of 0.6 and the STD of the SSTA of the western box of DMI displays value of SSTA 0.36 for the same period (table 3.1.2). Moreover, during positive phase of the IOD events the correlation of the with eastern box is elevated further with value -0.86, while the correlation of the DMI stays at the same value of 0.536 (table 3.1.2). Higher STD values of the SSTA of

eastern box during the positive IOD events and stronger correlation with the DMI indicates the dominant role of the SSTA of the eastern box in the positive mode of the IOD events.

The strong positive mode of the IOD events are developed during boreal summer-fall of 1994, 1997 and 2006 (**figure 3.1.2a**, black line), predominantly from the SSTA of the eastern box (**figure 3.1.2a**, blue line). According to previous studies, the positive mode of the IOD event was progressing towards strong values during boreal summer-fall of 2003, 2008 and 2012; and suddenly it suffers the termination of the event and cannot develop strong positive DMI values. The reason behind the abrupt development of the negative SSTA within the eastern box of the DMI during certain years along with the reasons of abrupt termination of developing events during some years are still under speculations.

This section explores the interannual behaviour of the SSTA of the east and western box of DMI and DMI itself and characterises the pIOD events. Next section 3.2 investigates the intraseasonal characteristics of the SSTA within the eastern box of the DMI and explores the individual regions within the area, which exhibits maximum variability of SSTA during the positive phase of the IOD.

## 3.2 SST variability in south eastern tropical Indian Ocean

Wyrtki (1962) suggested that, under the influence of the Southeast Monsoon, from June to November, the upwelling of cold water is a regular feature in the coastal waters of southern Java. Later, Susanto (2001) also noted, seasonal upwelling can occur in the region called by the **South Eastern Tropical Indian Ocean** (the SETIO) along southern Java coastline frequently and along the southern Sumatra coastline infrequently during boreal summer-fall (June to October). Hence, previous studies suggest that, beside the SETIO occupies the warm pool of the Indian Ocean, strong coastal upwelling along the southern Java and Sumatra coastline during boreal summer-fall of certain years can trigger strong surface cooling in the region, which is the primary reason behind the appearance of the negative SST anomalies in certain years in the eastern box of the DMI (Saji *et al.*, 1999; Webster *et al.*, 1999; Murtugudde *et al.*, 2000; Vinayachandran *et al.*, 2009).

### 3.2.1 Spatial signature of SST

The region South Eastern Tropical Indian Ocean (the SETIO) is defined in this study covering surface area of the Indian Ocean from 80°-110°E and Eq-10°S. The SST maps for the same region is prepared from daily satellite data of NOAA OI SST averaged over time for three different conditions as displayed in **figure 3.2.1** to investigate the spatio-temporal pattern of SST in the SETIO region, where marked black box displays the eastern box of the DMI (90°-110°E, Eq-10°S).

Time average SST distribution of the SETIO region during boreal summer-fall of strong pIOD event years is displayed in **figure 3.2.1a**; Likewise, time average SST distribution of the region during boreal summer-fall of all the years with neutral IOD conditions is displayed in **figure 3.2.1b**. The difference between SST values of previous two maps (**figure 3.2.1a** and **b**) is displayed in **figure 3.2.1c**. The SST distribution of all the neutral years (in IOD perspective) in **figure 3.2.1b** confirms the dominance of the eastern equatorial warm surface water in the SETIO region. While, distribution of SST during pIOD events exhibits strong presence of cold surface water in the coastal region of southern Java and southern Sumatra (**figure 3.2.1a**). The difference of the SST values between these two conditions, neutral IOD and pIOD, displays substantial drop of SST in the entire eastern box of the DMI during pIOD events (**figure 3.2.1c**). Though, unlike southern Java coastal region, entire southern

Sumatra coastline does not exhibit evenly distributed surface cooling and there is asymmetry between central and southern Sumatra SST anomalies, where the northern part of the coastline displays moderated cooling and southern part experiences strong surface cooling (**figure 3.2.1a**). Subregional features of the spatial distribution of SSTA of the eastern box of the DMI discussed here were not discussed in earlier studies.

### 3.2.2 Upwelling index

The “south easterly” wind prevails during boreal summer-fall in the SETIO region, which favors the coastal upwelling along the southern Java and Sumatra coastline (Susanto *et al.* 2001). The variability of the surface cooling triggered by coastal upwelling in the region may be developed from the variation of local winds of the region. Hence, the intraseasonal and interannual variability of the winds along the southern Java-Sumatra coastline is examined here using classical Upwelling Index (UI) defined by equation 2.1.1 (Bakun, 1973; Kämpf and Chapman, 2016). It is unreasonable to consider nearly 1700 kms long coastline of the southern Java-Sumatra as a single segment; hence, the coastline of the southern Java and Sumatra is divided in four independent segments as displayed in **figure 3.2.2**, where the southern Sumatra coastline has three individual boxes and entire southern Java is covered in single box. The reason behind this segmentation is the southern Java upwelling is the prominent feature according to the previous studies, while, upwelling along the southern Sumatra coastline is sporadic nature.

The area average averaged zonal and meridional wind stress are derived for the study period (1988-2016) at monthly time scale for the four boxes **figure 3.2.2** from cross calibrated satellite CCMP V2 data set to calculate the upwelling index. The derived upwelling index of four individual boxes (of **figure 3.2.2**), using equation 2.1.1, is then further seasonally averaged during boreal summer-fall season (June to September) of each year (of the study period, 1988-2016) and displayed in **fig 3.2.3a**. Area averaged time series of the SST anomaly is also derived for the same four boxes of **figure 3.5.2** from NOAA OI data for the same period at monthly time scale and displayed in **figure 3.2.3b**. The principle idea behind this exercise is to establish the relation between variability of the seasonal upwelling favourable winds (in the form of UI) of the region with the SST anomalies of the region at interannual time scale.

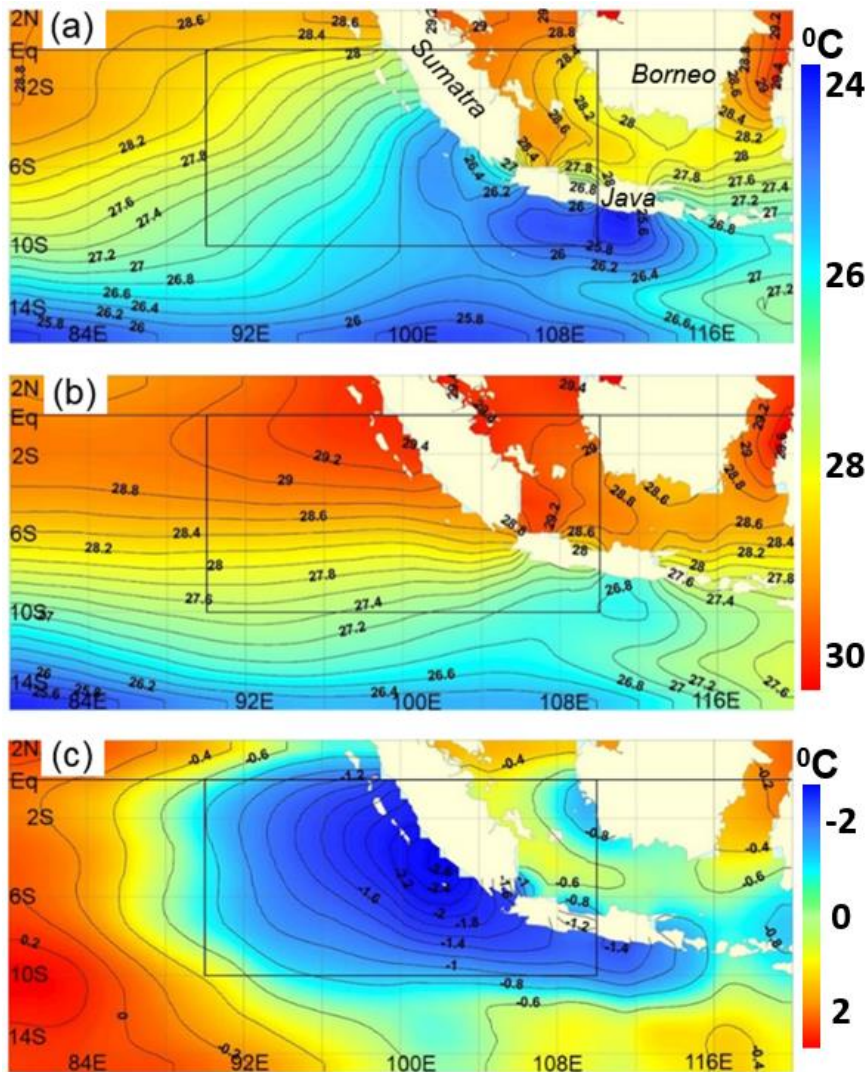


**Figure 3.2.1:** Maps shows sea surface temperature distribution over the south eastern tropical Indian Ocean, where panel (a) displays the average SST values during three positive IOD events (1994, 1997 and 2006), panel (b) displays the average SST values during all other 26 years from the period 1988-2016. Contour Interval in each panel is 0.2°C. Panel (c) displays the differences of values shown in (a) and (b). SST values are derived from NOAA-OI data set during boreal summer-fall season (July to November). The rectangle in both panels shows the eastern area used for calculation of the DMI.

The persistently strong upwelling index of the Java coastline is evident in **figure 3.2.3a** (dashed black line) which indicates the presence of the upwelling favourable winds in the region during boreal summer-fall of most years in the study period (1988-2016). The upwelling index along the Sumatra coastline exhibit distinctive behaviour as displayed in **figure 3.2.3a**, where the southernmost box (box 3) displays strong UI in the most season with minor interannual fluctuation and indicates the presence of the upwelling favourable winds during the boreal summer-fall of most years in the study period (1988-2016). While, the regions of northern two boxes (box 1 and box 2) exhibit strong interannual variation of the upwelling index (**figure 3.2.3a**, blue and red lines) and indicates the strong interannual variation of the upwelling favourable winds in the region. Moreover, the UI of the box1 indicates suppressed behaviour in the season of most years in the study period (1988-2016) with the limited appearance of positive values, which indicates a weak presence of upwelling favourable winds. The box 1 is near equator hence equatorial easterlies dominate the upwelling mechanics in the region, and **figure 3.2.3a** (blue line) indicates weak or no presence of the equatorial easterlies in the region. The regions of northern two boxes (box 1 and box 2) exhibit strong UI values only during pIOD event years 1994, 1997 and 2006 (**figure 3.2.3a**, marked arrows). The box 1 and box2 region also exhibits positive values of UI during the season of 1991, 200, 2007, 2008 and 2011; and these years represent weak or aborted pIOD events (Du *et al.*, 2013).

Unlike the time series of UI of all four boxes (**figure 3.2.3a**), the time series of the SSTA of all four boxes displayed in **figure 3.2.3b** exhibit identical variation. Pronounce UI of the southern Java coastline (**figure 3.2.3a**, dashed black line) should have developed negative SST anomaly during boreal summer-fall of all the years (1988-2016), though the limited presence of negative SSTA in the study period (**figure 3.2.3b**, dashed black line) makes the relation between local winds and SSTA of the region complex. Likewise, the strong UI of the southernmost box of the Sumatra (box 3, **figure 3.2.2**) cannot mark its signature in SSTA persistently. Contrarily, during certain years SST anomalies of all the boxes (of **figure 3.2.2**) exhibit strong positive values (**figure 3.2.3b**); for example, during boreal summer-fall of 1998, 2010 and 2016. Correlation values between SSTA and DMI in Java Box (fig 3.2.2) region is 0.55, for Box 3 region it is 0.32, for Box 2 region it is 0.21 and for Box 1 region it is 0.09. This poor correlation of SSTA with UI time-series in the study period (1988-2016)

indicates the complex relationship between the local surface winds and the SSTA in the region.

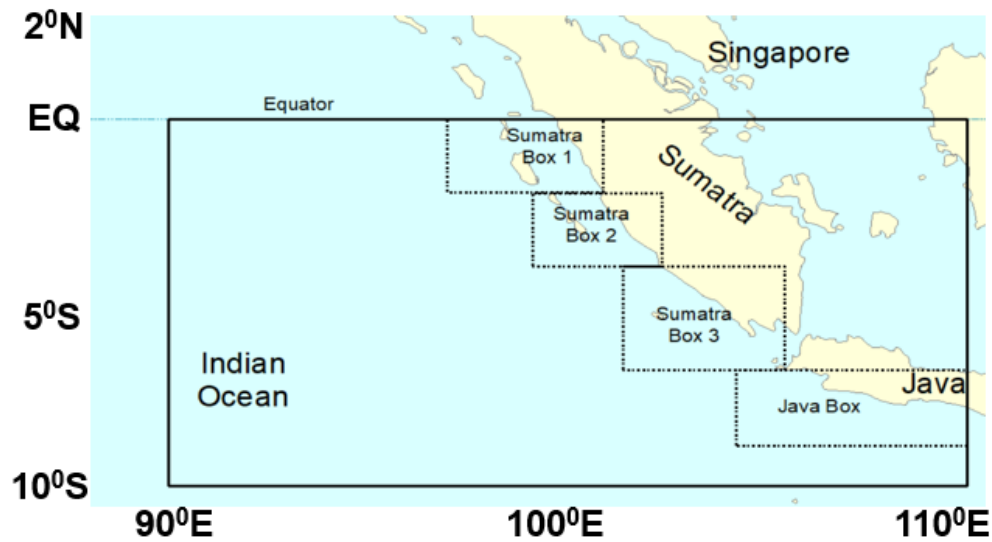


**Figure 3.2.2:** Map displays the schematics of south eastern tropical Indian Ocean, where large rectangle indicates eastern box of the DMI. Black dotted rectangles: regions are used to calculate area average the classical Bakun upwelling index based on the orientation of the adjacent coastline.

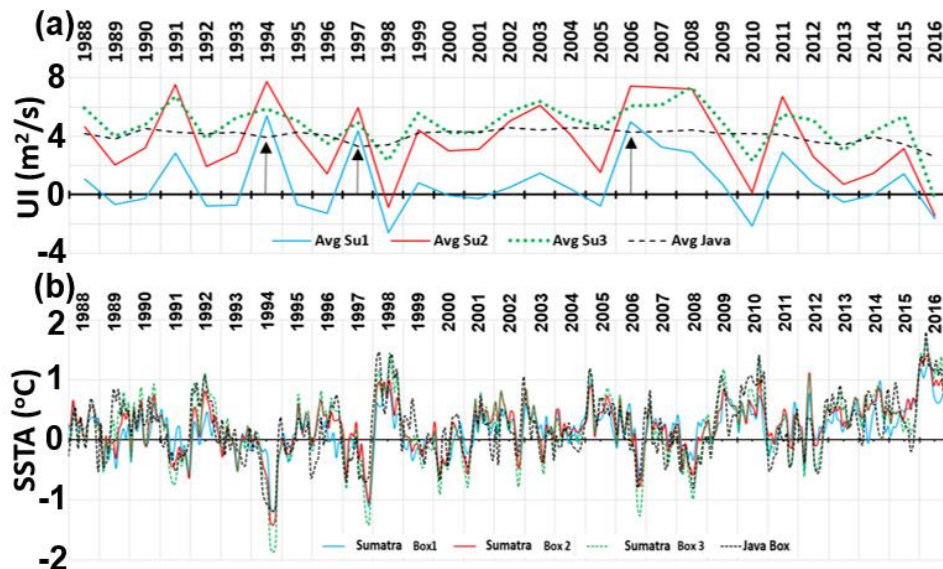


**Figure 3.2.3:** Panel (a) displays time series of seasonally averaged (June to September) Upwelling Index (UI) of Sumatra box 1, box 2, box 3 and Java box (of figure 3.1.4) using monthly CCMP V2 data. Black arrows indicate years of pronounced upwelling along the southern Sumatra-Java coastline. Panel (b) displays time series of area average monthly sea surface temperature anomalies (SSTA,  $^{\circ}C$ ) over the similar box regions of figure 3.1.4, derived from monthly NOAA OI data.

### 3.2.3 SST anomaly signature in the eastern box of DMI

The SSTA of all boxes along the southern Java-Sumatra coastline at interannual time scale exhibit co-varying characteristics as displayed in **figure 3.2.3b**. The weekly time series of SSTA average over the same four boxes along with the SSTA of the entire eastern box of DMI and DMI index itself is derived and displayed in **figure 3.2.4**, to explore the intraseasonal pattern of SSTA within the region. The SSTA signature of the Sumatra box 1 and box 2 (of **figure 3.2.2**) are merged due to identical behaviour of the SSTA and displayed in **figure 3.2.4**. The intraseasonal behaviour is examined for nine individual years in the study period in three different sets according to their IOD phases. 1998, 2001 and 2004 are selected as first set which represent the neutral IO conditions; secondly year 1994, 1997 and 2006 are selected which represent strong positive IOD conditions and third set is year 2003, 2008 and 2012 is selected which represent the weak or aborted IOD events.

The SSTA patterns of the 2001 and 2004 display the natural phase of the IOD condition as displayed in **figure 3.2.4** where DMI index oscillates between -1 to +1 value (**figure 3.2.4 b and c**, green shading). Blue horizontal arrow in each **figure** indicates the southern Java-Sumatra upwelling season (boreal summer-fall, June to September) and according to previous studies the IOD events are phase locked with this season; hence, it is also season of interest of these study. During the season of 2001 and 2004, no individual boxed region along the Java-Sumatra coastline exhibit negative SSTA values and as a result the entire eastern box of DMI exhibit positive value of SSTA in the season (**figure 3.2.4 b and c**, black line) under the influence of equatorial warm water. 1998 exhibits the negative phase of the IOD event, and as discussed previously, the negative phase of the IOD is the intensified version of the normal conditions; hence, the eastern equatorial warm surface water conditions are intensified during the boreal summer-fall of 1998. The spread of equatorial warm water reaches up to the southern Java coasts (**figure 3.2.4a**, blue shading), which normally exhibit cold surface water under the influence of persistent coastal upwelling as discussed previously (**figure 3.2.3a**). Consequently, the southern Java coastal region exhibit strong negative SSTA values during the season of 1998 with value above +2

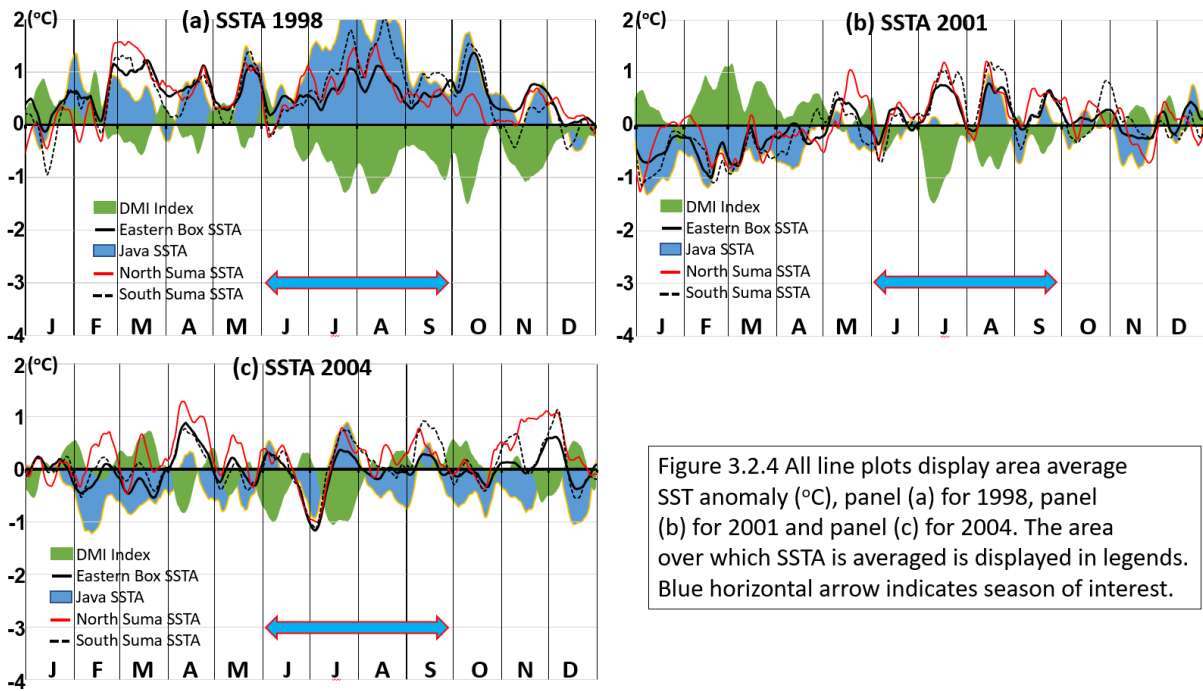


Figure 3.2.4 All line plots display area average SSTA anomaly ( $^{\circ}\text{C}$ ), panel (a) for 1998, panel (b) for 2001 and panel (c) for 2004. The area over which SSTA is averaged is displayed in legends. Blue horizontal arrow indicates season of interest.

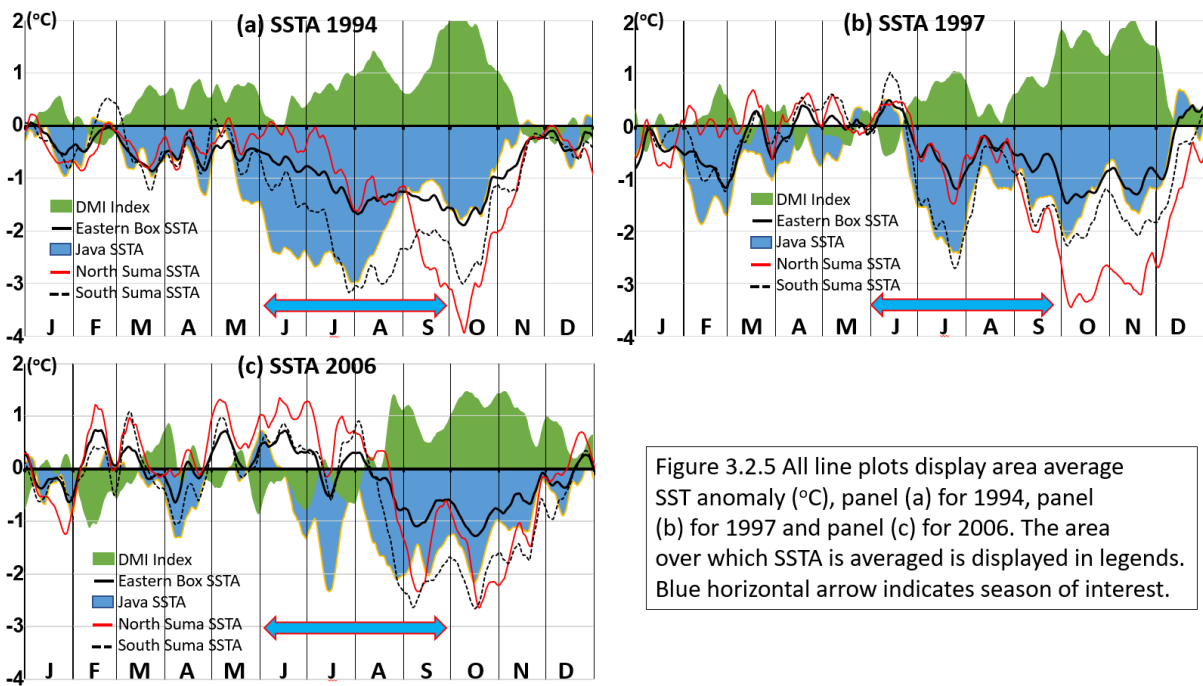


Figure 3.2.5 All line plots display area average SSTA anomaly ( $^{\circ}\text{C}$ ), panel (a) for 1994, panel (b) for 1997 and panel (c) for 2006. The area over which SSTA is averaged is displayed in legends. Blue horizontal arrow indicates season of interest.

(figure 3.2.4a, blue shading), along with the positive SSTA values along the southern Sumatra coastline (figure 3.2.4a, North and south Sumatra, red solid and black dashed line) and they all together trigger negative DMI values up to -1 during the boreal summer-fall of 1998 (figure 3.2.4a, green shading). Southward spread of the equatorial warm water indicate the role of equatorial remote forcing in the region which was discussed in number of previous studies, which suggest that the intensified

westerlies along the equatorial Indian Ocean triggers downwelling kelvin waves which injects the surface warm water and deepens the thermocline of the southern Java-Sumatra coastal region (Rao and Yamagata, 2004; Iskandar *et al.*, 2005, 2006; Sengupta *et al.*, 2007; Chen *et al.*, 2015; Delman *et al.*, 2016).

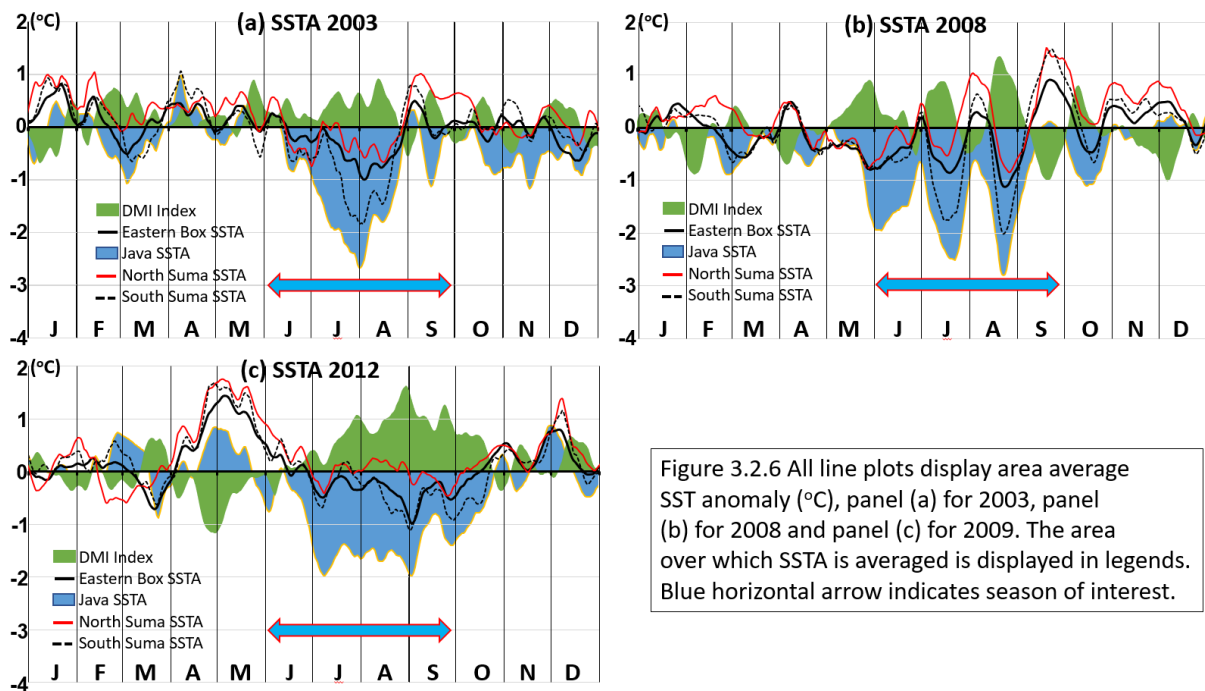


Figure 3.2.6 All line plots display area average SST anomaly ( $^{\circ}\text{C}$ ), panel (a) for 2003, panel (b) for 2008 and panel (c) for 2009. The area over which SSTA is averaged is displayed in legends. Blue horizontal arrow indicates season of interest.

Strong positive IOD phase is displayed during boreal summer-fall of 1994, 1997 and 2006 and it is interesting to visualize the progress of SSTA pattern in the different region of the southern Java-Sumatra coastline, as coastal upwelling in this region predominates the SSTA pattern of the region during positive phase of the IOD as discussed above (table 3.1.2). The southern Java coastline exhibits the strongest negative SSTA values during the season of all three pIOD years as displayed in **figure 3.2.5** (a, b and c; blue shading). Moreover, careful examination of line plots of **figure 3.2.5** reveals that the negative SSTA of the southern Java coastal region arrive earliest in each boreal summer-fall season (of **figure 3.2.5**, blue shading); which is followed by the negative SSTA values at the south Sumatra box and then northern box of the Sumatra exhibit negative SSTA finally. The SSTA of the eastern box of the DMI exhibits a cumulative effect from the SSTA of all three individual boxes along the southern Java-Sumatra coastline (**figure 3.2.5**, thick black line) and displays strong negative SSTA values which consecutively trigger strong DMI values in the boreal

summer-fall of 1994, 1997 and 2006 (**figure 3.2.5**, green shading). Early arrival of the negative SSTA at the southern Java coastal region and then northward progress of negative SSTA values along the southern Sumatra coastline suggest presence of complex but structured physical oceanographic process in the region which was not explored previously. Intermittent positive recovery in the developing negative SSTA signature of all boxes during August 1997 and late July 2006 (**figure 3.2.5 b and c**) is also matter of interest of this study, as it will lead to the understanding of the early termination of pIOD events during certain other years.

The aborted pIOD events are evident during the boreal summer-fall of 2003, 2008 and 2012 in table 3.1.1, where positive DMI value cannot sustain for longer time and as a result it cannot develop strong values in the season. During the boreal summer-fall of 2003, all the boxes of the southern Java-Sumatra coastline exhibits strong negative SSTA values from July 2003 onwards (**figure 3.2.6a**), which trigger positive DMI index during same time (**figure 3.2.5a**, green shading). The progress of the negative SSTA signature is abruptly withdrawn during end of August 2003 as displayed in **figure 3.2.5a** and strong positive DMI value cannot develop (**figure 3.2.5a**, green shading). Previous studies suggested the intraseasonal disturbance at the equatorial Indian Ocean is the primary reason behind this abrupt termination of negative SSTA (Rao and Yamagata, 2004). Later, during boreal summer-fall of 2008 and 2012 the progressing negative SSTA values of the southern Java-Sumatra coastline are also abruptly terminated before the DMI value reaches the strong positive values (**figure 3.2.6 b and c**). Moreover, boreal summer-fall of 2008 exhibit unique characteristics of SSTA in **figure 3.2.6b**, where the developing negative SSTA signature of all the boxes of the southern Java-Sumatra coastline suffers from positive recovery more than one occasion during June to September of 2008. These unusual characteristics of SSTA in the region makes it more difficult to understand the oceanographic and climatic process of the region.

This study thoroughly examines the intraseasonal and interannual variability of the local surface winds along the southern Java-Sumatra coastline during the boreal summer-fall season of the study period (1988-2016) to understand this complex behaviour of the SSTA of the SETIO region (the study region). It also explores the wind variability at the equatorial Indian Ocean during the same period, which may be

another source of the SSTA variability in the study region as claimed in number of previous studies. The response of the upper layer of the ocean in the study region to the local and remote wind variability is also meticulously examined. The central objective of the study is to investigate the atmospheric and physical oceanographic processes of the region which can establish a strong relation between them and helps to understand the complex climatic fluctuation of the region.

### 3.3 Statistical analysis of surface winds

This section investigates the climatological cycle and interannual variability of surface winds in the tropical Indian Ocean and its potential to trigger coastal upwelling along the coasts of Java and Sumatra.

#### 3.3.1 Climatological cycle

Air-sea interactions in the south-eastern tropical Indian Ocean (SETIO, 80°-110°E and Eq-10°S, see **Figure 3.3.1**) is crucial in understanding the mechanism inducing Indian Ocean Dipole events. In principle, sudden equatorial wind changes can lead to the formation of Kelvin waves that, via modification of the thermocline depth, can either support or hinder the development of coastal upwelling along the coasts of Sumatra and Java. Hence, the zonal equatorial winds across the entire Indian Ocean can have a remote impact in the SETIO upwelling. On the other hand, the regional winds with their coast-parallel wind stress in the Sumatra and Java region (black arrows in fig 1) can locally induce coastal upwelling. This subsection explores the climatological cycle of surface winds in the region with a focus on the equatorial Indian Ocean and The SETIO upwelling region.



**Figure 3.3.1:** Schematic of the study region highlighting the SETIO region (80°E to 110°E and EQ to 10°S).

### **(a) Zonal equatorial winds**

The eastern equatorial Pacific is characterised by strong trade winds (easterlies). The warm pool of the Pacific Ocean is anchored at the western end of the basin over the equatorial region. Due to higher sea surface temperature (SST), the region over the warm pool is vulnerable to the deep convective activity. This tropical convective activity has a highly unstable nature and trigger atmospheric disturbances at intraseasonal time scale. Moreover, this intraseasonal convective disturbances can trigger strong zonal wind events over the western equatorial Pacific Ocean (McPhaden 1991; Hartten 1992; Harrison and Vecchi 1997; Madden and Julian 1994).

In contrast, the Warm Pool is located in the eastern portion of the Indian Ocean. The temperature of the Warm Pool has its seasonal peak in April-May and attains minimum values in September (Vinayachandran *et al.* 1991; Zhang *et al.* 2008; Kim *et al.* 2012; Saji *et al.* 2015). It is widely accepted that the surface equatorial winds are generally weak especially over the eastern equatorial Indian Ocean and particularly in boreal summer (June to September) (Schott *et al.* 2009; Vianaychandra *et al.* 2009; Delman *et al.* 2016; Chen *et al.* 2016). However, twice a year, the equatorial Indian Ocean intermittently experiences strong westerlies driving Wyrtki jets during the inter-monsoon periods of spring (April-May) and fall (October-November) (Wyrtki 1973).

On the other hand, the effects of equatorial and coastal Kelvin waves on thermocline variability along the Sumatra and Java coasts were documented in detail in number of previous studies (Qiu *et al.* 1999; Murtugudde *et al.*, 2000; Iskandar *et al.*, 2005, 2006; Sengupta *et al.*, 2007; Chen *et al.* 2015; Delman *et al.* 2016). Previous studies also concluded that these Kelvin waves are the dominant forcing of intraseasonal variability of sea level and thermocline depth of the SETIO region (Sprintall *et al.* 2000; Susanto *et al.* 2001; Murtugudde *et al.* 2000; Iskandar *et al.* 2005; Chen *et al.* 2015; Delman *et al.* 2016). All these studies noted the presence of Kelvin wave activity during the boreal summer-fall season (June to September). Study by Feng and Wijffels (2002) noted that intraseasonal instabilities of the South Equatorial current (SEC) may also trigger intraseasonal variability of sea level and thermocline depth in the SETIO region. This study does not deny role of the SEC in intraseasonal thermocline variability of the SETIO region, but it tries to highlight some other fundamental atmospheric forcing who is dominantly responsible for the variability.

The first question addressed in this section is whether the equatorial wind variability in the form of wind bursts in the Indian Ocean is sufficient to trigger large-amplitude Kelvin waves in the region.

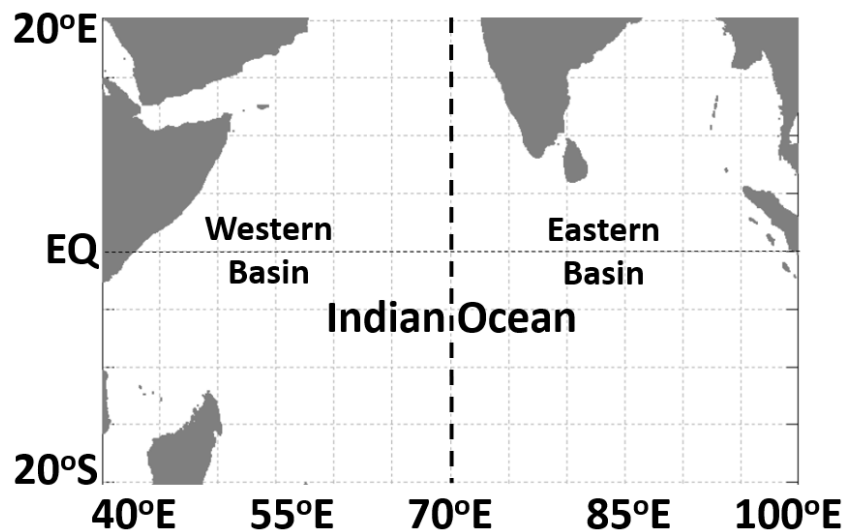


**Figure 3.3.2:** Schematic of tropical IO with east & west basins

Only few studies have documented sudden wind pulses in the equatorial Indian Ocean. Senan *et al.* (2003) noted the presence of the high-frequency westerly equatorial wind bursts (WWBs, 10 – 40 days longer) during early stages of the northern summer monsoon season, from 2000 to 2002. They named the WWBs “intraseasonal monsoon jets”. The explored jets had a basin-wide extent, similar to the wind forcing of Wyrтки Jets.

Subsequent studies using satellite data of high temporal resolution indicated that the equatorial Indian Ocean is the source of such high-energy surface zonal wind forcing during the period from June to September. These studies located the region of strong zonal winds from correlation statistics between sea level anomalies (SLA) at the coastal Sumatra/Java and zonal equatorial wind fields of the IO (Rao and Yamagata 2004; Iskandar *et al.* 2005, 2006; Sengupta *et al.* 2007; Chen *et al.* 2015; Delman *et al.* 2016). The consensus of these studies is that the strong zonal wind forcing develops within a narrow longitudinal band 70°-90°E of the equatorial Indian

Ocean. This smaller spatial coverage, only  $\sim 20^\circ$  in extent, of the wind forcing clearly separates them from the wind forcing that creates Wyrтки Jets.

Here, I derive monthly climatological mean of surface zonal wind speed from long-term satellite wind data (CCMP V2 data; 1988 – 2016; Atlas 2011) to verify the existence of strong zonal wind bursts during the boreal summer-fall period and to examine spatiotemporal characteristics of the zonal equatorial wind field in the Indian Ocean. Monthly climatological means of sea surface temperature (SST), outgoing long-wave radiation (OLR) and thermocline depths are also derived for this analysis. The NOAA SST OI data (from 1981 – 2016) is used to extract monthly SST climatology, ARGO data (2005 – 2016) are used to derive monthly climatology of thermocline depth using a newly proposed algorithm (Holte *et al.* 2017) and the NOAA OLR PSD operational dataset (Lee 2014) is used to derive the monthly climatology of satellite OLR from 1975 – 2016 as a proxy of convective activity in the tropical atmosphere.

The derived climatological values are then presented as Hovmoller diagrams to examine the behaviour of the annual cycle of monthly climatological values along the equatorial Indian Ocean (**Figure 3.3.3**). In a typical climatological year, the sea surface temperature (SST) along the equator of the Indian Ocean attains a single maximum (**Figure 3.3.3a**; orange and yellow shading). The SST peaks around April–May of the climatological year. The dominance of warm surface water in the eastern basin (**Figure 3.3.3a**; red shading) confirms the presence of the Warm Pool. On the other hand, the western equatorial Indian Ocean experiences surface cooling during the boreal monsoon due to the seasonal Somali upwelling, which lowers SST values during the period June to October (**Figure 3.3.3a**; blue shading).

The depth of the thermocline (**Figure 3.3.3b**) has a pronounced semi-annual cycle in the eastern basin ( $>70^\circ\text{E}$ ). Hence, as a signature of transient Wyrтки Jets, the thermocline depth has two maxima in the eastern basin (**Figure 3.3.3b**; red shading; Tomczak, M., & Godfrey, J. S., 2013; Wyrтки, 1973). Here the thermocline depth varies between 40-70m. Overall the thermocline is shallower in the western equatorial Indian Ocean (20-50m) throughout the year (**Figure 3.3.3b**; blue shading; Tomczak and Daniel, 1989). The existence of relatively warm water in conjunction with a relatively deep thermocline creates a large pool of anomalously high heat content in the eastern

equatorial Indian Ocean (Tomczak and Daniel, 1989; Vinayachandran and Shetye, 1991). Moreover, since the surface warming has single maxima in the eastern equatorial Indian Ocean in April-May, the warm water volume increases significantly during boreal summer-fall (June to September; ; Vinayachandran and Shetye, 1991). This enhanced warm water volume in the eastern equatorial IO (EEIO) is an energy source for atmospheric convection that tends to develop during boreal summer and fall.

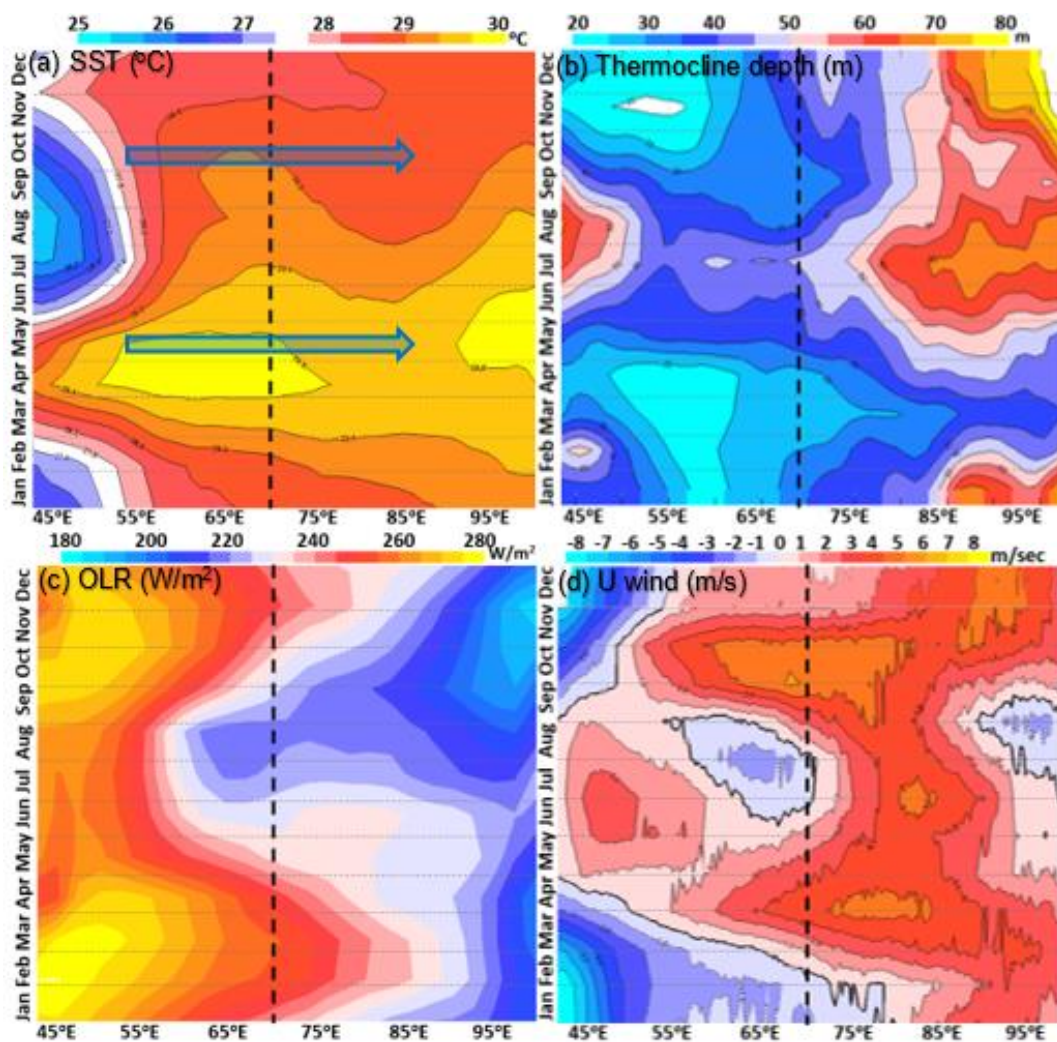


**Figure 3.3.3:** Time-longitude plots (Hovmoller diagram) along the equator of Indian the Ocean. Panel a) displays SST data from NOAA OI data over period of 1981-2016. Two horizontal thick arrows display the timing of spring and fall Wyrтки Jets. Panel b) represents values of thermocline depth from ARGO data over period of 2005-2016. Panel c) displays values of outgoing longwave radiation (OLR) from NOAA OLR data over period of 1975-2016. Panel d) shows values of zonal wind speed (m/s) from CCMP data over 1988-2015 period. All data are monthly climatological averages.

The outgoing long-wave radiation (OLR) data recorded from satellites can be used to detect the convective activity. Lower recorded values of OLR (satellite) corresponds to higher convective activity and vice versa, as cumulonimbus clouds (deep convective clouds) and atmospheric moisture content block the OLR.

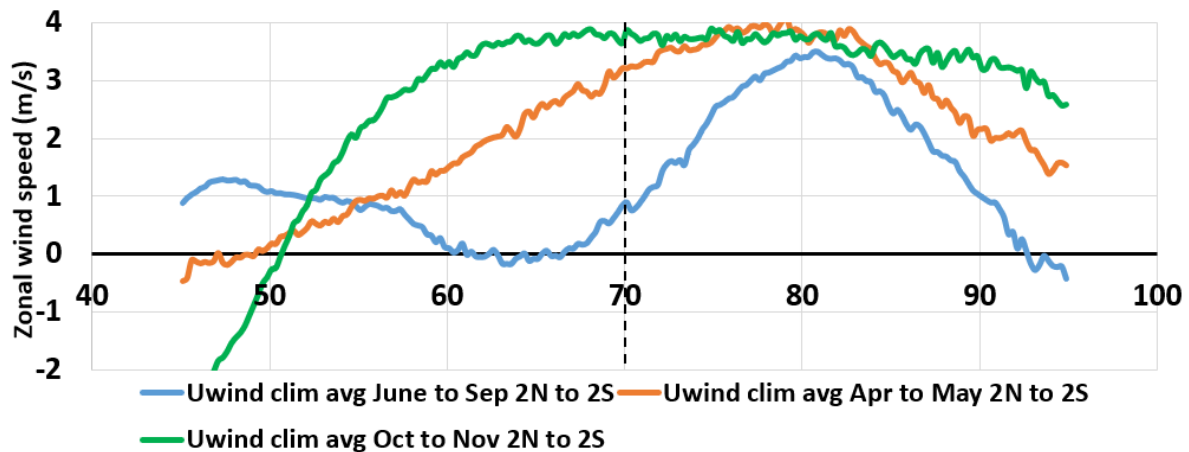


**Figure 3.3.4:** Seasonal averages of monthly climatological zonal wind velocity (m/s) along the equator of the Indian Ocean (40o-100oE) over the 1988-2015 period. Shown are the periods April-May, June-September, and October-November.

Higher convective activity (**Figure 3.3.3c**; blue shading) along the equator is located in the eastern Indian Ocean and coincides with the location of the warm pool (**Figure 3.3.3a**; orange and yellow shading). The deeper thermocline (**Figure 3.3.3b**; red and yellow shading) flowing 'spring Wyrтки jets' (see Vinayachandran *et al.* 2009) and the resultant enhanced warm water volume in the eastern equatorial Indian Ocean coincides with enhanced convective activity during boreal summer and fall (**Figure 3.3.3c**). The convective activity is characteristics by a high temporal variability, which possibly induces atmospheric instabilities in the troposphere and strong zonal wind events similar to those displayed in the western equatorial Pacific. Hence, the previously claim of 'weak' equatorial zonal surface winds during northern monsoon (June to September) needs to be re-evaluated.

According to the monthly climatological cycle of the surface zonal wind velocity, there are two larger-scale patches of strong westerlies extending from 50oE to 90oE (**Figure 3.3.3d**; red shading) that develop both in boreal spring (April-May) and fall (October-November), driving the Wyrтки Jets. Moreover, there are relatively strong (>3 m/s speed on a monthly average) westerlies around the year in the eastern basin

(**Figure 3.3.4d**; 70°E to 90°E, red shading). During the period between the spring and fall Wyrcki Jets (June to September), which is the focus of this study, the zone of strongest westerlies is found in the longitudinal band of 75°E to 85°E (**Figure 3.3.4d**; red shading), which is in agreement with the previous studies of Kelvin wave activities discussed above. During his season, zones of weak westerlies or easterlies are shifted towards the very eastern part (90°-100°E) of the equatorial Indian Ocean and also establish in the western basin (see **Figure 3.3.4d**). This distinct seasonal shift of westerly wind patterns along the equatorial Indian Ocean becomes more obvious with a focus on changes that occur during the period April-November (**Figure 3.3.4**). Here, strong westerlies related to spring (April-May) and fall (October-November) Wyrcki Jets can be identified again, and we can see the zone of average westerly winds that establishes in the zone 75°- 90°E.

The difference in the spatial extent of zones of strong westerlies in different seasons (as seen in **Figure 3.3.4**) agrees with previous studies of Kelvin-wave activities at the equatorial Indian Ocean (Rao and Yamagata 2004; Iskandar *et al.* 2005, 2006; Sengupta *et al.* 2007; Chen *et al.* 2015; Delman *et al.* 2016). The argument developing in this sub-section is that the enhanced warm water volume (deeper thermocline in **Figure 3.3.4b**) and enhanced convective activity (weaker OLR values in **Figure 3.3.4c**) over the eastern basin of the Indian Ocean during June and September (i.e. between the spring and fall Wyrcki Jets) may be characterized by transient short-lived westerly wind bursts. A detailed analysis of surface winds at short “synoptic” time scales will be discussed in section 3.3.2.

### **(b)Wind forcing along the coasts of Java and Sumatra**

As stated before, the eastern equatorial Indian Ocean is overall characterized by a deeper thermocline and relatively warm surface water. Given the dominance of eastern equatorial westerlies, equatorial upwelling cannot develop in the Indian Ocean. This situation is contrary to the typical state of the Pacific Ocean and the Atlantic Ocean, where the easterly trade winds create equatorial upwelling. Hence, the contribution of the Indian Ocean equatorial wave guide in southwestern Sumatra upwelling region is minimal or negative.

Nevertheless, Susanto *et al.* (2001) noted that seasonal coastal upwelling can develop along the coasts of Java and southern Sumatra during boreal summer and

fall (June to September). Susanto *et al.* (2001) suggested that this upwelling is the signature of classical wind-driven coastal upwelling. The classical Ekman-layer theory suggests that seasonal south-easterly winds develops in this region (marked arrows in **figure 3.3.5**) can trigger coastal upwelling, as they are coast parallel.

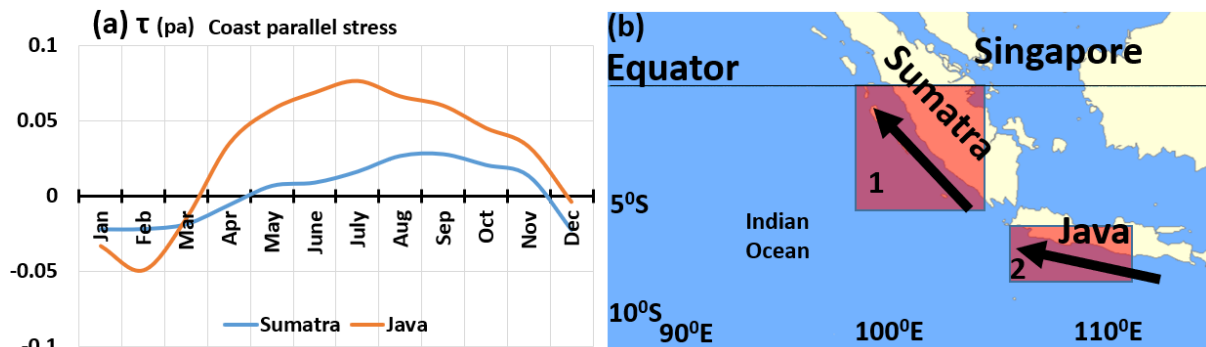


**Figure 3.3.5:** Climatological cycle of the coast parallel winds averaged for the regions shown in the right panel.

I derived monthly climatological mean of meridional and zonal components of surface winds for boxed averaged regions (regions 1 and 2 shown in **figure 3.3.5b**) along the coasts of Java and southern Sumatra from long-term satellite wind data (1988 – 2016; CCMP V2; Atlas 2011). Monthly climatological values of coast parallel stress are derived from this data and displayed in figure 3.5.5a to examine seasonal cycle of the upwelling favourable atmospheric forcing in the region.

The seasonal cycle of coast parallel stress along the coasts of Java (**figure 3.3.5a**, orange line) suggests that the region has upwelling favourable conditions during boreal summer-fall with positive coast parallel stress values. Moreover, the plot (of figure 3.5.5a, orange line) has pronounced seasonal peak in June and July with strong upwelling favourable values of 0.07 to 0.08 Pa in the region. This situation indicates presence of robust upwelling favourable conditions in the region during boreal summer fall season.

Conversely, the seasonal cycle of coast parallel stress along the southwest Sumatra coastline displays weak positive values during boreal summer fall season (figure 3.3.5a, blue line). Moreover, the annual peak of the plot (figure 3.3.5a, blue line) also displays weak values between 0.01 to 0.02 Pa during August and September. Weak positive values and lower annual peak of coast parallel stress along the southwest Sumatra coastline indicates poor presence of upwelling favourable

conditions in the season. Though, according to historical data strong coastal upwelling was observed in the region during certain historical years in this region.

Hence, seasonal coastal upwelling is not a regular feature along the southwest Sumatra coasts unlike southern Java coasts. The climatological cycle of coast parallel stress of Java-Sumatra region (figure 3.3.5) represents broader seasonal characteristics of upwelling favourable winds in the region. A detailed analysis of surface winds at interannual time scale along with its correlation analysis will be discussed in section 3.3.3.

### **3.3.2 Interannual variability of the zonal equatorial winds**

The climatological cycle of zonal winds at the equatorial Indian Ocean, as discussed in section 3.3.1a, exhibits strong westerlies in the eastern equatorial Indian Ocean and weak westerlies or easterlies in western equatorial Indian Ocean during boreal summer-fall season. Boreal summer-fall is the seasonal during which the coastal upwelling along Java and Southern Sumatra coastline can develop. The role of the surface zonal wind forcing along the equatorial Indian ocean is well established as the fundamental forcing of the equatorial Kelvin waves. The triggered Kelvin waves along the Indian Ocean equatorial wave guide have active role in the upwelling mechanism along the Java and southern Sumatra coastline as it can deepen the thermocline of the region by the coastal Kelvin waves. Hence, the interannual characteristics of the zonal winds along the equatorial Indian Ocean is examined in this section by extracting seasonal mean and standard deviation from seasonal using the daily wind fields.

#### **(a) Seasonal average and standard deviation: 1988 to 2016**

The equatorial Indian Ocean regime is divided into 4 zones as shown in **figure 3.3.6**, to evaluate seasonal characteristics (during June to September) of zonal wind speed ( $U_{sp}$ ) over each zone. Out of divided four zones, two central zones have  $20^\circ$  longitudinal coverage (**figure 3.3.6**, Box3:  $50^\circ\text{E}$  to  $70^\circ\text{E}$  and Box 2:  $70^\circ\text{E}$  to  $90^\circ\text{E}$ ) and two corner zones have  $10^\circ$  longitudinal coverage (**figure 3.3.6**, Box1:  $90^\circ\text{E}$  to  $100^\circ\text{E}$  and Box 1:  $40^\circ\text{E}$  to  $50^\circ\text{E}$ ). According to the climatological cycle of the zonal winds at the equatorial Indian Ocean, discussed in sec 3.3.1a (**figure 3.3.5**), only the Box 2 region (of **figure 3.3.6**) exhibits the strong westerly winds during boreal summer-fall (June to September) and other regions exhibits weaker zonal winds.

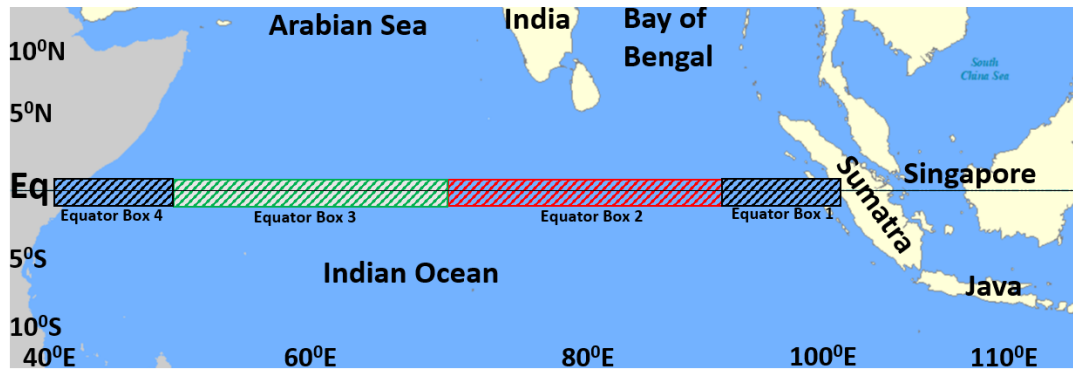


**Figure 3.3.6:** Schematic of tropical IO. Marked boxes represents the equatorial zones.

Seasonal average values and standard deviation of the zonal wind speed ( $U_{sp}$ ) averaged over each boxed region of **figure 3.3.6**, is derived from daily CCMP V2 satellite wind data and displayed in **figure 3.3.7** during boreal summer-fall. The values displayed in the top-right corner of each plot of **figure 3.3.7** (a to d) are long term seasonal average values over the entire study period (1988-2016) and marked with black dashed line in each plot. According to long-term average values the region of Box2 (**figure 3.3.7b**) exclusively shows stronger zonal component at 2.16 m/s, other three regions exhibit very weak zonal wind speed values, for box1:0.72 m/s (**figure 3.3.7a**), for box3:0.22 m/s (**figure 3.3.7c**) and for box4:0.92 m/s (**figure 3.3.7d**). Higher long-term seasonal average of zonal wind speed indicates box 2 region is the region of strong westerlies (Rao and Yamagata 2004; Iskandar *et al.* 2005, 2006; Chen *et al.* 2015; Delman *et al.* 2016).

The region of box 1 (of **figure 3.3.6**) is located at off Sumatra hence the zonal forcing of this region has significant contribution in the seasonal upwelling along the southern coastal Sumatra. The seasonal average values of the zonal wind speed ( $U_{sp}$ ) in box 1 region exhibits strong interannual fluctuations, with values ranging from -1.5 m/s to 2.5 m/s (**figure 7a**, blue line). In most years (in the study period) seasonal average of zonal wind speed displays positive values above 1.5 m/s. During boreal summer-fall of certain years zonal wind speed displays negative values of seasonal average; in 1994, 1997 and 2006 which were recorded as strong positive Indian Ocean Dipole (pIOD) event years. In 2007, 2008 and 2015 also the seasonal average zonal winds have negative values though they were recorded as weak or aborted pIOD events. The negative values indicate reversal of convectonal westerlies to easterlies in the season.

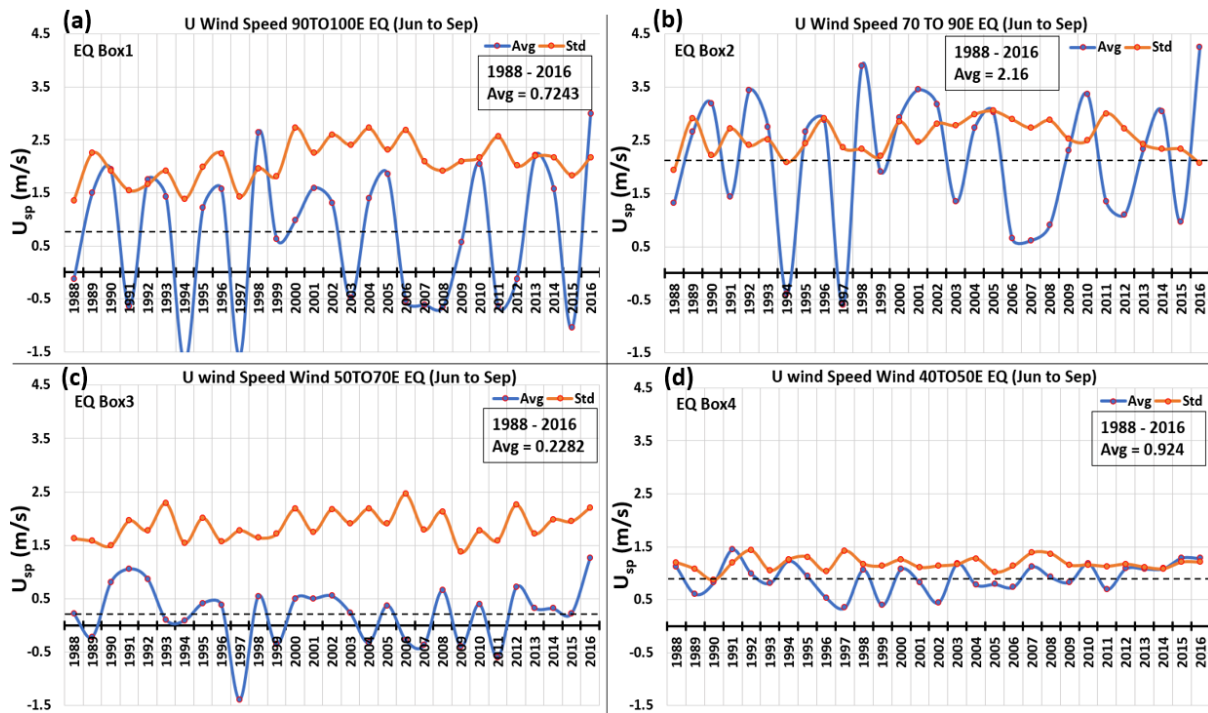


**Figure 3.3.7:** Seasonal average (June to September) and STD from seasonal average of zonal wind speed derived from daily wind fields of CCMP satellite data. Averaged over the marked regions shown in **figure 3.3.6**, where Panel a) displays values for Eq Box1 (90°E to 100°E), b) displays values for Eq Box 2 (70°E to 90°E), c) displays values for Eq Box 3 (50°E to 70°E) and (d) displays values for Eq Box 4 (40°E to 50°E).

The box 2 region (of **figure 3.3.6**) at the EIO exhibits strong interannual variations of the seasonal average values of  $U_{sp}$  in the range from -0.5 m/s to 3.5 m/s (**figure 3.3.7b**, blue line). Though, positive values above 2.5 m/s has dominance in the line plot (of **figure 3.3.7b**) which indicates the westerlies predominate in the region. During strong pIOD event years (1994, 1997 and 2006) seasonal average values of zonal wind speed decline to near zero values, which indicates their minimal role in the equatorial ocean dynamics. During aborted or weak pIOD event years; in 2007, 2008, 2011, 2012 and 2015; the seasonal average of zonal winds speed weakens to values between 0.5 m/s to 1.5 m/s which indicates suppressed effect of seasonal westerlies.

The seasonal average values of  $U_{sp}$  for box1 and box2 vary in accordance at interannual timescale (**figure 3.3.7 a and b**). When seasonal zonal wind speed values display higher positive values of in the box 2 region (**figure 3.3.7b**), box 1 region also displays the positive values with smaller positive values (compare to box 1). The  $U_{sp}$  values of box 1 region decline to negative values in the years 1991, 1994, 1997, 2003,

2006, 2007, 2008, 2011, 2012 and 2015 (fig 7a). Likewise, the Usp values of box2 decline below its long-term average in the same years though went negative only in 1994 and 1997 (**figure 3.3.7b**). Negative values of Usp indicates presence of easterlies in box 1 region, which can trigger the equatorial upwelling similar to which display in the eastern equatorial Pacific from trade winds, while weaker positive values cannot contribute in equatorial dynamics and negative zonal winds of box 1 has dominance during the period. Hence, box 1 and box 2 perform collectively active role in equatorial ocean dynamics with presence of conventionally westerlies which alters during certain event years together.

The zonal winds in the western basin of equatorial IO for boxes 3 and 4 (**figure 3.3.6**) exhibit weaker long-term mean and seasonal mean values (**figure 3.3.7 c, d**). Region of box3 exhibits a long-term seasonal average value of Usp is 0.22 m/s (**figure 3.3.7c**, dashed black line) and box4 has 0.92 m/s (**figure 3.3.7d**, dashed black line). Box3 exhibited positive and negative values of seasonal mean at interannual timescale (fig 7c), though values are very weak between -0.5 to 0.5 m/s which resemble weak easterlies or westerlies and indicate suppressed role in equatorial dynamics. Only in the year, 1997 box3 has considerable negative seasonal mean at -1.5 m/s (easterlies), which might support equatorial upwelling in the strong pIOD year. While box4 region exhibits long term seasonal mean value of zonal wind speed at 0.924 m/s (**figure 3.3.7d**) and it fluctuate around this value at interannual time scale.

The characteristics of equatorial winds in interannual statistics indicates that the western basin cannot exhibit notable interannual variation and displays weak zonal wind speed values. Hence, with weaker zonal forcing it cannot contribute to equatorial ocean dynamic and has no relation to active IOD events. On the other hand, eastern equatorial IO region (**figure 3.3.6**, box 1 and box 2) has active role in equatorial dynamics in all years of the study period with positive values during inactive IOD event years and weaker or negative values during active pIOD event years.

The STD of zonal wind speed from a seasonal mean for all the region of **figure 3.3.6** stay at average values between 1.5 to 2.5 and cannot shows considerable interannual variations (**figure 3.3.7 a to d**, orange line).

### **(b) Histogram statistics for 1988 to 2016**

The histogram of daily zonal wind speed values (Usp) averaged over each boxed region of **figure 3.3.6** is prepared from daily wind speed dataset (CCMP V2 satellite data) and displayed in **figure 3.3.8** to investigate the distribution of daily Usp values in the different zones of the equatorial IO. The histogram displayed in **figure 3.3.8** is for boreal summer-fall (June to September) of 1988 to 2016. The total number of days during boreal summer-fall (June to September) of 1988 to 2016 are 3539 days, hence the histogram distribution of each boxed region is displayed with a percentage share of the particular zonal wind speed values (Usp) compared to 3539 days.

Usp values are classified with certain names which indicate direction and strength of zonal component of surface winds, to explain the histogram plots. Positive zonal wind speed values (Usp) with values above 2 m/s are labelled as “westerlies”, and negative values below -2 m/s are labelled as “easterlies”. Likewise, Values of Usp above 4 m/s are tagged as “high energy westerlies” and values below -4 m/s are labelled as “high energy easterlies”. The values between -2 m/s to 2 m/s tagged by “weak easterly or westerly” as this study is interested in zonal component of the equatorial winds exclusively, though it can be noted that the values of Usp average over the boxed region of 10°–20° wide longitudinal coverage which may have directional ambiguity within the region.

The histogram distribution of box1 region (**figure 3.3.8a**) indicates dominance of “weak easterly or westerly” with 59% presence collectively. “Weak easterly” has 13% presence and “weak easterly” has 18% presence in histogram plot. “High energy westerly” records 10% presence while “high energy easterly” has negligible presence in the histogram of box1 region. The westerlies have dominance in box 2 region as displayed in histogram of **figure 3.3.8b** with collectively 54% presence. “High energy westerly” has 29% presence and “weak westerly” has 25% presence. “Weak westerly or easterly” has collective 38% presence and “weak easterly” has 6% presence in the histogram of box2. “High energy easterly” again has rare appearance in box2 region.

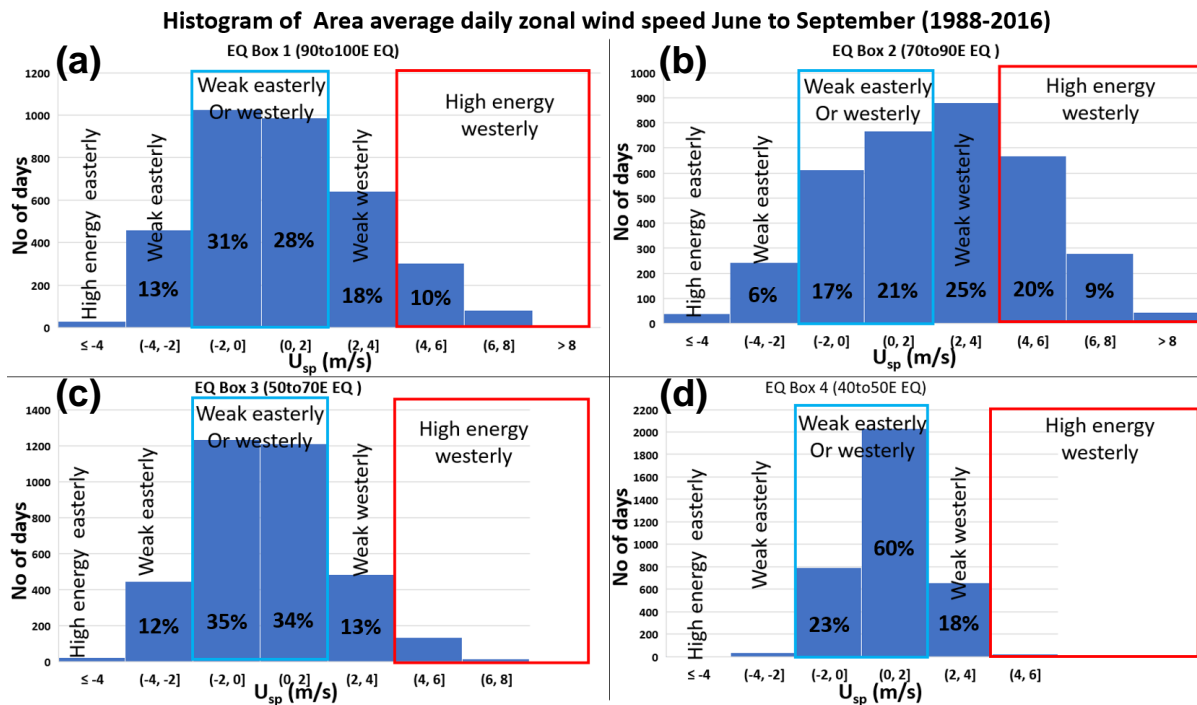


**Figure 3.3.8:** Histogram of area average daily zonal wind speed from CCMP satellite data over the boxed regions shown in **figure 3.3.6**, in boreal summer (June to September) of 1988 to 2016. Panel a) displays values for Eq Box1 (90°E to 100°E), b) displays values for Eq Box 2 (70°E to 90°E), c) displays values for Eq Box 3 (50°E to 70°E) and (d) displays values for Eq Box 4 (40°E to 50°E).

Region of box 3 displays dominance of weaker zonal winds with 69% presence of “weak easterly or westerly” in the histogram (**figure 3.3.8c**). “Weak westerly” has 13% presence followed by “weak easterly” with 12% presence. “High energy westerly” and “high energy easterly” cannot make noticeable appearance in the histogram.

Far western region of box 4 has dominance of “weak easterly or westerly” in the histogram (**figure 3.3.8d**) with collective presence of 83%. “Weak westerly” has 18% presence in the region while high energy components of zonal winds speed cannot register their presence in histogram.

Histogram statistics indicates active role of box2 region with considerable presence of “high energy westerly” along with “weak westerlies” though it can trigger downwelling kelvin waves which has destructive effects in the upwelling mechanism along the Java and southern Sumatra coastline. Box1 region also displays “westerly” component with secondary dominance after “weak easterly or westerly” and indicates presence of westerlies in the region. Western basin cannot exhibit strong zonal values in any direction and has no active role as zonal forcing.

### (c) Histogram statistics for 1994, 1997 and 2006

Histogram statistics of the  $U_{sp}$  values in the boreal summer-fall of the years active pIOD years 1994, 1997 and 2006 is prepared and displayed in **figures 3.3.9, 10 and 11**. The total number of days in each boreal summer-fall season (June to September) is 122 days; hence the histogram distribution of each boxed region is displayed with a percentage share of the particular zonal wind speed values ( $U_{sp}$ ) compared to 122 days. To visualise the changes of zonal surface forcing from average long-term values (figure 3.3.8) to individual years (figure 3.3.9 to 3.3.11), all the percentage values of these **figures** are displayed in table 1.

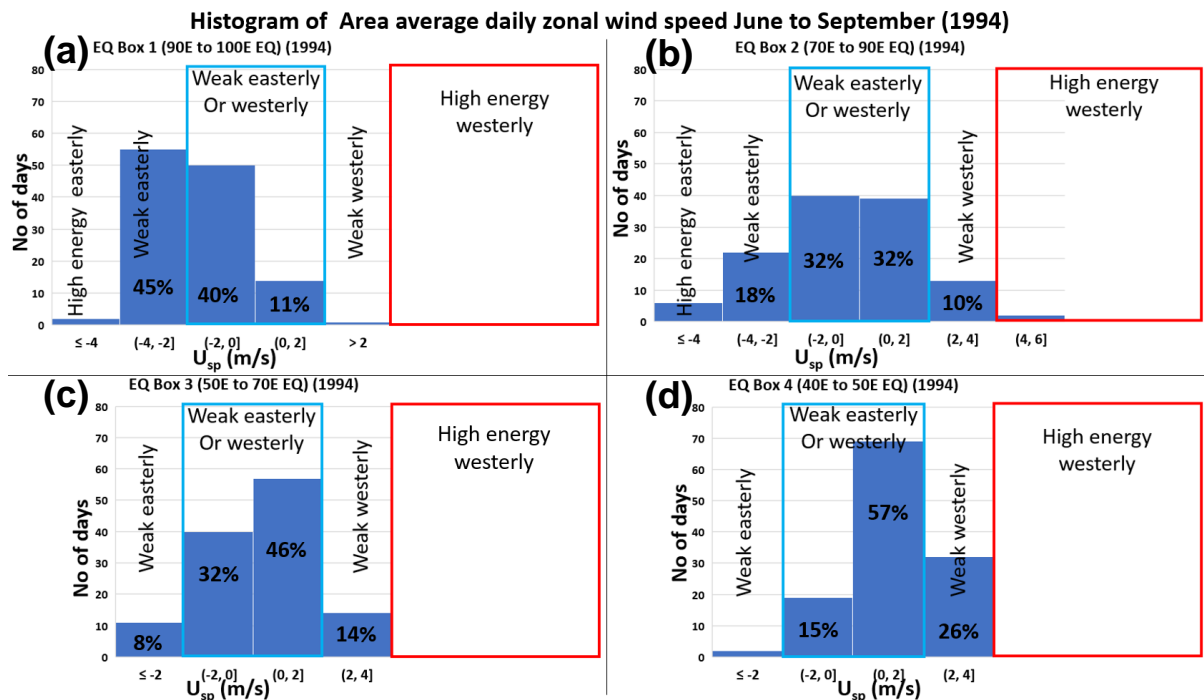


**Figure 3.3.9:** Histogram of area average daily zonal wind speed from CCMP satellite data over the boxed regions shown in **figure 3.3.6**, in boreal summer (June to September) of 1994. Panel a) displays values for Eq Box1 (90°E to 100°E), b) displays values for Eq Box 2 (70°E to 90°E), c) displays values for Eq Box 3 (50°E to 70°E) and d) displays values for Eq Box 4 (40°E to 50°E).

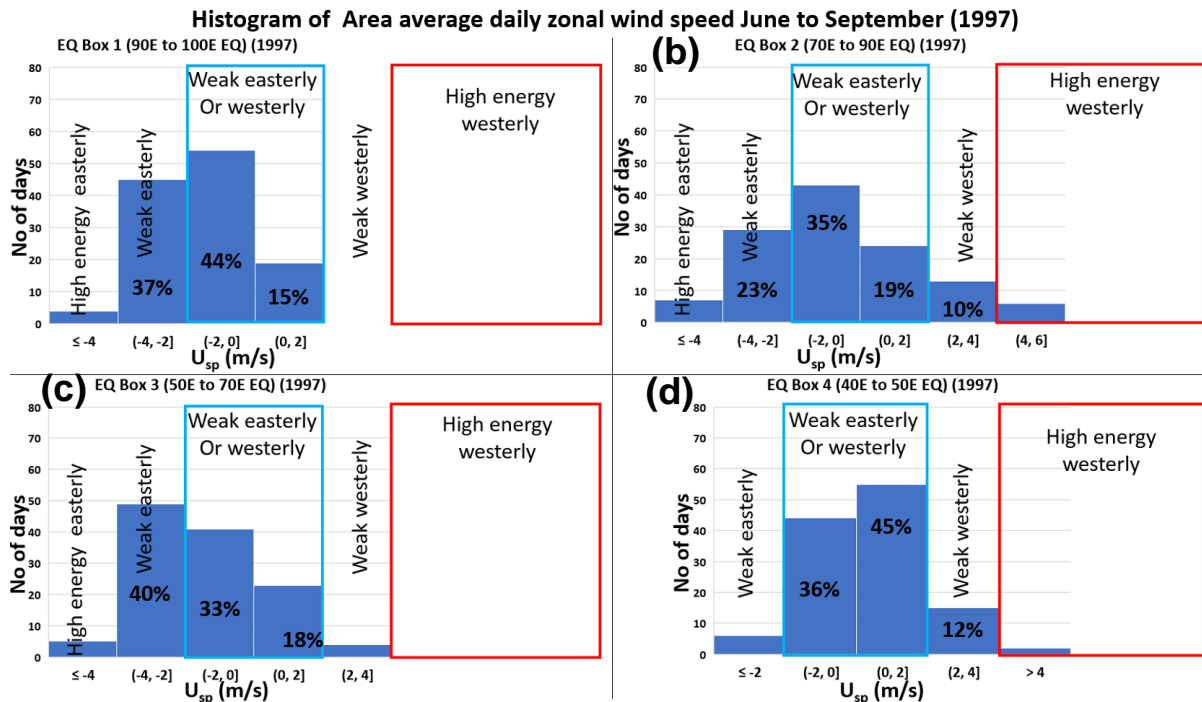


**Figure 3.3.10:** Histogram of area average daily zonal wind speed from CCMP satellite data over the boxed regions shown in **fig 6**, in boreal summer (June to September) of 1997. Panel a) for Eq Box1 (90E to 100E), (b) for Eq Box 2 (70E to 90E), (c) for Eq Box 3 (50E to 70E) and (d) for Eq Box 4 (40E to 50E).

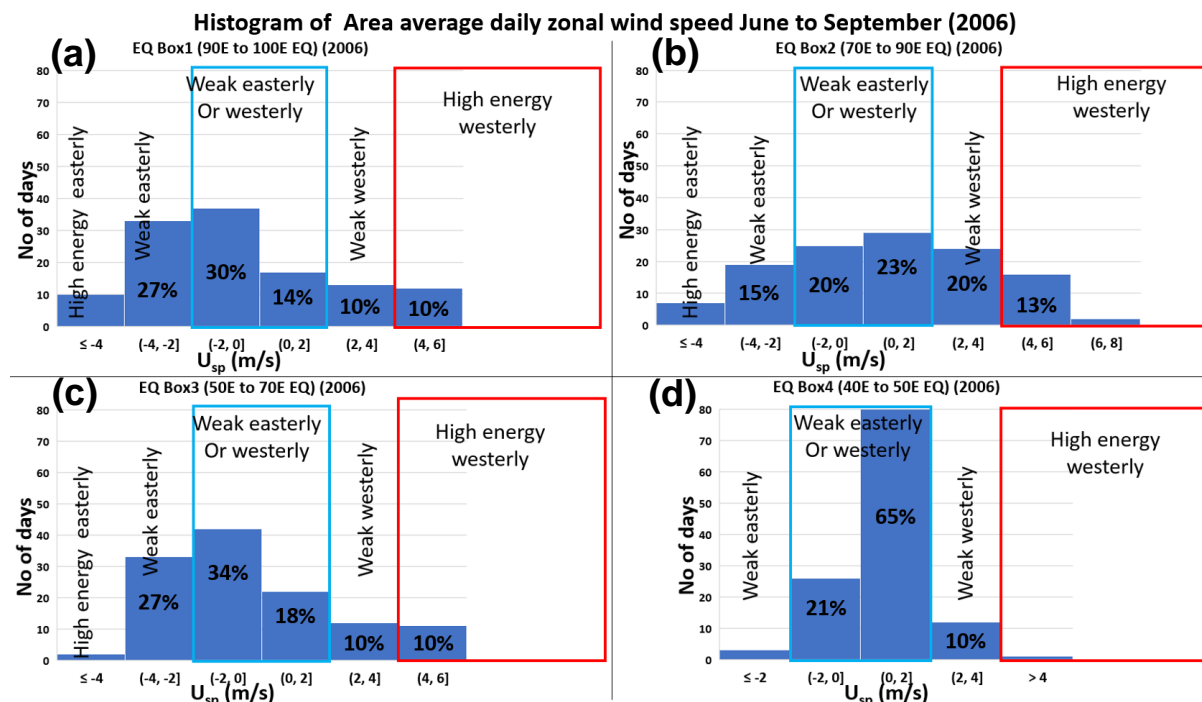


**Figure 3.3.11:** Histogram of area average daily zonal wind speed from CCMP satellite data over the boxed regions shown in **figure 3.3.6**, in boreal summer (June to September) of 2006. Panel a) displays values for Eq Box1 (90°E to 100°E), b) displays values for Eq Box 2 (70°E to 90°E), c) displays values for Eq Box 3 (50°E to 70°E) and (d) displays values for Eq Box 4 (40°E to 50°E).

**Table 3.3.1:** Percentage values from Histogram of **figure 3.3.8** to **figure 3.3.11**. The heading in the table can be read as HEW: high energy westerly, W: westerly, HE: high energy easterly, E: easterly, Weak: weak easterly or westerly.

Box1	HEW	W	HE	E	Weak	Box3	HEW	W	HE	E	Weak
All years	10	28		13	60	All years		13		12	70
1994				45	51	1994		14		8	78
1997			3	40	60	1997		3		44	51
2006	10	20	3	30	44	2006	10	20		27	52
Box2	HEW	W	HE	E	Weak	Box4	HEW	W	HE	E	Weak
All years	30	55		6	38	All years		18			82
1994		10	4	22	64	1994		26		2	72
1997		10	6	29	54	1997		12		6	81
2006	13	33	5	20	43	2006		10		3	86
All values are in percentage (%)											

Previously displayed destructive westerlies in histogram of box 1 in the previous section 3.3.2b is disappeared in boreal summer-fall of 1994 and 1997. “Weak westerly” and “high energy westerly” of box 1 is completely disappeared in histogram of 1994 and 1997 (**figure 3.3.9a, 3.3.10a; table3.3.1**). On the other hand, a drastic increase in the presence of easterlies is displayed in box 1 region in 1994 and 1997 with 45% and 40% values respectively (**figure 3.3.9a, 3.3.10a; table3.3.1**), compared to 13% presence displayed in the same region for the entire study period (1988-2016, **figure 3.3.8a**).

Moreover, high energy easterlies were displayed in 1997 with 3% contribution. Though, the dominance of “weak easterly or westerly” sustained in both individual years with 51% and 60% values in 1994 and 1997. Presence of easterlies and disappearance of westerlies in 1994 and 1997 can support seasonal coastal upwelling along the Java and Sumatra coastline.

Dominance of westerlies in Box2 region as displayed previous sub-section 3.3.2 b, is diminished in 1994, 1997 with disappearance of “high energy westerly” (**figure 3.3.9b, 10b, table3.3.1**). The reduced presence of “weak westerly” in 1994 and 1997 with 10% presence in histogram of box 2 region. While, the same box 2 region displays a notable increase in “weak easterly” with 18% and 23% presence in 1994 and 1997 along with 4% and 6% presence of “high energy easterly” (**figure 3.3.9b,**

3.3.10b, table3.3.1). Considerable, increase of “weak easterly or westerly” is also displayed with 64% and 54% in 1994 and 1997 respectively.

Box 2 region also displays the decrease of “high energy westerly” and “weak westerly” in 2006 with 13% and 20% values (figure 3.3.11b, table3.3.1). Presence of “weak easterly” is increased to 20% along with 5% presence of “high energy easterly” in 2006 in box 2 region. A minor increase in “weak easterly or westerly” is recorded at 43% value.

Hence, the dominating destructive westerlies of the box2 region (witnessed in previous sub-section 3.3.2b) were altered into constructive easterlies along with weaker zonal winds during strong positive Indian Ocean dipole (pIOD) event of 2006. This reformed situation supported the seasonal Sumatra upwelling by suspension of the downwelling Kelvin waves.

The western equatorial Indian Ocean region cannot display notable changes in the characteristics of zonal winds during strong pIOD events years (figure 3.3.9 to 3.3.11: c and d, table1) compare to previous sub-section 3.3.2b. Box 3 region displays a rise in easterly presence with 44% value in 1997 (figure 3.3.10c, table3.3.1) and decreased presence of westerlies to 3%, compare to the percentage share of section 3.3.2 b. This situation further supports the seasonal upwelling along Java and southern Sumatra coasts following box2 and box1 in boreal summer of 1997.

Comparison of histogram statistics of Usp values between long-term values and during pIOD event years, suggests a reversal of zonal forcing in the eastern equatorial IO (EEIO). This reversal of zonal winds supports seasonal coastal upwelling along the southern Sumatra and Java coasts. The question arises here, how the zonal winds of the EEIO reverses in the boreal summer of the particular years? Is this reversal a precursor of the pIOD events which may act as the trigger of the event or they are the aftermath of the event?

Moreover, is a shift in the zonal surface forcing of the equatorial IO lone responsible for the development of enhanced coastal upwelling and unconventional surface cooling at the Sumatra and Java coasts in pIOD event years? Else uncommon coupling between local surface forcing (at Java/Sumatra coasts itself) and ocean dynamics also have a crucial role in developing strong pIOD event? If local forcing has

an active role in these years, then the question is which local region displays the change in the direction of winds from conventional behaviour and how they differ from other average years? To answer these questions, we will evaluate the statistics of Java Sumatra coastal winds in the next section 3.3.3.

### **3.3.3 Interannual variability of winds along the southern coastal Java and Sumatra**

The climatological cycle of the coast parallel stress along the coastal Java and Sumatra, as noted previously (sec 3.3.1b), indicates that strong upwelling favourable winds develop at the coastal Java regularly from June to August. While, the southern coastal Sumatra displays weak upwelling favourable winds in August and September normally. The interannual statistics of coast parallel stress along the coastal Java and Sumatra is performed in this sub-section to evaluate its seasonal characteristics in each season from 1988 to 2016. To keep the homogeneity with interannual statistics of equatorial winds (discussed in previous section) and to avoid the Wyrcki Jets related anomalies in the region, the boreal summer-fall period (June to September) is selected to perform interannual statistics.

#### **(a) Seasonal average and standard deviation**

I derive the seasonal average values and standard deviation (STD) of coast parallel stress along the coastal Java and southern Sumatra. Daily wind fields of the CCMP V2 satellite data set, from 1988 to 2016, is used to extract seasonal mean and STD values. The derived values of seasonal average and STD is displayed in **figure 3.3.12**, where values in top right corner indicates long term seasonal average and marked by dashed straight line in each panel.

The long term seasonal average value of coast parallel stress along the coastal Java exhibit strong value at 0.053 Pa. The seasonal average values of coastal parallel stress along the coastal Java does not exhibit substantial interannual variation (**figure 3.3.12a**) and stay strong around long-term average value. In few years seasonal value of coast parallel stress reaches above 0.06 Pa while in 1989 and 1998 it drops to 0.04 Pa. The STD of coast parallel stress from seasonal mean has higher values in 1989 and 1998 indicates higher intraseasonal variation. Moreover, in 1995, 2005, 2010 and 2013 STD show higher values and indicates higher intraseasonal variation of coast parallel stress. Hence, intraseasonal process in the region might be responsible for

the interannual variation of seasonal mean of coast parallel stress though it is limited for the coastal Java region.

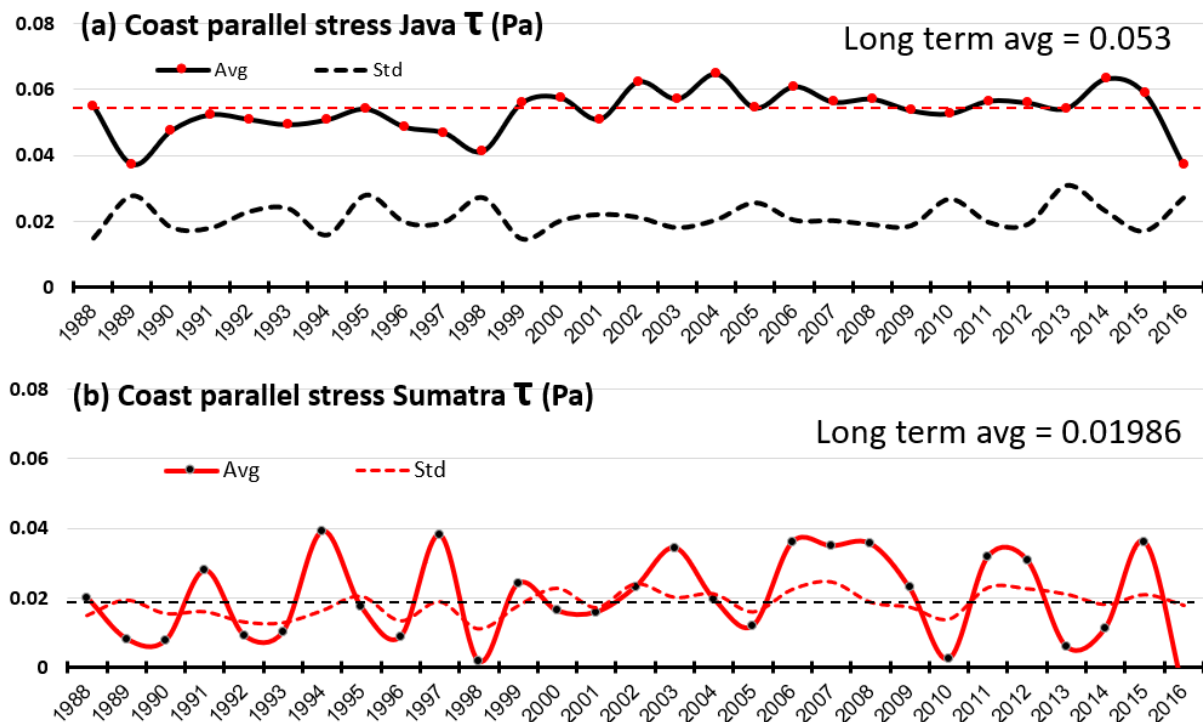


**Figure 3.3.12:** Seasonal average (June to September) and STD from seasonal of coast parallel stress average over the regions shown in **fig 5b** derived from daily wind fields of CCMP V2 satellite data for 1988 to 2016. Panel a) displays values along the coasts of Java and panel b) displays values along the southern coastal Sumatra.

The long-term average value of seasonal mean of coast parallel stress is weak 0.01986 Pa along the southern coastal Sumatra. Moreover, the seasonal mean of coast parallel stress displays strong interannual variations at the southern Sumatra coasts (**figure 3.3.12b**). In 1994, 1997 and 2006 coast parallel stress displays higher values at 0.04 Pa and indicates enhanced upwelling favourable conditions along the southern Sumatra coasts. These years were documented as strong positive Indian Ocean dipole event years, when strong coastal upwelling along Java and Sumatra coasts triggered substantial surface cooling in the eastern equatorial Indian Ocean (EEIO).

Moreover, in 2003, 2007, 2008, 2012 and 2015 coast parallel stress displays higher seasonal mean and indicates upwelling favourable conditions, though in these years surface cooling cannot develop in the EEIO and hence they were considered as aborted IOD events. Rao and Yamagata (2004) noted that the intraseasonal

disturbance in the eastern equatorial Indian Ocean terminated the positive Indian Ocean Dipole event in 2003. This situation indicates coastal winds at Java and Sumatra is not exclusively responsible for sea surface temperature anomalies (SSTA) in the region and suggests parallel role of other intraseasonal processes in ocean-atmosphere interaction of the region.

Seasonal mean of coast parallel stress displays lowest values in 1998 and 2010 at nearly 0.0 Pa when upwelling favourable winds were suppressed in the season and these years were documented as the negative Indian Ocean Dipole event years. Other years display weaker seasonal mean of coast parallel stress hence upwelling along the southern Sumatra coasts cannot develop.

Hence, seasonal mean of coast parallel stress displays strong interannual variations along the southern Sumatra coasts, while it displays robust values along Java coasts with little interannual variations. Higher values of coast parallel stress along southern Sumatra coasts in pIOD event years and lower values in other years is indicative and suggest active role of southern Sumatra coastal upwelling in development of surface cooling in the region.

#### **(b) Histogram statistics along the coasts of Java**

Histogram plots of daily coast parallel stress values along the Java coasts are prepared and displayed in **figure 3.3.13**, for entire study period and also for pIOD event years individually, to investigate the distribution of stress values in daily winds and to explore the dominating values. Daily counts of stress values are converted in percentage compared to total number of counts for comparison. For entire study period total day counts are 3538 and for individual years it is 122, and percentage of daily counts of different stress values are derived from these values.

In the case of entire study period (**figure 3.3.13a**) strong coast parallel stress values dominate in the season with 34% presence of 0.04 to 0.06 Pa values and 40% presence of greater than 0.06 Pa values with collocated presence of these higher stress values reaches 74%. Lower than 0.04 Pa values have limited presence (in **figure 3.3.13a**) with combined percentage of 26% and individual presence of 18% and 8% for 0.02 to 0.04 Pa and less than 0.02 Pa respectively.

In 1994 daily presence of coast parallel stress values above 0.04 Pa remains unchanged compare to entire study period with 74% (**figure 3.3.13b**) while their distribution is rearranged as 0.04 to 0.06 Pa values are elevated to 48% and values greater than 0.06 Pa are decreased to 26%. Stress values weaker than 0.02 Pa are disappeared and values between 0.02 to 0.04 Pa are increased to 25%. In 1997 presence of higher stress values displays minor downturn with 68% presence is recorded for stress values above 0.04 Pa, while stress value below 0.04 Pa exhibits minor upsurge with 32% presence (**figure 3.3.13c**).

2006 displays a strongest transformation of coast parallel stress along the Java coastline with highest ever recorded stress values in the season at 84% presence of stress values above 0.04 Pa. Moreover, presence of stress values above 0.06 Pa is elevated to 54% which is also strongest in the study period following by 28% presence of stress values between 0.04 to 0.06 Pa.

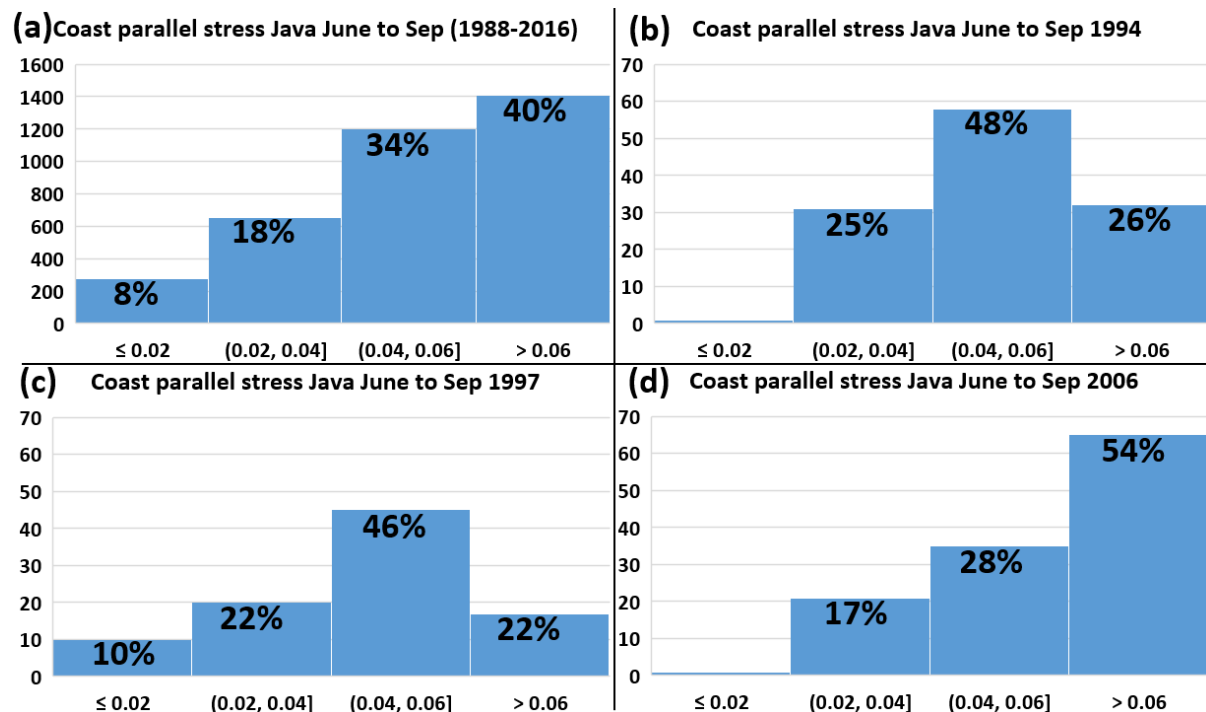


**Figure 3.3.13:** Histogram of area average daily coast parallel stress derived from satellite CCMP V2 data and averaged over the coastal Java region shown in **figure 3.3.5b**. Panel a) displays histogram for June September 1988-2016, b) for June to September of 1994, c) for June to September 1997 and d) for June to September 2006.

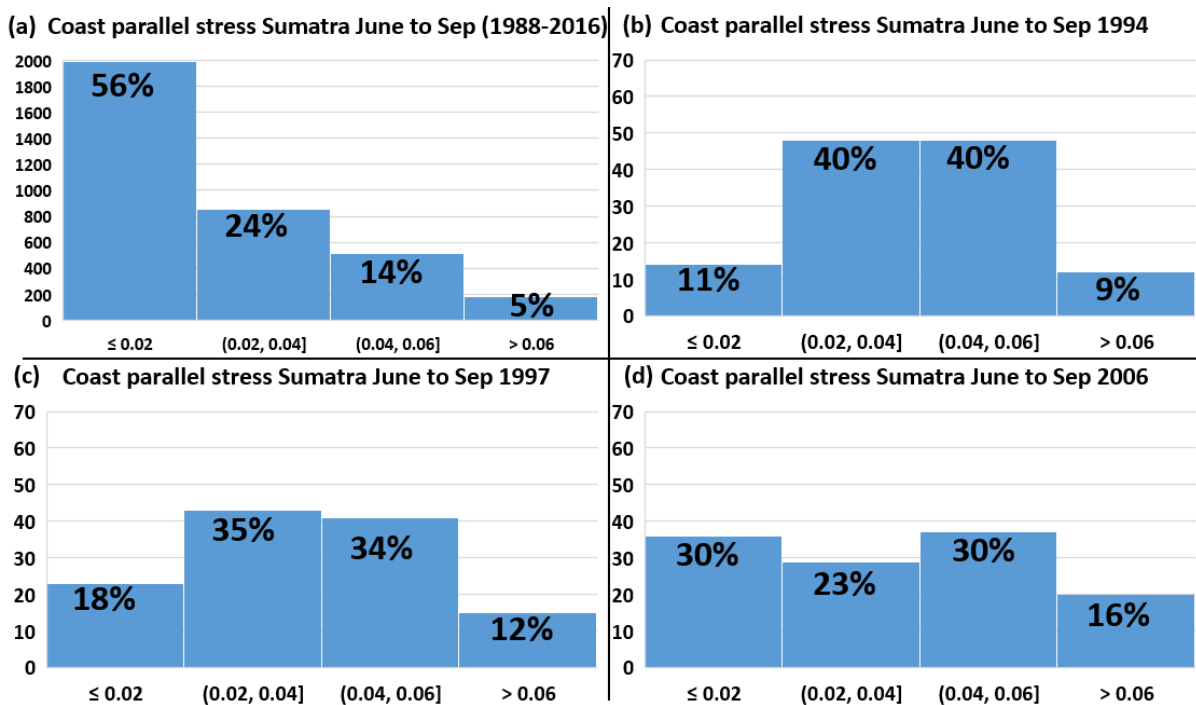


**Figure 3.3.14:** Histogram of area average daily coast parallel stress derived from satellite CCMP V2 data and averaged over the coastal Java region shown in **figure 3.3.5b**. Panel a) displays histogram for June September 1988-2016, b) for June to September of 1994, c) for June to September 1997 and d) for June to September 2006.

### (c) Histogram statistics along the coasts of Sumatra

Similar histogram plots, as discussed above for the coastal Java, is prepared for the southern coastal Sumatra displayed in **figure 3.3.14**, for entire study period and also for pIOD event years individually.

Characteristics of coast parallel stress in daily values are reversed to the Java coastline with weak values dominates in the histogram of entire study period (**figure 14a**). Coast parallel stress values less than 0.02 Pa has 56% presence in entire study period and 0.02 to 0.04 Pa has 24% presence. Strong stress values above 0.04 Pa has collective presence of 19% with 5% contribution of values above 0.06Pa. This situation indicates weak coast parallel stress prevails in the region in boreal summer-fall season.

In strong positive Indian Ocean Dipole event years values of coast parallel stress are elevated as seen in **figure 3.3.14** (b) to (d). In 1994 stress values higher than 0.04 Pa has 49% presence in the season with 9% share of values higher 0.06Pa. Stress values between 0.02 to 0.04 Pa has 40% presence and weaker stress values less than 0.02 Pa has 11% presence. In 1997 stress values above 0.04 Pa has 46%

presence with 12% share of values above 0.06 Pa. Values between 0.02 Pa to 0.04 Pa has 35% presence and values below 0.02 Pa has 18% presence in the boreal summer-fall of 1997.

In 2006 strong values of coast parallel stress above 0.04 Pa are elevated to 46% presence with 16% contribution of values above 0.06 Pa in the season. Values between 0.02 to 0.04 Pa has 23% presence and values below 0.02 Pa has 30% presence in the boreal summer-fall of 2006.

The characteristics of the coast parallel stress discussed above along the coastal Java and southern Sumatra is summarized in table 2. As displayed in table 2, strong coast parallel stress values, above 0.04 Pa, dominate along the Java coastline in entire study period though these strong values are further elevated in pIOD event years. The southern coastal Sumatra displays weaker coast parallel stress values conventionally and in strong pIOD event years coast parallel stress displays substantial rise. Hence the Java coastline displays robust upwelling favourable wind forcing in the season, while the southern Sumatra coastline has conventionally weak upwelling favourable forcing which is elevated in particular years.

**Table 3.3.2:** Values displayed in Histogram of **figure 3.3.14** to **figure 3.3.16** in table format for ease of comparison. The heading in the table can be read as HEW: high energy westerly, W: westerly, HE: high energy easterly, E: easterly, Weak: weak easterly or westerly, HES: high energy southerly, S: southerly, HN: high energy northerly, N: northerly, Weak: weak southerly or northerly. Brown shading indicates upwelling favourable component for the particular region.

Coast parallel stress (Pa)									
Java	<0.02	0.02 to 0.04	0.04 to 0.06	>0.06	Sumatra	<0.02	0.02 to 0.04	0.04 to 0.06	>0.06
All years	8	18	34	40	All years	56	24	14	5
1994		31	58	52	1994	11	40	40	9
1997	10	20	45	17	1997	18	35	34	12
2006		21	35	65	2006	30	23	30	16
All values are in percentage (%)									

### Section summary

The striking feature of the interannual statistics discussed in section 3.3.2a and 3.3.3b is the concerning behaviour of interannual variation of the zonal winds of the eastern equatorial Indian Ocean (solid blue line, fig 3.3.7b) with the interannual variation of the meridional winds along southern coastal Sumatra region (solid black

line, fig 3.3.12d). The weakening of the westerlies at the eastern equatorial Indian Ocean concurs with enhanced southerly winds along the southern Sumatra coastline, and strong westerlies at the eastern equatorial Indian Ocean coincide with weaker southerlies of the southern Sumatra coastline. While, the western equatorial Indian Ocean and southern Java coastal region cannot exhibit remarkable interannual variation of surface winds.

According to interannual statistics and histogram, the surface winds along the southern Java coastline display minor growth upwelling favourable winds during the pIOD event years compares to normal conditions, as they are robust in all the seasons. The histogram statistics also confirm that surface winds along southern Sumatra coastline display substantial variation during the pIOD event years compare to normal conditions, with the remarkable rise of the upwelling favourable winds. Consequently, during pIOD years, strong upwelling favourable winds are developed along both the adjacent coastline of southern Java and Sumatra which is rare, which play the crucial role in the upwelling dynamics of the region during boreal summer-fall pIOD years.

The fundamental question is, which processes govern interannual variation of the surface winds along southern coastal Sumatra and over the eastern equatorial Indian Ocean in the season? The possibilities are very high that they are part of a single atmospheric system as they exhibit co-varying interannual characteristics. Previous studies noted the zonal wind event over the eastern equatorial Indian Ocean as remoter forcing of the eastern equatorial Kelvin waves, the mechanism behind this zonal wind events are still ambiguous.

Concurrent behaviour of the seasonal mean of zonal winds at the EEIO and meridional winds at coastal Sumatra at interannual time scale pointing out a possibility that they are part of the single climatic phenomena (process/system)? If the answer is yes, then is this climatic phenomenon discovered in previous studies? Is this climatic process normally present in all years and is weaken or disappeared in pIOD years, or does it appear only in pIOD years and alters the surface forcing of the region? Next section will try to get the answers to these questions by evaluating the surface atmospheric fluctuations in the region.

In the next section, the intraseasonal behaviour of the zonal winds over the eastern equatorial Indian Ocean along with intraseasonal variation of the atmospheric convective activity over the study region is examined. It uncovers the characteristics of the atmospheric intraseasonal oscillations over the study region using wavelet decomposition and frequency analysis. It also explores the regional atmospheric processes which can explain the intraseasonal fluctuations.

### **3.4 High frequency convective events and anomalous atmospheric circulation**

This section investigates the characteristics of intra-seasonal wind variability in conjunction with tropical atmospheric convection in the eastern intertropical Indian Ocean. The focus is hereby placed on the boreal summer-fall period, which is the period when pIOD events develop.

#### **3.4.1 Tropical convection over the Indian Ocean**

Tropical convection in the atmosphere is a fundamental phenomenon of complex variability at intraseasonal time scale with erratic nature. Previous studies found that the Madden–Julian Oscillation (MJO) is the dominant mode of the intraseasonal variability of tropical atmospheric convection (Madden and Julian 1971; Hendon and Glick 1997; Webster *et al.* 2002; Shinoda *et al.* 2013). Moreover, the MJO is the most prominent mode of atmospheric variability connecting zonal wind variations along the equator with local convective oscillations at an intraseasonal timescale.

The region of interest in this study is the south-eastern tropical Indian Ocean (SETIO). Previous studies suggested that the MJO is weaker or non-active in the boreal summer-fall season (from June to September) in the tropical Indian Ocean (Madden and Julian, 1971; Webster *et al.*, 2002; Wheeler and Hendon, 2004; Chen *et al.*, 2015). On the other hand, Rao and Yamagata (2004) noted that, in this season, intraseasonal zonal wind variation in the eastern equatorial Indian Ocean is directly linked with regional convective activities, which has been confirmed by recent studies (Duan *et al.*, 2013; Chen *et al.*, 2015, 2016, 2017). The question arises, if the MJO is inactive in the tropical Indian Ocean during the boreal summer-fall season, then which mechanism governs the intraseasonal atmospheric variations in the region?

To answer this question, let us first explore the climatological cycle of atmospheric convective activity and surface winds in the SETIO region.

### (a) Climatological cycle

Daily data retrieved from NOAA's OLR PSD satellite dataset (1976-2016) are used to prepare monthly climatological maps. Likewise, monthly climatological maps of wind components are prepared from daily wind fields derived from the CCMP V2 data set.

The season of interest in this study is the boreal summer-fall season (June-September), noting that this season is preceded and followed by the generation of strong eastward equatorial Wyrтки jets in April/May and October/November. In order to capture this variability, it makes sense to prepare climatological maps for the periods April-May (**Figure 3.4.1a**), June-September (**Figure 3.4.1b**) and November-December (**Figure 3.4.1c**). Low OLR values represent enhanced cloud formation associated with a deep atmospheric convective activity, and higher OLR values represent weak convective activity. Meehl (1987) suggests that OLR values below a threshold of 220 W/m<sup>2</sup> are characteristic of deep convective activity.

The primary reason behind the selection of three different periods is to separate intraseasonal processes associated with the existence of Wyrтки jets triggered from the regular semiannual wind reversal in the equatorial Indian Ocean (see Duan *et al.*, 2013; Deshpande *et al.*, 2017) from processes associated with the IOD variability investigated here. The convective maximum is typically located near the Intertropical Convergence Zone (ITCZ), and in the Pacific, the ITCZ stays north of the equator year-round (see **Figure 3.4.1a-d**). The other diagonal zone of reduced OLR in the south Pacific is affiliated with the South Pacific Convergence Zone (SPCZ; K. van der Wiel *et al.*, 2016).

In the Indian Ocean, the centre of deep tropical convection is located over the eastern equatorial region During January to May and October to December (see **Figure 3.4.1a, 4.1b and 4.1d**), but not during boreal summer-fall months, when it shifts northward into the Bay of Bengal (see **Figure 3.4.3b**). During this period the second centre of deep convection established over the South China Sea in the tropical Pacific. Kikuchi and Wang (2009), Shukla (2014) and Adams (*et al.*, 2016) noted that

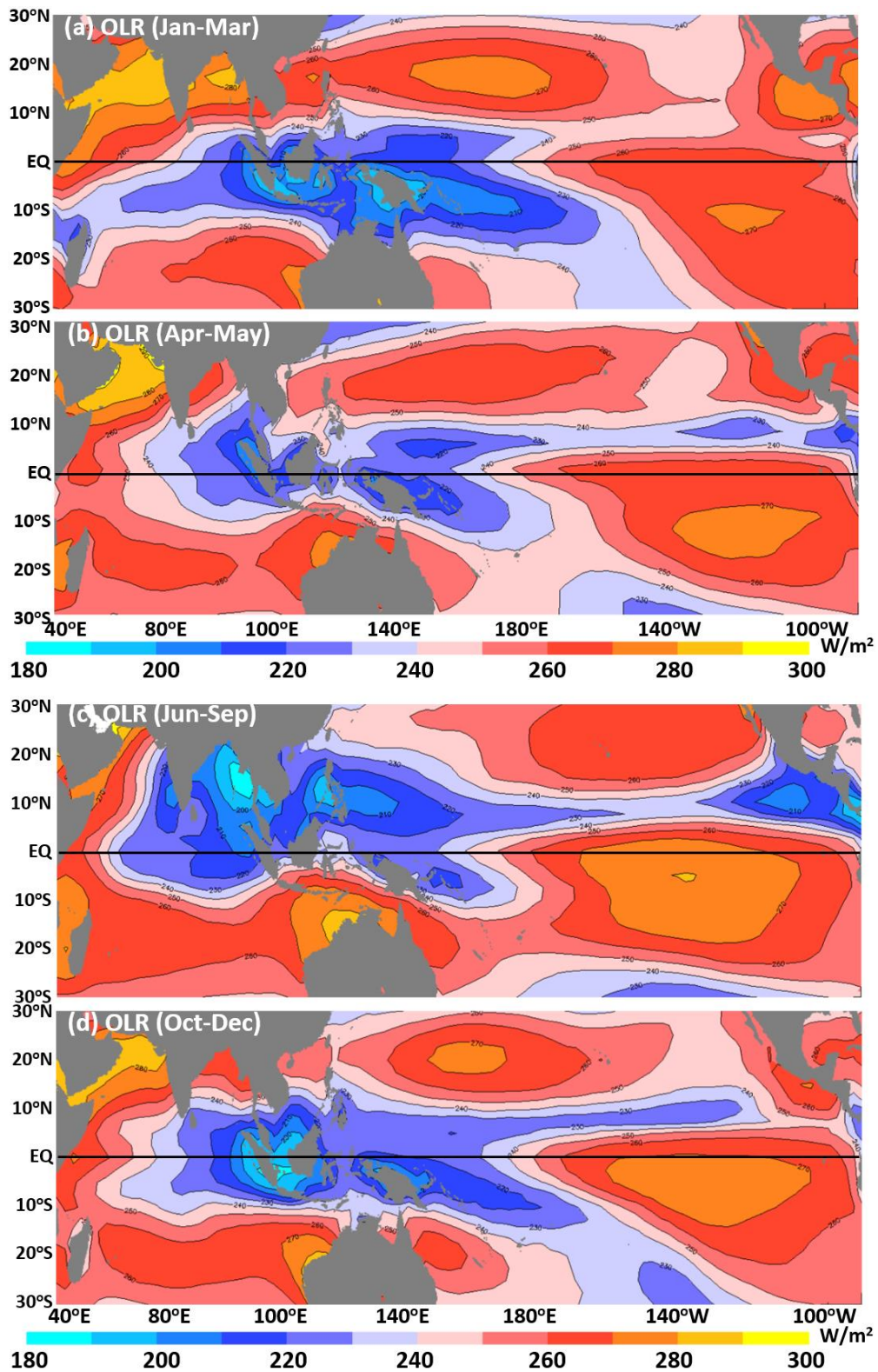


**Figure 3.4.1:** OLR values (OLR,  $W/m^2$ ) as seasonal average in the climatological year (1975-2016) derived from daily satellite data (NOAA PSD data) over the tropical Indian Ocean and the Pacific Ocean. Panel (a) displays monthly climatological values averaged over Jan-Mar, (b) same as (a) but averaged over April-May, panel (c) same as (a) but averaged over Jun-Sep, panel (d) same as (a) but averaged over Oct-Dec.

mean atmospheric columnar moisture content shifts towards summer hemisphere in boreal summer particularly over the tropical Indian Ocean and dominant convective intraseasonal oscillation exists over the northern hemisphere of Indian Ocean. Hence, the investigation of the convective activity over the tropical IO during boreal summer-fall is preformed individually.

Previous **figure 3.4.1c** is recreated with focus on the tropical Indian Ocean region and displayed in **figure 3.4.2** and wind vectors of the boreal summer-fall season are superimposed, to understand the exclusive climatological pattern of the atmospheric moisture content over the tropical Indian Ocean during boreal summer-fall. As evident in **figure 3.4.2**, the centre of deep convective activity is settled over northern-eastern part of the Bay of Bengal (at 10°-20°N, 90°-100°E) with min OLR values 180 to 200 W/m<sup>2</sup>.

The red box in **figure 3.4.2** indicates study area (the SETIO) covers 80°-110°E and Eq-10°S. As noted previously, OLR values below 220 W/m<sup>2</sup> can be considered as a deep convective activity; hence, the study region exhibits a region of secondary maxima of convective activity with OLR values between 200-220 W/m<sup>2</sup>. The wind vectors indicate surface winds attract towards the centre of deep convection in the northern hemisphere (in **figure 3.4.2**), while in the southern hemisphere and far from the centre of convection winds follows contours of the OLR values, which may follow the isotherms of SST.

The surface winds in the study region (red box, **figure 3.4.2**) has a south-easterly direction. Moreover, at the equatorial Indian Ocean surface winds have three different orientation during boreal summer-fall, southerly in the central EIO, south-easterly in the eastern EIO and south-westerly winds in the western EIO (**figure 3.4.2**). Hence, the seasonal average winds of the equatorial Indian Ocean exhibit weaker zonal component, and the meridional (southerly) component is predominant during boreal summer-fall. This situation is contrary to **figure 3.3.3d** and **figure 3.3.4** of sec 3.3.1a, which displays strong zonal component (westerly) in the eastern equatorial Indian Ocean in daily wind fields during boreal summer-fall. Though, it should be noted that figure 3.3.4 displays daily wind field values.

The missing piece of the information here may be the intraseasonal oscillation of convective activity related to secondary maxima is displayed over the study region (the SETIO) in **figure 4.2** which may trigger intraseasonal convective oscillations and can trigger abrupt zonal wind events. A grid-based standard deviation is performed in next sub-section, to confirm the presence of convective oscillations and related zonal winds variation over the study region at intraseasonal time scale during boreal summer-fall.

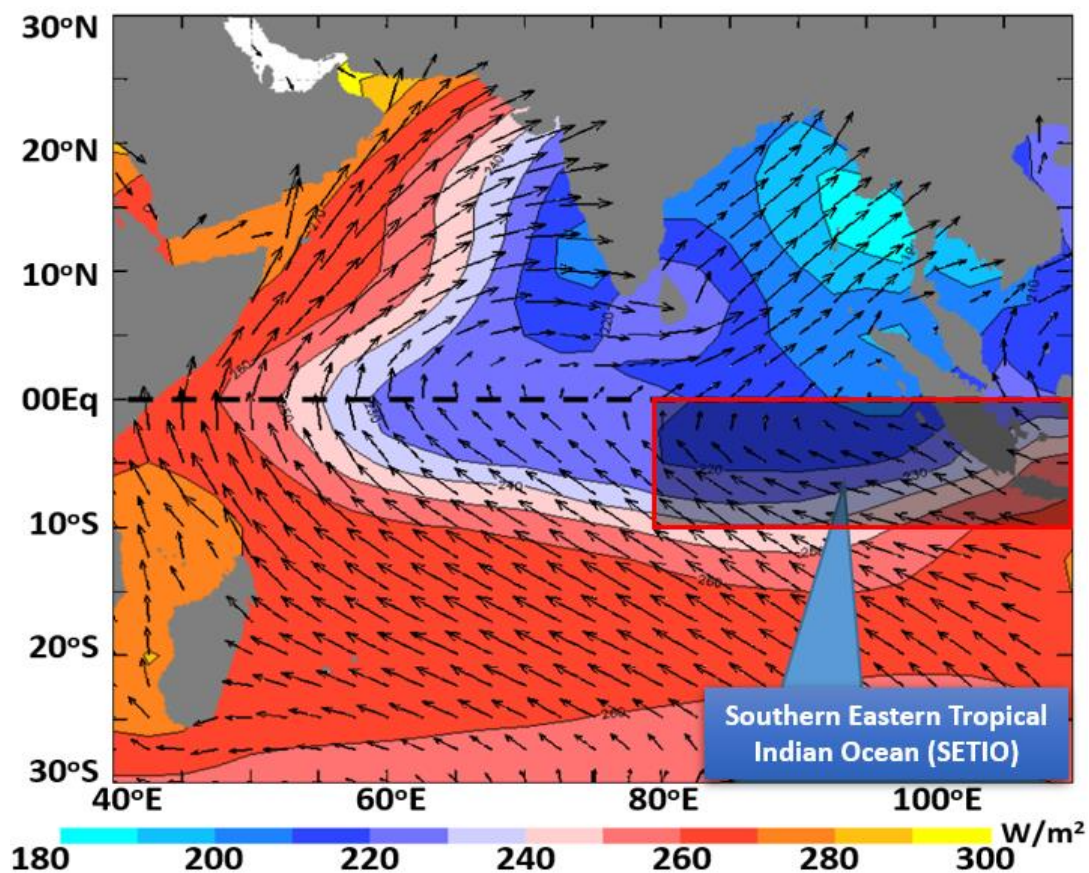


**Figure 3.4.2:** The maps display seasonal average climatological values (1975-2016) of Outgoing Longwave Radiation (OLR,  $W/m^2$ , as a proxy of tropical convection) in boreal summer-fall (from June to September) derived from daily satellite data (NOAA PSD data) over the tropical Indian ocean. Marked box region indicates the region of interest: the SETIO ( $80^{\circ}E$  to  $110^{\circ}E$  and  $EQ$  to  $10^{\circ}S$ ).

### (b) Standard deviation (STD) of convective activity and zonal wind

A grid-based standard deviation is applied to each pixel of the daily OLR values, and zonal wind speed values over the tropical Indian Ocean from June to September of 1988 to 2016 and result is displayed in **figure 3.4.3a** and **3.4.3b**.

It is known fact that the convective activity in tropics has erratic nature with strong intraseasonal variability, and the STD map of the OLR data (**figure 3.4.3a**) confirms highly variable characteristics of the tropical convection with two regions of higher STD values, one in deep Bay of Bengal and other is over the study region. Both regions of higher STD values agree with the first and second maxima of seasonal average OLR values of **figure 3.4.2**. The STD map of zonal wind speed (**figure 3.4.3b**) also exhibits similar two locations with higher STD values, in the deep Bay of Bengal and over the Study region as a centre of intraseasonal variability along with the third centre in the Arabian Sea.

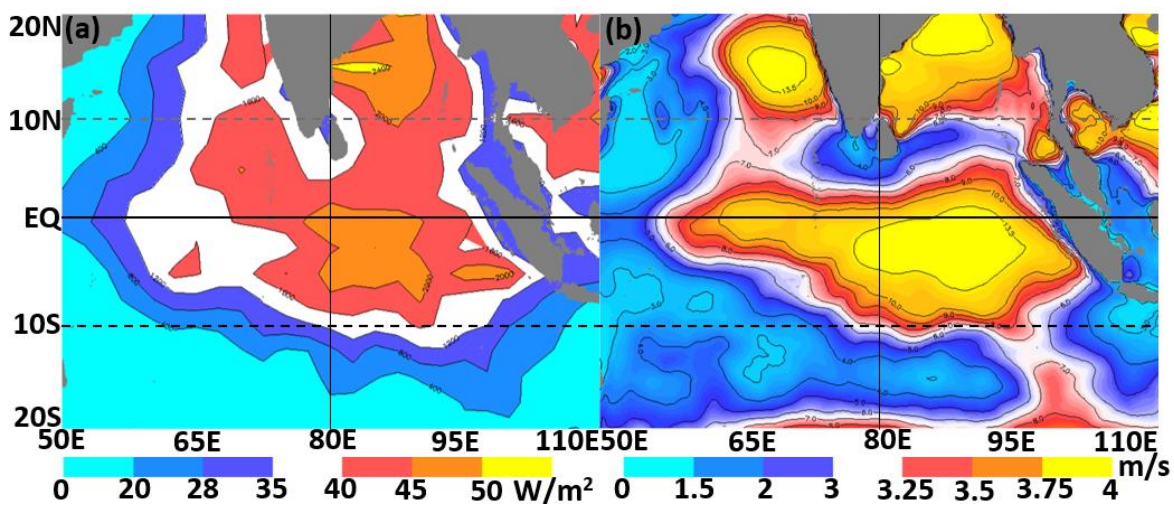


**Figure 3.4.3:** (a) Standard deviation of daily OLR values ( $W/m^2$ , NOAA OLR PSD data) over the period Jun-Sep of 1988-2016 (b) Standard deviation of zonal wind speed (m/s, CCMP V2 data) over the period Jun-Sep of 1988-2016.

Strong STD values of OLR and zonal winds in the study region confirms the presence of intraseasonal convective variability and related zonal wind variation during boreal summer-fall. Though previous studies noted the intraseasonal zonal wind variation at the eastern equatorial Indian Ocean The intraseasonal convective oscillations is unknown for the study region are directly linked with regional convective activities, which has been confirmed by recent studies (Rao and Yamagata, 2004; Duan *et al.*, 2013; Chen *et al.*, 2015, 2016, 2017). No previous study distinctly explains the process which governs the regional convective oscillations and zonal wind variations is displayed over the study region during boreal summer-fall. As noted above, the MJO is weaker during boreal summer-fall and previous studies exclusively focused towards northern hemisphere for intraseasonal convective oscillations. Henceforth, the detailed investigation of the nature, periodicity and synoptic structure

of intraseasonal convective oscillations and related surface wind variation during boreal summer-fall over the study region is attempted in this section.

### 3.4.2 Temporal characterisation of convective events

Several studies have been performed to understand the intraseasonal behaviour of the zonal winds and related atmospheric processes over the equatorial Indian Ocean. The zonal surface winds display strong intraseasonal variations particularly over the eastern equatorial Indian Ocean, as witnessed in **figure 3.4.3b** along with of the convective variability over the study region, as displayed in **figure 3.4.3**.

As noted previously, the primary mode of intraseasonal variability MJO is weaker or inactive over the study region in this season. Hence the question here is, if the MJO is inactive in the season, then which mechanism governs the atmospheric instabilities at intraseasonal time scale in the region?

Rao and Yamagata (2004) attempted the temporal characterisation the zonal wind events in the eastern equatorial Indian Ocean and proposed that the longer duration of zonal wind events with temporal coverage of 64 days is present in the region. They proposed that the source of the zonal wind events is the intraseasonal disturbance (ISD) and further suggested that this ISD is the reason behind the early termination of the developing positive IOD event of 2003. Iskandar *et al.* (2005) performed the spectral decomposition of zonal winds at the eastern equatorial Indian Ocean, with the help of wavelet analysis, to understand the periodicity of the zonal wind variability in the region. They found that high-frequency zonal wind variability, with a periodicity of 20-40 days, exists along the eastern equatorial IO (EEIO) located between 70°-90°E though these studies were limited to a smaller period of 2 to 3 years. On decadal scale, a wavelet analysis by Ashok *et al.* (2003) suggests that the equatorial zonal winds associated with IOD are mainly associated with local SST anomalies but may be connected with the Pacific SST anomalies during 1997 as consequence of a mega El Nino co-occurred with a mega-IOD.

Later Chen *et al.* (2015, 2016) and Delman *et al.* (2016) attempted the intraseasonal variability of the zonal wind along the equatorial Indian Ocean for a decadal length of the study period and performed the statistical co-relation between

zonal winds and the sea level anomalies (SLA). Their correlation analysis with sea level anomalies indicates the presence of the high-frequency zonal wind variabilities over the eastern equatorial Indian Ocean. Though, high frequency (bi-weekly mode) convective oscillation and associated anomalous surface circulation over the study region during boreal summer-fall are never noticed.

With the help of frequency analysis, the temporal characterisation of zonal winds and the convective oscillations over the study region is performed during boreal summer-fall of the 28 years (1988 to 2016).

**(a) Spectral characteristics of Intraseasonal variability (ISV) of convective activity and zonal wind:**

The area average daily time series of zonal winds over the eastern equatorial region (70°-90°E and 5°S-5°N), and area average OLR anomaly over the study region (80°-110°E, Eq-10°S) is derived for June to September of 1988 to 2016. A power spectral density (PSD) is computed for both OLR time series and zonal wind time series to reveal the dominant frequency of the intraseasonal oscillations.

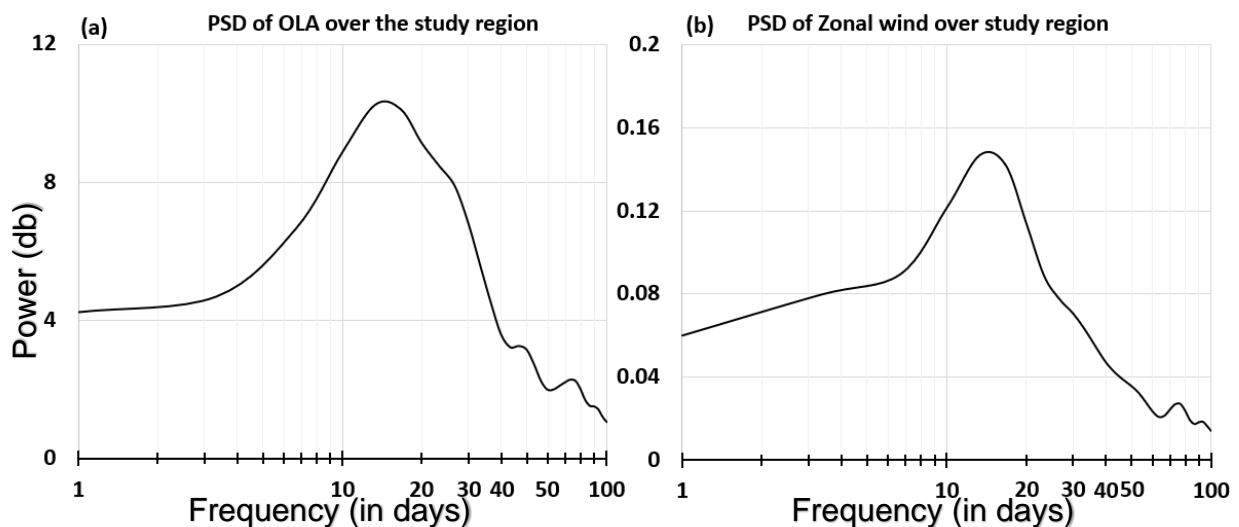


**Figure 3.4.4:** Panel (a) displays the power spectral density plot for the OLR values average over the study region and panel (b) displays the power spectral density plot for the zonal winds speed values average over the eastern equatorial Indian Ocean.

The PSD is obtained individually for boreal summer-fall of each year (of the study period), and the computed individual PSDs are averaged over the entire study period of 28 years (1988-2016). The final PSD displayed un **figure 3.4.4(a, b)** is the average values over the entire study period. During boreal summer-fall (June to

September), the spectral peak in the PSD of the OLR data and the zonal winds is located between 10-20-day (**figure 3.4.4 a, b**). Note that, since the core frequency of oscillations can change from year to year, the resultant mean spectrum is relatively smooth. The PSD of **figure 3.4.4** suggests the 10-20-day periodicity of intraseasonal of convective activity and zonal wind variation.

Further, the wavelet spectrum analysis is performed for the derived area average time series of zonal wind speed and OLR anomaly, to verify the distribution of dominant frequencies in the time domain. Two-tier wavelet treatment is applied to remove unwanted the low frequency (or higher period, more than two months) fluctuations and to capture the high-frequency variability exclusively within the range of 2 days to 40 days. It will avoid the anomaly trend longer than 60 days to interannual time scale. The sample rate of input signals is daily; hence, the period of events in the wavelet spectrum is also in days.

The primary reason behind the selection of this frequency range is the PSD of **figure 3.4.4** which indicates 10-20-day oscillations dominate over the study region the boreal summer-fall season and it is possible to capture the intraseasonal variability at lower or higher periods as well. Previous studies also displayed the atmospheric fluctuations over the eastern equatorial Indian Ocean with the similar frequency range of 20-40 days (Iskandar *et al.*, 2005; Duan *et al.*, 2103; Chen *et al.*, 2015, 2106, 2107; Delman *et al.*, 2016).

The retrieved wavelet spectrums are shown in **figure 3.4.5 (a, b)**, where the colour shading from cyan to red indicates values past the 95% significance level. Note that, in the wavelet spectrum, the amplitude exhibits the power of fluctuation and not the actual event. The wavelet power spectrum of **figure 3.4.5(a)** reveals that the strong intraseasonal oscillation of zonal winds with 7-21 days periodicity over the eastern equatorial Indian Ocean. The wavelet of OLR anomaly in **figure 3.4.5(b)** also displays intraseasonal variation with the periodicity of 7-21 days and which indicates similar periodicity of the eastern equatorial zonal winds.

The shorter periodicity of intraseasonal variation of equatorial zonal winds and connectivity suggests the presence of short-lived convective episodes and related zonal wind events in the boreal summer-fall in the study region.

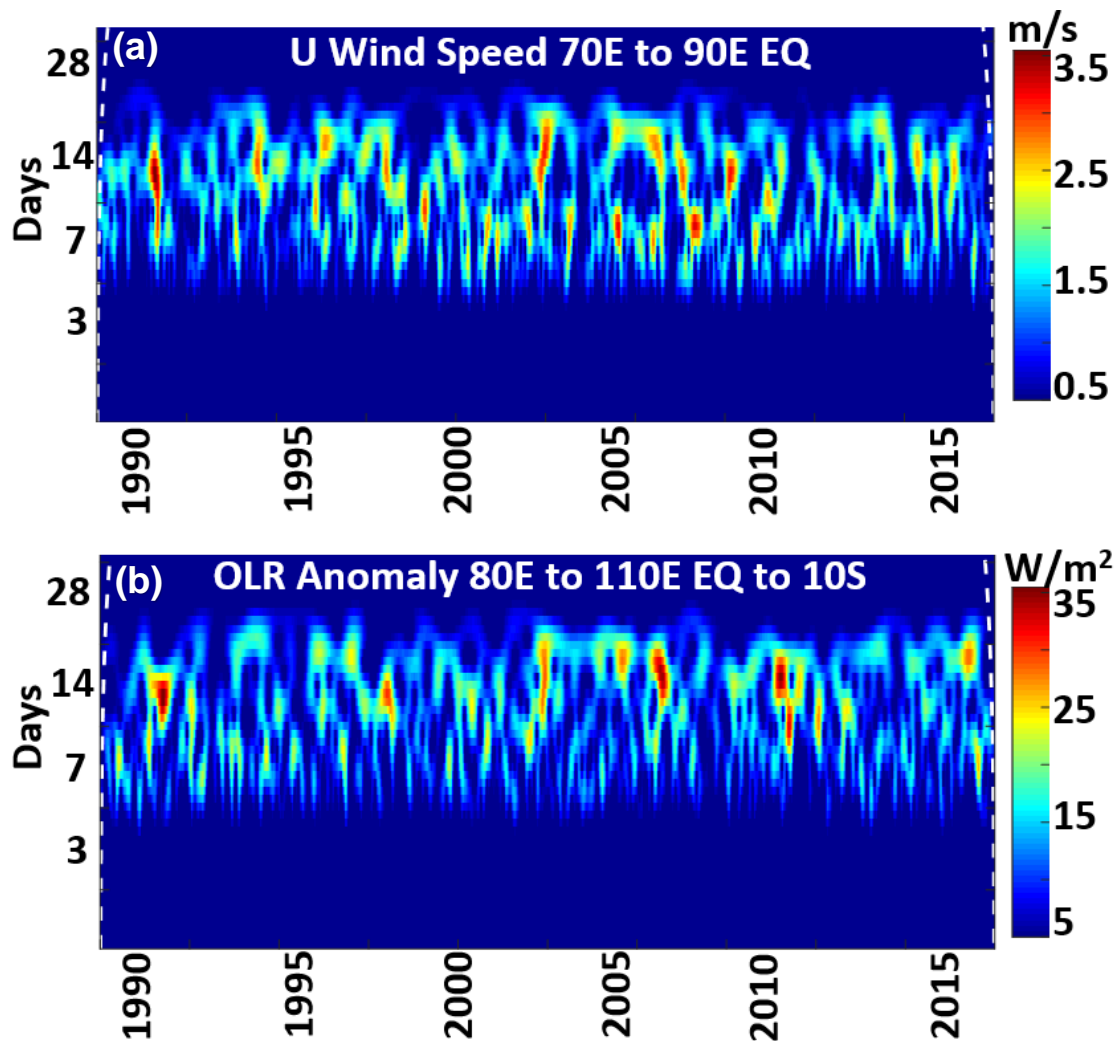


**Figure 3.4.5:** (a) Normalised wavelet spectrum daily time series of the area average zonal wind speed from June to September of 1988 to 2016 and (b) OLR anomalies daily time series from June to September of 1988 to 2016 in the SETIO region using Morse Wavelet. Colour shading cyan to red indicates the region of 95% confidence and a dashed line indicates area under edge effect, while dark blue shading is low background values.

The low periodicity (8-20-day) of connectivity variability and zonal wind variation displayed in the wavelet of **figure 3.4.5** disconnect this climatic oscillation from the MJO which has 30-60-day periodicity. The high frequency coupled oscillations of the atmospheric connection and the eastern equatorial zonal winds displayed in **figure 3.4.5** was not noticed previously over the study region in this particular season (June to September). The question here is, which process can explain these high-frequency

coupled oscillations and integrate them into a single synoptic-scale system? The answer to this question is explored in next sub-section.

### **(b) QBWO mode oscillations in the study region**

In the previous efforts on analysis of spectral structure of the zonal winds and convective activity over the tropics of the Indian Ocean and the western Pacific Ocean, the dominant presence of 10–20-day oscillation mode has been found (Murakami and Frydrych 1974; Murakami 1975; Zangvil 1975; Krishnamurti and Bhalme 1976; Krishnamurti and Ardanuy 1980; Chen and Chen 1993; Kiladis and Wheeler 1995; Numaguti 1995; Wen and Zhang, 2007).

In the 1970s and 1980s high-frequency mode of intraseasonal oscillation was explored in the tropical IO during the northern summer monsoon, known as 10-20-day mode of Indian Monsoon (Chen and Chen, 1993). In recent studies, this high-frequency mode is known as Quasi-biweekly Oscillation (QBWO) which is one of the most significant modes of the tropical variation on a time scale in between day-to-day weather and the Madden–Julian Oscillation (MJO) (Madden and Julian 1971, 1972; Wen and Zhang, 2007; Kikuchi and Wang, 2009).

Wen and Zhang (2007) and Chatterjee and Goswami (2004) confirms that QBWO is dominant mode over the eastern equatorial IO (EEIO) in boreal spring and summer (March to May). Though, none of the previous studies discussed the existence of this high-frequency mode in the south, eastern tropical IO (SETIO), particularly in boreal summer-fall (June to September).

The high-frequency oscillations of the zonal winds and atmospheric convective activity displayed in **figure 3.4.5**, with a periodicity of 10-20-day, during the boreal summer-fall over the study region dissociate them from the category of the MJO and put them under the category of the “biweekly mode” QBWO oscillation. The bandpass filter is applied to the previously derived area average daily time series of the OLR anomaly (1988-2016), to confirm further the dominance of the QBWO mode in the intraseasonal variability of atmospheric convective activity during the boreal summer-fall. The bandpass filter with criteria of 1 to 8 days, 8 to 20 days (QBWO) and 20 to 60

days (MJO/ISV) is applied to the daily time series of OLR anomaly and variance of each filtered time is derived for comparison.

Entire filtered time series for such an extended period of 28 years (1988 to 2016) is difficult to display here; hence, filtered time series of the typical year 2000 is displayed in **figure 3.4.6a** for the reference. **Figure 3.4.6a** displays three-line plots, where each line plot represents a particular range of filtered OLR anomaly data as displayed in legends. Line plots of “bi-weekly” mode filtered OLR anomaly for the entire study period (June to September of 1988-2016), is displayed in the appendix section.

The variance of each filtered time series (of **figure 3.4.6a**) is derived for the entire study period (1988-2016) and displayed in **figure 3.4.6b**, to reveal the dominant mode in intraseasonal variation. The variance of ultra-high frequency oscillations is very low compared to the other two modes of variance (1st bar of **figure 3.4.6b**); hence, this mode is ruled out in comparison. The variance of the other two modes, the QBWO and the MJO, are in the comparable range (2nd and 3rd bar of **figure 3.4.6**).

The ratio of the variance of any two-time series indicates the relative dominance of anyone oscillation mode (between two different modes). If the ratio of the variance of the QBWO to the MJO (QBWO/MJO) is greater than one, it indicates the dominance of the QBWO mode in the atmospheric convective oscillation over the region; while the ratio less than 1 indicates the dominance of the MJO in the region. The derived ratio variance of QBWO to MJO mode time series is calculated and displayed in a box in the top left corner of **figure 3.4.6** which has value 1.11 (greater than one), and it suggests the dominance of the QBWO mode in the intraseasonal atmospheric convective variability over the study region during boreal summer-fall.

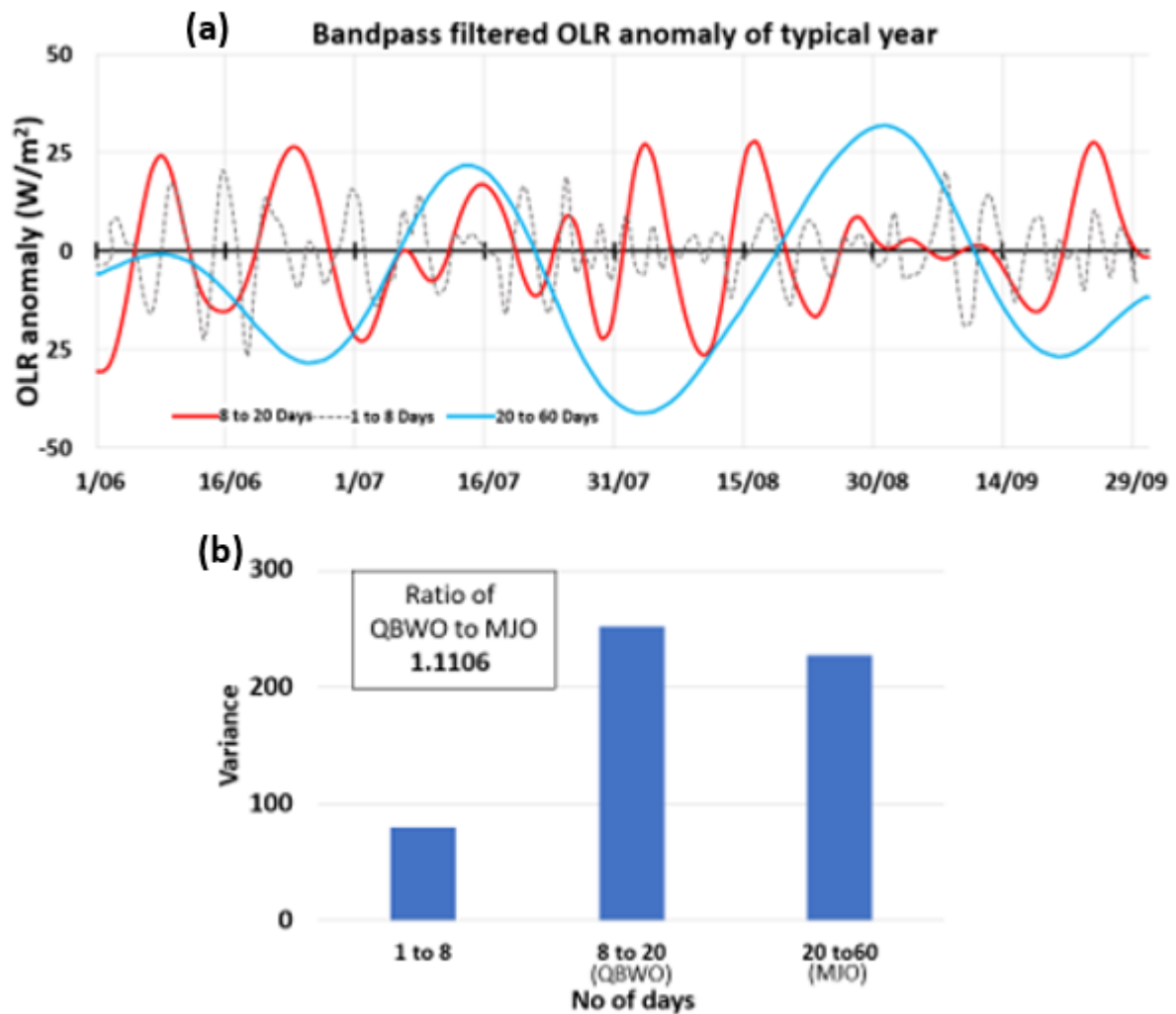


**Figure 3.4.6:** (a) Bandpass filtered OLR anomaly over the study region in 2000 (b) Variance of 1 to 8 days, 8 to 20 days (QBWO) and 20 to 60 days (MJO) bandpass filtered time series of OLR anomaly displayed in (a). Variance displayed is for the entire study period of 1988 to 2016.

Although the filtered time series of the OLR anomaly at the QBWO mode in **figure 3.4.6a** (red line) indicates the presence of six to seven full cycles during boreal summer-fall of 2000, the typical length of any single event (in days) is not clear from the spectral analysis. The length of the typical QBWO mode atmospheric convective event over the study region is derived in the next section using the autocorrelation function. The synoptic structure of the related atmospheric processes is examined in sub-section 3.4.3b, which will define the relationship between the QBWO mode atmospheric convective oscillations of the study region and the zonal wind events of the eastern equatorial Indian Ocean.

### 3.4.3 Synoptic structure of the convective events and anomalous atmospheric circulation

The previous section confirms the quasi bi-weekly oscillations (QBWO) as the dominant mode of intraseasonal variability (ISV) of the atmospheric convective activity of the study region during the boreal summer-fall. The temporal cycle of a typical event, the synoptic structure of a typical event and atmospheric processes which can explain the relationship between the anomalous surface circulation of the region and the QBWO mode atmospheric convective oscillations are assessed in this section.

#### (a) Length of typical QBWO mode convective event from Autocorrelation

The QBWO mode filtered time series of the OLR anomaly (1988-2016) displayed in **figure 3.4.6a** (red line) is used here to retrieve the duration of the typical atmospheric convective cycle over the study region using autocorrelation function. The autocorrelation coefficient is derived for the entire time series of 3538 days (June to September of 1988-2016), and the central maxima of the autocorrelation statistics are plotted in **figure 3.4.7**. In **figure 3.4.7**, days from -8 to +8 represents a typical full cycle of an atmospheric convective event (marked in a red box), which indicates a 16 days cycle of a single event. Hence, autocorrelation statistics reveal that the typical intraseasonal atmospheric convective event over the study region has a cycle of 16 days during boreal summer-fall.

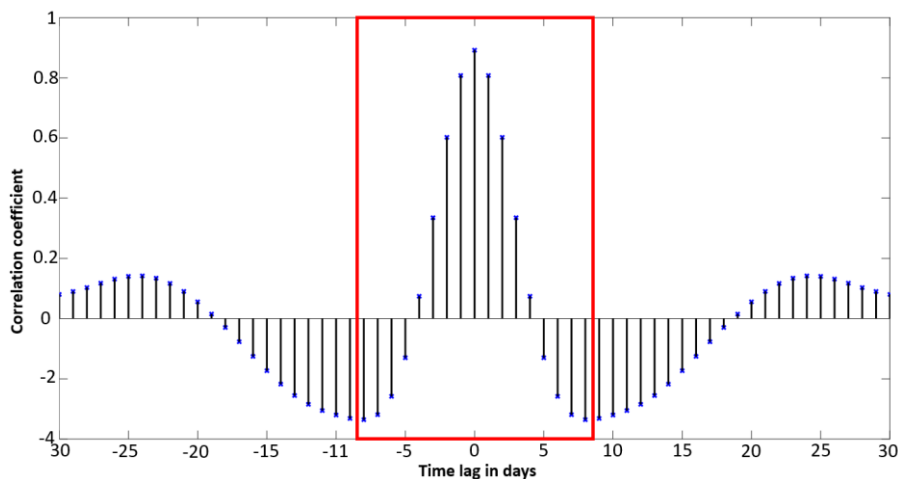


**Figure 3.4.7:** Autocorrelation of 8-20-day filtered OLR anomaly over the study region.

## **(b) A composite structure of 157 convective events**

Many previous studies attempted the analysis of the synoptic structure of the “bi-weekly” mode (QBWO) high frequency atmospheric convective events over the different region of the world. The fundamental outcome of all the previous studies suggests that the atmospheric convective events at “bi-weekly mode” (QBWO) are typically characterised by the atmospheric convective convergence and heating from intensified convection in the lower atmosphere of the region (Chen and Chen 1993, Chatterje and Goswami 2004, Wen and Zhang 2007). The atmospheric convective heating further triggers atmospheric Rossby waves in the lower atmosphere over the region with synoptic-scale coverage of 1000kms to 6000kms.

Wen and Zhang (2007) explored the synoptic structure of the QBWO mode atmospheric convective events during boreal spring at the off-Sumatra region of the Indian Ocean and revealed twin-cyclonic structure in the lower atmosphere triggered from Rossby wave response of convective heating in the lower atmosphere over the off-Sumatra region. The twin cyclone system has one northern and one southern vortex structure, the northern one is located north of the equator with centre around 95°E 5°N, and the southern one is located south of the equator with centre around 95°E 5°S. Chen and Chen (1993), Chatterje and Goswami (2004) explored the synoptic structure of the QBWO mode atmospheric convective events during later season of boreal summer over the tropics of the Indian Ocean and revealed similar twin vortices structure from the atmospheric Rossby wave response over the tropical Indian Ocean.

The fundamental difference between the twin vortices system of boreal spring and boreal summer is the location of the northern vortices. Chen and Chen (1993) suggests that during boreal summer the northern vortex structure of the twin vortices system is located in far north around 18°N over the deep Bay of Bengal (BOB) while the southern vortex structure is located south of the equator centred around 2°-8°S. The vortex structure located over the deep BOB of is possibly related to the centre of deep convection which is settled over the deep BOB during boreal summer as discussed in previous section 3.4.1 (**figure 3.4.1b** and **figure 3.4.2**).

The previous studies are restricted to the analysis of the vertical structure of atmosphere during the convective episodes, while this study interested in the

anomalous surface circulation triggered during the convective episodes particularly over the study region (the SETIO). Anomalous surface circulation triggered during the atmospheric convective events of boreal summer over the study region (the SETIO) was not attempted in any of the previous studies because the convective events during boreal summer over the region themselves were under speculation, and they are revealed in this study.

The standard deviation (STD) maps of atmospheric convection (OLR) and zonal winds (Usp) over the tropical Indian Ocean displayed in **figure 3.4.3** (subsection 3.4.1b) along with spectral analysis performed for the same entities in sub-section 3.4.2 reveals the presence of the “bi-weekly mode” atmospheric convective events and subsequently triggered zonal wind events over the study region during boreal summer-fall (June to September). Henceforth, this study is interested in the synoptic structure the “biweekly mode” atmospheric convective events triggered over the study region during boreal summer.

During the 28 years of the study period (1988-2016), a total of 157 atmospheric convective events are detected over the study region with an event length of 12-20 days (“bi-weekly mode”). The OLR anomaly maps, the wind speed anomaly maps and wind stream-function anomaly maps of each 157 events are prepared. According to the autocorrelation plot (**figure 3.4.7**), the most active phase of convection over the study region can be considered as day 0, and the weakest phase of convection can be considered as  $\pm 8$  days for a typical 16 days cycle of the “bi-weekly mode” atmospheric convective event. Note that, all atmospheric convective events captured during the study period (157 events) have not precisely the same 16 days of the cycle; hence, the convective cycle of each event is divided into nine phases and the nearest point is selected to prepare the **figures** with every two-day interval. Hence for each atmospheric convective cycle, nine composite maps of the OLR anomaly, wind speed anomaly and wind stream function anomaly are prepared for the 16 days of the cycle.

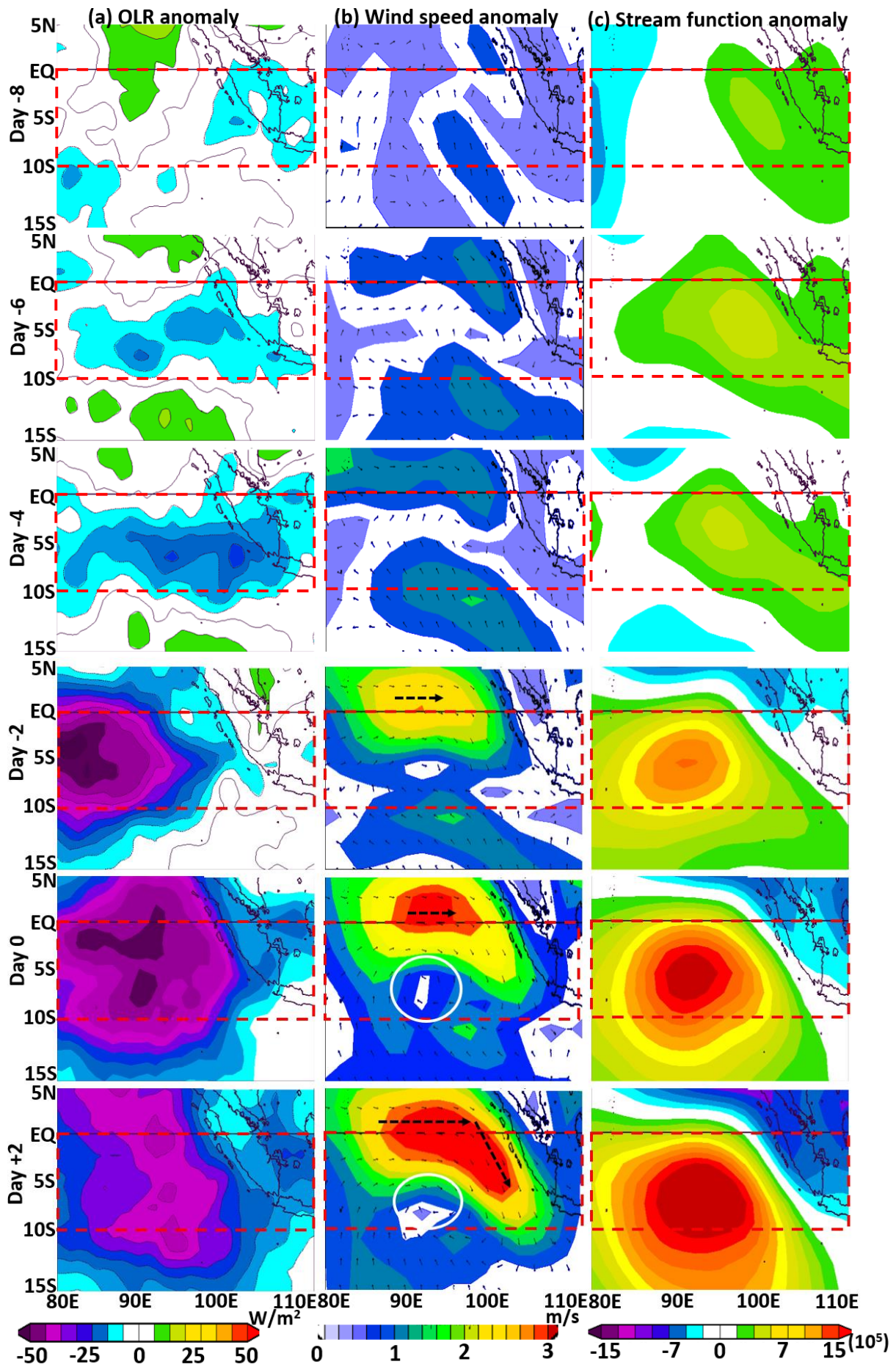
All maps prepared for each event is then composite as the single event and nine composite maps are prepared as a single composite event and displayed in **figure 3.4.8** and their statistically significant are tested above 95% values. Maps of **figure 3.4.8** explain the synoptic structure of each atmospheric convective cycle triggered at “bi-weekly mode” and consecutively triggered anomalous surface

circulation over the study region during the boreal summer-fall of the entire study period (1988-2016). The composite nine OLR anomaly maps (for 157 events) are displayed in **figure 3.4.8(a)**; likewise, nine composite maps of wind speed anomaly with wind vectors are displayed in **figure 3.4.8(b)**, and nine composite maps of wind stream function anomaly are displayed in **figure 3.4.8(c)**.

The spatial coverage of the composite maps (of **figure 3.4.8**) is extended compared to the study region (the SETIO) with 50 extension in north and south to visualise extended coverage of atmospheric convective activity; hence, the horizontal extent of each map is 5°N-15°S and 80°-110°E. As discussed previously, positive values of OLR anomaly in **figure 3.4.8(a)** represents suppressed convection over the region, and more open sky conditions and negative values represent deep atmospheric convective activity. In wind speed anomaly maps of **figure 3.4.8(b)** shading represent wind speed anomaly values, and arrows indicate altered wind direction. Likewise, in the stream function anomaly maps of **figure 3.4.8(c)** positive values represent converging wind flow and negative values indicate diverging flow.

According to the autocorrelation of the convective cycle (**figure 3.4.7**), day -8 represent the weakest phase of the convection. Day -8 in **figure 3.4.8a** confirms the suppressed atmospheric convection and weakest phase convective activity over the study region with the lowest values of ORL anomaly. During this suppressed atmospheric convection phase, wind speed anomaly and stream function anomaly in maps of the day -8 in **figure 3.4.8(b)** and (c) do not exhibit notable anomaly values, which indicate normal seasonal mean surface circulation and wind direction in the region.

Day -6 and day -4 represent the growth stage of convection over the study region with negative values of OLR anomaly in **figure 3.4.8(a)**. Though during this phase (day -6 to day -4) the maps of wind speed anomaly and wind stream-function anomaly do not display strong anomaly values; hence, normal seasonal mean surface circulation persists over the region.



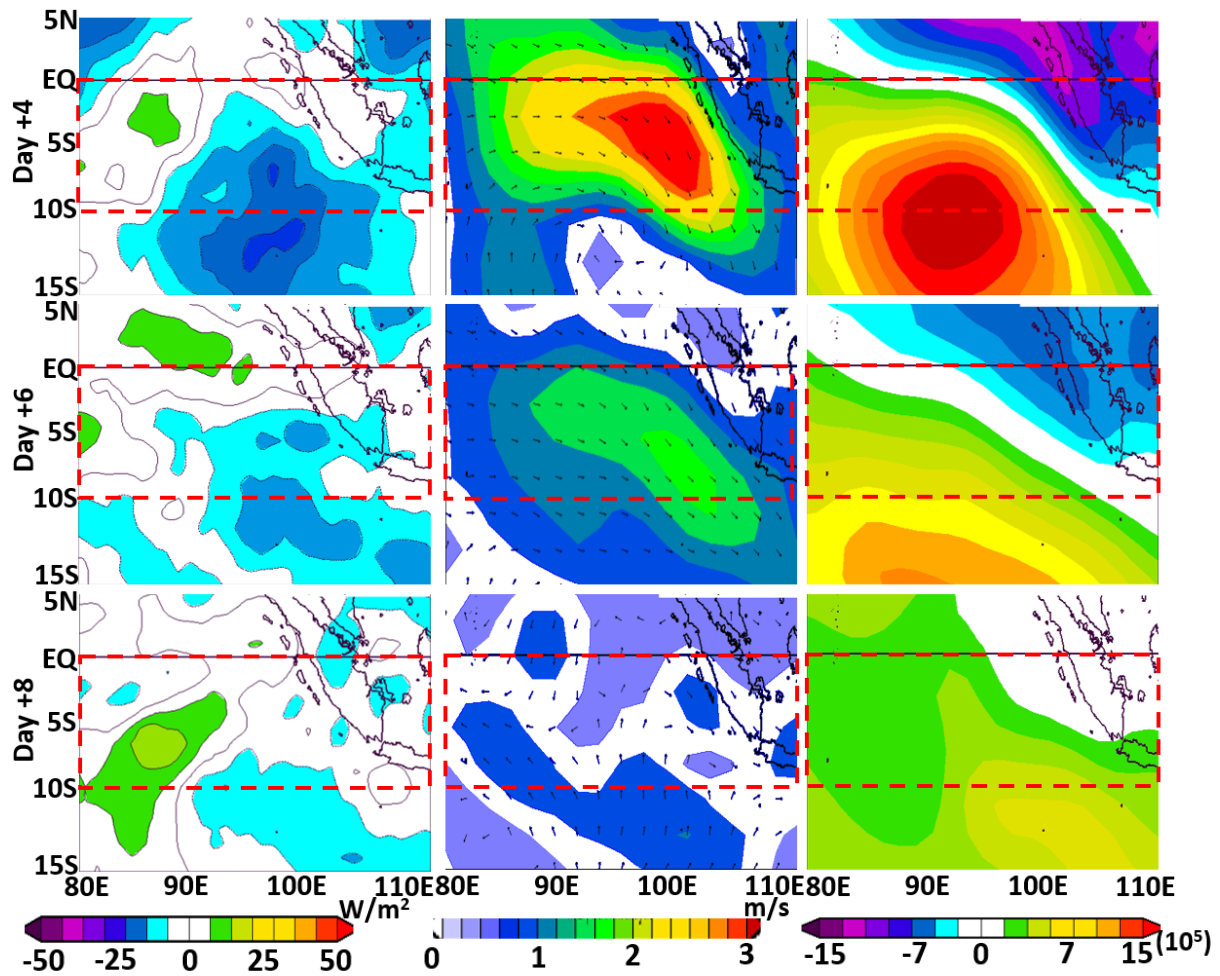


**Figure 3.4.8:** Maps display anomaly values (from daily 1988-2016 climatology) of composite 157 atmospheric convective events captured during boreal summer-fall of the study period (198—2016) over the study region. Panel (a) shows OLR ( $\text{W}/\text{m}^2$ ) anomaly, (b) displays wind speed anomaly ( $\text{m}/\text{s}$ ) and 1000 Mb wind vectors ( $\text{m}/\text{s}$ ), (c) displays anomaly of wind stream function at 0.995 sigma.

At day -2, the OLR anomaly map displays higher negative OLR anomaly values, which indicate strong atmospheric convection is aggregated over the study region (**figure 3.4.8a**). Under the influence of the convective aggregation surface wind of the eastern equatorial Indian Ocean attracts towards the centre of higher atmospheric convection (and updraft); hence, the equatorial westerlies are triggered over the eastern equatorial Indian Ocean as displayed in **figure 3.4.8b** (day -2) which is marked by an eastward arrow. Surface winds along the south Sumatra coastline are also attracted towards the centre of higher atmospheric convection at the same time (day -2); hence, the seasonal “south-easterly” of the region are reverted to the “north-easterly” winds.

At day 0, the atmospheric convection reaches to its peak phase over the region (**figure 3.4.8**, day 0); hence, under the influence of the intensified convective convergence, the equatorial westerlies are further intensified along with the stronger “north-easterlies” along south Sumatra coastline. As a consequence of two anomalously triggered wind flows, the eastern equatorial “westerlies” and the southern coastal Sumatra “north-easterlies”, the wind stream-function shows converging values in the region **figure 3.4.8c** (day 0).

On day +2, under the effect of atmospheric convective heating in the lower atmosphere, the atmospheric Rossby wave is triggered. The triggered atmospheric Rossby wave is visible in wind vectors superimposed on wind speed anomaly map (**figure 3.4.8b**, day +2) as a cyclonic circulation with a centre around 5°S 90°E (marked with a white circle) and also in wind stream-function map (**figure 3.4.8c**, day +2) with converging values. According to the wind stream-function map (**figure 3.4.8c**, day +2), the coverage of the triggered cyclonic circulation is a synoptic scale. During this phase (at day +2) consecutively triggered equatorial “westerlies” and south Sumatra “north-easterlies” are strongest with highest anomaly values as displayed in the wind speed anomaly map (**figure 3.4.8b**, day +2).

The composite synoptic structure of a typical atmospheric convective cycle is explored here, which explains the maintenance mechanism of the typical atmospheric bi-weekly mode convective cycle at over the study region during boreal summer-fall. The composite synoptic structure also explains how seasonal mean surface circulation is altered as a synoptic-scale cyclonic circulation under the influence triggered atmospheric Rossby wave during the mature stage of convection over the study region. The triggered cyclonic circulation over the region comprises two anomalous wind flow, one is the equatorial “westerlies” over the eastern equatorial Indian Ocean, and the other is reversed “north-easterlies” along the south Sumatra coastline. Later, when the atmospheric convection disappears (over the region), the surface circulation returns to the seasonal mean directions. Moreover, the convective heating in the atmosphere is not symmetric along the equator (it is confined to southern hemisphere), hence a mixed Rossby-Gravity wave response can be observed in on day -6 (**figure 3.4.8**), which is also seen in the relevant panels of **figure 3.4.10**.

Kikuchi and Wang (2008) noted that the atmospheric convective system with a typical cycle of sub-monthly timescale can be characterized in three different categories according to their zonal propagation tendencies; eastward propagating, westward propagating and continuous convective systems. According to **figure 3.4.8**, the synoptic structure of the “bi-weekly mode” convective events displayed over the study region; evolves, matures and dissipates over the same region; hence, it falls under the category of the continuous convective systems.

As discussed previously, the studies also suggested that the atmospheric convective oscillation at “bi-weekly mode” comprises the twin vortex system, one is situated north of the equator, and the other is south of the equator. According to Chen and Chen (1993) during boreal summer-fall, the northern vortex structure of the “bi-weekly mode” convective oscillations is located in far north around 18°N over the deep Bay of Bengal which is far from the of the region of interest of this study and hence it is out of the scope of this study.

### **(c) A composite structure of six convective events of 2000**

The composite structure of the surface circulation explored in section 3.4.3b is in the form of anomaly values and not the absolute values. Hence, to confirm the influence of atmospheric convective event on the surface wind circulation using absolute wind speed and convergence values over the study region year 2000 is selected.

The 8-20 days filtered time series of the area average OLR anomaly (average over the study region) is displayed in **figure 3.4.9a**, and area average filtered time series of zonal wind speed values (averaged over the eastern equatorial Indian Ocean region) is displayed in **figure 3.4.9b**. The composite of both filtered time-series (of **figure 3.4.9 a and b**) is displayed in **figure 3.4.9c**, which represents coupled “bi-weekly” mode oscillation of the atmospheric convection over the study region and the eastern equatorial zonal winds. Similar coupled “bi-weekly” mode oscillation is present in filtered time series of OLR anomaly and zonal wind speed during the boreal summer-fall of almost every year during of the study period (1988-2016), and **figures** for the same during the boreal summer-fall of the entire study period are displayed in the Appendix section.

As evident in **figure 3.4.9a**, six cycles of atmospheric deep convective phase are present with considerable amplitude, and the duration of each cycle is approximately 12-20 days. Similar 12-20 days oscillations are also visible in the filtered time series of zonal wind speed with six cycles in the season **figure 3.4.9b**. Composite line plot of **figure 3.4.9c** displays harmonic progress of “bi-weekly” oscillation of the atmospheric convection and the zonal wind events, and six cycles are present in the plot.

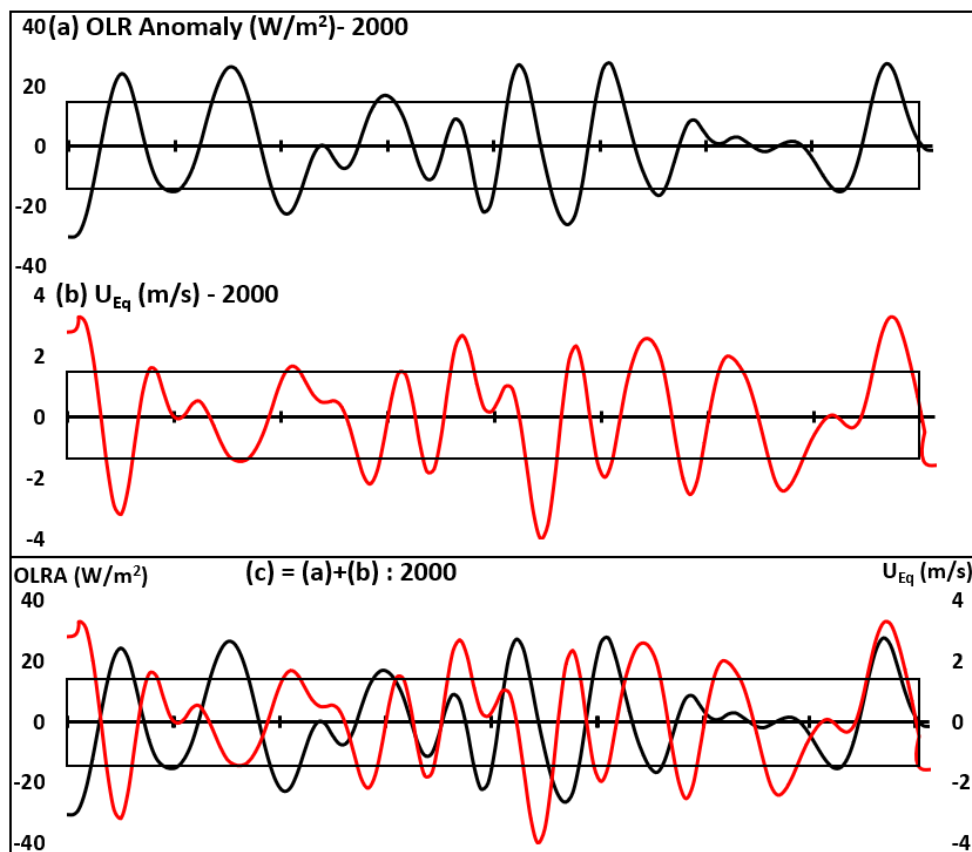


**Figure 3.4.9:** The 8-20 days filtered time series from June to September 2000 of (a) OLR anomaly over the study region, (b) zonal wind speed over the eastern equatorial Indian Ocean and (c) is (a) + (b).

For a typical 16 days of the atmospheric convective cycle with two days of interval, nine composite maps of the OLR anomaly is prepared for all six events capture during boreal summer-fall of 2000 (**figure 3.4.9**). Similar nine composites maps of surface circulation as wind vectors (length of arrow indicates wind speed) and the divergences of surface winds are also derived along with wind streamlines.

All nine maps prepared for all six events are then composite as the single event and nine composite maps are prepared as a single composite event and displayed in

**figure 3.4.10** to explain the synoptics structure of each atmospheric convective cycle and anomalous surface circulation during the event.

The OLR anomaly maps in **figure 3.4.10** represent atmospheric convection, wind vector maps and wind streamlines (superimposed on the divergence maps) display the orientation of surface winds circulation. In the wind divergence maps of **figure 3.4.10**, positive values (red and yellow shading) represent divergence of surface winds while negative values (blue and cyan shading) represent the convergence of surface winds.

Day -8 represents the weakest phase of atmospheric convection over the study region; hence, on this day, ORL anomaly map displays the dominance of the positive values in the region (**figure 3.4.10a**). According to the seasonal surface circulation of the eastern tropical Indian Ocean during boreal summer-fall (as displayed in **figure 3.4.2**), the maps of **figure 3.4.10** can be categorised into three zones. One is the eastern equatorial region in which the seasonal “south-westerly” dominates from 80°E to 95°E and 5°N to 5°S. Another is the southern coastal Java and adjacent southern coastal Sumatra region in which seasonal “south-easterly” are dominant, which drives the seasonal coastal upwelling along the southern Java and south Sumatra coastlines. The third region is the region south of 10°S in which seasonal “south-easterly” are predominant, though this third region is not the region of interest of this study. The wind vector map of the day -8 (**figure 3.4.9a**) displays surface circulation similar to **figure 3.4.2** and confirms the seasonal average wind directions in the season during the weakest phase of convection.

Day -6 the atmospheric convection starts building up over the study region (**figure 3.4.9b**), still the surface circulation has seasonal mean directions. Divergence map displays divergence of winds at southern coastal Java and southern coastal Sumatra region (**figure 3.4.9b**, day -6) under the influence of developing atmospheric convection which attracts surface winds.

On the day -4 the atmospheric convection becomes stronger over the region (**figure 3.4.10c**) which attracts the surface winds of the region, as a result, seasonal the “south-westerlies” of the eastern equatorial Indian Ocean reorients and becomes “westerlies” over the far eastern equatorial IO from 90°E to 100°E. Further, the

seasonal “south-easterly” of the southern Sumatra coastal region exhibit reversal under the influence of developing atmospheric convection between 20°N to 20°S in wind vector map (**figure 3.4.10c**). Reversal of seasonal winds triggers “north-easterly” winds in the region, consecutively develops convergence between anomalous “north-easterly” and seasonal “south-easterlies” between 0°S to 20°S along the south Sumatra coastline which as visible in divergence maps of **figure 3.4.10c** (blue shade).

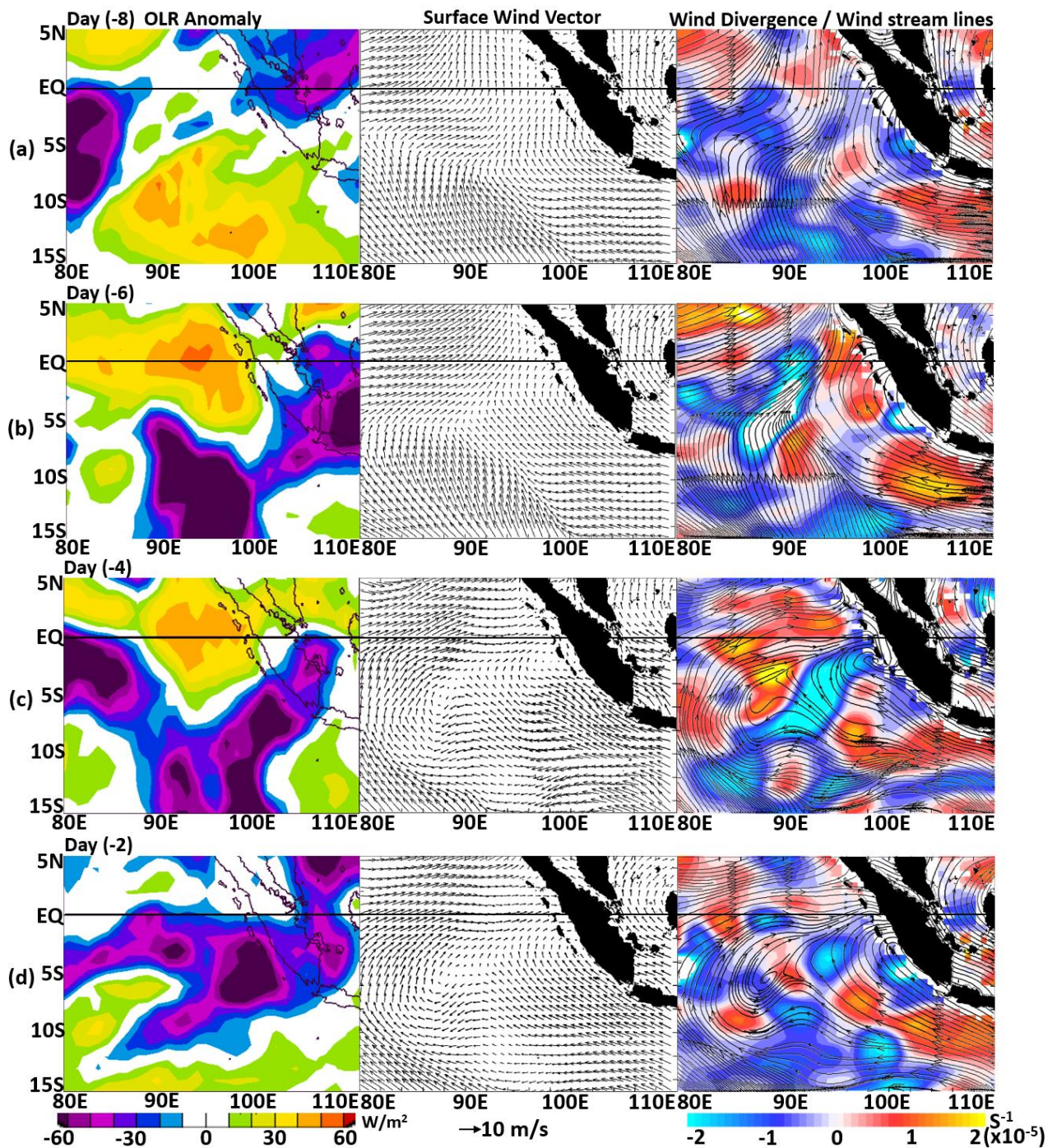


**Figure 3.4.10:** The composite maps of six convective events triggered during boreal summer-fall of 2000 displayed in **figure 3.4.9**. Left panels display OLR anomalies,

middle panels display surface wind vectors, and right panels display surface wind divergence with wind streamlines (right).

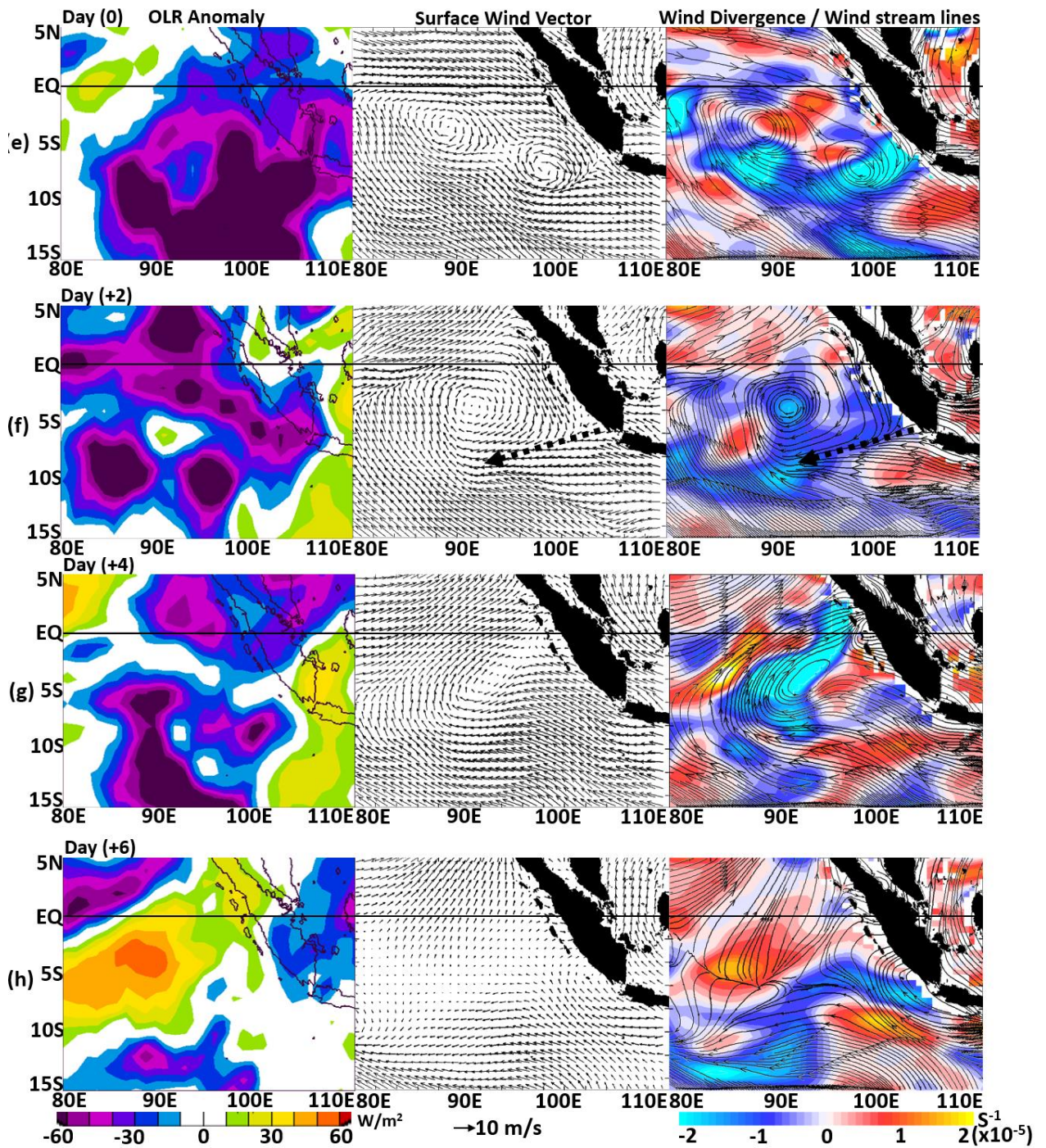
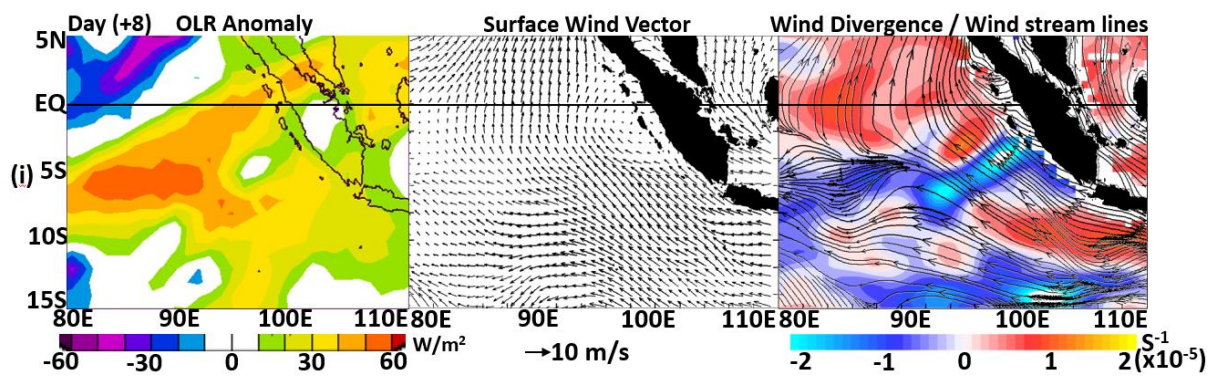


Figure 3.4.10: (Continued)



**Figure 3.4.10:** (Continued)

On the day -2 the centre of deep atmospheric convective activity is developed west of the southern Sumatra coastline at 5°S and 95°E (**figure 3.4.10d**). Reorientation of equatorial winds intensifies with an extended region of the “westerlies” in the eastern equatorial Indian Ocean, and the reversal of seasonal winds along the southern Sumatra coastline extends up to 4°S. Seasonal “south-easterlies” of south Sumatra coastline attract towards the centre of deep convection and shift westward in the region. Hence cyclonic circulation starts developing in the region under the influence of atmospheric convective convergence, which can be visualised as curved streamlines over the centre of the study region (3.4.10d, streamlines are superimposed over the divergence map).

Day 0 represents the strongest phase of the atmospheric convection over the study region when the entire region is covered with the strongest atmospheric convection, as displayed in the OLR anomaly map with negative values (**figure 3.4.10e**, below  $-40 W/m^2$ ). Under the influence of intensified atmospheric convective convergence and triggered updraft, the entire eastern equatorial Indian Ocean (80°-100°E) is covered by strong “westerlies”. Under the influence of intensified eastern equatorial “westerlies” and peak phase of atmospheric convection, the seasonal “south-easterlies” of entire southern Sumatra coastal region reverse completely to “north-westerlies”. Under the influence of westward shift of seasonal “south-easterly” of the study region and other wind disturbances described here, two small cyclonic circulations are triggered in the region as displayed in wind vector map of (**figure 3.4.10e**). This wind convergence is also visible in the divergence map of Day 0 (**figure 3.4.10e**) with two intensified convergence area (cyan shading).

On Day +2 under the effect of atmospheric convective aggregation and heating in the lower atmosphere, an atmospheric Rossby wave is triggered in the lower atmosphere which is visible in the wind vector and wind streamline map as a cyclonic circulation with centre at 5°S 90°E (**figure 3.4.10f**). The coverage of the triggered cyclonic circulation is synoptic-scale which covers a region of more than 1000 km (85°E to 98°E and Eq to 10°S) as evident in the wind-streamline map of day +2 (of **figure 3.4.10f**). Anomalous cyclonic circulation consecutively triggers strong surface wind convergence over the region as displayed in wind divergence map of day +2. The cyclonic circulation changes the direction of “seasonal westerly” of the eastern equatorial Indian Ocean and triggers strong “westerlies” in the region as the northern branch of a cyclonic circulation along as visible in wind vector map of day +2. Likewise, it (the cyclonic circulation) also reverses the seasonal “south-easterlies” along the south Sumatra coastline and triggers “north-westerlies” as the eastern branch of the cyclonic circulation as displayed in wind vector map of day +2. Abrupt “easterlies” are triggered at 6°S as south branch of cyclonic circulation from the interaction between reversed “north-westerlies” and seasonal “south-easterlies” at the southern Sumatra coast, and it is marked by the dashed arrow where tail of the arrow indicates the location of convergence of two wind fronts.

On day +4 (**figure 3.4.10g**), convection in the atmosphere enters in a decay phase and it starts dispersing towards north and south of the study region under the influence of enhanced divergence in the upper atmosphere (at 850hPa) as part of the updraft. Surface wind convergence starts decaying in the region and wind vectors at the eastern equatorial IO initiate reorientation towards seasonal “south-westerly” direction as displayed in wind vector map of day +4 (**figure 3.4.10g**). Likewise, winds along the southern coastal Sumatra initiate reorientation towards seasonal “south-easterly” direction.

Two days later, from day +6 to +8 the atmospheric convection over the study region disappears completely and exhibits the weakest phase of convection as evident in **figure 3.4.10h** and **figure 3.4.10i** and the surface circulation of the region also returns to the seasonal mean directions as displayed in wind vector map of the day +6 and +8. This situation is identical to the conditions of the day -8 (**figure 3.4.10a**). In

this way, the atmospheric convection over the study region completes the 16 days cycle of the deep convective event.

Above composite synoptic structure of the atmospheric convective system is similar to what displayed in **figure 3.4.8**, moreover, it (**figure 3.4.10**) precisely explain the surface circulation triggered during the mature phase of the event.

#### **(d) Anomalous surface wind circulation in the study region**

Above sub-section (section 3.4.3.c) reveals the relation between the atmospheric deep convective event and anomalous changes in surface circulation over the study region and reveals the presence of cyclonic circulation during mature phase of tropical convection over the study region (**figure 3.4.10**). The schematics of study region with seasonal wind directions and abruptly triggered cyclonic circulation is displayed in **figure 3.4.11** where red box displays the study area. The solid arrows in the **figure 3.4.11** indicate the seasonal directions of winds while dashed arrows display abruptly triggered winds. The giant synoptic scale circle (with dashed outline) displays the cyclonic circulation where equatorial “westerlies” over the eastern equatorial Indian Ocean and reversal of seasonal “south-easterly” along the south Sumatra coastline are the striking features of this cyclonic circulation.

Abruptly triggered “westerlies” over the eastern equatorial Indian Ocean, as northern branch of cyclonic circulation, can be considered as a short duration “westerly pulse” which has a typical life of 8 to 10 days (from day -4 to day +4, **figure 3.4.10**) with more than 10 degrees of zonal coverages (80°-100°E). Hence, these abrupt westerlies fit into the definition of westerly wind burst (WWB) which is occasionally evident in the western equatorial Pacific during El Niño trigger phase (Keen *et al.*, 1988; Harteen *et al.*, 1996; Zhang *et al.*, 1996; Chen *et al.*, 1996). The equatorial ocean dynamics suggests that abrupt “westerly pulses” can trigger downwelling Kelvin waves (Harrison and Giese, 1988; McPhadene *et al.*, 1988) along the equatorial wave guide. A detailed discussion on the effects of “westerly pulses” and consecutively triggered downwelling Kelvin waves is performed in the next section 3.6. The contradicting feature (with previous studies) here is no equatorial easterlies can be witnessed in any phase of the atmospheric convective cycle (**figure 3.4.10**), which confirms the dominance of westerly events over the eastern equatorial Indian Ocean and it is

unique and different from the claims of previous studies (Wen and Zhang 2008; Chen *et al.*, 2016).

Other prominent feature of the cyclonic circulation is the reversal of seasonal “south-easterly” to “north-westerly” along the south Sumatra coastline which was not noticed in any previous studies. This feature is crucial in understanding of the coastal upwelling of the region, as the seasonal “south-easterly” can trigger coastal upwelling at south Sumatra coasts while reversed “north-westerly” can suppress upwelling in the region. According to **figure 3.4.10**, reversed “north-westerly” has life cycle of almost 8 to 10 days (from day -4 to day +4, **figure 3.4.10**); hence, these reversed winds can suspend the seasonal coastal upwelling of the region temporarily for 8 to 10 days. Consecutively developed stronger “north-westerlies” in the southern coastal Sumatra region which can further trigger downwelling coastal Kelvin waves. The downwelling Kelvin waves can deepen the thermocline at the southern Sumatra and Java coasts by travelling poleward can. Hence, a reversal of winds in the region is crucial in understanding of the seasonal coastal upwelling along the Java and south Sumatra coastline, and the comprehensive analysis of its effects on ocean dynamics will be discussed in detail later in section 3.5.

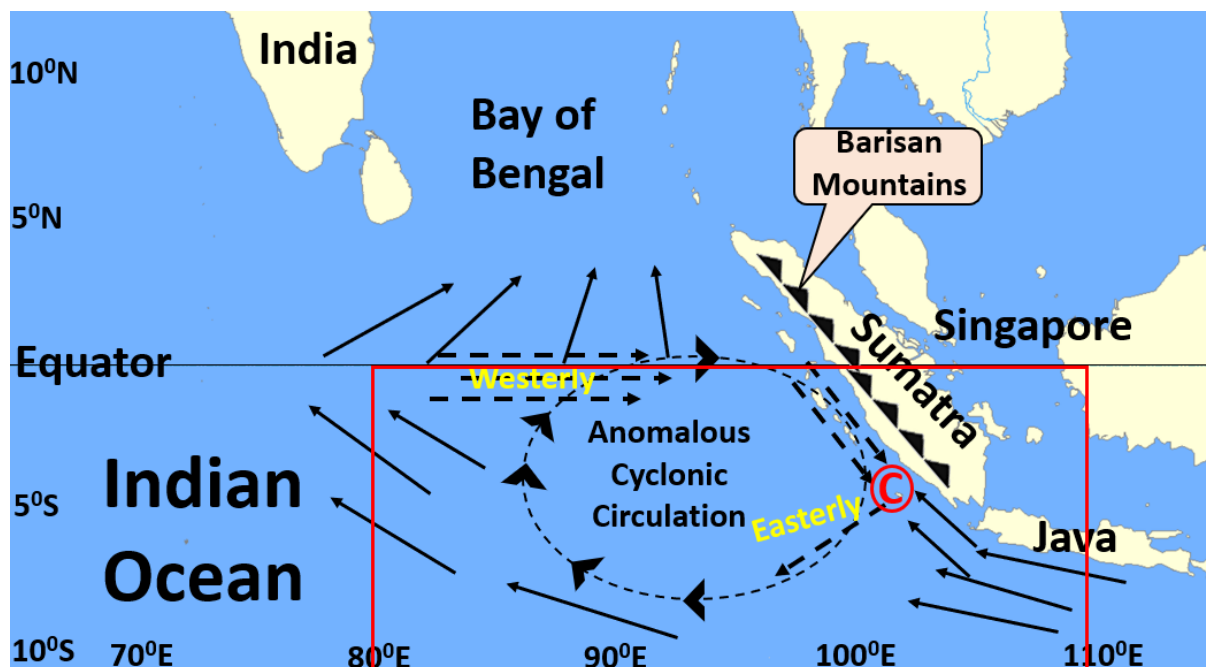


**Figure 3.4.11:** Schematics of anomalous cyclonic circulation over the study region under the influence of Rossby wave response from convective heating. Solid arrows indicate seasonal wind directions, dashed arrows indicate anomalous winds from cyclonic circulation and red box displays study region.

The abruptly triggered “north-westerly” (dashed arrows) and seasonal “south-easterly” (solid arrows) along south Sumatra coastline collide at location C marked **figure 3.4.11** (in red font and red circle). This collision triggered anomalous easterlies as marked with westward dashed arrow from location C in **figure 3.4.11**. Conversely the westerlies cannot develop from this collision (at location C) under the influence of “Barisan Mountains” range which blocks eastward flow (**figure 3.4.11**). The region of this wind fronts collision (the location C) at south Sumatra coastline is not identical during each cyclonic circulation triggered from the atmospheric convective phases and it can displace meridionally and zonally from location C, which depends on the location and synoptic coverage of the cyclonic circulation. The location of collision of wind fronts (location C) is very crucial in understanding of the variability of coastal upwelling along the south Sumatra coastline as it defines the extent of reversed “north-westerly” in the region. For example, in **figure 3.4.10f** collision of “north-westerly” and “south-easterly” develops at 6°S; hence, the entire southern Sumatra coastline (from the equator to 6°S) witnessed the reversed “north-westerly” for 8-10 days.

The cyclonic circulation triggered over the study region from the atmospheric convective events can be described as low latitude atmospheric low-pressure cells or low latitude cyclonic circulation. This low latitude cyclonic circulation is topographically trapped on the eastern side by the “Barisan Mountains” range. This synoptic cyclonic circulation is triggered in the south eastern tropical Indian Ocean (SETIO, the study region); hence, I called it a “SETIO cyclone”. Further in this study I will use this name to address the similar cyclonic circulations triggered in the region during the boreal summer-fall of the different years in study period (1988-2016).

The synoptic structure of the atmospheric convective events displayed in **figure 3.4.8**, **figure 3.4.10** and **figure 3.4.11** indicates that the coastal Java winds remain unaltered during the “SETIO cyclones”. Hence, seasonal “south-easterly” along the southern Java coastline remains uninterrupted during the any “SETIO cyclone”, as seen in **figures 3.4.10** and **3.4.11** where Java coastline is located around 10°S and 110°E.

According to **figure 3.4.9**, six to seven atmospheric convective cycles are triggered during the boreal summer-fall of 2000 and **figure 3.4.10** displays the composite structure of all these events; hence, a series of six to seven “SETIO

cyclones” are triggered in the region during June to September 2000. Similar number of short durations “westerly pulses” are triggered consecutively over the eastern equatorial Indian Ocean, along with similar numbers of wind reversal are triggered along the south Sumatra coastline in the season of 2000. Series of short-lived “westerly pulses” and multiple times reversal of winds along the south Sumatra coastline in a season has devastating effects on the seasonal coastal upwelling.

An event-based analysis approached is attempted to perform the structural and procedural analysis of atmospheric convective events of certain years in next section 3.5 and all other years are displayed in the appendix section for the reference.

### **Section summary**

This section discovers the existence of high frequency intraseasonal oscillations (“bi-weekly mode”) of atmospheric convection over the study region (the SETIO) during boreal summer-fall using spectral analysis. It also explains the maintenance mechanism of this high frequency atmospheric convective cycles by demonstrating its synoptic structure. Further, the synoptic structure of the atmospheric convective events uncovers the consecutively triggered anomalous surface circulation within the study region, which is triggered by the atmospheric Rossby wave response to the atmospheric convective heating. This synoptic scale anomalous cyclonic circulation of the region is named the “SETIO cyclone” in this section. Abrupt short-lived surface “westerlies” over the eastern equatorial Indian Ocean and reversal of seasonal “south-easterlies” along the south Sumatra coastline are the crucial consequences of the “SETIO cyclones”. Abrupt equatorial “westerlies” are noticed in previous studies (Rao and Yamagata, 2004; Iskandar *et al.*, 2005, 2006; Chen *et al.*, 2016; Delman *et al.*, 2016) though the trigger mechanism of them was not clear in any previous studies. Associated wind reversal along the south Sumatra coastline is not noticed in any previous studies and they are discovered in this study.

Next section 3.5 will explore the presence of the “SETIO cyclones” triggered from “bi-weekly” atmospheric convective events over the study region during boreal summer-fall of certain individual years of the study period (1988-2016) in the form of event analysis. Later in the same section, the investigation on effects of the “SETIO cyclones” on seasonal coastal upwelling along the south Sumatra and Java coastline is performed which is the prime motive of this study.

### 3.5 Event analysis of cyclonic circulation in the IOD perspective

The discovery of the high frequency (bi-weekly) atmospheric convective oscillations over the southern eastern tropical Indian Ocean (SETIO) during boreal summer-fall in the previous section suggests that, it can trigger anomalous cyclonic wind circulation in the lower atmosphere of the study area followed by abrupt wind events in the region. This section explores the presence of similar “bi-weekly” mode atmospheric convective oscillations and consecutively triggered wind events, at interannual time scale with event analysis method, and uncovers the effects on ocean dynamics of the region.

#### 3.5.1 Cyclonic events of individual years

The synoptic structure of the atmospheric convective event discussed in previous section 3.4.3 reveals the presence of anomalous cyclonic wind circulation in the lower atmosphere during the mature phase of the event and I named it the “SETIO cyclones”, which is triggered from the Rossby wave response of the atmospheric convective heating in the lower atmosphere. The “SETIO cyclone” consecutively triggers abrupt short-lived “westerly wind pulse” over the eastern equatorial Indian Ocean, along with abrupt “north-easterly” winds along the southern Sumatra coastline. This section explores the presence of “bi-weekly” mode atmospheric deep convective events and sequentially triggered “SETIO cyclones” over the study region, and also explores related wind events during boreal summer-fall of nine selected years of the study period (1988-2016) as event analysis.

##### (a) “SETIO cyclones” of 1998, 2001 and 2004

To perform the event analysis in the perspective of Indian Ocean Dipole events, I selected the criteria of three strong positive IOD event years which are 1994, 1997 and 2006; three aborted or weak positive IOD event years which are 2003, 2008 and 2012; and three years with neutral conditions which are 1998, 2001, 2004 (Meyers *et al.*, 2007; Du *et al.*, 2013). The period with neutral IOD conditions is discussed first, and the line plot of OLR anomaly averaged over the study region Ocean is displayed in **figure 3.5.1** along with area averaged zonal wind speed over the eastern equatorial Indian for the boreal summer-fall of 1998, 2001 and 2004.

The values of OLR anomaly below  $-10 \text{ W/m}^2$  and values of zonal wind speed above  $5 \text{ m/s}$  are shaded in **figure 3.5.1** to identify the atmospheric deep convective events and eastern equatorial “westerly” wind events. Six atmospheric deep-convective episodes are present during June to September 1998 with 12-20 days period in **figure 3.5.1a** (blue shading) and they are marked with arrows. During each “bi-weekly” mode atmospheric convective episode, strong “westerlies” are triggered as evident in **figure 3.5.1** (orange shading). Likewise, seven and eight “bi-weekly” mode atmospheric convective episodes are present during boreal summer-fall of 2001 and 2004 respectively (**figure 3.5.1b** and **figure 3.5.1c**, marked arrow) followed by similar number of strong “westerly” events.

Hence, **figure 3.5.1** confirms the presence of series of “bi-weekly” mode atmospheric deep-convective events over the study region, which can consecutively trigger the “SETIO cyclone” over the study region. The series of strong “westerly” wind events over the eastern equatorial Indian Ocean during boreal summer-fall of 1998, 2001 and 2004 are triggered from the “SETIO cyclones” of the region. To verify these claims and to examine the synoptic structure of consecutively triggered each “SETIO cyclone” during the atmospheric convective events, the streamline and wind vector maps of the study region are prepared at the days marked by arrow in **figure 3.5.1** and displayed in **figure 3.5.2**.

As per discussion in section 3.4.3c, anomalous cyclonic circulation is triggered on day +2 of the “bi-weekly mode” atmospheric convective cycle; hence, similar days (day +2) are identified for each atmospheric convective episode of **figure 3.5.1** (marked arrows) and composite maps of wind vectors and wind streamlines are prepared for the study area and displayed in **figure 3.5.2**. The presence of the “SETIO cyclone” is evident in all maps of **figure 3.5.2**, which confirms the presence of the anomalous cyclonic circulation during mature phase of all atmospheric convective episodes displayed in **figure 3.5.1** (marked arrows).

The location of the centre of low-pressure of each “SETIO cyclone” is not exactly similar for each event and it varies over the study region as evident in **figure 3.5.3**; likewise, the extent of each system is also different from event to event though all events have mostly synoptic scale coverage. More details on the location of centre

of low pressure along with extent of each event detected during study period (1988-2016) is discussed later in section 3.5.4 in tabular format.

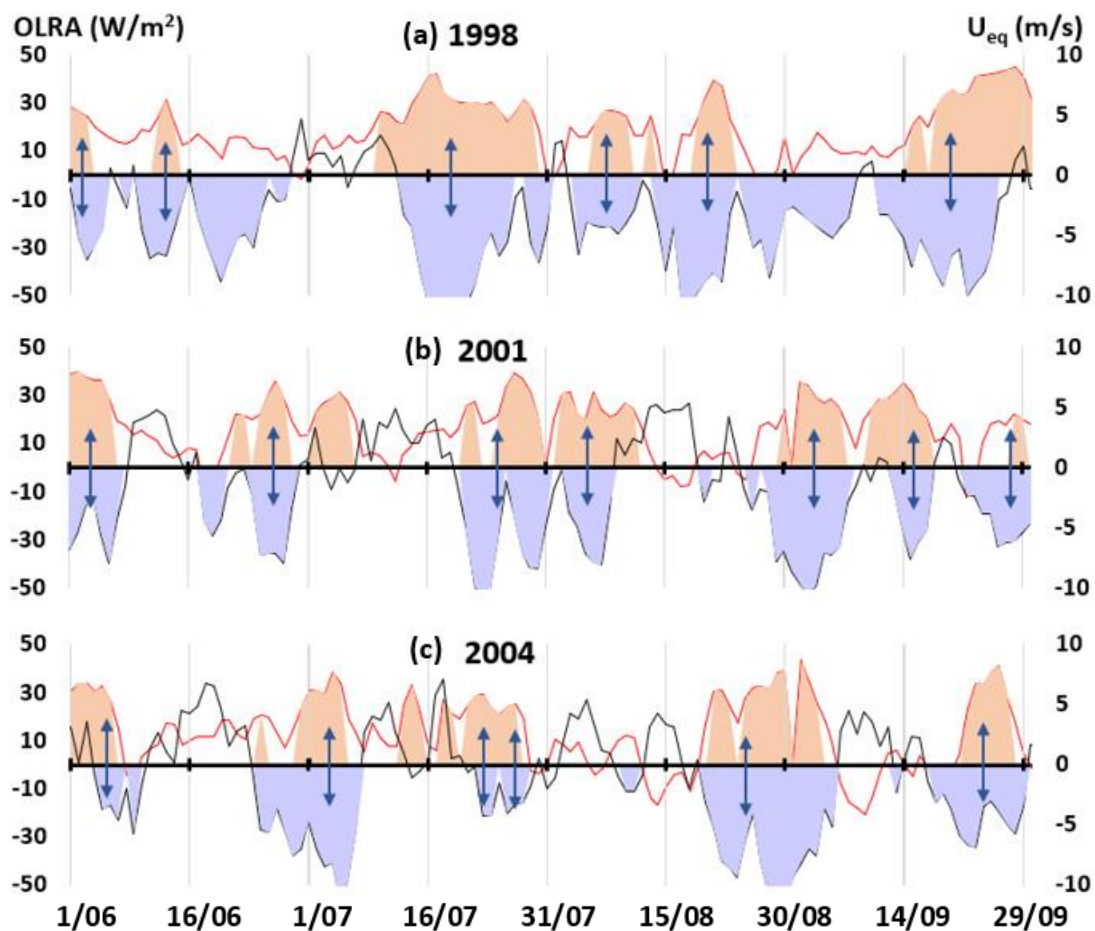


**Figure 3.5.1:** Each panel displays time series of OLRA anomaly averaged over 80°-110°E, Eq-10°S (black line and blue shading) and zonal wind speed averaged over 70°-90°E, 5°N-5°S (red line, orange shading). The values of OLR anomaly below -10 W/m<sup>2</sup> and values of zonal wind speed above 5 m/s are shaded, and arrows indicate deep convective event.

The eastern equatorial “westerly” events displayed in **figure 3.5.1** with orange shading, is present as northern branch of the “SETIO cyclones” in each map of **figure 3.5.2**. These “westerlies” have wind speed more than 5 m/s and have zonal coverage of more than 10 degrees along the equator (as mentioned previously in section 3.4.3d); hence, they fit into the definition of equatorial “westerly wind bursts”. “Westerly wind bursts” have a crucial role in equatorial ocean dynamics as they can trigger downwelling equatorial Kelvin waves which can deepen the thermocline of the region and which is challenging condition for the upwelling signature to reach the surface.

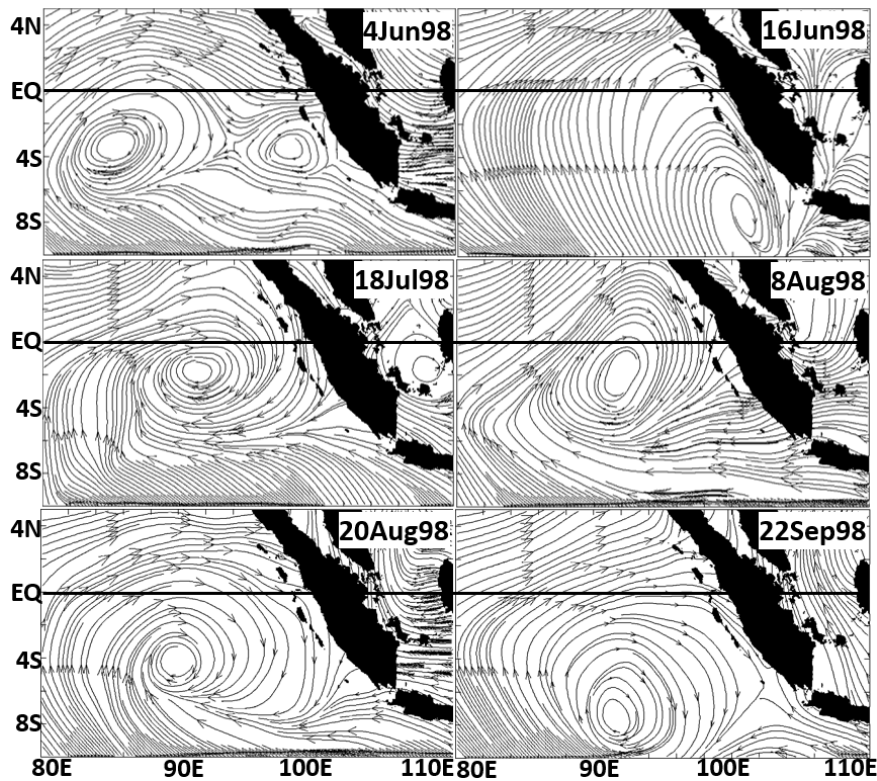


**Figure 3.5.2a:** Each map displays the surface circulation with the streamlines and wind vectors over the study region during the mature phase of atmospheric convective phase of 1998.

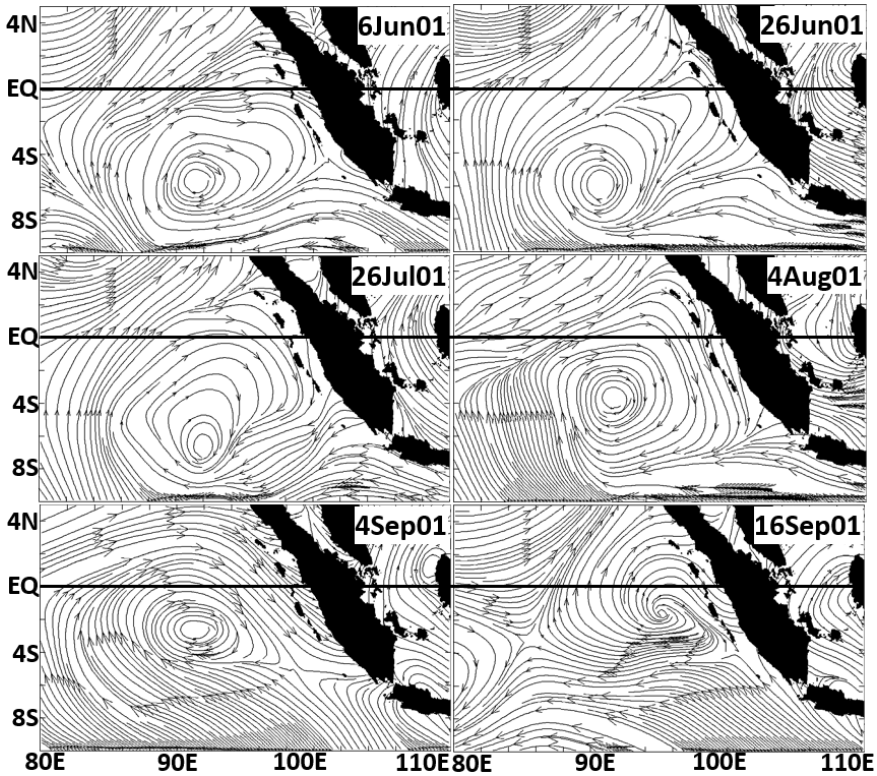


**Figure 3.5.2b:** (continued) surface circulation during the mature phase of atmospheric convective phase of 2001.

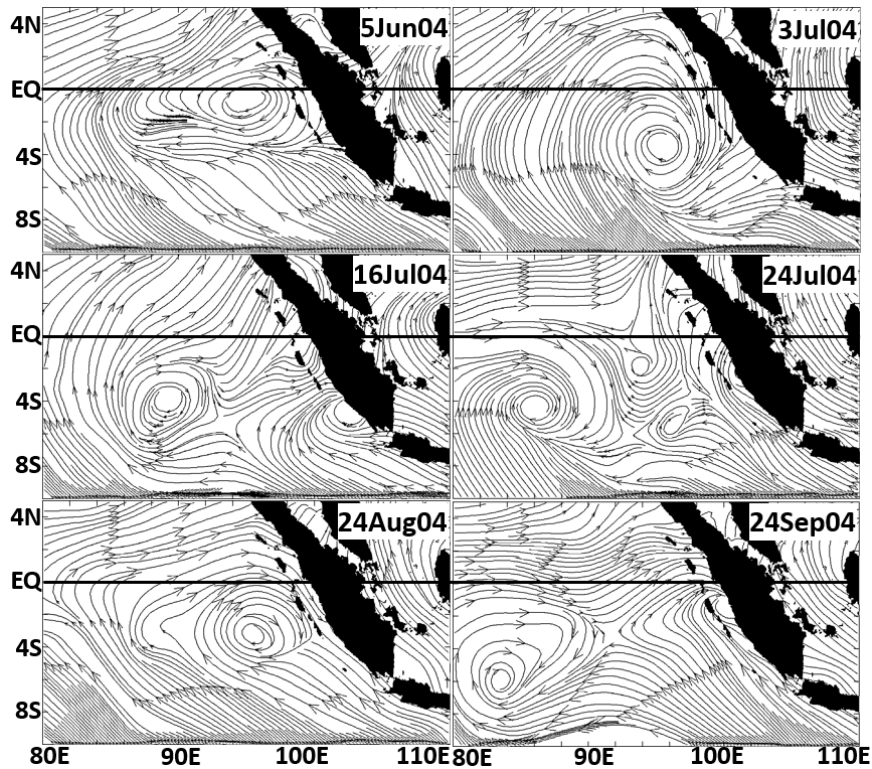


**Figure 3.5.2c:** (continued) surface circulation during the mature phase of atmospheric convective phase of 2004.

The other consequence of the “SETIO cyclones” is reversal of seasonal “south-easterlies” along southern Sumatra coastline, which was revealed in section 3.4.3, is evident in maps of **figure 3.5.2** as an eastern branch of “SETIO cyclone” as “north-easterly” flow. Though the maps of **figure 3.5.1** displays the condition of a single day; hence, to visualise the orientations of winds throughout the season along the southern Sumatra coastline on daily time scale, the daily time series of wind vector rolls are prepared at six different pinpoint locations along the southern Sumatra coastline. The schematics of Java and southern Sumatra coastal region is displayed in **figure 3.5.3**, where six pinpoint locations marked with numbers are used to derive wind vectors and red boxes are used to calculate area average coast parallel wind stress. The number of each pinpoint locations of **figure 3.5.4** also indicates the geographical southern latitudes (for example 1°S to 6°S) and black arrows in the **figure** indicates seasonal wind direction during boreal summer-fall.

Area averaged coast parallel stress for the coastal Java and southern coastal Sumatra regions (**figure 3.5.3**, red boxes) are derived from daily satellite wind fields (CCMP V2) and displayed as daily time series in the top panel of **figure 3.5.4** (dashed red and solid black lines) along with the time series of area average daily values of OLR anomaly (in the same panel, blue shading and thin black line) over the study

region. The blue shading in OLR anomaly line plots displays values below  $-10 \text{ w/m}^2$  which indicates deep convective events and the locations of consecutively triggered “SETIO cyclones” in time domain are marked by two-sided arrows (retrieved from **figure 3.5.1**). The period of each plot of **figure 3.5.4** is identical to **figure 3.5.1** which is the boreal summer-fall of selected neutral years.

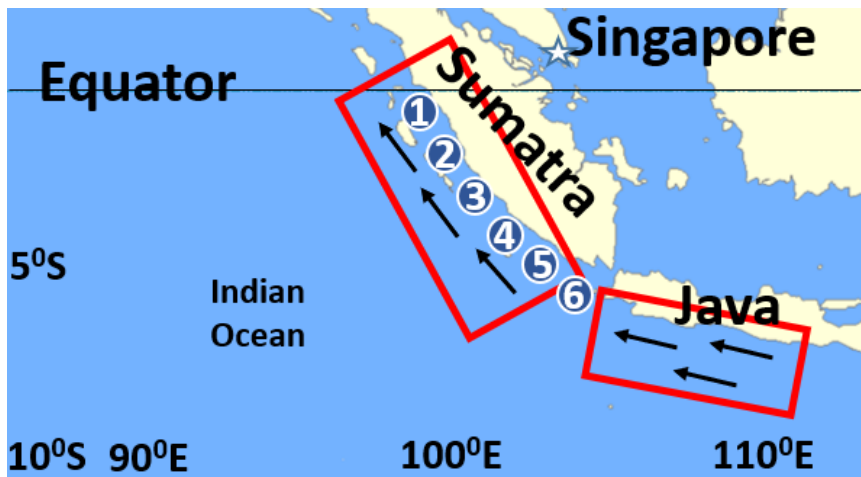


**Figure 3.5.3:** Schematics of Java and Sumatra coastal region. Red box area is used to calculate area average coast parallel stress and pinpoint locations with number are used to prepare wind roll plot. Black arrows indicate ideal coast parallel direction along respective coastline.

Further to decompose the characteristics of winds at multiple locations along southern Sumatra coastline and to visualise wind directions on daily timescale the wind vector roll plots are prepared and displayed in **figure 3.5.4**. The bottom panels of **figure 3.5.4** display the wind roll in time domain for similar period of top panel and indicates daily wind flow direction (not the direction from which wind comes) at six pinpoint locations along the southern Sumatra coastline (marked with number in **figure 3.5.3**). Ideal coast parallel orientation along southern Sumatra coastline is displayed in black arrow (in legends of each panel) and it is a unit vector as well with  $0.01 \text{ Pa}$  value of wind stress.

### Surface winds of 1998

The season of 1998 commences with two “SETIO cyclone” (**figure 3.5.4a**, marked arrow); three more “SETIO cyclones” are triggered during July and August 1998 (**figure 3.5.4a**, marked arrow). According to the synoptic structure of these “SETIO cyclones” in **figure 3.5.2a**, the completely disorient and reverse the seasonal “south-easterly” winds along the southern Sumatra coastline. Hence, wind vectors at locations  $1^{\circ}\text{S}$  to  $4^{\circ}\text{S}$  are disoriented from seasonal “south Easterly” direction during early June till late August 1998 (**figure 3.5.4a**, wind roll of  $1^{\circ}\text{S}$  to  $4^{\circ}\text{S}$ ).

From mid-August to mid-September 1998 is the suppressed phase of atmospheric convection (**figure 3.5.4a**, top panel, gap between last two marked arrows) and hence no “SETIO cyclones” are triggered. As a result, the wind vectors gain the coast parallel direction at locations 3°S to 6°S (**figure 3.5.4a**, wind roll of 3°S to 6°S) from mid-August to mid-September 1998, though the wind vectors at locations 1°S to 2°S cannot gain the coast parallel direction (**figure 3.5.4a**, wind roll of 1°S to 2°S). Later, during second half of September 1998 the atmospheric convection is again aggregated over the study region (**figure 3.5.1a**, blue shading) and consecutively the “SETIO cyclone” is triggered on 22 September 1998 (**figure 3.5.4a** marked arrow, **figure 3.5.2a**), which again disorients the wind vectors along the entire southern Sumatra coastline (**figure 3.5.4a**, wind roll of 1°S to 6°S) in late September 1998.

The southern Java coastline stays outside the coverage of the “SETIO cyclones” as evident in the maps of **figure 3.5.2a**; hence, the surface winds of the region remain unaffected during the “SETIO cyclone” phases and retains its seasonal coast parallel wind direction throughout the season. Hence the wind vector roll plots are not prepared for the southern Java region. Instead the line plot of area average coast parallel winds stress is prepared and displayed in top panel of **figure 3.5.4a** (red dashed line). The area average coast parallel stress along southern Java coastline displays values from 0 to 0.03 Pa in June and July under the influence of the weaker seasonal mean winds over the entire study region (**figure 3.5.4a**, red dashed line). Later, from August onwards it gains strong coast parallel stress values above 0.05 Pa and stays above this value till the end of the season.

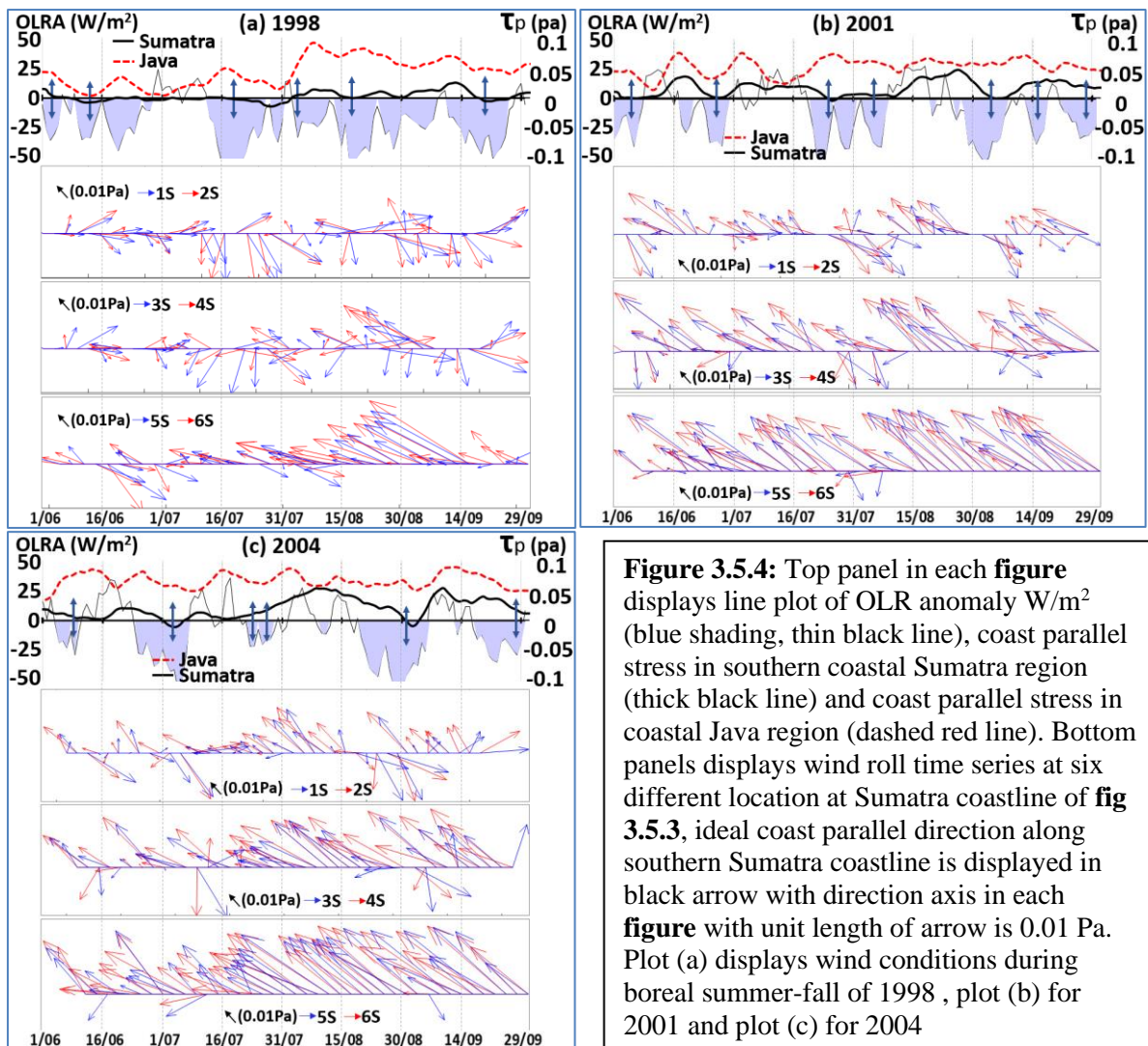


**Figure 3.5.4:** Top panel in each figure displays line plot of OLR anomaly W/m<sup>2</sup> (blue shading, thin black line), coast parallel stress in southern coastal Sumatra region (thick black line) and coast parallel stress in coastal Java region (dashed red line). Bottom panels displays wind roll time series at six different location at Sumatra coastline of **fig 3.5.3**, ideal coast parallel direction along southern Sumatra coastline is displayed in black arrow with direction axis in each figure with unit length of arrow is 0.01 Pa. Plot (a) displays wind conditions during boreal summer-fall of 1998, plot (b) for 2001 and plot (c) for 2004

During suppressed phase of atmospheric convection the wind vectors at locations 5°S and 6°S (**figure 3.5.4a**) are stronger compare to its northern locations (1°S to 4°S), the reason behind this difference is the locations 5°S and 6°S, which has least exposure of the “SETIO cyclones” as evident in the wind streamlines maps of **figure 3.5.2a**; hence, these locations (5°S and 6°S) suffer least wind reversal and can gain the seasonal “south easterly” winds very rapid during the suppressed phase of atmospheric convection. The reason behind the weaker winds at 5°S and 6°S during June and July 1998 is the weaker seasonal mean winds over the entire study region during early season which is also evident in the line plot of area average coast parallel stress along the Java coastline (**figure 3.5.4**, top panel, red dashed line).

It can be concluded from **figure 3.5.2a** and **figure 3.5.4a** that, the seasonal winds along the entire southern Sumatra coastline is mostly affected by the “SETIO cyclones”, which disorient the seasonal “south-easterly” winds of the region multiple

time in the season. As a result, persistent area average coast parallel winds stress cannot develop throughout the season of 1998 along the southern Sumatra coastal region (**figure 3.5.4a**, top panel, thick black line). The series of strong atmospheric convective events over the study region (**figure 3.5.1a** and **3.5.4a** top panel, blue shading) and consecutively triggered “SETIO cyclones” over the study region during boreal summer-fall of 1998, destroy the season coast parallel winds along the southern Sumatra coastline throughout the season as evident in **figure 3.5.4a** **figure 3.5.2a**.

### **Surface winds of 2001**

During the season of 2001, total seven atmospheric convective events are present (**figure 3.5.1b**, **3.5.4b**) which consecutively trigger similar number of the “SETIO cyclones” (**3.5.4b** marked arrows in top panel) and their synoptic structures are displayed in **figure 3.5.2b**. According to **figure 3.5.2b** the coverage of “SETIO cyclone” of September 2001 stays away from locations 5°S and 6°S and hence these locations gain strong coast parallel winds during this period (**figure 3.5.4b**, bottom most panel). The “SETIO cyclones” triggered during June to August 2001 has minor effects on the surface winds of locations 5°S and 6°S and they are disoriented temporally during the “SETIO cyclone” phases (**figure 3.5.4b**).

The wind vectors at locations 10S to 40S are disoriented from seasonal mean “south-easterly” direction (**figure 3.5.4b**, wind rolls of 10S to 40S) during each “SETIO cyclone” period of the season (**3.5.4b**, marked arrows in top panel). Hence, strong area average coast parallel stress cannot develop till early August 2001 in the southern Sumatra coastal region as displayed in **figure 3.5.4b** (thick black line, top panel).

The wind vectors at locations 1°S to 4°S gain seasonal mean coast parallel direction (**figure 3.5.4b**, wind rolls of 1°S to 4°S) temporarily during the suppressed phase atmospheric convection from early August to late August 2001 (the gap between two arrows in top panel of **figure 3.5.4b**) and no “SETIO cyclone” is triggered. Consecutively, strong area average coast parallel wind stress is developed in the region (**figure 3.5.4b**, top panel, thick black line). Though this strong coast parallel winds cannot sustain for a longer period and they are disoriented (**figure 3.5.4b**, wind rolls of 1°S to 4°S) by three atmospheric convective events of September 2001 (**figure**

3.5.1b, blue shading) and consecutively developed “SETIO cyclones” (**figure 3.5.2b**). Disorientation of wind vectors declines the value of area average coast parallel stress of the southern coastal Sumatra coastal region during September 2001 as evident in **figure 3.5.4b** (top panel, thick black line).

During June and July 2004, the wind vectors at location 5°S and 6°S exhibits strong disorientation during the “SETIO cyclone” phases (**figure 3.5.10a**, wind roll of 5°S to 6°S, bottom most panel). Later in the season, during August and September 2004 the wind vectors at location 5°S and 6°S exhibits strong “south easterly” winds (**figure 3.5.10a**, wind roll of 5°S to 6°S) and they suffer minor disorientation from the “SETIO cyclones”. During season of 2001, strong coast parallel wind stress is developed along southern Java coastline from the beginning of the season with values above 0.05 Pa as evident in area average line plot of coast parallel stress in **figure 3.5.4b** (top panel, red dashed line). After fluctuation in strength from early June to mid-July 2001, the area average coast parallel stress of the southern Java coastal region gains strong coast parallel values from mid-July 2001 till end of the season (**figure 3.5.4b**, top panel, red dashed line).

#### **Surface winds of 2004**

Six atmospheric convective events are developed during June to September of 2004 as displayed in the top panel of **figure 3.5.4c** (top panel, blue shading) and similar numbers of the “SETIO cyclones” are also triggered (**figure 3.5.2c** and **figure 3.5.4c**, top panel, marked with arrows).

The wind vectors at locations 1oS to 4oS are disoriented from seasonal mean “south-easterly” direction (**figure 3.5.4c**, wind roll plot of 1°S to 4°S) during the “SETIO cyclone” phases. As a result, strong area average coast parallel stress cannot develop in the southern Sumatra coastal region till mid-July 2004 as displayed in **figure 3.5.4c**(top panel, thick black line). The suppressed phase of atmospheric convection is developed over the study region during August 2004 (**figure 3.5.1c**, **3.5.4c** top panel) and no “SETIO cyclone” is triggered. Hence, during the same period (Aug 2001) strong “south-easterly” winds are developed along entire southern Sumatra coastline (from locations 1°S to 4°S) as displayed in **figure 3.5.4c** (wind vector roll plots of 1°S to 4°S). Consecutively, strong area average coast parallel winds stress values are developed

in the region (**figure 3.5.4c**, top panel, thick black line) with values above 0.05 Pa during August 2004.

This strong coast parallel winds cannot sustain for a longer period in the region and they are disoriented (**figure 3.5.4c**, wind roll of 1°S to 4°S) immediately after under the influence of the atmospheric convective events of end of August 2001 and consecutively triggered “SETIO cyclone” (**figure 3.5.4c**, **figure 3.5.2c**). The winds in the region gain the coast parallel direction in mid-September 2004 (**figure 3.5.4c**, wind roll of 1°S to 4°S), as a result strong area average coast parallel winds stress values are again developed temporarily during mid-September 2004 in the southern Sumatra coastal region (**figure 3.5.4c**, top panel, thick black line). These strong area average coast parallel winds stress values are again destroyed by the atmospheric convective episode and the “SETIO cyclone” of late September 2004 (**figure 3.5.4c**, marked arrow).

During June and July 2004, the wind vectors at location 5°S and 6°S exhibits strong disorientation during the “SETIO cyclone” phases (**figure 3.5.10a**, wind roll of 5°S to 6°S, bottom most panel). Later in the season, during August and September 2004 the wind vectors at location 5°S and 6°S exhibits strong “south easterly” winds (**figure 3.5.10a**, wind roll of 5°S to 6°S) and they suffer minor disorientation from the “SETIO cyclones”. During the season of 2004, strong area average coast parallel wind stress is developed along southern Java coastline from the advent of the season with values above 0.05 Pa as evident in **figure 3.5.4c** (top panel, red dashed line) and it retains strong values throughout the season without any notable variations.

### **Summary of 1998, 2001 and 2004**

In summary, the series of “biweekly” mode atmospheric deep convective events and consecutively triggered “SETIO cyclones” over the study region during boreal summer-fall of the neutral IOD event years, disorients the seasonal “south easterly” wind along the southern Sumatra coastline several times, a result the substantial coast parallel wind stress cannot develop in the region. Though, the coast parallel stress along the southern Sumatra coastline can achieve temporary strong values, though only during the suppressed phase of atmospheric convection over the study region as no “SETIO cyclones” can be triggered during the period.

For example, during boreal summer-fall of 1998 the series of “bi-weekly mode” atmospheric convective events over the study region and subsequently triggered “SETIO Cyclones” do not provide substantial gap during which the coastal parallel winds can sustain along the southern Sumatra coastline. Hence, weak coast parallel wind stress values predominate in the region throughout the season. While, during boreal summer-fall of 2001 and 2004 a short phase of the suppressed atmospheric convection over the study region with duration of 15 days and 1 month is present, and during this suppressed convective phase coast parallel winds are developed along the southern Sumatra coastline temporarily. While the seasonal winds along the southern Java coastline remains unaltered during these atmospheric convective episodes and strong coast parallel wind stress is developed in the region during most of the seasons.

Hence, it can be concluded that “bi-weekly” mode atmospheric convective episodes over the study region and subsequently triggered “SETIO Cyclones” profoundly affect the seasonal “south easterly” winds of the southern Sumatra coastal region.

#### **(b) Absence of “SETIO cyclones” in 1994, 1997 and 2006**

To investigate the characteristics of the atmospheric convective events and related surface circulation over the study region during boreal summer-fall of the strong positive IOD years; 1994, 1997 and 2006; line plots of OLR anomaly average over the study region and zonal winds averaged over the eastern equatorial Indian Ocean are prepared and displayed in **figure 3.5.5** (identical to **figure 3.5.1**).

Study area suffers from the suppressed phase of atmospheric convective episode from advent of the season of 1994 (**figure 3.5.5a**) and hence no strong “westerly” event is triggered at the eastern equatorial Indian Ocean. Though one brief atmospheric convective episode with short “westerly” event is evident in early June 1994 (**figure 3.5.5a**, marked arrow). During the season of 1997, a single atmospheric convective event is developed (**figure 3.5.5b**, marked arrow) during which a short episode of “westerly” is also triggered as evident in **figure 3.5.5** (of 1997). During 2006, two atmospheric convective episodes and related “westerly” episodes are triggered as displayed in **figure 3.5.5c** (marked arrow) during the initial phase of the season.

Hence **figure 3.5.5**, displays suppressed atmospheric convection phases and open sky conditions over the study area during the boreal summer-fall of 1994, 1997 and 2006 predominantly. Supressed atmospheric conditions indicate limited presence of the sequentially triggered “SETIO cyclones”; and rare present of them is recorded on day +2 of the four atmospheric convective episodes displayed in **figure 3.5.5** (on in 1994, one in 1997 and two in 2006). Synoptic structure of these four “SETIO cyclones” are displayed in **figure 3.5.6** with composite wind vector and streamline maps to visualise the surface circulation.

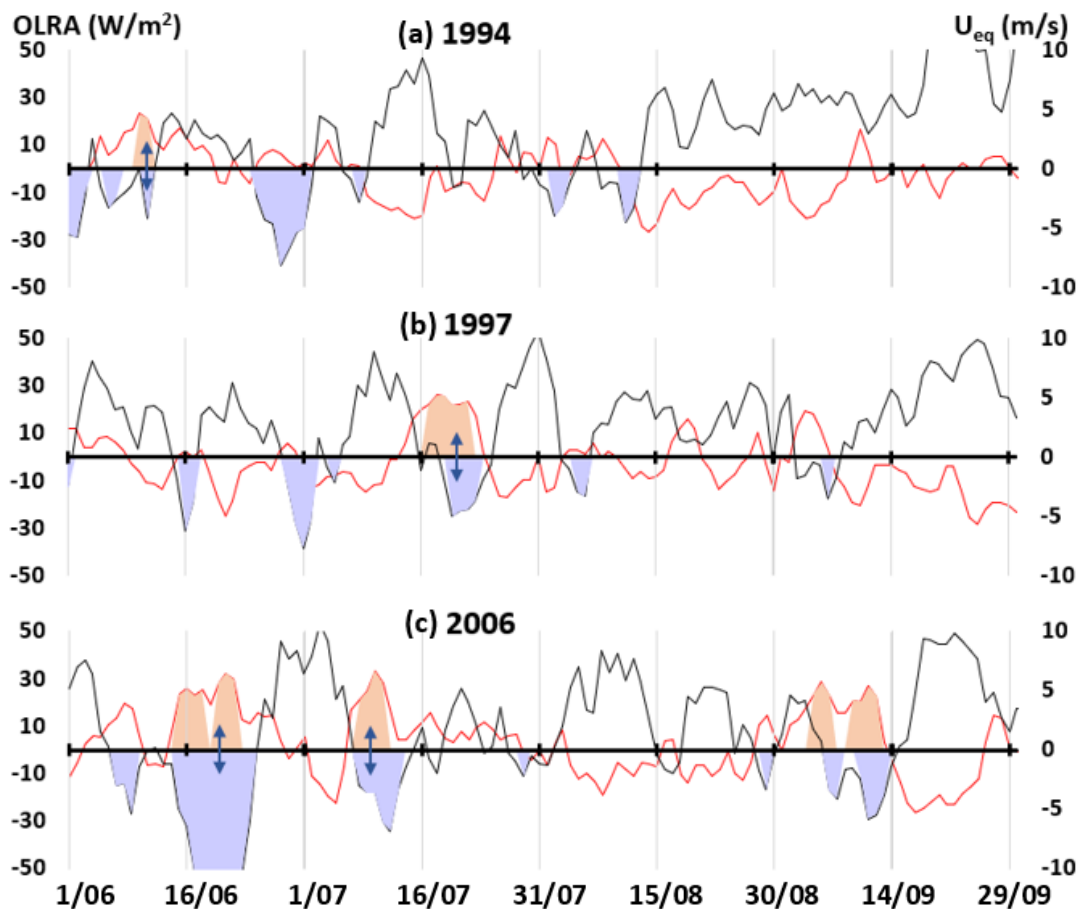


**Figure 3.5.5:** Time sires of OLRA anomaly averaged over  $80^{\circ}$ - $110^{\circ}$ E,  $Eq-10^{\circ}$ S (black line and blue shading) and zonal wind speed averaged over  $70^{\circ}$ - $90^{\circ}$ E,  $5^{\circ}$ N- $5^{\circ}$ S (red line, orange shading). The values of OLR anomaly below  $-10 W/m^2$  and values of zonal wind speed above  $5 m/s$  are shaded, and arrows indicate deep atmospheric convective event.

A “SETIO cyclone” with small coverage and weak streamlines is triggered on 8th June 1994 as displayed in **figure 3.5.6**, as result of short and weak atmospheric convective event of June 1994 displayed in **figure 3.5.5a**. The smaller coverage of this “SETIO cyclone” (of 8th June 1994, **figure 3.5.6**) and far out location of centre of

low pressure (at 4°S 88°E) from the southern Sumatra coastline is evident in **figure 3.5.6**; hence, it cannot alter the seasonal “south easterly” winds of the southern Sumatra coastal region. Later in the season of 1994, the atmospheric convection disappears over the study region and dry phase persists during the season of 1994 (**figure 3.5.5a**), as a result no “SETIO cyclone” is further triggered.

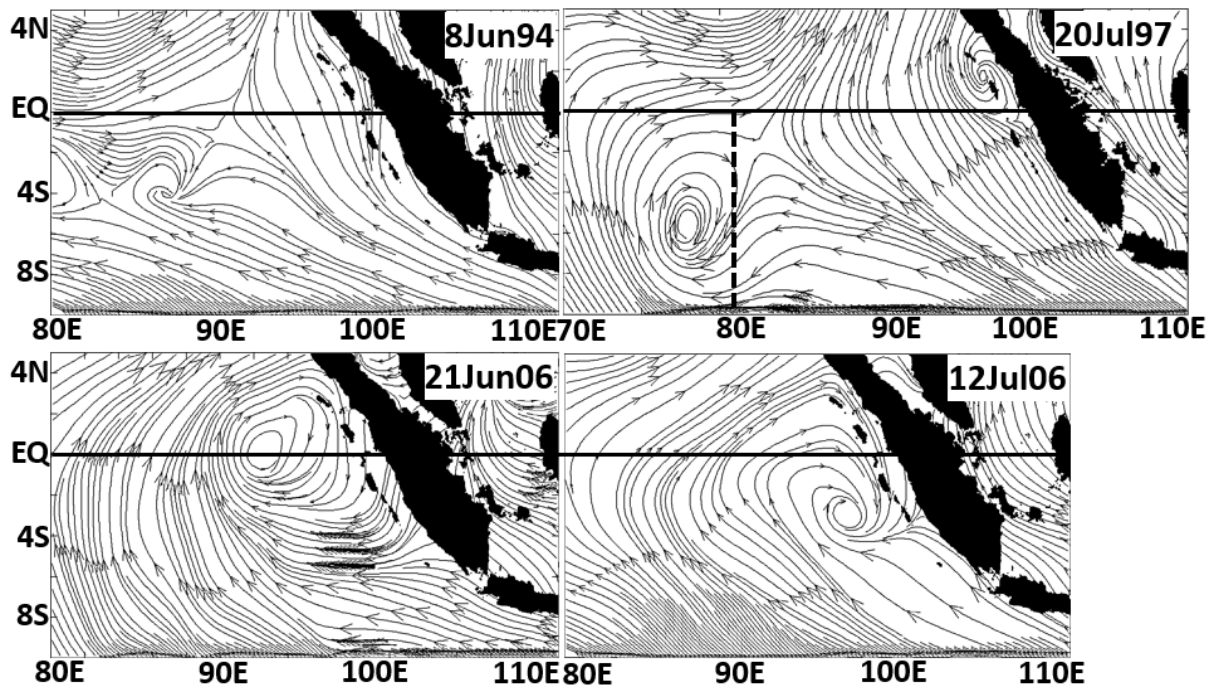


**Figure 3.5.6:** Maps display the surface circulation with the streamlines and wind vectors of the study region during the peak convective phase of 1994, 1997 and 2006.

The atmospheric convective episode of mid-July 1997 is stronger and longer (**figure 3.5.5b**, blue shading) than the episode of June 1994; hence, it triggers a strong cyclonic circulation with synoptic coverage (identical to “SETIO cyclone”) at 20 July 1997 as displayed in **figure 3.5.6**. Though, the centre of low pressure of this cyclonic circulation along with its entire synoptic coverage is developed outside of the SETIO region as displayed in **figure 3.5.6** (of 20 July 1997) which has extended coverage compare to other maps of **figure 3.5.6**, where the study area (the SETIO) has extent up to 80°E in the western part and it is marked by a vertical dashed line in the map. Due to its location outside of the SETIO region (80°-110°E) this cyclonic circulation cannot be tagged as a “SETIO cyclone”, and due to similar reason, it cannot affect the seasonal “south easterly” winds of the southern Sumatra coastal region (**figure 3.5.6**). Later during the season of 1997, the atmospheric convection disappears over the

study region and dry phase persists (**figure 3.5.5b**); hence, no “SETIO cyclone” is further triggered.

Two atmospheric convective events of June-July 2006 over the study region are stronger and longer compare to events of 1994 and 1997 (**figure 3.5.5c**, blue shading); hence, two strong “SETIO cyclones” are triggered consecutively on 21 June 2006 and 12 July 2006 as displayed in **figure 3.5.6**. The centre of low pressure of the “SETIO cyclone” of 21 June 2006 is located north of the equator along (oustr side the SETIO) along with its most coverage (**figure 3.5.6**) hence it cannot alter the seasonal “south easterly” winds along the southern Sumatra coastline. The “SETIO cyclone” triggered on 12th July 2006 has a centre at 98°E 3°S which is very close to the southern Sumatra coastline (**figure 3.5.6**) hence it alters the surface winds of the region and reverses it up to 4°S. After this event of July 2006 atmospheric convection is entered in the supressed phase over the study region (**figure 3.5.5c**) and dry atmospheric conditions persists throughout the season and no “SETIO cyclone” is further triggered.

Further to decompose the characteristics of winds at multiple locations along southern Sumatra coastline and to visualise wind directions on daily timescale the wind vector roll plots are prepared and displayed in the bottom panels of **figure 3.5.7** (identical to **figure 3.5.4**). The wind rolls in bottom panels of **figure 3.5.7** indicate daily wind flow direction (not the direction form which wind comes) at six pinpoint locations along the southern Sumatra coastline (marked with number in **figure 3.5.3**). Ideal coast parallel orientation along southern Sumatra coastline is displayed in black arrow (in legends of each panel) and it is a unit vector as well with 0.01Pa value of wind stress.

Area averaged coast parallel stress for the coastal Java and southern coastal Sumatra regions (**figure 3.5.3**, red boxes) are derived from daily satellite wind fields (CCMP V2) and displayed as daily time series in the top panel of **figure 3.5.7** (dashed red and solid black lines) along with the time series of area average daily values of OLR anomaly (in the same panel, blue shading and thin black line) over the study region (identical to **figure 3.5.4**). The blue shading in OLR anomaly line plots displays values below  $-10 \text{ w/m}^2$  which indicates atmospheric deep convective events.

The Locations of consecutively triggered “SETIO cyclones” are not marked in top panel of **figure 3.5.7 a and b**, because the cyclones circulation of 1994 and 1997 cannot affect the seasonal winds of the region as discussed previously. Locations of consecutively triggered “SETIO cyclones” during June and July 2006 are marked by two-sided arrows in top panel of **figure 3.5.7c** (retrieved from **figure 3.5.5**). The period of each plot of **figure 3.5.4** is identical to **figure 3.5.1** which is the boreal summer-fall.

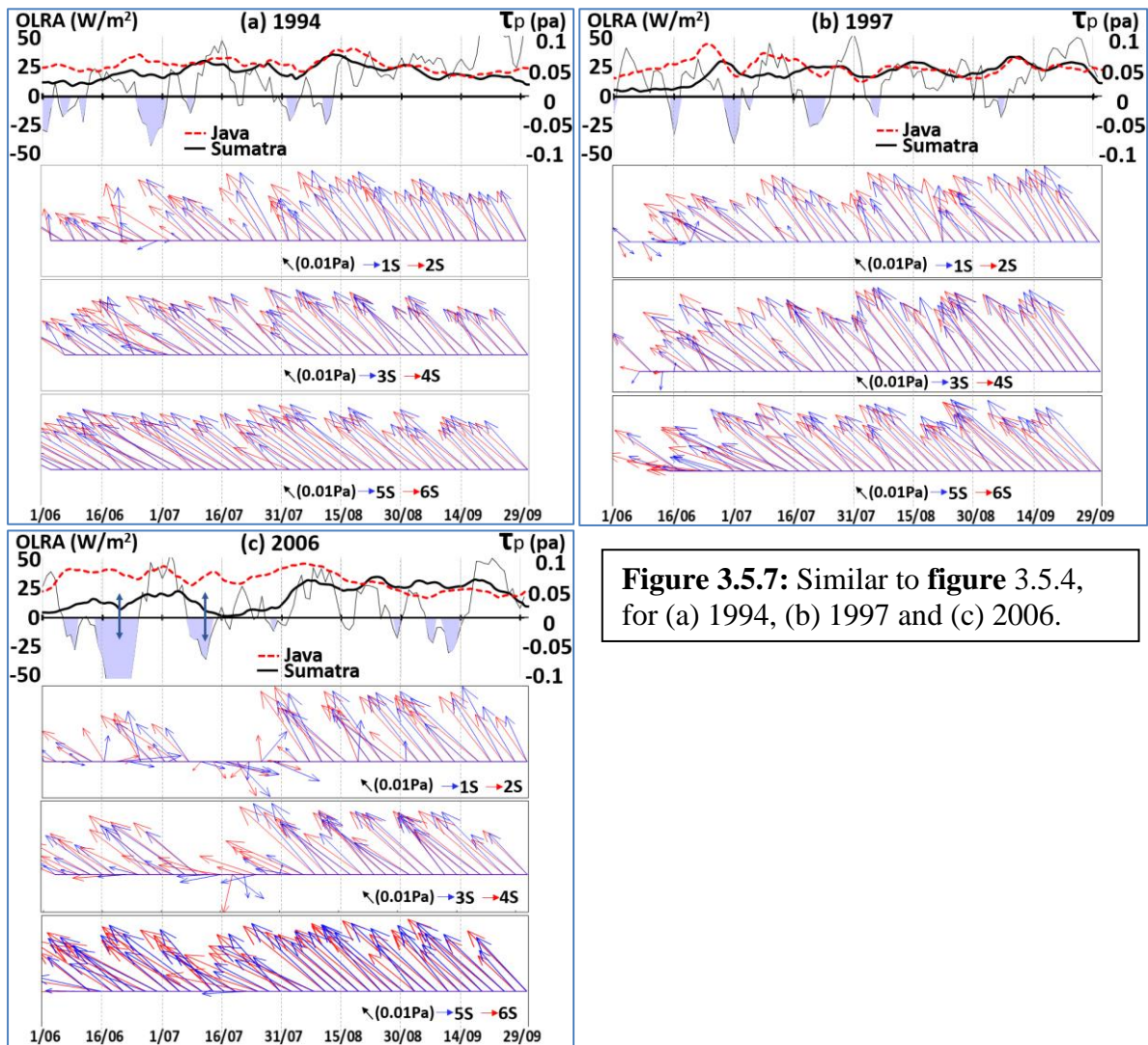


**Figure 3.5.7:** Similar to **figure 3.5.4**, for (a) 1994, (b) 1997 and (c) 2006.

### Surface winds of 1994

During the season 1994 the area average coast parallel stress of the southern Java coastal region shows strong values above 0.05 Pa from the advent of the season (**figure 3.5.7a**, top panel, red dashed line) and retains its strength throughout the season. As discussed previously, no “SETIO cyclone” is triggered during the season of 1994 which can alter the surface winds of the region; hence, surface winds at six

pinpoint locations along the southern Sumatra coastline gains seasonal “south-easterly” direction with strong wind speed values throughout the season (**figure 3.5.7a**, wind vector rolls of 1°S to 6°S, bottom three panels). As a result, the area average coast parallel stress of the southern Sumatra coastal region exhibits values above 0.03 Pa in June 1994 (**figure 3.5.7a**, top panel, thick black line) which later develops above 0.05Pa from July 1994 and stays above this value till the end of season.

### **Surface winds of 1997**

During the season 1997 the area average coast parallel stress of the southern Java coastal region shows strong values above 0.05 Pa from the advent of the season (**figure 3.5.7b**, top panel, red dashed line) and retains its strength throughout the season. The season of 1997 also suffers from suppressed atmospheric convection over the study region and no “SETIO cyclone” is triggered during the season of 1997 which can alter the surface winds of the region; hence, surface winds at six pinpoint locations along the southern Sumatra coastline also gains seasonal “south-easterly” direction with strong wind speed values throughout the season (**figure 3.5.7b**, wind vector rolls of 1°S to 6°S, bottom three panels). As a result, the area average coast parallel stress of the southern Sumatra coastal region exhibits values above 0.05Pa from 20th June 1997 onwards in **figure 3.5.7a** (top panel, thick black line) and stays above this value till the end of season.

### **Surface winds of 2006**

The area average coast parallel wind stress of the coastal Java region shows unique characteristics during initial stage of the season of 2006 with strong values near 0.1 Pa during 1st June to 15th August 2006 as displayed in **figure 3.5.7c** (top panel, red dashed line). Later in the season this strong value of coast parallel wind stress suffers minor down fall though it stays above 0.05Pa value throughout the season of 2006.

Strong convection is developed over the study region during the initial stage of the season of 2006 which triggers two strong atmospheric convective events over the region as shown in **figure 3.5.5c**, which consecutively triggers “SETIO cyclones” in the region on 21 June 2006 and 12 July 2006 (marked by arrows in **figure 3.5.5c**) and related surface circulation is shown in **figure 3.5.6**. As discussed above the “SETIO

cyclone” of 21 June 2006 cannot affect the surface winds of the southern Sumatra coastal region. As a result coast parallel winds are developed at six pinpoint location along the southern Sumatra coastline during late June and early July of 2006 as displayed in **figure 3.5.7c** (wind vector rolls of 1°S to 6°S, bottom three panels) and consecutively strong area average coast parallel stress is also developed in the region with value up to 0.05 Pa during late June and early July of 2006 (**figure 3.5.7c**, top panel, thick black line).

Later, during mid-July of 2006, the seasonal coast parallel winds of the southern Sumatra coastal region are disoriented at locations 1°S to 4°S (**figure 3.5.7c**, wind vector rolls of 1°S to 4°S) under the influence of the “SETIO cyclone” of 12 July 2006 (marked arrow in **figure 3.5.5c**, **figure 3.5.6**). This disorientation of the seasonal “south easterly” in mid-July of 2006 declines previously developed strong value of area average coast parallel stress of the southern Sumatra coastal region as displayed in **figure 3.5.7c** (top panel, thick black line).

Later, from August 2006 onwards the study region suffers from suppressed atmospheric convection and no “SETIO cyclone” is further triggered in the season; hence, surface winds at six pinpoint locations along the southern Sumatra coastline also gains seasonal “south-easterly” direction with strong wind speed values throughout the season (**figure 3.5.7b**, wind vector rolls of 1°S to 6°S, bottom three panels). As a result, the area average coast parallel stress of the southern Sumatra coastal region exhibits values above 0.05Pa from mid-June 1997 onwards in **figure 3.5.7a** (top panel, thick black line) and stays above this value till the end of season.

### **Summary of 1994, 1997 and 2006**

The suppressed phase of atmospheric convection over the study region followed by absence of “SETIO cyclone, is the suitable conditions for the seasonal “south easterly” winds to thrive along the southern Sumatra coastline, which further develops strong coast parallel wind stress in the region. The seasonal coast parallel winds along the southern Java coastline remains unaltered during any atmospheric convective episodes and strong coast parallel wind stress dominates in the region during boreal summer-fall of all the years discussed above.

### (c) “SETIO cyclones” of 2003, 2008 and 2012

In this subsection the atmospheric convective events are investigated during the boreal summer-fall of weak or aborted pIOD years 2003, 2008 and 2012. To investigate the characteristics of the atmospheric convective events and related surface circulation over the study region during boreal summer-fall 2003, 2008 and 2012; line plots of OLR anomaly average over the study region and zonal winds averaged over the eastern equatorial Indian Ocean are prepared and displayed in **figure 3.5.8** (identical to **figure 3.5.1**).

During June to September of 2003 three strong atmospheric convective episode is developed (**figure 3.5.8a**, blue shading) along with similar number of “westerly” events over the eastern equatorial Indian Ocean (**figure 3.5.8a**, orange shading). During the season of 2008, two atmospheric convective events are developed as displayed in **figure 3.5.8b** (blue shading) with similar number of episode of “westerlies” are also triggered (**3.5.8b**, orange shading).

The atmospheric convective episode of August 2003 and August 2008 exhibit a unique behaviour with longer than normal temporal coverage (three weeks), and each of this event comprises series of more than one individual event as evident in **figure 3.5.8** (a and b, blue shading). The atmospheric convective episode of July 2003 triggers from 10th July, and it has three consecutive short events which extends up to 31st August (**figure 3.5.8a** blue shading). While, episode of July 2008 also has three consecutive events which starts from 20th August and has temporal coverage up to 14th September 2008 (**figure 3.5.8b**, blue shading). During the season of 2012, four atmospheric convective episodes and related “westerly” events are developed as displayed in **figure 3.5.8c**.

To examine the synoptic structure of “SETIO cyclone” which are consecutively triggered during these atmospheric convective events, the streamline and wind vector maps of the study region are prepared at the days marked by arrows in **figure 3.5.8** and displayed in **figure 3.5.9**. The presence of the synoptic scale “SETIO cyclone” is evident in all maps of **figure 3.5.9**, which confirms the presence of the anomalous cyclonic circulation during mature phase of all atmospheric convective episodes of the study area (**figure 3.5.8**, blue shading and marked arrows). Each “SETIO cyclone” triggers “westerly” event over the eastern equatorial Indian Ocean as evident in **figure**

3.5.9 and **figure 3.5.8** (orange shading), and more importantly they also reverse the seasonal “south easterly” of the southern Sumatra coastline.

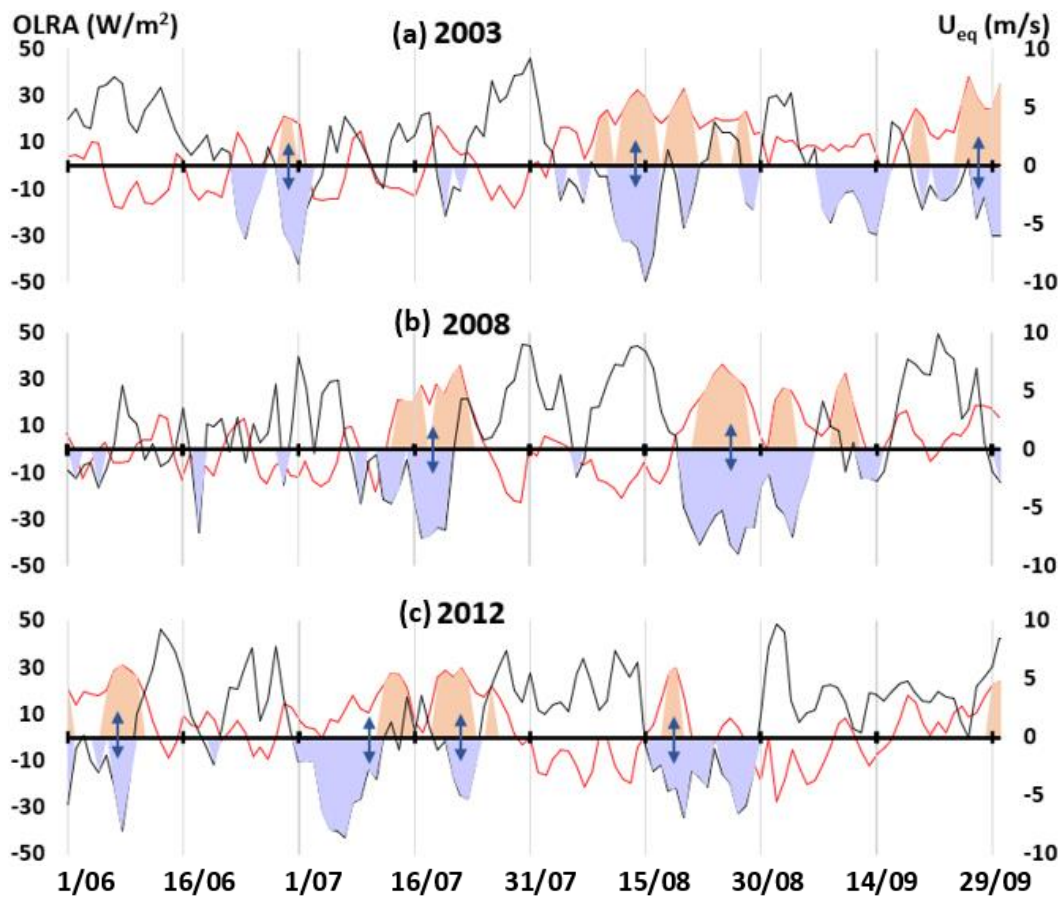


**Figure 3.5.8:** Time series of OLRA anomaly averaged over  $80^{\circ}$ - $110^{\circ}$ E,  $Eq-10^{\circ}$ S (black line and blue shading) and zonal wind speed averaged over  $70^{\circ}$ - $90^{\circ}$ E,  $5^{\circ}$ N- $5^{\circ}$ S (red line, orange shading). The values of OLR anomaly below  $-10 W/m^2$  and values of zonal wind speed above  $5 m/s$  are shaded, and arrows indicate deep convective event.

Further to decompose the characteristics of winds at multiple locations along southern Sumatra coastline and to visualise wind directions on daily timescale the wind vector roll plots are prepared and displayed in the bottom panels of **figure 3.5.10** (identical to **figure 3.5.4**) for six pinpoint locations along the southern Sumatra coastline (marked with number in **figure 3.5.3**). Ideal coast parallel orientation along southern Sumatra coastline is displayed in black arrow (in legends of each panel) and it is a unit vector as well with  $0.01 Pa$  value of wind stress.

Area averaged coast parallel stress for the coastal Java and southern coastal Sumatra regions (**figure 3.5.3**, red boxes) are derived from daily satellite wind fields

(CCMP V2) and displayed as daily time series in the top panel of **figure 3.5.10** (dashed red and solid black lines) along with the time series of area average daily values of OLR anomaly (in the same panel, blue shading and thin black line) over the study region (identical to **figure 3.5.4**). The blue shading in OLR anomaly line plots displays values below  $-10 \text{ w/m}^2$  which indicates atmospheric deep convective events. Locations of consecutively triggered “SETIO cyclones” during atmospheric deep convective event are marked by two-sided arrows in top panels of **figure 3.5.10** (retrieved from **figure 3.5.8**). The period of each plot of **figure 3.5.8** is identical to **figure 3.5.1** which is the boreal summer-fall. There are fewer atmospheric deep convective events are triggered during the boreal summer-fall of 2003 (three), 2008 (two) and 2012 (four) as evident in **figure 3.5.8**, compare to the seasons of 1998 (six), 2001 (seven) and 2004 (six) **figure 3.5.1**.

### **Surface winds of 2003**

During the season 2003 the area average coast parallel stress of the southern Java coastal region shows strong values above  $0.05 \text{ Pa}$  from the advent of the season (**figure 3.5.10b**, top panel, red dashed line) and retains its strength throughout the season as this region is outside the synoptic coverage of the SETIO cyclones of the season. The wind vectors at location  $5^\circ\text{S}$  and  $6^\circ\text{S}$  exhibits strong “south easterly” winds in the region mostly in the season (**figure 3.5.10a**, wind roll of  $5^\circ\text{S}$  to  $6^\circ\text{S}$ , bottom most panel) and they suffer minor disorientation from the “SETIO cyclones” of the season (**figure 3.5.10a**, wind roll of  $5^\circ\text{S}$  and  $6^\circ\text{S}$ ).

In the season of 2003, the wind vectors at locations  $1^\circ\text{S}$  to  $4^\circ\text{S}$  gain seasonal “south easterly” (coast parallel) direction during early June 2003 (**figure 3.5.10a**, wind roll of  $1^\circ\text{S}$  to  $4^\circ\text{S}$ ). As a result, the area average coast parallel stress of the southern Sumatra coastal region gains strong values in early June 2003 up to  $0.05 \text{ Pa}$  (**figure 3.5.10a**, top panel, thick black line). Later, the “SETIO cyclone” is triggered on 2nd July 2003 (**figure 3.5.10a** marked arrow, **figure 3.5.9**) and the wind vectors at locations  $1^\circ\text{S}$  to  $4^\circ\text{S}$  are disoriented during late June 2008, and consecutively the area average coast parallel stress of the southern Sumatra coastal region is also declined.

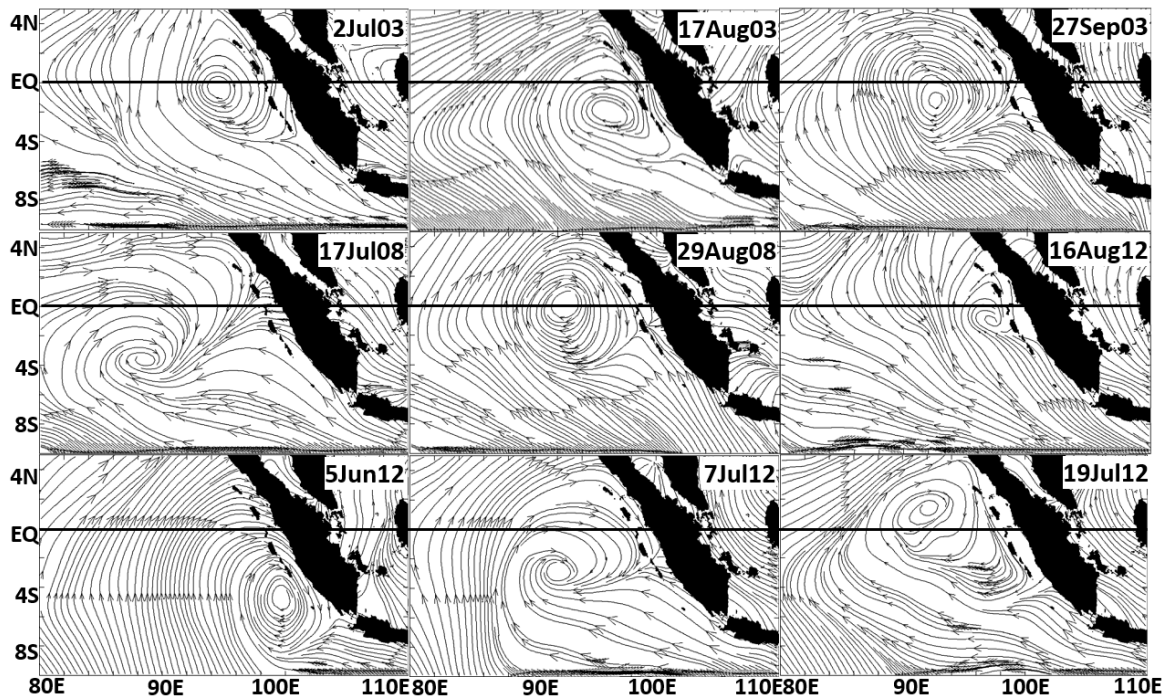


**Figure 3.5.9:** Maps display the surface circulation with the streamlines and wind vectors of the study region during the peak convective phase of 2003, 2008 and 2012.

Though, suddenly after this event, the wind vectors at locations  $1^{\circ}\text{S}$  to  $4^{\circ}\text{S}$  recover its seasonal “south easterly direction” from early July 2003 (**figure 3.5.10a**, wind roll of  $1^{\circ}\text{S}$  to  $4^{\circ}\text{S}$ ) and this situation persists up to mid-August 2003, which is the suppressed phase of atmospheric convection (**figure 3.5.8a**, **3.5.10a**, blue shading) and no “SETIO cyclone” is triggered during the period. Consecutively, area average coast parallel stress of the southern Sumatra coastal region recovers strong values rapidly and reaches to 0.1 Pa (**figure 3.5.10a**, top panel, thick black line) and it holds the strong values till 15th August 2003.

Later, longer than normal atmospheric convective event of mid-August 2003 (**figure 3.5.8a**) and consecutively triggered strong “SETIO cyclone” (**figure 3.5.9**, 17 August 2003) reverses the coast parallel winds at locations  $1^{\circ}\text{S}$  to  $4^{\circ}\text{S}$  (**figure 3.5.10a**, wind roll of  $1^{\circ}\text{S}$  to  $4^{\circ}\text{S}$ ). As a result, the area average coast parallel stress of the southern Sumatra coastal region is declined, and it shows near zero values on 17th August 2003 (**figure 3.5.10a** top panel, thick black line).

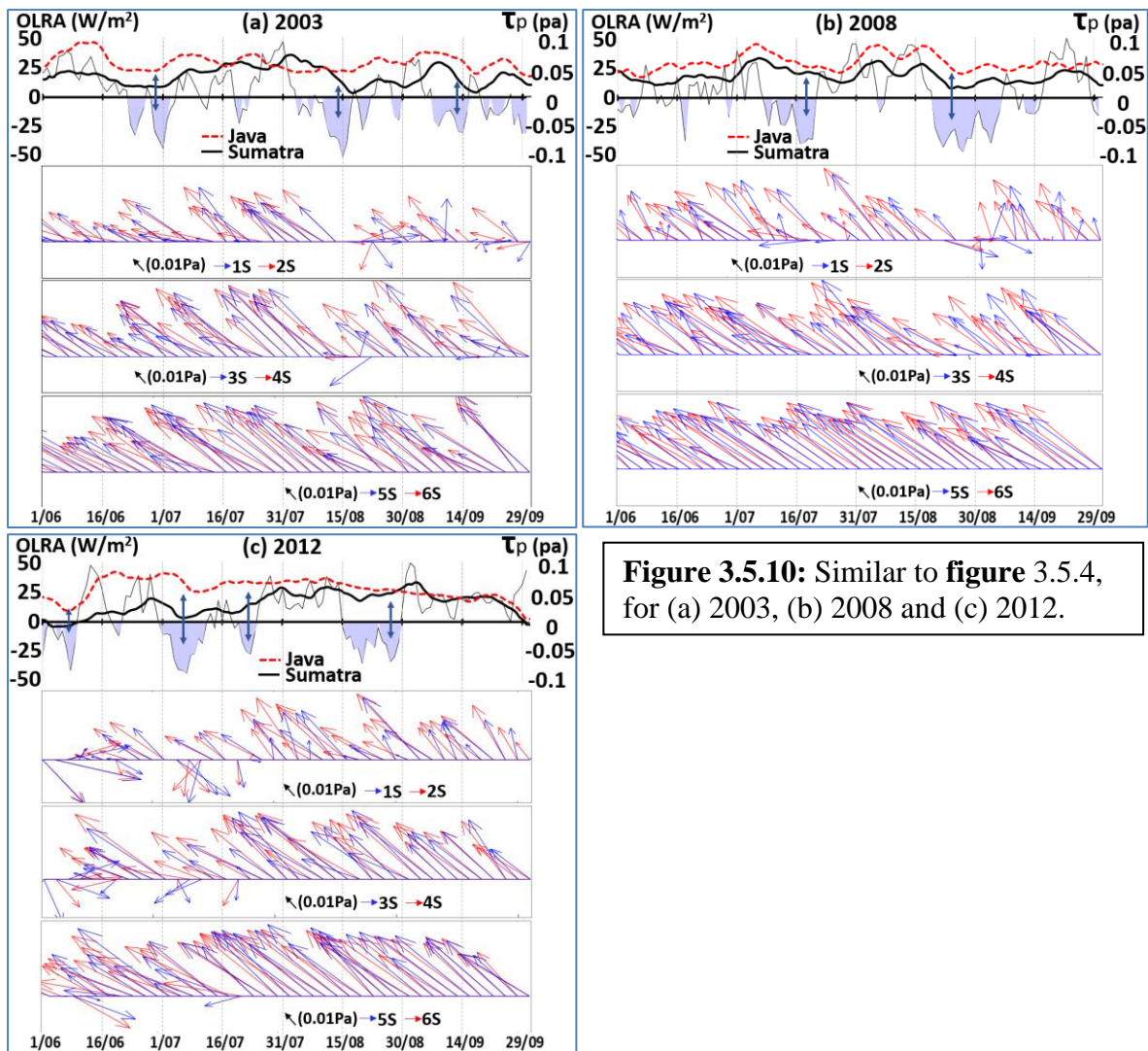


**Figure 3.5.10:** Similar to figure 3.5.4, for (a) 2003, (b) 2008 and (c) 2012.

Further, again the wind vectors at locations 1°S to 4°S gain the coast parallel direction temporarily during first half of the September 2003 (**figure 3.5.10a**, wind roll of 1°S to 4°S), and they are again disoriented under the influence of one more atmospheric convective event and consecutively triggered the “SETIO cyclone”, during second half of the September 2003 (**figure 3.5.8a** marked arrow, **figure 3.5.9** - 27th September 2003). Hence, area average coast parallel stress recovers strong values though temporarily during first half of the September 2003 (**figure 3.5.10a**, bottom panel) and it is again declined during second half of the September 2003 (**figure 3.5.8**, **figure 3.5.9** - 27th September 2003).

### Surface winds of 2008

During the season 2008 the area average coast parallel stress of the southern Java coastal region shows strong values above 0.05 Pa from the advent of the season (**figure 3.5.10b**, top panel, red dashed line) and retains its strength throughout the season as this region is outside the synoptic coverage of the SETIO cyclones of the season. The wind vectors at location 5°S and 6°S exhibits strong “south easterly” winds in the region mostly in the season (**figure 3.5.10b**, bottom most panel) and they have minor effect of the “SETIO cyclones” of the season.

The wind vectors of 2008 (**figure 3.5.10b**, bottom panel) at locations 1°S to 4°S gain seasonal “south easterly” (coast parallel) direction during early June till mid-July 2008 (**figure 3.5.10b**, wind roll of 1°S to 4°S), which are disoriented during mid-July under the influence of the “SETIO cyclone” triggered of 17th July 2008 (**figure 3.5.10b** marked arrow, **figure 3.5.9**). Consequently, the area average coast parallel stress of the southern Sumatra coastal region gains strong values in early June 2008 up to 0.01 Pa, which is temporarily destroyed under the influence of the “SETIO cyclone” during end of mid-July 2008 (**figure 3.5.10b**, top panel, thick black line).

Though, suddenly after this event of mid-July 2008, the wind vectors at locations 1°S to 4°S recover its seasonal “south easterly direction” (**figure 3.5.10b**, wind roll of 1°S to 4°S) and this situation persists up to end of August 2008, which is the suppressed phase of the atmospheric convection (**figure 3.5.8b**, **3.5.10b**). Hence, from mid-July 2008 area average coast parallel stress recovers strong values recovers the value and it holds strong values till 25th August 2008 and can reach to 0.6 Pa (**figure 3.5.10b**, top panel, thick black line).

A longer than normal atmospheric convective events during end of August 2008 (**figure 3.5.8b**, blue shading) and consecutively triggered strong “SETIO cyclone” (**figure 3.5.9**, 29 August 2008) reverses the coast parallel winds at locations 1°S to 4°S (**figure 3.5.10b**, wind roll of 1°S to 4°S). As a result, during end of August 2008 the area average coast parallel stress of the southern Sumatra coastal region is declined and it reaches near zero value from 25th August to 30th August 2008 (**figure 3.5.10b** top panel, thick black line).

Later in the season the wind vectors at locations 1°S to 4°S gain the coast parallel direction with very weak winds and scattered direction (**figure 3.5.10b**, wind roll of 1oS to 4oS) and cannot gain strong coast parallel winds. Hence, the area average coast parallel stress cannot recover to strong values and remains at weaker values below 0.03Pa (**figure 3.5.10b** top panel, thick black line).

### **Surface winds of 2012**

The area average coast parallel wind stress of the coastal Java region shows unique characteristics during initial stage of the season of 2008 which exhibits strong values of 0.1 Pa from 15th June to 1st August 2008 as displayed in **figure 3.5.10c** (top panel, red dashed line). Later in the season these strong values of coast parallel wind stress suffer minor down fall though it stays above 0.05Pa value throughout the season of 2008. The wind vectors at location 5°S and 6°S exhibits strong “south easterly” winds in the region mostly in the season (**figure 3.5.10b**, bottom most panel) and they have minor effect of the “SETIO cyclones” of the season.

The season of 2012 commences with the “SETIO cyclone” (**figure 3.5.10c**, marked arrow); hence, wind vectors at locations 1°S to 4°S are disoriented from seasonal “south Easterly” direction during early June till mid-June 2012 (**figure 3.5.10c**, wind roll of 1°S to 4°S). Later, the wind vectors at locations 1°S to 4°S along the southern Sumatra coastline gains seasonal “south easterly” direction from 15th June 2012 onwards (**figure 3.5.10 c**, wind roll of 1°S to 4°S), and as a result the area average coast parallel wind stress of the southern Sumatra coastal region develops to strong values from the second half of June 2012 (**figure 3.5.10 c**, top panel, black thick line).

Before the seasonal coast parallel wind vectors archive higher wind speed values, the “SETIO cyclone” is triggered on 7th July 2012 over the study region (**figure 3.5.10c** marked arrow and **figure 3.5.9**). Under the influence of this “SETIO cyclone”, the wind vectors at locations from 1°S to 4°S are disoriented (**figure 3.5.10 c**, wind roll of 1°S to 4°S). Once the phase of this “SETIO cyclone” ends, the next “SETIO cyclone” is triggered immediately after on 19th July 2012 in the region (**figure 3.5.10c** marked arrow and **figure 3.5.9**). Under its influence the wind vectors at locations from 1°S to 4°S are again disoriented as displayed in **figure 3.5.10c** (wind roll of 1°S to 4°S). Hence, the area average coast parallels wind streets of the southern Sumatra coastal

region cannot gain strong values and stays near zero values during entire July 2012 (**figure 3.5.10c**, top panel, black thick line), under the influence of two consecutive “SETIO cyclones” of the same month.

Later in August 2012 one more “SETIO cyclone” is triggered on 16th August 2012 (**figure 3.5.10c** marked arrow and **figure 3.5.9**). The synoptic structure of this “SETIO cyclone” indicates that it is weaker in strength and also not at the synoptic scale; hence, it cannot affect the seasonal winds along the southern Sumatra coastline as evident in the wind vectors of locations 1°S to 6°S in **figure 3.5.10c** (bottom panels). No other “SETIO cyclone” is triggered during August and September 2012, which is the suppressed phase of atmospheric convection (**figure 3.5.8c**). As a result, strong coastal parallel wind stress is developed in the southern Sumatra coastal region from end of July 2012 to end of September 2012 as displayed in **figure 3.5.10 c** (top panel, thick black line). At the end of the season (from October 2012 onwards) seasonal wind reversal of the tropical Indian Ocean reverses the “south easterlies” of the study region and coast parallel “north easterly” winds are withdrawn.

### **Summary of 2003, 2008 and 2012**

The suppressed phase of atmospheric convection over the study region followed by absence of “SETIO cyclone, is the suitable conditions for the season coast parallel winds along the southern Sumatra coastline to thrive. During this suppressed phase strong coast parallel stress is developed in the southern Sumatra coastal region, similar to the situation during the strong pIOD event years. Though, abruptly developed atmospheric convective phase over the study region destroys the coast parallel “south easterly” winds in the southern Sumatra coastal region by setting up “SETIO cyclone” over the study region. The seasonal coast parallel winds along the southern Java coastline remains unaltered during any atmospheric convective episodes and strong coast parallel wind stress dominates in the region during boreal summer-fall of all the years discussed above.

### 3.5.2 Ocean response to the cyclonic events

Wyrтки (1962) discovered the existence of coastal upwelling along the southern Java coastline. Later, Susanto *et al.* (2001) performed the detail analysis of the coastal upwelling mechanism along the southern Java and Southern Sumatra coastline. Previous studies agree on the fact that the SST anomalies within the coastal upwelling region can be explained by the classical Ekman theory of wind driven coastal upwelling. In late 2018, Kämpf and Kavi (2018) proposed the simple theory of coastal upwelling along coastline of finite horizontal extent, which can explain and evaluate the upwelling processes along a coast of finite length precisely. This sub section explores the seasonal coastal upwelling processes along the Java and Sumatra coastline with the help of this theory in the perspective of positive Indian Ocean dipole events.

#### **Schematics of the Java-Sumatra upwelling region**

As discussed in pervious sub section (3.5.1), seasonal winds along the southern Sumatra coastline is profoundly influenced by the atmospheric convective episodes of the region. The theory of coastal upwelling with a finite length (Kämpf and Kavi, 2018) can be utilised to explain the coastal upwelling processes of the region precisely by dividing the entire southern Java and Sumatra coastline into the individual segments, which is under the influence of highly varying wind conditions of an extended coastline. The contribution of upwelling within each segment from wind condition of that segment can be calculated. Later by adding upwelling value of all the segments together a total upwelling response along the entire coastline can be calculated.

Identical to the original proposal in the paper of this theory (Kämpf and Kavi, 2018), I consider the nine segments of the southern Java and Sumatra coastline, and each segment is considered to calculate wind driven upwelling effects within it. The segments are marked with number in **figure 3.5.11** where corresponding number of each location displays the geographical latitudes as well (1°S to 9°S). Red boxes in the region (displayed in **figure 3.5.11**) is to extract the area average sea surface temperature anomalies.

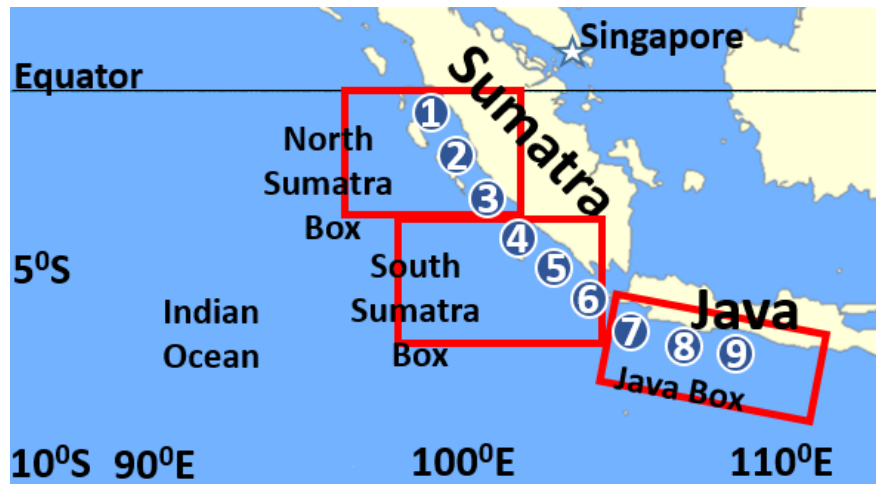


**Figure 3.5.11:** Schematics of study region, where red box regions are used to calculate area average MLD (m),  $\Delta\rho$  ( $\text{kg/m}^3$ ) and SST ( $^{\circ}\text{C}$ ). Pinpoint location with number are used to calculate coastal upwelling index where number of each location indicates southern geographical latitude as well.

#### (a) Mixed layer properties

The theory of coastal upwelling proposed by Kämpf and Kavi (2018) requires subsurface stratification and mixing scheme of the subsurface water in the region precisely. The study region (the SETIO) suffers from the scarcity of subsurface observations and data in the last century with no moorings in the region and no ARGO coverage until 2005. Advent of ARGO coverage in the region provide the monthly characteristics of the subsurface water of the region from 2005 onwards. I derived the monthly area average values of mixed layer depth (MLD) using Holte (2017) algorithm for three different regions marked by red boxes in the **figure 3.5.11** and displayed in **figure 3.5.12a**. The difference between density of layer at 100m depth and MLD is also derived and displayed in **figure 3.5.12b**.

The mixed layer is typically determined using subsurface temperature and density profiles. As an accurate knowledge of the mixed layer is important to many studies and this study as well. MLD climatology aims to capture the variability of the mixed layer on monthly and greater time scales.

Holte et al. (2017) presented a data set from of a global climatology and database of mixed layer properties computed from nearly 1,250,000 delayed-mode and real-time Argo profiles collected from 2000 to present. Holte et al. (2017) considered the mixed layer as the uniform surface layer that is assumed to owe its homogeneity to turbulent mixing. The climatology provides estimates of monthly mixed

layer depth (mean, median, maximum, and standard deviation) and properties (mean density, temperature, and absolute salinity) on global 1o gridded maps. These fields are averages over the entire Argo record, producing a representative annual cycle of monthly mixed layer properties. Also provided is a database of the mixed layer properties, including the location and date, of every individual Argo profile used to assemble the climatology.

The individual profile output can be used to construct time series of mixed layer properties in specific regions of interest. The climatology is calculated with a hybrid algorithm for detecting the MLD (Holte and Talley, 2009) as well as with standard threshold criteria (de Boyer Montégut et al., 2004); the MLDs calculated by the two methods are referred to as algorithm and threshold MLDs. The climatology and database are updated annually to include new profiles; these data sets, as well as the algorithm's MATLAB code, are available online at <http://mixedlayer.ucsd.edu>.

The primary advantage of Holte's (et al., 2017) climatology is that it uses a more accurate method for identifying the MLD, as will be shown by a "quality index" analysis. It also incorporates more density profiles than have been available in previous climatology.

The MLD values in upper box region (**figure 3.5.11**) of southern coastal Sumatra has long-term (2005-2016) average value of 48.86m with standard deviation of 11.1 during boreal summer-fall (June to September). The MLD values in lower box region (**figure 3.5.11**) of southern coastal Sumatra has long-term (2005-2016) average value of 42.61m with standard deviation of 7.8. The MLD values in Java box region (**figure 3.5.11**) has long-term (2005-2016) average value of 39.52m with standard deviation of 4.4.

As we discussed previously, the study region suffers from the scarcity of sub surface observations. Though the presence of ARGO in the region from 2005 onwards, it was limited to one or two profile in a month in the southern Java-Sumatra upwelling region till 2010. The STD values of each MLD and density difference is smaller with range of 4-12 and 0.5-0.8, hence I accepted long term average values of MLD and  $\Delta\rho$  in the theoretical calculation of coastal upwelling. I accepted MLD = 45m considered as  $h_0$  according to the theory discussed above, and  $\Delta\rho = 2.28 \text{ kg/m}^3$ , for

the study region, theoretical coastal upwelling index is calculated using these subsurface properties. The accepted value of MLD falls within the range of STD of all the three boxed regions as discussed in previous paragraph.

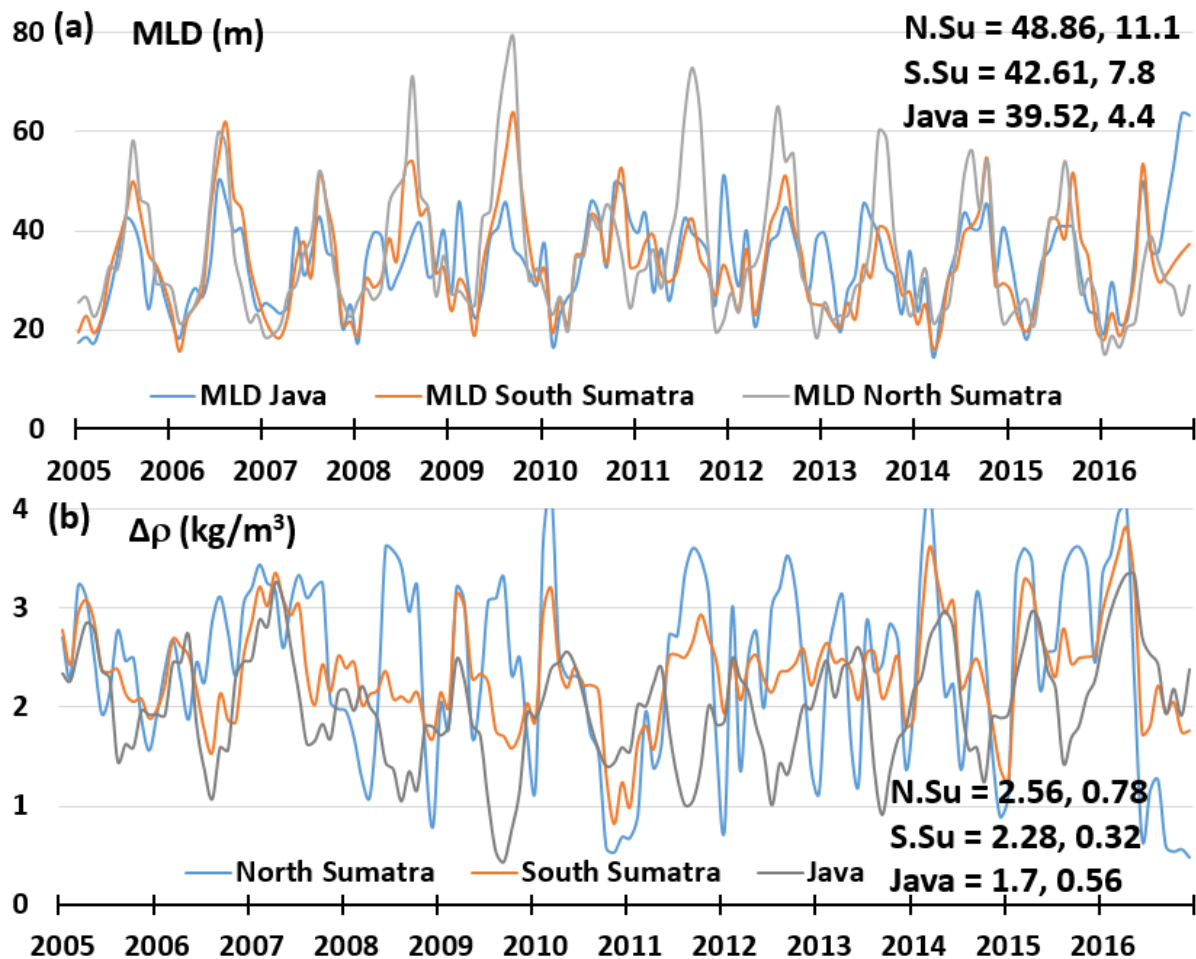


**Figure 3.5.12:** Monthly time series of area average values in red box regions of figure 3.5.11. Panel (a) displays mixed layer depth and panel (b) displays density difference between mixed layer density to density at 100 m depth. The values written on each plot (right-side) indicates boreal summer-fall long term average (2005-2016) and STD (2005-2016).

The permanent warm pool of the Indian Ocean is anchored on the eastern coast; hence, the eastern Indian Ocean is characterised by warm surface water and deep thermocline. The permanent salinity dipole persists in the equatorial Indian Ocean, as the eastern equatorial Indian Ocean can be characterised as the surface fresh water with continuous fresh water input from the Bay of Bengal and local year-round precipitation, while the western Indian Ocean suffers from lack year-round fresh water input and hence it is characterised by the saline water. Previous studies with their modelling efforts in the tropical Indian Ocean suggest that, strong eastward equatorial

“Wyrтки Jets” injects the denser and more saline water of the Arabian Sea straight to the sub-surface layer of similar density in the eastern equatorial Indian Ocean (Masson *et al.*, 2002). This process creates sub-surface salinity stratified “barrier layer” in the eastern equatorial Indian Ocean, which separates the cold thermocline water from the surface mixed layer (Sprintall and Tomczak, 1992; Masson *et al.*, 2002, Qu and Meyers, 2005). The barrier layer modulates the mixing of heat and momentum exchange between surface mixed layer and the thermocline, which was studied previously (Masson *et al.*, 2002, 2004; Qiu *et al.*, 2012). Though, the scarcity of subsurface data in the region with considerable temporal resolution, makes the actual effects of the barrier layer on turbulent mixing and heat exchange ambiguous.

### **(b) Theory of coastal upwelling along finite length coast**

I consider the nine segments of the southern Java and Sumatra coastline as displayed in **figure 3.5.11**, and according to the theory of coastal upwelling mentioned above each segment has initial value of mixed layer depth which has symbol  $h_0$ . As mentioned above I considered value of  $h_0 = 45\text{m}$  for each segment. The theory calculates the vertical displacement of the MLD values ( $h_0$ ) for each segment under the influence of the coastal winds, which represents vertical movement of the thermocline. As explained in the original paper (Kämpf and Kavi, 2018) the vertical displacement of the thermocline accumulates along the coasts in the direction of Kelvin wave propagation and hence cumulative change in MLD values ( $h_0$ ) is defined as  $\Delta h_i$ . I am using here the same equations of the  $\Delta h_i$  to calculate the cumulative change in  $h_0$  at each segment where  $i$  indicates the number of each segment from 1 to 9 as displayed in **figure 3.5.11**.

The theory suggests that when  $\Delta h_i > h_0$  it is favourable conditions for upwelling to develop at that segment ( $i$ th) of the coastline. Hence, the  $\Delta h_i$  values reveal the point of full upwelling along the finite length coastline. I calculated the daily  $\Delta h_i$  values for each segment of **figure 3.5.11** along the southern Java and Sumatra coastline from daily wind satellite wind fields for the entire study period (1988-2016). The daily plots of  $\Delta h_i$  for selected nine years discussed in previous sub section 3.5.1 is prepared and displayed in **figure 3.5.13**, **3.5.14** and **3.5.15** for event analysis in positive IOD events perspective. Daily area average values of SST anomalies (SSTA) over the red boxes of **figure 3.5.11** is also derived from NOAA OI data set and displayed in **figure 3.5.13**

for comparison. The daily plots of  $\Delta h_i$  and SSTA for all other years in the study period (1988-2016) is displayed in Appendix section for the reference.

Nine individual segments are defined in **figure 3.5.11** to calculate the local wind effect of each segment on coastal upwelling precisely. According to the theory,  $\Delta h_i$  represents the cumulative values; hence, I displayed the plot of  $\Delta h_i$  for only three individual segments (3°S, 6°S and 9°S) for ease of explanation, as these three segments satisfactorily demonstrate the cumulative coastal upwelling of the entire coastline. The selected three individual segments (3°S, 6°S and 9°S) also represent three red box regions of **figure 3.5.11**, which are used to derive the area average SSTA values. The resultant  $\Delta h_i$  values have higher variation and sharp peaks in daily values; hence, 7 days running mean from the centre is applied to the  $\Delta h_i$  values and displayed in **figures 3.5.13, 3.5.14 and 3.5.15 (a) to (c)**. Similar seven days running mean from the centre treatment is applied to the daily SST anomaly values and displayed in **figures 3.5.13, 3.5.14 and 3.5.15 (d) to (e)**. Initial value of the MLD  $h_0 = 45\text{m}$  is marked by horizontal black line in each line plot of  $\Delta h_i$  to visually interpret the criteria  $\Delta h_i > h_0$ , which reveals the region of full upwelling and suppressed upwelling.

According to the theory of classical upwelling the coast parallel wind stress can trigger the coastal upwelling in the region. The wind conditions along the southern Java and Sumatra coastline is discussed in previous section 3.5.1, which suggests that the winds in southern coastal Java region are coast parallel during the boreal summer-fall of all years in the study period (1988-2016). While the winds along the southern Sumatra coastline are heavily influenced by the convective coupled anomalous surface circulation over the study region. Winds conditions at six pinpoint locations along the southern Sumatra coastline during boreal summer-fall are displayed in **figures 3.5.4, 3.5.7 and 3.5.10**. The source of wind variability in the region was also discussed in detail in section 3.5.1, which suggest that the “SETIO cyclones” damage the seasonal coast parallel winds along the southern Sumatra coastline. The position of the “SETIO cyclones” in time domain is also displayed by two sided arrows in **figures 3.5.13, 3.5.14 and 3.5.15 (a) to (c)** for ease of explanation (adopted from **figures 3.5.4, 3.5.7 and 3.5.10**).

### (c) Neutral IOD event years 1998, 2001 and 2004

The daily plots of  $\Delta hi$  and SSTA for 1998, 2001 and 2004 are displayed in **figure 3.5.13**, and these years represent the neutral IOD conditions. **Figure 3.5.11** (a) to (c) displays  $\Delta hi$  values for boreal summer-fall, where yellow shades represents  $\Delta hi$  at 3°S, blue shades represents  $\Delta hi$  at 6°S and grey shades represents  $\Delta hi$  at 9°S. **Figure 3.5.11** (d) to (e) displays SST anomaly values for red box regions of **figure 3.5.11**.

#### Ocean response in 1998

During the season of 1998, full upwelling condition cannot develop along the entire southern Sumatra coastline (up to 6°S) as displayed in **figure 3.5.13a** ( $\Delta hi@3^{\circ}S < 50$  and  $6^{\circ}S < 50$ ). During early phase of the season (June and July 1998) entire southern Sumatra coastline (up to 6°S) shows zero or negative values of  $\Delta hi$  as shown in **figure 3.5.13a**, as a result of reversed of zero value of coast parallel wind stress in the region (**figure 3.5.4a**). The primary reason behind this suppressed upwelling throughout the season at entire southern Java-Sumatra coastline is weak coast parallel wind stress in the region (**figure 3.5.4a**, top panel). Year 1998 was recorded as strong negative phase of the IOD conditions, where higher than normal SST was recorded in the SETIO region. Which consecutively reinforces the strong convection in the region and intensified the SETIO cyclone activities in the region during boreal summer fall, which is responsible for low coast parallel stress in the region.

During June and July 1998, the southern Java coastline cannot reach to the full upwelling values (**figure 3.5.13a**,  $\Delta hi@9^{\circ}S < 50$ ). The primary reason behind the suppressed upwelling along the southern Java coastline is late arrival of seasonal “south easterlies” in the region as evident in the line plot of area average coast parallel stress along the Java coastline (**figure 3.5.4**, top panel, red dashed line). Later in the season, during August and September 1998, coast parallel wind stress gain the strong values in the region along with strong coast parallel stress at locations 5°S and 6°S (**figure 3.5.4**, bottom most panel); hence, under the influence strong coast parallel wind stress from locations 5°S to 9°S the southern Java coastline exhibits the full upwelling conditions during August and September 1988 as displayed in **figure 3.5.13a** ( $\Delta hi@9^{\circ}S > 50$ ).

During late September 1998 coast parallel stress is destroyed at southern Sumatra coastline (**figure 3.5.4**, 3.5.2a) and consecutively upwelling favourable

conditions at southern Java coastline is withdrawn, as displayed in **figure 3.5.13a** where  $\Delta\text{hi}@9^{\circ}\text{S} < 50$  during late September 1998. The reason behind the withdrawal of upwelling favourable conditions along the southern Java coastline is that the  $\Delta\text{hi}$  values are cumulative; hence, under the influence of weak or negative values of  $\Delta\text{hi}$  at precursor locations (Southern Sumatra coastline) upwelling along Java coastline cannot develop, though local southern Java coast parallel wind stress exhibits strong values.

Lack of upwelling favourable conditions in the southern Sumatra coastal region cannot alter the surface warm water of the region, as a result the SST anomalies of the entire southern Sumatra and southern Java coastal regions (all three-box region of **figure 3.5.11**) shows positive values as displayed in **figure 3.5.13d** and indicates presence of warmer than normal surface waters in the region. The full upwelling conditions along the southern Java coastline during second half of the season (**figure 3.5.13a**, grey shading) cannot create negative SST anomaly in the region. The possible reason behind this situation is, the continuous flow of warm water in the region from the equatorial warm pool through south equatorial current (or south equatorial counter current, SECC; Schott *et al.*, 2009) and from the Indonesian throughflow (Sprintall *et al.*, 2009); hence, upwelling conditions of the smaller region cannot exhibit its signature on the surface water.

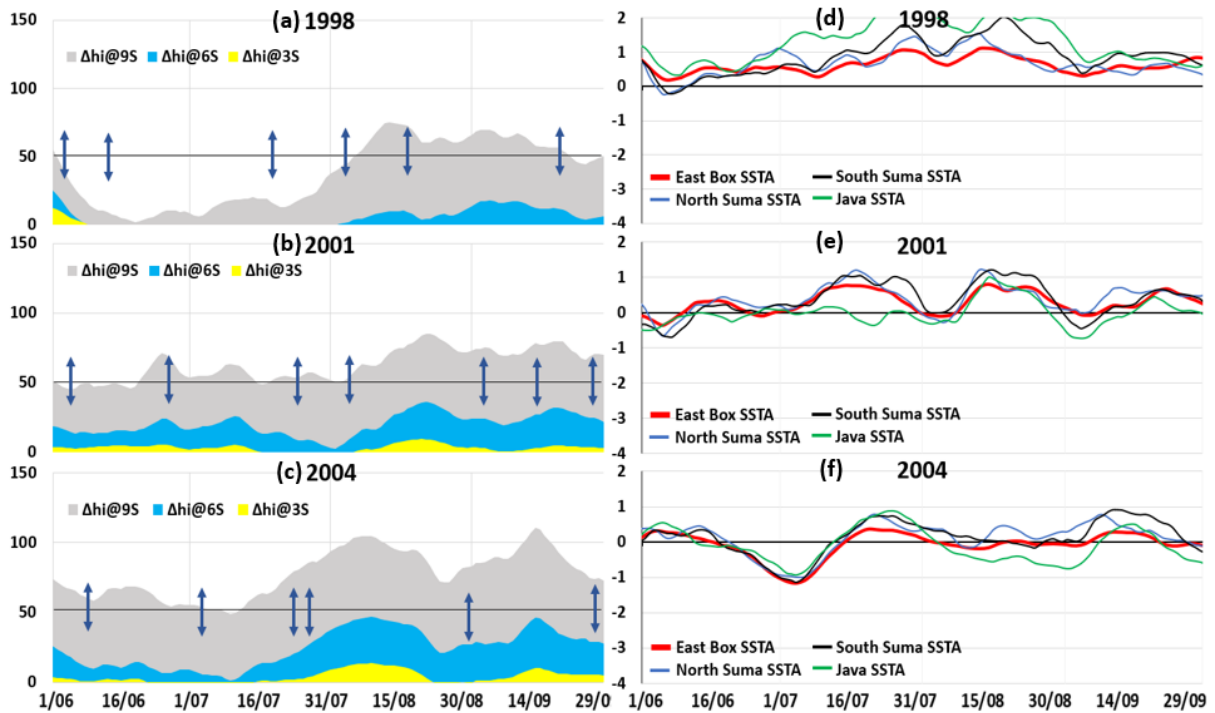


**Figure 3.5.13:** Panels (a) to (c) represents daily time series of  $\Delta h_i$  (m) at locations 3S, 6S and 9S marked in **figure 3.5.8**, black line indicates long term mixed layer value and two-sided arrows indicates deep convective events adopted from **figure 3.5.1**. Panels (d) to (e) represents SST anomalies ( $^{\circ}\text{C}$ ) over boxed region of **figure 3.5.8**.

### Ocean response in 2001

During the season of 2001, full upwelling cannot develop along the entire southern Sumatra coastline (up to  $6^{\circ}\text{S}$ ) as displayed in **figure 3.5.13b** ( $\Delta h_i@3^{\circ}\text{S} < 50$  and  $\Delta h_i@6^{\circ}\text{S} < 50$ ), as a result of weak coast parallel wind stress in the region (**figure 3.5.4b**). During late July and early August 2001, entire southern Sumatra coastline (up to  $6^{\circ}\text{S}$ ) shows near zero values of  $\Delta h_i$  as shown in **figure 3.5.13b**, as a result of reversed of zero value of coast parallel wind stress in the region (**figure 3.5.4b**).

In the season of 2001, strong coast parallel wind stress is developed along southern Java coastline from the advent of the season, consecutively full upwelling conditions are also triggered from 20th June 2001 as displayed in **figure 3.5.13b** ( $\Delta h_i@9^{\circ}\text{S} > 50$ ), which almost persists till the end of season of 2001. Though, from end of July till early August 2001 the coast parallel stress in the southern Sumatra coastal region suppresses to near zero values (**figure 3.5.4b**), consecutively upwelling favourable conditions along southern Java coastline has minor downfall during this

period as displayed in **figure 3.5.13b**( $\Delta hi@9^{\circ}S > 50$ ) because the  $\Delta hi$  values are cumulative.

Lack of upwelling favourable conditions in the southern Sumatra coastal region cannot alter the surface warm water of the region, as a result the SST anomalies of the entire southern Sumatra and southern Java coastal regions (all three-box region of **figure 3.5.11**) shows positive values as displayed in **figure 3.5.13e** and indicates presence of warmer than normal surface waters in the region. The full upwelling conditions along the southern Java coastline during second half of the season (**figure 3.5.13b**, grey shading) cannot create negative SST anomaly in the region. The possible reason behind this situation is, the continuous flow of warm water in the region from the equatorial warm pool through south equatorial current (or south equatorial counter current, SECC; Schott *et al.*, 2009) and from the Indonesian throughflow (Sprintall *et al.*, 2009); hence, upwelling conditions of the smaller region cannot exhibit its signature on the surface water.

Although, southern Java coastline displays two abrupt pulse of negative values of SST anomaly (**figure 3.5.13e**, green line) along with SST anomaly of all other boxes during early period of August and September 2001 in **figure 3.5.13e** (red, blue and black lines), which indicates the coastal upwelling Kelvin waves activity in the region. The Kelvin waves activity is discussed in next sub section 3.5.2c.

#### **Ocean response in 2004**

During the season of 2004, full upwelling cannot develop along the entire southern Sumatra coastline (up to  $6^{\circ}S$ ) as displayed in **figure 3.5.13c** ( $\Delta hi@3^{\circ}S < 50$  and  $\Delta hi@6^{\circ}S < 50$ ), as a result of weak coast parallel wind stress in the region (**figure 3.5.4c**). Moreover, during the early season of 2004 entire southern Sumatra coastline (up to  $6^{\circ}S$ ) shows low values of  $\Delta hi$  from June to July 2004 (**figure 3.5.13b**, blue and yellow shading). The suppressed phase of the atmospheric convection developed over the region from late July till late August 2004 (**figure 3.5.1c**), during this phase southernmost location of the Sumatra coastline ( $6^{\circ}S$ ) rises near the full upwelling conditions as displayed in **figure 3.5.13b** (blue shading,  $\Delta hi@6^{\circ}S > 50$ ), though this full upwelling conditions at  $6^{\circ}S$  is destroyed by the “SETIO cyclone” of 24th August 2004 which reverses the coast parallel winds of the region (**figure 3.5.2b**, **figure 3.5.4b**).

In the season of 2001, strong coast parallel wind stress is developed along southern Java coastline from the advent of the season, consecutively full upwelling conditions are also triggered in the region as displayed in **figure 3.5.13b** (grey shading,  $\Delta\text{hi}@9^{\circ}\text{S} > 50$ ), which almost persists till the end of season of 2001. The upwelling favourable conditions are stronger in the season at southern Java coastline.

Entire southern Sumatra and Java coastline display a strong negative pulse of SST anomaly during early July 2004, which indicates the coastal upwelling Kelvin waves activity in the region, which will be discussed in sub-section 3.5.2c. For rest of the season, lack of upwelling favourable conditions in the southern Sumatra coastal region cannot alter the surface warm water conditions of the region, as a result the SST anomalies of the regions (all three-box region of **figure 3.5.11**) shows positive values as displayed in **figure 3.5.13f**. Later, during August 2004 the southern Java coastline shows minor negative values of SST anomaly (**figure 3.5.13e**), which is reverted to positive values later.

The full upwelling conditions along the southern Java coastline during the season (**figure 3.5.13b**, grey shading) cannot create negative SST anomaly in the region. The possible reason behind this situation is, the flow of warm water in the region through south equatorial current (or south equatorial counter current, SECC; Schott *et al.*, 2009) and from the Indonesian throughflow (Sprintall *et al.*, 2009) as discussed previously.

#### **Summary of Ocean response in 1998, 2001 and 2004**

The coast parallel winds along the southern Java coastline remains unaltered during the “SETIO cyclone” phases, as a result strong coast parallel wind stress predominates in the region during boreal summer-fall. Hence, the intraseasonal and interannual variation of wind stress along the Java coastline are related to other regional and global climatic phenomena.

Though, according to the theory of coastal upwelling along finite coast, to develop a full upwelling condition at certain segment of coastline strong upwelling favourable winds should present at precursor locations. Which means, to develop a full upwelling condition along the Java coastline sufficient preconditioning is necessary

along the southern Sumatra coastline and the southern Java coastline is not independent in the case of upwelling.

The series of “SETIO cyclones” triggered over the study region during boreal summer-fall, disorients the seasonal “south easterly” winds along the southern Sumatra coastline several times, a result the substantial coast parallel wind stress cannot develop in the region. Hence, during that time the upwelling cannot develop in the region. Moreover, weak coast parallel stress along the southern Sumatra region cannot provide sufficient preconditioning to the southern Java coastline, consecutively the southern Java coastline suffers weak upwelling conditions as well during several instances in the season. The lack of full upwelling conditions in the region and presence of equatorial surface warm water makes the sea surface temperature of the southern Java-Sumatra coastal region warmer.

The coast parallel wind stress along the southern Sumatra coastline can achieve temporary strong values, though only during the absence of “SETIO cyclones”. For example, in boreal summer-fall of 2004, during August no “SETIO cyclone” is triggered for the entire month; hence, coast parallel winds are developed along the southern Sumatra coastline temporarily. Consequently, southern Sumatra coastline at 6°S exhibits near full upwelling condition and southern Java coastline exhibit strong upwelling conditions. Similar, brief episode of strong upwelling at 6°S and 9°S is evident in mid-September 2004. During these brief episodes of strong upwelling signature southern Java coastline exhibit temporary negative SSTA values, though SSTA of the southern Sumatra coastline stays positive or natural values.

Hence, it can be concluded that “SETIO Cyclones” triggered over the study region during boreal summer-fall destroys the upwelling favourable conditions along the southern Sumatra coastline profoundly, and during certain consecutive episodes of the “SETIO cyclone” the destructive effect is so strong the it destroys the coastal upwelling along Java coastline remotely from the cumulative effect.

#### **(d) Positive IOD event years 1994, 1997 and 2006**

The daily plots of  $\Delta h_i$  and SSTA for 1994, 1997 and 2006 are displayed in **figure 3.5.14**, and these years represent the strong positive phase of IOD conditions. **Figure 3.5.14** (a) to (c) displays  $\Delta h_i$  values for boreal summer-fall, where colour shading is

similar to which explained in previous sub section (c). **Figure 3.5.14** (d) to (e) displays SST anomaly values for red box regions of **figure 3.5.11**.

### **Ocean response in 1994**

Entire season of 1994 exhibits suppressed atmospheric convection phase over the study region (**figure 3.5.5a**) and consecutively no “SETIO cyclone” is triggered; hence, there is no other atmospheric interference to the seasonal “south easterly” winds along the southern Java and Sumatra coastline. As a result, strong upwelling favourable winds are developed along southern Sumatra coastline (**figure 3.5.7a**) from the advent of the season and it persists till the end season of season. Consecutively strong upwelling favourable condition is developed at the southern Sumatra coastline from the advent of the season which reaches at full upwelling conditions during late June 1994 and it persists till end of September 1994 as displayed in **figure 3.5.14a** (blue shading,  $\Delta\text{hi}@6^{\circ}\text{S}>50$ ). As a result of strong upwelling favourable winds along southern Java coastline (**figure 3.5.7a**) and strong upwelling favourable conditions at the precursors locations (**figure 3.5.14a**, at  $6^{\circ}\text{S}$ , yellow shading) full upwelling condition is developed in the region from the advent of the season and it persists till the end season of season as displayed in **figure 3.5.14a** (grey shading,  $\Delta\text{hi}@9^{\circ}\text{S}>50$ ).

Rarely developed strong upwelling condition along the southern Sumatra coastline triggers an upwelling jet transient to the South Java Current (SJC) (Sprintall *et al*, 1999) and suggested by Kämpf and Kavi, 2018, which they called the “South East Sumatra Current (SESC)” (**figure 6a** of Kämpf and Kavi, 2018). This rarely triggered SESC blocks the south equatorial current (or south equatorial counter current, SECC; Schott *et al.*, 2009) and blocks the flow of equatorial warm water to southern Sumatra and Java coastal region. Hence, the strength of the SJC is also increased and strong northwards horizontal advection of upwelled cold-water triggers strong negative SST anomaly in the entire box of southern Java (**figure 3.5.14d**, green line) from the advent of the season. The SST anomaly of Southern Java coastline displays negative values below  $-1^{\circ}\text{C}$  from the advent of the season as displayed in **figure 3.5.14d** (green line), which gains strong negative values from late June till early-September 1994 with values below  $-2^{\circ}\text{C}$ .

Full upwelling conditions at southern Sumatra (at 6oS) from late June 1994 (blue shading, **figure 3.5.14a**) along with transient the SJC and the SESC intensify northward advection of upwelled cold water; hence, SST anomaly plot of southern box of Sumatra coastline (**figure 3.5.11**) exhibits negative values below  $-1^{\circ}\text{C}$  for the entire season as displayed in **figure 3.5.14d** (black line). Later, from second half of the July till early September 1994 the SST anomaly of southern box of Sumatra coastline stays below  $-2^{\circ}\text{C}$  (**figure 3.5.14d**, black line).

Locations  $1^{\circ}\text{S}$  to  $3^{\circ}\text{S}$  along the Southern Sumatra coastline (**figure 3.5.11**) cannot reach to full upwelling conditions in the season (**figure 3.5.13a**, yellow shading). Though, under the influence of northward progress of negative SST anomaly through horizontal advection and the intensified SESC, northern box of the coastal Sumatra region exhibits values SST anomaly values below  $-1^{\circ}\text{C}$  from late August 1994, and it reaches below  $-2^{\circ}\text{C}$  in September 1994 as displayed in **figure 3.5.14d** (blue line). Moreover, north-eastward progress of intensified the SESC and advection of cold upwelled water in the region develops strong cold-water wedge extending westward in the eastern box of IOD events as displayed in **figure 5c** and **6a** of the original paper of Kämpf and Kavi, 2018. Hence, SST anomaly of the entire eastern box of the DMI index shows negative SST anomaly values at  $-1^{\circ}\text{C}$  and below from late June till the end of the season, with cumulative effect of strong negative SST anomaly of all three individual boxes discussed here.

### **Ocean response in 1997**

The season of 1997 also suffers suppressed atmospheric convection phase over the study region (**figure 3.5.5b**) and consecutively no “SETIO cyclone” is triggered during the season; hence, strong seasonal “south easterly” winds persist along the southern Sumatra region for the entire season (**figure 3.5.7b**). As a result, Strong upwelling favourable condition is developed at the southern Sumatra coastline from late June 1997 and it persists till end of September 1997 as displayed in **figure 3.5.14b** (blue shading,  $\Delta\text{hi}@6^{\circ}\text{S}>50$ ). As a result of strong upwelling favourable winds along southern Java coastline (**figure 3.5.7b**) and strong upwelling favourable conditions at the precursors locations (**figure 3.5.14b**, at  $6^{\circ}\text{S}$ , yellow shading) full upwelling condition is developed in the region from the advent of the season and it persists till the end season of season as displayed in **figure 3.5.14b**(grey shading,  $\Delta\text{hi}@9^{\circ}\text{S}>50$ ).

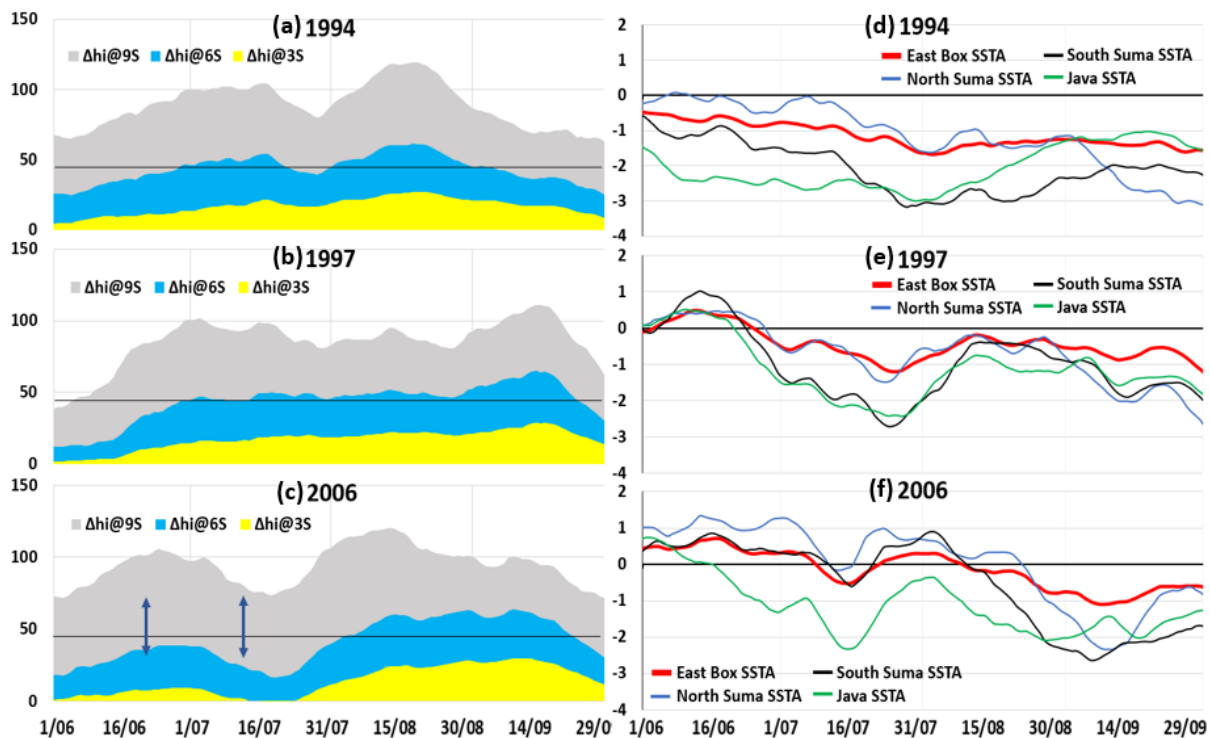


**Figure 3.5.14:** Panels (a) to (c) represents daily time series of  $\Delta h_i$  (m) at locations 3S, 6S and 9S marked in **figure 3.5.8**, black line indicates long term mixed layer value and two-sided arrows indicates deep convective events adopted from **figure 3.5.1**. Panels (d) to (e) represents SST anomalies over boxed region of **figure 3.5.8**.

The SST anomaly plot of all three boxed region (red boxes of **figure 3.5.11**) and eastern box of DMI display negative values from late June till mid-August 1997 as displayed in **figure 3.5.14e**, under the influence of north ward advection of upwelled cold water through rarely triggered transient the SJC and the SESC as discussed previously. Abrupt strong positive correction in SST anomalies of all the boxed region prompted during mid-August (**figure 3.5.14e**) indicates the coastal Kelvin wave activity in the region. After passage of coastal Kelvin wave, the SST anomalies of all boxes gain strong negative values within 10 days, which later persists till the end of the season (**figure 3.5.14e**).

### Ocean response in 2006

During early season of 2006 two strong “SETIO cyclone” are triggered (**figure 3.5.6**) from the two atmospheric convection phases (**figure 3.5.5c**) in the region; hence, the southern Sumatra coastline suffers from lack of upwelling favourable winds from advent of the season till late July 2006 as displayed in **figure 3.5.7c** and full upwelling conditions cannot develop in the region as displayed in **figure 3.5.14c** (blue shading,  $\Delta h_i@6^{\circ}S < 50$ ). Later, from late July 2006 onwards the study region enters in

the suppressed phase of atmospheric convection (**figure 3.5.5c**) and no “SETIO cyclone) is further triggered. Consecutively, strong coast parallel wind stress is developed along the southern Sumatra coastline (**figure 3.5.7c**) which triggers full upwelling conditions in the region as displayed in **figure 3.5.14c** (blue shading,  $\Delta\text{hi}@6^{\circ}\text{S}>50$ ). During the season of 2006 southern Java coastline displays unique characteristics with strongest ever coast parallel wind stress in the region. Consecutively, as a result of strong upwelling favourable conditions at precursor locations (at  $6^{\circ}\text{S}$ , **figure 3.5.14c**, blue shading) and strongest ever coast parallel stress in the region from the advent of the season, full upwelling is developed at the Java coastline from advent of the season and persists till the end of the season (**figure 3.5.14c**, grey shading,  $\Delta\text{hi}@9^{\circ}\text{S}>50$ ) .

The SST anomaly plot of Southern Java coastline follows the upwelling signature of the region and displays strong negative values below  $-1^{\circ}\text{C}$  from late June 2006 till end of the season as displayed in **figure 3.5.14f** (green line). Abrupt strong positive correction in SST anomalies of the southern Java coastline during late July 2006 indicates the coastal downwelling Kelvin wave activity in the region. The “SETIO cyclone” of 12th July 2006 (**figure 3.5.6**) triggered strong coastal downwelling Kelvin waves by abrupt reversal of southern coastal Sumatra winds (**figure 3.5.7c**). As discussed in section 3.4.3d, the “SETIO cyclone” can trigger WWB episode at the eastern equatorial Indian Ocean, which also may be the source of the coastal downwelling Kelvin wave activity in the region and it will be discussed in detail later in sub-section 3.5.2c.

Under the influence of local wind reversal and downwelling Kelvin waves of early season, SST anomalies of the southern Sumatra boxes cannot exhibit negative values till late July 2006 (**figure 3.5.14f**, blue and red lines), and as a result SST anomaly the entire eastern box of DMI cannot show negative values till same period (**figure 3.5.14f**, black line). Strong negative SST anomaly values are developed from early-August 2006 onwards in the region which is visible in the line plots of all the boxes in the region (**figure 3.5.14f**), which gains stronger values with further progress of the season as a result of north-eastward advection of upwelled cold water in the region through transient the SJC and the SESC.

### **Summary of Ocean response in 1994, 1997 and 2006**

Boreal summer fall of pIOD years can be characterised as the suppressed phase of atmospheric convection over the study region (absence of “SETIO cyclone), which is suitable conditions for the seasonal “south easterly” winds to thrive in the region and strong coast parallel stress develops in the region. Strong coast parallel stress along entire southern Sumatra and Java coastline can develop an unusually strong full-upwelling conditions along the entire coastline. As a result, strongest coastal upwelling is triggered at southern Java coastline during pIOD event years, where strong preconditioning at the precursor locations of the southern Sumatra coastline plays crucial role. The growth of rarely developed full upwelling conditions at both adjacent coastline of southern Java-Sumatra triggers strong negative values of SSTA at locations 5°S to 9°S of **figure 3.5.11**. Zonal and meridional growth of negative SSTA is already discussed in the spatial distribution of SST in **figure 3.2.1a** of this study.

Though, locations 1°S to 3°S along the Southern Sumatra coastline (**figure 3.5.11**) never reach to the full upwelling conditions in any season of any year as seen in **figure 3.5.13** and **3.5.14**. The primary reason behind this situation is weaker winds in the region in each season as evident in **figure 3.5.4**, **3.5.7** and **3.5.10**. The negative SST anomalies developed in these northern locations during positive IOD events are the results of the north-eastward progress of strong negative SST anomaly values developed at southern Java (locations 7°S to 10°S) and Southern Sumatra (locations 5°S and 6°S) to the northern locations and entire eastern box of the IOD. The negative SST anomalies progresses north-eastward in the region from southern locations as horizontal advection of cooler surface water.

The negative SST at locations 5°S to 10°S are triggered from full upwelling conditions discussed above in this section. The mechanism of horizontal “north-eastwards” progress of the negative SST anomalies is explained in detail in Kämpf and Kavi, 2018 (**figure 6a**). They suggested that the rare upwelling along the southern Sumatra coast triggers another upwelling jet transient to the South Java Current (SJC) (Sprintall *et al*, 1999) and they called it South East Sumatra Current (SESC). This rarely triggered SESC interacts with the south equatorial current (or south equatorial counter current, SECC; Schott *et al.*, 2009) in the region and develops strong cold-

water wedge extending westward in the eastern box of IOD events, see **figure 5c** and **6a** of Kämpf and Kavi, 2018.

The growth of rarely developed full upwelling conditions at both adjacent coastline of southern Java-Sumatra triggers strong negative values of SSTA in the region, and north-eastward deviation of upwelled cold water as the SESC develops strong surface cooling over the entire eastern box of the DMI.

#### **(e) Weak or aborted IOD event years 2003, 2008 and 2012**

The daily plots of  $\Delta hi$  and SSTA for 2003, 2008 and 2012 are displayed in **figure 3.5.15**, and these years represent the strong positive phase of IOD conditions. **Figure 3.5.15** (a) to (c) displays  $\Delta hi$  values for boreal summer-fall, where colour shading is similar to which explained in previous sub section (c). **Figure 3.5.15** (d) to (e) displays SST anomaly values for red box regions of **figure 3.5.11**.

#### **Ocean response in 2003**

Strong coast parallel winds are developed in the southern Java region from the advent of the season of 2003, along with comparative weaker winds in the southern Sumatra coastal region (**figure 3.5.10a**). Coast parallel winds at location  $1^{\circ}\text{S}$  to  $4^{\circ}\text{S}$  is weak during early June and strong at location  $5^{\circ}\text{S}$  to  $9^{\circ}\text{S}$  (**figure 3.5.10a**). As a result, strong upwelling favourable conditions are developed at southern Sumatra locations though it cannot reach to full upwelling conditions (**figure 3.5.15a**, blue shading,  $\Delta hi@6^{\circ}\text{S}<50$ ). During same period (June 2003), strong coast parallel stress value at the southern Java coastal region (**figure 3.5.10a**, top panel, black line) and near upwelling conditions at precursor locations (at  $6^{\circ}\text{S}$ ) trigger full upwelling conditions at southern at southern Java coastline from the advent of the season.

Later, during early July 2003 the “SETIO cyclone” is triggered (marked arrow, **figure 3.5.10a**, **figure 3.5.15a**), which temporarily destroys the coast parallel wind stress at southern coastal Sumatra region from late June till 10th July 2003 (**figure 3.5.10a**, bottom panels). Hence, upwelling conditions suffer downfall at southern Sumatra locations during the same period (**figure 3.5.15a**, blue shading) and stays below full upwelling conditions ( $\Delta hi@6^{\circ}\text{S}<50$ ). Later from 10th July onwards, the study region suffers from the suppressed phase of the atmospheric convection (**figure 3.5.8a**) and no “SETIO cyclone” is triggered till mid-August 2003. Hence, strong coast

parallel winds are developed along the southern Sumatra coastline from mid-July to mid-August 2003 (**figure 3.5.10a**) and consecutively the same region displays full upwelling conditions mid-July to mid-August 2003 (**figure 3.5.15a**, blue shading,  $\Delta h_i@6^\circ S > 50$ ). Later, two “SETIO cyclones” of mid-August and mid-September 2003 destroys previously developed upwelling favourable winds along the southern Sumatra coastline and consecutively full upwelling conditions are withdrawn in the southern Sumatra coastal region as visible in **figure 3.5.15a** (blue shading,  $\Delta h_i@6^\circ S < 50$ ), and these suppressed upwelling conditions persist till the end of season.

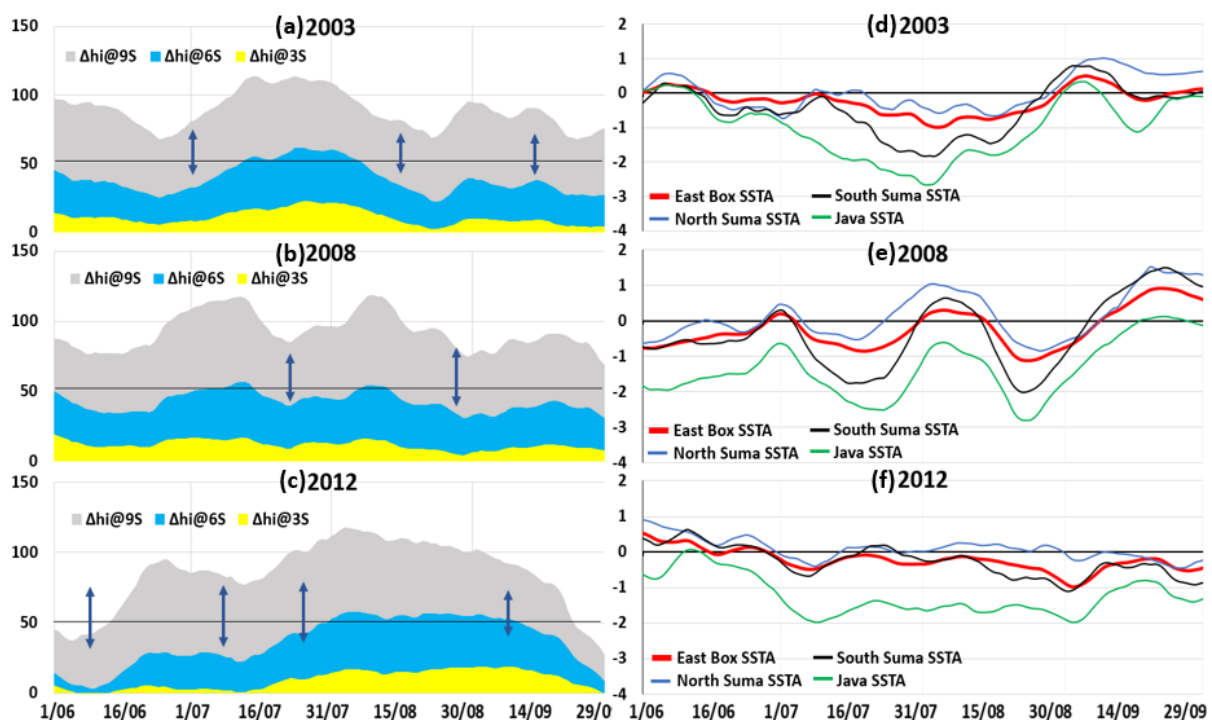


**Figure 3.5.15:** Panels (a) to (c) represents daily time series of  $\Delta h_i$  (m) at locations 3S, 6S and 9S marked in **figure 3.5.8**, black line indicates long term mixed layer value and two-sided arrows indicates deep convective events adopted from **figure 3.5.1**. Panels (d) to (e) represents SST anomalies ( $^\circ C$ ) over boxed region of **figure 3.5.8**.

Full upwelling conditions along the southern Java coastline also suffers downfalls during the “SETIO cyclone” phases of the season, under the cumulative effect of previous locations ( $3^\circ S$ ,  $6^\circ S$ ), though it maintains full upwelling conditions till the end of the season (**figure 3.5.15a**, grey shading), under the influence of strong coast parallel winds at location  $5^\circ S$  to  $9^\circ S$  throughout the season (**figure 3.5.10a**). As a result, full upwelling is developed at southern Java coastline from early June 2003 as displayed in **figure 3.5.15a** ( $\Delta h_i@9^\circ S > 50$ ) and it persists during the enteric season.

From early June 2003 southern Sumatra gain coastal parallel wind stress, though it is not enough that the thermocline of the region can reach to the surface as displayed in **figure 3.5.15a** where  $\Delta\theta_i@6^\circ\text{S}$  (blue shading) is just below 50m mark in early June.

The SST anomaly plot of Southern Java coastline follows the strong upwelling signature of the region and displays negative values below  $-1^\circ\text{C}$  from late June 2003 as displayed in **figure 3.5.14d** (green line). Later, the SST anomaly plot of Southern Java coastline gains lower negative values during late July till mid-August 2003 with values below  $-2^\circ\text{C}$ , under the full upwelling conditions at precursor location ( $6^\circ\text{S}$ ). The southern box of Sumatra coastline also displays value below  $-1^\circ\text{C}$ , during full upwelling conditions of from late July till late August 2003 at  $6^\circ\text{S}$  (**figure 3.5.15a**), as displayed in **figure 3.5.15d** (black line). Northern box of the southern Sumatra coastline (of **figure 3.5.11**) display moderated negative SST anomaly for the similar period from late July till late August 2003 as displayed in **figure 3.5.15d** (blue line) with values up to  $-0.5^\circ\text{C}$ . The reason of moderated strength of negative SST anomaly of northern box of the southern Sumatra coastline is due to weaker upwelling in the region and shorter phase of full upwelling at  $6^\circ\text{S}$ ; hence, cold water northward advection and the SESC are present only from late July till late August 2003.

Stronger and longer atmospheric convective episode of mid-August 2003 (**figure 3.5.8a** and **3.5.10a**) destroys the upwelling signature at southern coastal Sumatra, consecutively destroys the negative SST anomalies of the entire southern Java-Sumatra coastal region (**figure 3.5.15d**), which later cannot recover till the end of the season. The SST anomaly of the entire eastern box of the DMI follows the signature of all individual three boxes through zonal advection (**figure 3.5.15d**, red line). Hence, **figures 3.5.15 (a, d)** indicate that the developing coastal upwelling and negative SST anomalies of the southern Coastal Java-Sumatra are abruptly destroyed by the strong atmospheric convective episode over the study region and consecutively triggered "SETIO cyclone" of mid-August 2003. Later, strong atmospheric convection is relocated over the study region and more "SETIO cyclone" is triggered in mid-September 2003, which further create destructive conditions for the coastal upwelling of the region.

### Ocean response in 2008

Strong coast parallel winds are developed in the southern coastal Java region from the advent of the season of 2008, along with strong coast parallel winds in the southern Sumatra coastal region (**figure 3.5.10b**). As a result, strong coastal parallel wind stress in southern Sumatra coastal region from mid-June 2008 (**figure 3.5.10b**), location 6°S gain full upwelling conditions from late June 2008 as displayed in **figure 3.5.15b** (blue shading,  $\Delta\text{hi}@6^{\circ}\text{S} > 50$ ). Full upwelling condition is developed at southern Java coastline from early June 2003 as a result of strong coast parallel stress in the region (**figure 3.5.10b**, top panel, red dashes line) and strong upwelling favourable conditions at precursor location (6°S) as displayed in **figure 3.5.15b** ( $\Delta\text{hi}@9^{\circ}\text{S}>50$ ) which persists during the entire season.

The “SETIO cyclone” triggered during mid July 2008 (**figure 3.5.10b,3.5.15b**, marked arrow) temporarily destroys the seasonal coast parallel wind stress of the southern coastal Sumatra region (**figure 3.5.10b**), and this situation destroys the full upwelling conditions in the region during mid-July 2008, which is visible in the **figure 3.5.15b** (blue shading,  $\Delta\text{hi}@6^{\circ}\text{S}<50$ ). After this minor disturbance the full upwelling conditions are restored in the region till end of August 2008 (**figure 3.5.15b**, blue shading,  $\Delta\text{hi}@6^{\circ}\text{S}>50$ ) as a result of the suppressed phase of the atmospheric convection over the study region (**figure 3.5.8b, 3.5.10b**) and absence of the “SETIO cyclone”. Later, a stronger and longer atmospheric convection phase of late August 2008 over the study region (**figure 3.5.8b and 3.5.10b**) and consecutively triggered “SETIO cyclone” destroys previously developed upwelling favourable winds of the southern Sumatra coastal region and full upwelling condition is withdrawn as visible in **figure 3.5.15b** (blue shading,  $\Delta\text{hi}@6^{\circ}\text{S}<50$ ), and these suppressed upwelling conditions persist till the end of season.

Full upwelling conditions along the southern Java coastline also suffers downfalls during the “SETIO cyclone” phases of the season, under the cumulative effect of previous locations (3°S, 6°S), though it maintains full upwelling conditions till the end of the season (**figure 3.5.15b**, grey shading), under the influence of strong coast parallel winds at location 5°S to 9°S throughout the season (**figure 3.5.10b**).

The SST anomaly plot of 2008 displays unique characteristics and follows the fluctuating upwelling signature of the region. The SST anomaly plot of the southern

Java coastal region displays strong negative values below  $-2^{\circ}\text{C}$  from the advent of the season as displayed in **figure 3.5.15e** (green line). As discussed above, upwelling signature of the entire region suffers downfalls (**figure 3.5.15b**) during mid-August 2008; consecutively, SST anomaly of the southern Java coastal region exhibits positive correction during the temporarily withdrawn phases of full upwelling condition of the region.

Southern Sumatra coastal region exhibits negative values of SST anomaly from the advent of the season, and it gains strong negative values below  $-1^{\circ}\text{C}$  in mid-July and mid-August as displayed in **figure 3.5.15e** (black line). Though it is disturbed by temporarily withdrawn phases of full upwelling conditions of the region (**figure 3.5.15b**) twice in the season during early July and early August 2008. SST anomaly of entire eastern Box of the DMI index also exhibits the similar characteristics with values below  $-1^{\circ}\text{C}$  in mid-July and mid-August as displayed in **figure 3.5.15e** (red line). Later, strong “SETIO cyclone” of late August destroyed the previously developed full upwelling signature of the region and strong surface cooling of the entire region is reverted to positive values (**figure 3.5.15e**), which cannot recover during rest of the season.

Hence, **figures 3.5.15 (b, e)** indicate that the developing coastal upwelling and negative SST anomalies of the southern Coastal Java-Sumatra are abruptly destroyed by the strong atmospheric convective episode of mid-July and late August 2008 and consecutively triggered “SETIO cyclone”.

### **Ocean response in 2012**

The season of 2012 commences with the “SETIO cyclone” (**figure 3.5.10, 3.5.15c**, marked arrow); hence, coast parallel winds arrive late in the region from mid-June 2012 (**figure 3.5.10c**). As a result of strong upwelling winds at location  $5^{\circ}\text{S}$  and  $6^{\circ}\text{S}$  (**figure 3.5.10c**, bottom panel) and strong coast parallel stress in the southern coastal Java region (**figure 3.5.10c**, top panel, red dashed line), the southern coastal Java region displays full upwelling conditions from mid-June 2008 as displayed in **figure 3.5.15c** (grey shading,  $\Delta\text{hi}@9^{\circ}\text{S}>50$ ). Under the influence of early season consecutively triggered two “SETIO cyclones” (**figure 3.5.10c, 3.5.15c**, marked arrows), which destroys coast parallel winds along the southern Sumatra coastline (**figure 3.5.10c**), full upwelling conditions cannot develop at southern Sumatra coastline till end of July 2008 (**figure 3.5.15b**, blue shading,  $\Delta\text{hi}@6^{\circ}\text{S}<50$ ). Later, from

early August 2008, under the effect of suppressed atmospheric convection phase over the study region (**figure 3.5.8c, 3.5.10c**) and absence of “SETIO cyclone”, winds along the southern Sumatra coastline gain strong coast parallel winds (**figure 3.5.10c**) and displays full upwelling conditions (**figure 3.5.15b**, blue shading,  $\Delta\text{hi}@6^{\circ}\text{S}>50$ ), which persists till end of the season. Seasonal wind reversal from October 2012 reverses “south easterlies” of the region and suspend the full upwelling conditions of the region.

The SST anomaly plot of Southern Java coastline follows the upwelling signature of the region and displays negative values below  $-1^{\circ}\text{C}$  from late June 2012 as displayed in **figure 3.5.15f** (green line). It gains strong negative values from early July till early-September 2012 under the effect of strong upwelling signature at location  $6^{\circ}\text{S}$  during the same period. Strong negative values SST anomaly of the southern box of Sumatra coastline (**figure 3.5.15f**, black line) is developed during full upwelling phase of mid-August to mid-September 2008, and value up to  $-1^{\circ}\text{C}$  is developed in late August 2012. The SST anomaly plot of the entire eastern Box of DMI follows the same characteristics and displays maximum negative values during late August and early September 2012 as displayed in **figure 3.5.15f** (red line). Seasonal wind reversal from October 2012 suspend the upwelling signature of the region, which consecutively reverted the SST anomalies of the region to positive values (**figure 3.5.15f**).

Hence, **figures 3.5.15 (c, f)** indicate that the full coastal upwelling and negative SST anomalies of the southern Coastal Java-Sumatra region develops late in the season, from late June 2012 at southern Java and from early August 2012 at southern Sumatra coastline. The lately developed upwelling signature cannot sustain longer in the region and consecutively destroyed by the seasonal wind reversal of October 2012.

### **Summary of ocean response in 2003, 2008 and 2012**

The suppressed phase of atmospheric convection over the study region followed by absence of “SETIO cyclone, is the suitable conditions for the season coast parallel winds along the southern Sumatra coastline to thrive. During this suppressed phase strong coast parallel stress is developed in the southern Sumatra coastal region, similar to the situation during the strong pIOD event years. Though, abruptly developed atmospheric convective phase over the study region destroys the coast parallel “south easterly” winds in the southern Sumatra coastal region by setting up

“SETIO cyclone” over the study region. Consecutively, previously developed full upwelling conditions along the southern Sumatra coastline is withdrawn and surface cooling in the region is suspended. The withdrawal of upwelling in the region also suspend the north-eastward advection of cold water by terminating the SESC. The coast parallel seasonal winds along the southern Java coastline remains unaltered during any atmospheric conditions, as a result surface cooling signature prevails with the presence of SJC in the region till the full upwelling conditions.

### 3.5.3 Westerly wind bursts and Sea Level anomalies

Destructive consequences of the deep atmospheric convective episodes over the study region and consecutively triggered “SETIO cyclones” on southern Sumatra coastal upwelling is discussed in section 3.5.1 and 3.5.2. The “SETIO cyclones” has one more destructive effect on the southern Sumatra-Java upwelling region which is discussed in this sub section.

The “SETIO cyclones” triggers abrupt “westerly pulses” at the scale of westerly wind bursts (WWB) over the eastern equatorial Indian Ocean as northern branch of the “SETIO cyclone” as discussed previously in section 3.4.3. According to equatorial ocean dynamics the WWBs can trigger downwelling Kelvin waves, which can deepen the thermocline of the region by travelling poleward along the southern Sumatra-Java coastline. The existence of the WWBs over the eastern equatorial Indian Ocean is not new and it was reported in previous studies along with its effect in the region, though I am discussing here in the perspective of positive IOD events with and to fulfil certain discrepancies witnessed in previous studies. As I mentioned previously, the southern Java-Sumatra coastal region suffers from scarcity of data; hence, I explore the WWB triggered variability with sea height anomaly of the region from satellite data. Good coverage of ARGO profiles in the region, which I consider at least one profile in the region every 7 days, is available from 2010 onwards. Hence, I explore the MLD variability along with sea height anomalies for 2012, only year in my selected events analysis having this ARGO profile availability.

#### (a) Neutral IOD event years 1998, 2001 and 2004

The Hovmoller diagrams of daily zonal wind speed and daily sea level anomalies are prepared from multiplatform cross calibrated satellite wind and AVIOS SLA data and both Hovmoller plots are prepare at the equatorial Indian Ocean (50° to 100°E) for boreal summer-fall and displayed as pair side-by-side in **figure 3.5.16**. Red colour in each Hovmoller plot indicates positive values and blue shading indicates negative values. Vertically tilted line plot at the end of each pair of Hovmoller plots in **figure 3.5.16** displays the sea level anomaly (SLA) values at four pinpoint locations along the southern Sumatra-Java coastline (at locations 1oS, 3oS, 6oS and 9oS of **figure 3.5.11**). **Figure 3.5.16** displays the plots for the years discussed above in section 3.5.1 and 3.5.2.

### WWBs of 1998

Hovmoller plot of zonal wind speed over the equatorial Indian Ocean is displayed in **figure 3.5.16a**, Hovmoller plot of SLA over the equatorial Indian Ocean is displayed in **figure 3.5.16b** and line plot of the SAL along southern Sumatra-Java coastline is displayed at the end of twin Hovmoller plots (**figure 3.5.16 a, b**). The horizontal arrows marked in the vertical line plots of SLA indicates location of the “SETIO cyclones” in time domain.

The presence of series of “WWBs” over the eastern equatorial Indian Ocean (70o-100Eo) is evident in **figure 3.5.16a** (red and yellow shading), where each WWB is triggered from the “SETIO cyclone” (compare red shading in 3.5.16a and horizontal arrows of vertical line plot of SLA). Series of strong equatorial downwelling Kelvin waves are triggered over the eastern equatorial Indian Ocean (**figure 3.5.16b**, dashed arrows) in the season of 1998, from each WWB event of the same region. These equatorial downwelling Kelvin waves then travel poleward along the southern Sumatra-Java coastline, which is visible in vertical line plot of SLA adjacent to **figure 3.5.16b** (positive peaks). The vertical line plot displays SLA values along the southern Sumatra-Java coastline, and each peak in positive SLA values displays the downwelling Kelvin wave activity.

Consecutively, positive SLA values dominate over the eastern equatorial Indian Ocean (red shading in **figure 3.5.16d**) and along the Java-Sumatra coastline (positive peaks in vertical SLA plot). The depth of the thermocline is the mirror image of the sea level of the region; hence, dominance of higher sea surface height values indicates deeper than normal thermocline depth in the region. The deeper than normal thermocline make it difficult for the upwelling processes to raise the thermocline to surface in the region.

During the absence of the “SETIO cyclones” (gap between horizontal arrows of vertical line plot of SLA), which is also a suppressed phase of atmospheric convection over the study region (**figure 3.5.1a**), zonal winds exhibits weak westerly component (**figure 3.5.16a**, light orange shading) under the influence of seasonal “south westerly” winds of the region (see **figure 3.4.2**, section 3.4). No notable easterly is present over the eastern equatorial Indian Ocean (70°-100°E) during the season of 1998, as claimed in certain previous studies.

Scattered weak easterlies present over the western equatorial Indian Ocean (**figure 3.5.16a**, blue shading in 50°-70°E), though it cannot affect the sea level anomalies and consecutively thermocline of the eastern equatorial Indian Ocean, because they are weak (wind speed < 5m/s) and they are shadowed by the strong WWB episodes of east.

### **WWBs of 2001**

The presence of series of “WWBs” over the eastern equatorial Indian Ocean (70°-100°E) is evident in **figure 3.5.16c** (red and yellow shading), where each WWB is triggered from the “SETIO cyclone” (compare red shading in 3.5.16c and horizontal arrows vertical SLA plot). Series of strong equatorial downwelling Kelvin waves are triggered over the eastern equatorial Indian Ocean (**figure 3.5.16d**, dashed arrows) in the season from each WWB event of the same region. Consecutively, positive SLA values are developed over the eastern equatorial Indian Ocean (red shading in **figure 3.5.16d**) and along the Java-Sumatra coastline (positive peaks in vertical SLA plot). The series of downwelling Kelvin waves over the eastern equatorial Indian Ocean and along the southern Sumatra-Java coastline keeps the sea level height higher than normal and consecutively make deeper than normal thermocline in the region. The deeper than normal thermocline make it difficult for the upwelling processes to raise the thermocline to surface in the region.

During absence of the “SETIO cyclones”, zonal winds exhibits weak westerly component (**figure 3.5.16c**, light orange shading) under the influence of seasonal “south westerly” winds of the region (**figure 3.4.2**, section 3.4). Scattered Weak easterlies (wind speed < 5m/s) are present over the eastern equatorial Indian Ocean (70o-100oE) during early July, late August and late September 2001 (**figure 3.5.16c**, blue shading). Presence of basin wide easterlies during early June and mid-July 2001 (**figure 3.5.16c**, blue shading) triggers upwelling equatorial Kelvin waves over the region (**figure 3.5.16d**, light blue shading in 70°-100°E), which can consecutively raise the depth of the thermocline in the region.

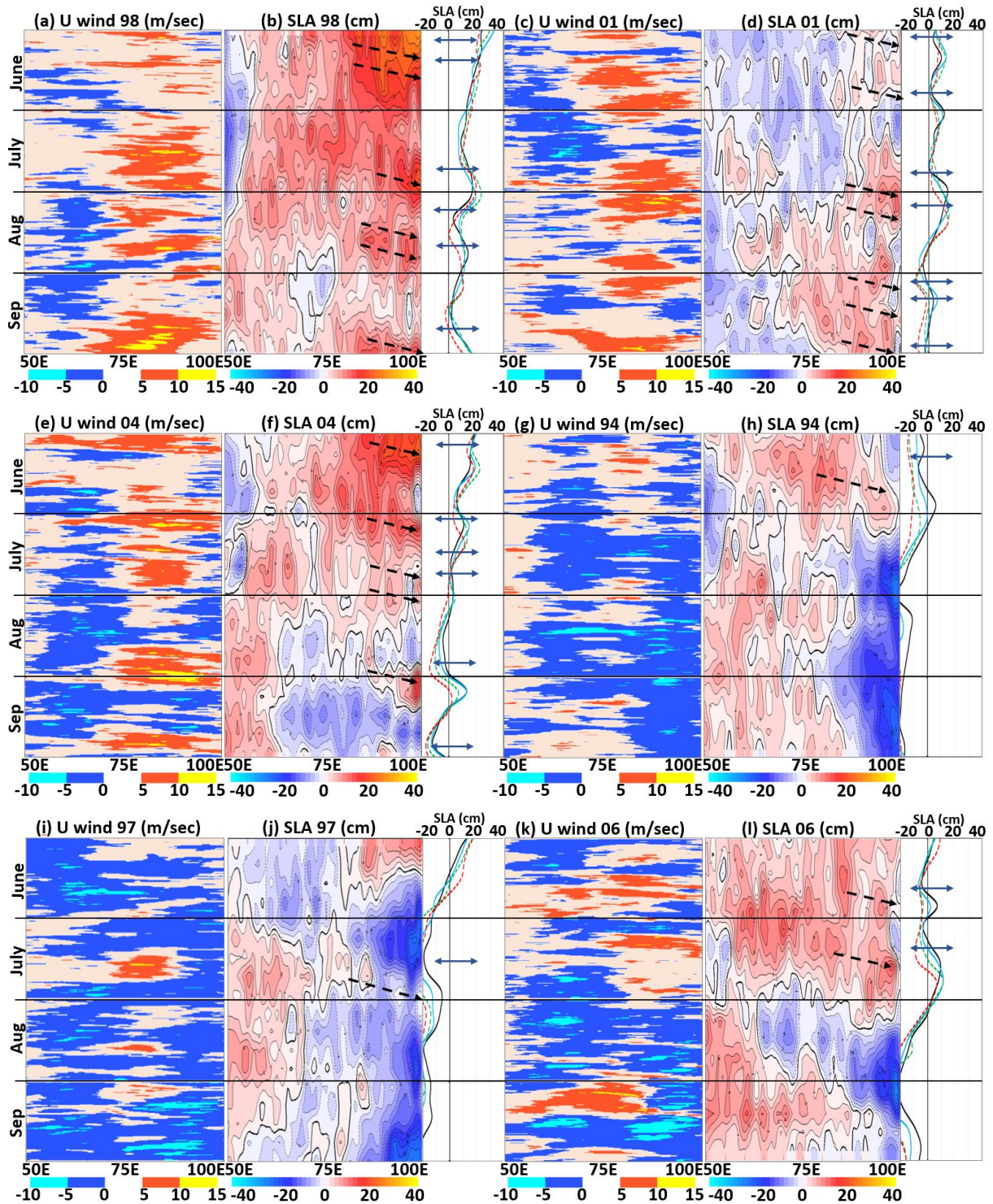


**Figure 3.5.16:** Panels (a), (c), (e), (g), (i), (k), (m), (o) and (q) displays Hovmoller plot of zonal wind speed (m/s) at the equator of the Indian Ocean. Panels (b), (d), (f), (h), (j), (l), (n), (p) and (r) displays the Hovmoller plot of sea level anomalies (m) at the equator of the Indian ocean. Line plot adjacent to each sea level anomaly plot displays sea level anomalies at four pinpoint locations ( $1^{\circ}\text{S}$ ,  $3^{\circ}\text{S}$ ,  $6^{\circ}\text{S}$  and  $9^{\circ}\text{S}$ ) along the southern Java and Sumatra coasts marked in **figure 3.5.11**.

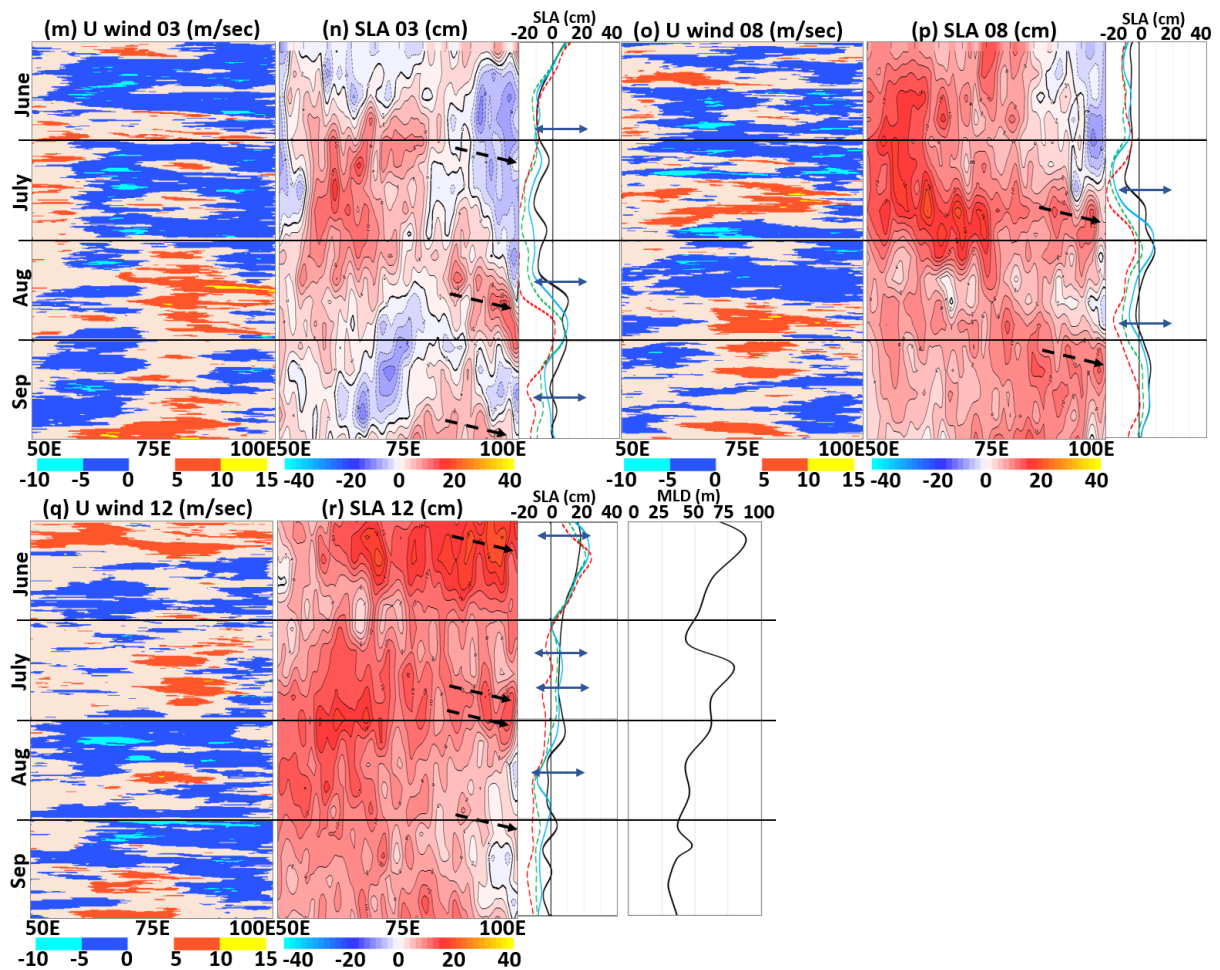


**Figure 3.5.16:** Continue **figure 3.5.16**.

Easterlies persist over the western equatorial Indian Ocean during early season (**figure 3.5.16c**, blue shading in 40°-70°E) which trigger moderated strength equatorial upwelling Kelvin waves during June and July 2001 (**figure 3.5.16d**, light blue shading in 40°-70°E), and drop the sea level to negative anomaly values in the western and middle equatorial Indian Ocean during early July 2001 (**figure 3.5.16d**, blue shading). Though the negative values of the SLA of western equatorial Indian Ocean are shaded by the events in the east.

### WWBs of 2004

The presence of series of “WWBs” over the eastern equatorial Indian Ocean (70o-100Eo) is evident in **figure 3.5.16e** (red and yellow shading), where each WWB is triggered from the “SETIO cyclone” (compare red shading in 3.5.16e and horizontal arrows vertical SLA plot). Series of strong equatorial downwelling Kelvin waves are triggered over the eastern equatorial Indian Ocean (**figure 3.5.16f**, dashed arrows) in

the season from each WWB event. As a result, positive SLA values are developed over the eastern equatorial Indian Ocean (red shading in **figure 3.5.16f**) and along the Java-Sumatra coastline (positive peaks in vertical SLA plot). The series of downwelling Kelvin waves over the eastern equatorial Indian Ocean and along the southern Sumatra-Java coastline keeps the sea level height higher than normal during June and July 2004 (**figure 3.5.16f**, dominance of red shading) and consecutively make deeper than normal thermocline depth in the region.

Later in the season, during early August and mid-September 2004 a month long gap between the consecutive “SETIO cyclone” (gap between horizontal arrows of vertical line plot of SLA); hence, zonal winds exhibits two episodes of weak easterly over the eastern equatorial Indian Ocean (**figure 3.5.16e**, blue shading in 70°-100°E) under the influence of seasonal “south easterly” of the study region (SETIO). Hence, under the influence of basin wide two episodes of weak easterlies during early August and mid-September 2004 over the eastern equatorial Indian Ocean (**figure 3.5.16e**, blue shading) the upwelling Kelvin waves are triggered over the eastern equatorial Indian Ocean (**figure 3.5.16f**, blue shading). Consecutively, lower than normal sea level in the eastern equatorial Indian Ocean region (**figure 3.5.16f**, blue shading) and along the southern Sumatra-Java coastline (negative peaks in vertical SLA plot) and shallower thermocline conditions are developed towards the end of the season. Sporadic weak easterlies present over the western equatorial Indian Ocean (**figure 3.5.16a**, blue shading), though it cannot affect the thermocline of the eastern equatorial Indian Ocean, as they are shaded by the strong episodes of WWB.

#### **(b) Positive IOD event years 1994, 1997 and 2006**

The Hovmoller diagrams of daily zonal wind speed and daily sea level anomalies are displayed as pair side-by-side in **figure 3.5.16**. Colour coding is explained previously follows here. Vertically tilted line plot at the end of each pair of Hovmoller plots in **figure 3.5.16** displays the sea level anomaly (SLA) values at four pinpoint locations along the southern Sumatra-Java coastline (at locations 1oS, 3oS, 6oS and 9oS of **figure 3.5.11**).

#### **Absence of WWBs in 1994**

Erratic westerlies present over the eastern equatorial Indian Ocean during June 1994 (**figure 3.5.16g**, red shading) as a consequence of smaller atmospheric

convective episode (**figure 3.5.5a** and **figure 3.5.6**). Downwelling Kelvin wave is triggered during June 1994 over the eastern equatorial Indian Ocean (dashed arrow in **figure 3.5.16h**), as a result positive SLA values are developed over the eastern equatorial Indian Ocean (red shading in **figure 3.5.16h**) and also along the southern Sumatra-Java coastline (positive peaks in vertical SLA plots), as a consequence of early season erratic eastern equatorial westerlies.

Later, the season of 1994 suffers from the suppressed atmospheric convection over the study region and no “SETIO cyclone” is triggered, as a result the easterlies develop over the entire equatorial Indian Ocean from July 1994 (**figure 3.5.16g**, blue shading) and persists till the end of season. Hence, the series of upwelling Kelvin waves are triggered over the eastern equatorial Indian Ocean, which create negative SLA values over the eastern equatorial Indian Ocean and along the southern Sumatra-Java coastline as displayed in **figure 3.5.16h** (blue shading) and adjacent vertical line plot of SLA (negative peaks), which persists till the end of season. The upwelling Kelvin waves create lower than normal sea level (negative SLA) and shallower thermocline in the region which supports the upwelling in the region.

### **WWBs of 1997**

The study area suffers from the suppressed atmospheric convection over the study region (**figure 3.5.5b**) from the advent of the season, as a result the easterlies develop over the eastern equatorial Indian Ocean from June 1997 as displayed in **figure 3.5.16i** (blue shading) and persists till the end of season. Strong upwelling Kelvin waves are triggered, and as a result negative SLA values present over the eastern equatorial Indian Ocean from the advent of the season as displayed in **figure 3.5.16j** (blue shading) from easterlies of the eastern equatorial Indian Ocean. The dominance of the upwelling Kelvin waves in the season develops lower than normal sea level (negative SLA values) and shallower thermocline in the region which supports the upwelling in the region.

Though, during mid-July 1997 a “SETIO cyclone” is triggered (**figure 3.5.6**) which temporarily triggered abrupt “WWB” event over the eastern equatorial Indian Ocean as displayed in **figure 3.5.16i** (red shading). Once the “SETIO cyclone” phase is over, the easterlies dominate over the entire equatorial Indian Ocean, with scattered presence of westerlies. During September 1997, strong easterlies are developed in

the eastern equatorial Indian Ocean (**figure 3.5.16i**, cyan shading). Downwelling Kelvin wave is triggered over the central equatorial Indian Ocean during mid-July 1997 (**figure 3.5.16j**, dashed arrow) as consequence of the WWB event of the same period, which temporarily raise the sea level in the region (**figure 3.5.16j**, positive peaks in vertical SLA plot).

### **WWBs of 2006**

Presence of early season two “SETIO cyclone” during late-June and early July 2006 (horizontal arrows in vertical SLA plot), trigger abrupt “WWB” events over the eastern equatorial Indian Ocean as displayed in **figure 3.5.16k** (red shading). Downwelling Kelvin waves are present during June and July 2006 over the eastern equatorial Indian Ocean as displayed in **figure 3.5.16l** (dashed arrows) and along the southern Sumatra-Java coastline as visible in adjacent vertical line plot SLA (positive peaks), as a consequence of “WWB” episodes.

From August 2006 onwards the easterlies dominate the entire equatorial Indian Ocean (**figure 3.5.16k**, blue shading). According to previous studies atmospheric convection shifts westward in tropics of the Indian ocean during the surface cooling period of the eastern tropical Indian Ocean. Hence, under the same conditions a strong “westerly” episode is triggered over the western equatorial Indian Ocean during early September 2006 (**figure 3.5.16k**, red shading). The series of upwelling Kelvin waves are triggered from early, as result the negative SLA dominates over the eastern equatorial Indian Ocean August as displayed in **figure 3.5.16l** (blue shading) and along the southern Sumatra-Java coastline as visible in adjacent vertical line plot of SLA (negative peak). This negative SLA values persist till the end of season. The “westerly” episode of early September 2006 over the western equatorial Indian Ocean trigger the downwelling Kelvin waves (**figure 3.5.16l**, red shading) which raise minor positive values of SLA of the eastern equatorial Indian Ocean.

### **(c) Weak or aborted IOD event years 2003, 2008 and 2012**

The Hovmoller diagrams of daily zonal wind speed and daily sea level anomalies are displayed as pair side-by-side in **figure 3.5.16**. Colour coding is explained previously follows here. Vertically tilted line plot at the end of each pair of Hovmoller plots in **figure 3.5.16** displays the sea level anomaly (SLA) values at four

pinpoint locations along the southern Sumatra-Java coastline (at locations 1oS, 3oS, 6oS and 9oS of **figure 3.5.11**).

### **WWBs of 2003**

From the advent of the season of 2003, the study area suffers from the weak atmospheric convection over the study region (**figure 3.5.8a**) and no “SETIO cyclone” is triggered, as a result the easterlies develop over the entire equatorial Indian Ocean from June 2003 as displayed in **figure 3.5.16m** (blue shading) which persists till early August 2003. As a result, strong upwelling Kelvin waves are triggered over the eastern equatorial Indian ocean from the advent of the season as displayed in **figure 3.5.16n** (blue shading), and lower SLA persists till early August 2003 over the eastern equatorial Indian Ocean **3.5.16n** (blue shading) and along southern Java-Sumatra coastline as visible in vertical line plot of SLA (negative peaks).

During late June a “SETIO cyclone” is triggered (horizontal arrow in vertical SLA plot), which consecutively triggers scattered “westerly” events over the eastern equatorial Indian Ocean (**figure 3.5.16m**, red shading), though they cannot form a single WWB scale event. The scattered “westerly” events of late June cannot mark its signature in the sea level anomalies of the eastern equatorial Indian Ocean as downwelling Kelvin waves, and positive SLA cannot develop during the period (**figure 3.5.16n**, vertical SLA plot).

Later, strong “SETIO cyclone” is triggered during mid-August 2003 (horizontal arrow in vertical SLA plot), which consecutively triggers “WWB” events during the same period as displayed in **figure 3.5.16m** (red shading). Strong WWB event of mid-August triggers downwelling Kelvin waves over the eastern equatorial Indian Ocean during mid-August (**figure 3.5.16n**, dashed arrow). The related atmospheric convective episode over the study region (of mid-August 2003) was so strong (**figure 3.5.8a**) that it restores the tropical convection over the eastern tropical Indian Ocean, and consecutively terminate the presence of “easterlies” in the region. One more “SETIO cyclone” is triggered during mid-September 2003 (**figure 3.5.9**), which again triggers the “WWB” event in the region (**figure 3.5.16m**, red shading). Scattered upwelling Kelvin waves are present during mid-September (**figure 3.5.16n**, light blue shade) which are later destroyed by the downwelling Kelvin wave of the late

September (**figure 3.5.16n**, dashed arrow) from the WWB event of the mid-September 2003.

In summary, early season of 2003 exhibits the dominance of “easterly” driven upwelling Kelvin waves over the eastern equatorial Indian Ocean which supports upwelling conditions in the region with lower than normal sea level (negative SLA) and shallower thermocline. Though, later during second half of the season the negative SLA values are destroyed by the series of WWB events and consecutively triggered downwelling Kelvin waves, raise the sea level above normal values (positive SLA).

During entire season weak and strong “easterly” winds are present over the western equatorial Indian Ocean, though it cannot mark its signature in the sea level anomalies of the eastern equatorial Indian Ocean and they are shadowed by the events in the east.

### **WWBs of 2008**

From the advent of the season 2008, the study area suffers from the weak atmospheric convection over the study region (**figure 3.5.8b**) and no “SETIO cyclone” is triggered, as a result the easterlies are developed over the eastern equatorial Indian Ocean from June 2008 as displayed in **figure 3.5.16o** (blue shading) which persists till mid-July 2008. Consecutively, upwelling Kelvin waves are triggered over the eastern equatorial Indian ocean during early season, and lower than normal sea level (negative SLA) is present in the region from June till mid-July 2008 as displayed in **figure 3.5.16p** (blue shading) and vertical SLA plot.

Strong “SETIO cyclone” is triggered during mid-July 2008, which consecutively triggers “WWB” events during the same period as displayed in **figure 3.5.16o** (red shading). Strong “WWB” event of mid-July 2008 triggers strong downwelling Kelvin wave and destroys previously developed negative sea level anomalies and develops positive sea level anomalies coastline (red shading in **figure 3.5.16p**, positive peaks in vertical SLA). Later in the season weak “easterly” persists from late July till mid-August 2008 (**figure 3.5.16u**, blue shading), though they cannot mark their signature in the sea level anomalies of the eastern equatorial Indian Ocean as downwelling Kelvin waves, and positive SLA cannot develop during the period (**figure 3.5.16n**, vertical SLA plot).

One more “SETIO cyclone” is triggered during late August 2008, which again triggers the “WWB” event in the region (**figure 3.5.16o**, red shading). The atmospheric convective episode of the study region during late August is longer than normal (**figure 3.5.8b**) as discussed previously in section 3.5.1a, which triggers three consecutive “WWB” events (three) over the eastern equatorial Indian Ocean from late August to mid-September 2008 as displayed in **figure 3.5.16o** (red shading). As a result, the series of downwelling Kelvin waves are triggered over the eastern equatorial Indian Ocean (**figure 3.5.16p**, marked arrows), which substantially raise the sea level of the eastern equatorial Indian Ocean and along the southern Java-Sumatra coastline (red shading in **figure 3.5.16p**, positive peaks in vertical SLA).

In summary, early season of 2008 exhibits the dominance of “easterly” driven upwelling Kelvin waves over the eastern equatorial Indian Ocean which supports upwelling conditions in the region with lower than normal sea level (negative SLA) and shallower thermocline. Later, from mid-July negative SLA values are destroyed by the series of WWB events and consecutively triggered downwelling Kelvin waves.

### **WWBs of 2012**

The season of 2012 has reversed condition compare to the years discussed above (2003 and 2008). Three “SETIO cyclones” are triggered during early stage of the season (**figure 3.5.9**); during early June, early July and mid-July 2012; which consecutively trigger “WWB” events over the eastern equatorial Indian Ocean as displayed in **figure 3.5.16q** (red shading). Three strong “WWB” events of early season of 2012 triggers series of downwelling Kelvin waves (**figure 3.5.16r**, dashed arrows) and develop positive sea level anomalies (**figure 3.5.16r**, red shading) over the eastern equatorial Indian Ocean, which persist till early August 2012.

Later, from early August 2012 easterlies dominate the entire equatorial Indian Ocean (**figure 3.5.16q**, blue shading) as result of weak atmospheric convection over the study region (**figure 3.5.8c**) and absence of the “SETIO cyclone”, which persist till the end of the season. Weak easterlies of the region from early August 2012 moderately recovers the positive sea level anomalies of the eastern equatorial Indian Ocean, which stays just below long-term average values with moderated negative anomalies (light blue shading in **figure 3.5.16r**, near zero values in vertical SLA plot).

The “westerly” events of mid-August are weaker (**figure 3.5.16q**, red shading), and it triggers minor positive disturbance in the sea level anomalies of the eastern equatorial Indian Ocean (dashed arrow in **figure 3.5.16r**, small positive peaks in vertical SLA plot). The “WWB” events of late September 2012 (**figure 3.5.16q**, red shading) triggers downwelling Kelvin waves which may later rise the sea level of the eastern equatorial Indian Ocean, though it is out the range of the **figure 3.5.16.r**.

At the end of Hovmoller plot 3.5.16r, notice two vertical line plots, first one displays the SLA along the southern Java-Sumatra coastline as discussed previously. Second vertical plot displays the area average mixed layer depth values in the southern Sumatra coastal region. From 2010 onwards sufficient ARGO profiles are present in the region that area average MLD plot can be prepared with considerable temporal resolution. According to this second vertical line plot, MLD values of the southern Sumatra coastal region follows the Kelvin wave activity of the region; hence, during first half of the season of 2012 displays deeper MLD values. Later, during second half of the season of 2012 MLD values exhibits decay and the thermocline rise near 25m depth during later September 2012.

### **Summary of WWBs**

The series of “SETIO cyclones” during boreal summer-fall triggers series of WWB events over the eastern equatorial Indian Ocean. The presence of WWB is known in the eastern equatorial Indian Ocean for a long time, and it was claimed in number of previous studies that these intraseasonal WWB episodes deepens the thermocline of the eastern equatorial Indian Ocean and along the southern Java-Sumatra coastline by triggering downwelling Kelvin waves. Though, no previous studies can precisely claim the mechanism responsible for the trigger of these WWB episode. This study explains that the “SETIO cyclone” triggers the WWB episode over the eastern equatorial Indian Ocean as the northern branch of the cyclonic circulation over the SETIO region. The actual effect of downwelling Kelvin waves on the depth of thermocline is still under speculation as this region suffers from the lack high temporal resolution subsurface data. The presence and effects of barrier layer, which is the unique property of the region, is also ambiguous for the obvious reasons.

Presence of denser ARGO coverage along with couple of permeant moorings in the southern Java-Sumatra coastal region can improve spatio-temporal resolution

of the sub surface observations of the region, which further improve our understanding of the subsurface physical oceanic processes and effects of the barrier layer, which is still under speculation and depends on the modelling studies solely.

### 3.5.4 Suppressed convection is a precursor or an aftermath?

The atmospheric convective aggregation over the southern eastern tropical Indian Ocean (80°-110°E, Eq-10°S) is proved as dominating factor in this study so far which can create synoptic scale anomalous surface wind disturbances in the study region called “SETO cyclone” in this study (section 3.4.3). The “SETIO cyclone” has devastating consequences on the seasonal coastal upwelling of the southern Java and Sumatra region as discussed in section 3.5.1 and 3.5.2. The relation of atmospheric convective variability with wind events of the region is not new and it was noted in many previous studies. The shift of the atmospheric convection from eastern tropical Indian Ocean to the western tropical Indian Ocean during positive IOD events was noted in previous studies.

There is a near-perfect seesaw relationship in tropical convection between the eastern and western boxes of IOD as well (in accordance to the IOD phases); whenever convection is enhanced in the eastern side, it is suppressed in the west and vice versa (Saji *et al.*, 1999; Behera *et al.*, 1999; Guan, 2003; Gadgil *et al.*, 2003 2004).

All previous studies agree on the fact that, intensified easterly winds over the eastern equatorial Indian Ocean shallows the thermocline depth, consecutively the seasonal south easterlies of the Java Sumatra coastal region intensified, and negative SST anomalies are triggered in the region. Thus, once the thermocline is preconditioned from strong south easterly or anomalous easterlies, suppression or westward shift in convection over the eastern equatorial Indian Ocean happens through negative SST anomaly of the region, which further takes the IOD events to maturity (Kajikawa *et al.*, 2001; Fischer *et al.*, 2005; Han *et al.*, 2006; Rao *et al.*, 2009, Vinayachandran *et al.*, 2009). The common conclusion from all these studies is, cold SST anomalies (negative SSTA) of the eastern equatorial Indian Ocean suppress atmospheric convection in the east and comparatively warm SSTA enhances convection in the west. Which indicates all the studies believed that, shift in tropical convection as an aftermath of the negative SST anomaly.

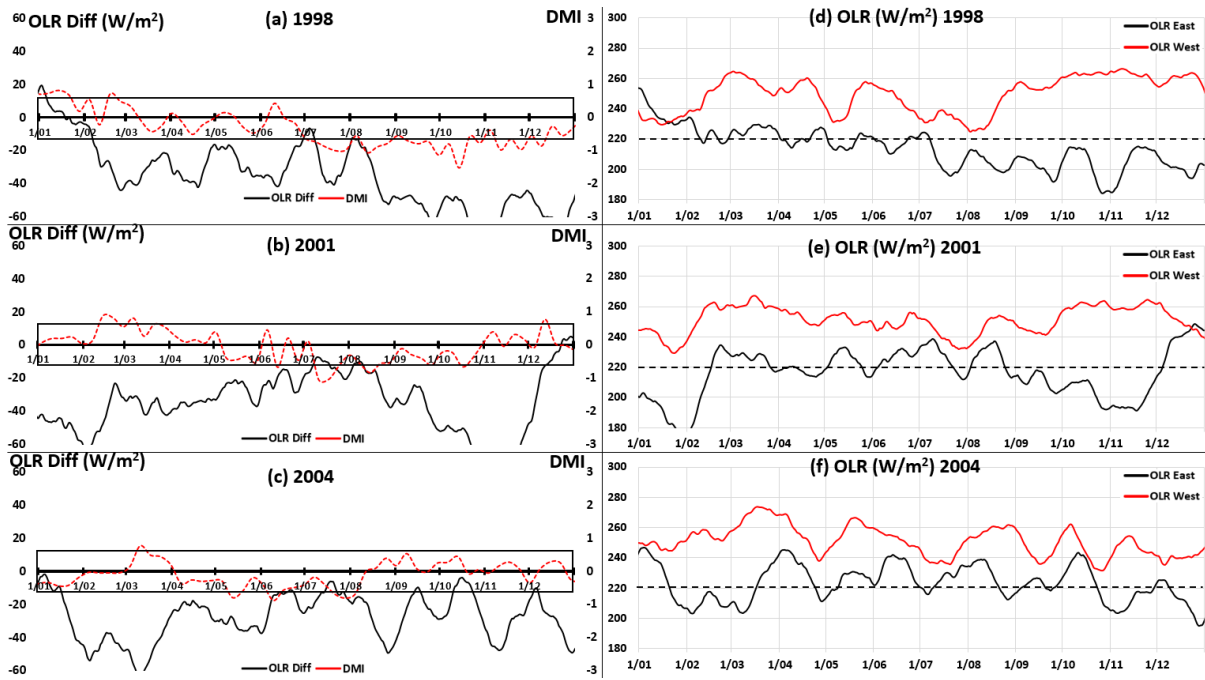


**Figure 3.5.17:** Panels (a) to (c) represents OLR difference (black line,  $W/m^2$ ) between DMI east box and west box along with Dipole mode index (red dashed line, DMI). Panels (d) to (f) indicates OLR values ( $W/m^2$ ) of east box of DMI (black line) and west box of DMI (red line) individually.

I prepared a daily time series of the area average OLR over the eastern box of the DMI index and western box of the DMI index from daily satellite observation derived from NOAA PSD dataset. For ease of explanation the 7-day running mean from centre (3 days before and 3 days after) is applied to each time series. The year displayed and discussed in this sub section is similar discussed previously during the event analysis of section 3.5.1 and 3.5.2. To evaluate the claims of seesaw relationship, I start with the neutral years, during which tropical convection of the Indian Ocean is located over the eastern box of the DMI index. **Figure 3.5.17** displays the OLR of eastern box and western box in (d) to (f) and difference between OLR east and west along with DMI index in (a) to (c). For value of OLR average over the wide region of the scale of DMI box, 220 ( $W/m^2$ ) can be considered as deep atmospheric convection (Meehl, 1987); hence this value is marked with dashed black line in (d) to (e) of **figure 3.5.17** for reference.

During boreal summer-fall of 1998, 2001 and 2004 OLR values of the eastern box of DMI exhibits values below 220 ( $W/m^2$ ) (**figure 3.5.17** d to f, black line) and confirms the presence of deep atmospheric convection over the eastern box of the DMI. While, OLR value of the western box of DMI stays above value 220 ( $W/m^2$ )

(figure 3.5.17 d to f, red line) which indicates suppressed tropical convection. As a result, the difference between OLR values of eastern and western box of DMI (OLR east – OLR west) displays negative values during boreal summer-fall of 1998, 2001 and 2004 as displayed in figure 3.5.17 (a) to (c) (black line). Apparently, the DMI index during boreal summer-fall of 1998, 2001 and 2004 shows neutral values in figure 3.5.17 (a) to (c) (red line), because they are natural IOD event years.

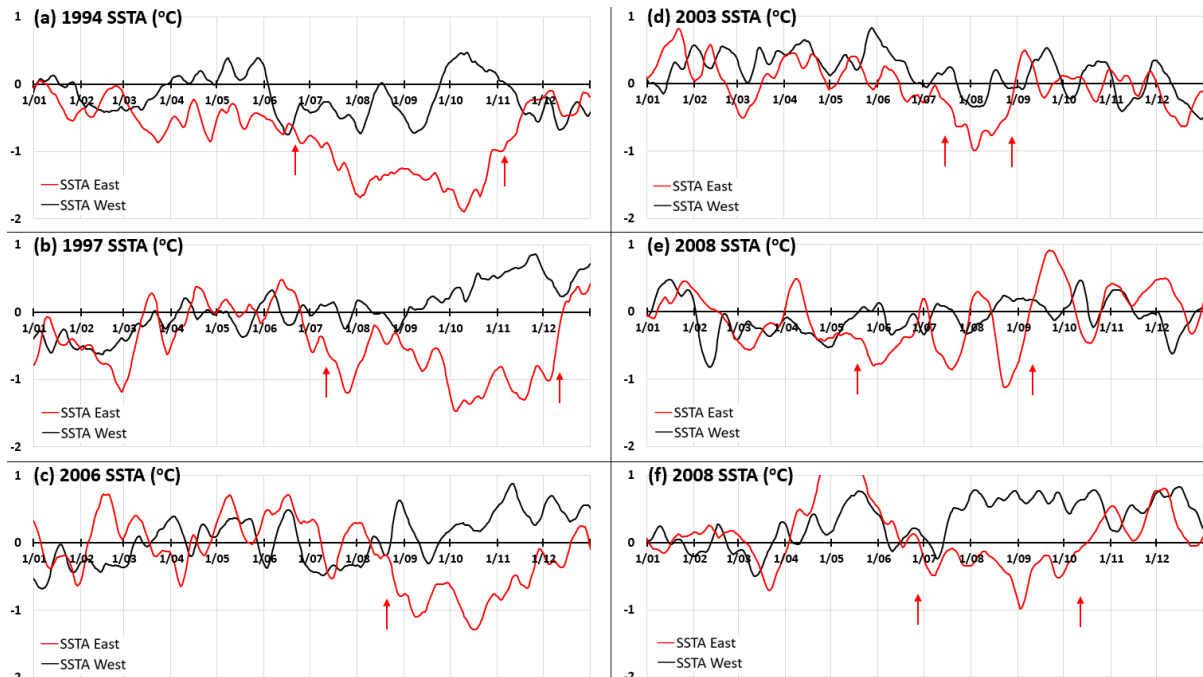


**Figure 3.5.18:** Red line in each plot displays SSTA anomaly of east box of DMI, and black line displays SSTA anomaly of west box of DMI.

The situation is different During boreal summer-fall of 1994, 1997 and 2006, as they are the positive IOD event years. According to previous studies during pIOD event years, negative SSTA of the eastern equatorial Indian Ocean suppress the atmospheric convection in the east and comparatively warm SSTA enhances convection in the west (as discussed previously). Hence, first I explore the area average values of SSTA of eastern box of DMI during boreal summer of these years and then compare it with the suppression of the convection over the eastern tropical Indian Ocean. **Figure 3.5.18** displays the daily time series of SSTA for the eastern and western box of the DMI. **Figure 3.5.19** and **3.5.20** displays the daily time series of OLR values for the eastern and western box of the DMI, the difference between them and DMI index.

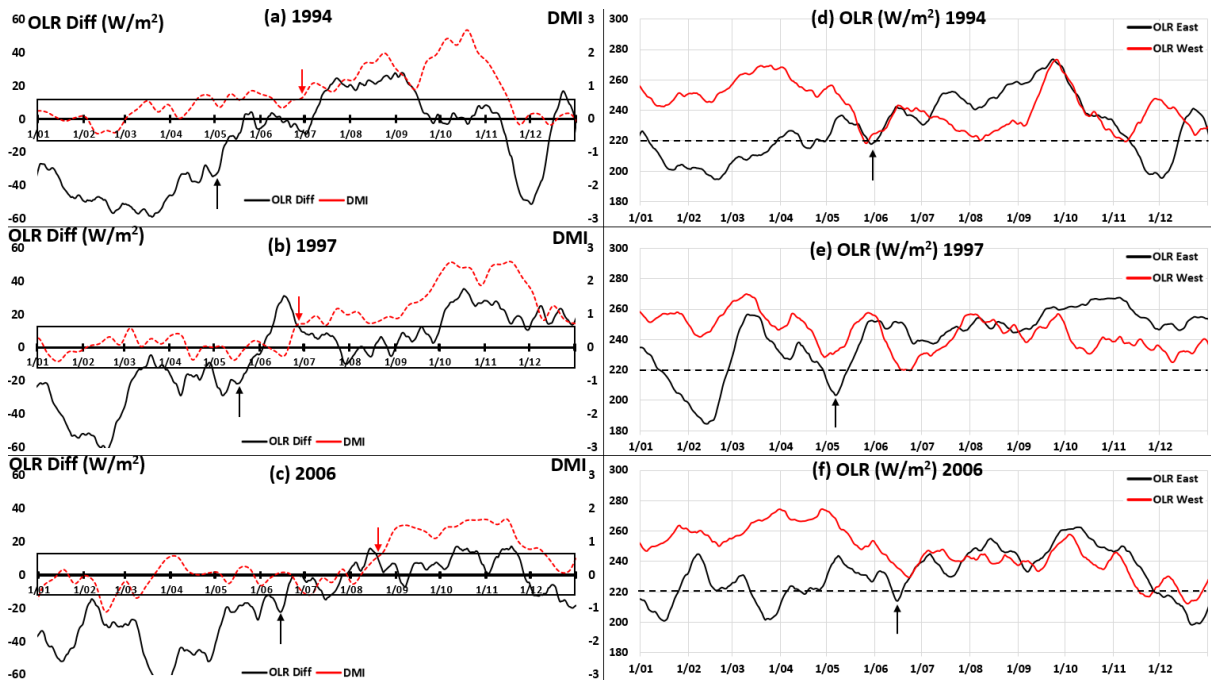


**Figure 3.5.19:** Panels (a) to (c) represents OLR difference (black line,  $W/m^2$ ) between DMI east box and west box along with Dipole mode index (red dashed line, DMI). Panels (d) to (f) indicates OLR values ( $W/m^2$ ) of east box of DMI (black line) and west box of DMI (red line) individually.

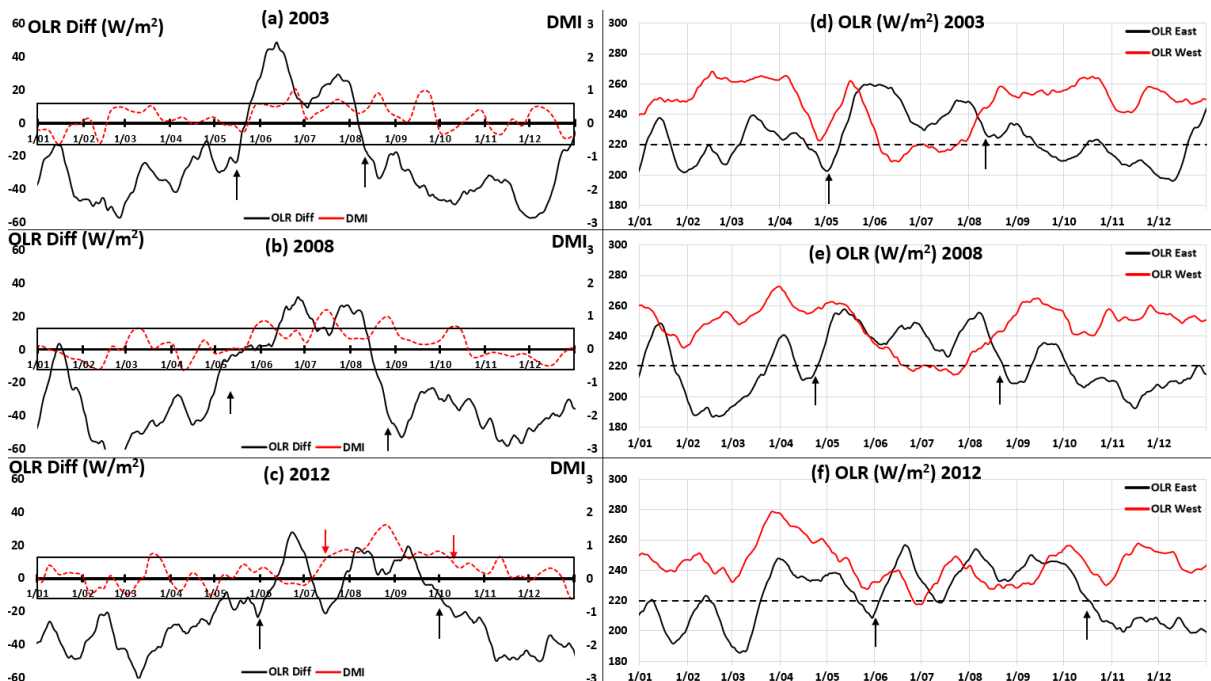


**Figure 3.5.20:** Panels (a) to (c) represents OLR difference (black line,  $W/m^2$ ) between DMI east box and west box along with Dipole mode index (red dashed line, DMI). Panels (d) to (f) indicates OLR values ( $W/m^2$ ) of east box of DMI (black line) and west box of DMI (red line) individually.

In 1994, substantially negative values of SSTA in the eastern box of the DMI are developed from mid-June 1994 (**figure 3.5.18a**, red line, red arrow). Though, the same eastern box of DMI suffers from the suppressed phase of convection from early May 1994, with OLR values 220 ( $W/m^2$ ) and above (**figure 3.5.19d**, black line, black arrow). As a result, the difference between OLR values of eastern and western box of DMI (OLR east – OLR west) rises towards positive values from early May 1994 onwards (**figure 3.5.19a**, black line, black arrow). Later, DMI value gains above 1 STD value from early July 1994 (**figure 3.5.19a**, red dashed line, red arrow).

**Table 3.5.1:** Displays summary of **figure 3.5.18**, **3.5.19** and **3.5.20**.

Year	Suppression of convection (East)	East Box cooling	DMI above 1STD
1994	Early May	Mid June	Early July
1997	Mid May	Mid July	Early July
2006	Mid June	Mid August	Mid August
2003	Early May	Mid July	Not reached
2008	Late April	Mid May	Not Reached
2012	Early June	Early July	Mid July

In 1997, strong negative values of SSTA in the eastern box of the DMI are developed from mid-July 1997 (**figure 3.5.18b**, red line, red arrow). Though, the same eastern box of DMI suffers from the suppressed phase of convection from mid-May 1997, with OLR values 220 ( $W/m^2$ ) and above (**figure 3.5.19e**, black line, black arrow). As a result, the difference between OLR values of eastern and western box of DMI (OLR east – OLR west) rises towards positive values from mid-May 1997 onwards (**figure 3.5.19b**, black line, black arrow). Later, DMI value gains above 1 STD value from early July 1997 (**figure 3.5.19b**, red dashed line, red arrow).

In 2006, strong negative values of SSTA in the eastern box of the DMI are developed from mid-August 2006 (**figure 3.5.18b**, red line, red arrow). Though, the same eastern box of DMI suffers from the suppressed phase of convection from mid-June 2006, with OLR values 220 ( $W/m^2$ ) and above (**figure 3.5.19f**, black line, black arrow). As a result, the difference between OLR values of eastern and western box of DMI (OLR east – OLR west) rises towards positive values from mid-June 2006

onwards (**figure 3.5.19c**, black line, black arrow). Later, DMI value gains value above 1 STD value from mid-August 2006 (**figure 3.5.19c**, red dashed line, red arrow).

In 2003, SSTA of the eastern box of the DMI gains substantial negative values from mid-July 2003 (**figure 3.5.18b**, red line, red arrow). Though, the same eastern box of DMI suffers from the suppressed phase of convection from early-May 2003, with OLR values 220 ( $\text{W/m}^2$ ) and above (**figure 3.5.19f**, black line, black arrow). As a result, the difference between OLR values of eastern and western box of DMI (OLR east – OLR west) rises towards positive values from mid-May 2003 onwards (**figure 3.5.19c**, black line, black arrow). The DMI value cannot rise above 1 STD value during the season of 2003 (**figure 3.5.19c**, red dashed line).

In 2008, SSTA of the eastern box of the DMI gains substantial negative values from mid-May 2008 (**figure 3.5.18b**, red line, red arrow). Though, the same eastern box of DMI suffers from the suppressed phase of convection from late-April 2008, with OLR values 220 ( $\text{W/m}^2$ ) and above (**figure 3.5.19f**, black line, black arrow). As a result, the difference between OLR values of eastern and western box of DMI (OLR east – OLR west) rises towards positive values from mid-May 2008 onwards (**figure 3.5.19c**, black line, black arrow). The DMI value cannot rise above 1 STD value during the season of 2008 (**figure 3.5.19c**, red dashed line).

In 2012, SSTA of the eastern box of the DMI gains substantial negative values from early-July 2012 (**figure 3.5.18b**, red line, red arrow). Though, the same eastern box of DMI suffers from the suppressed phase of convection from early-June 2012, with OLR values 220 ( $\text{W/m}^2$ ) and above (**figure 3.5.19f**, black line, black arrow). As a result, the difference between OLR values of eastern and western box of DMI (OLR east – OLR west) rises towards positive values from early-June 2012 onwards (**figure 3.5.19c**, black line, black arrow). The DMI value cannot rise above 1 STD value from mid-July 2012 (**figure 3.5.19c**, red dashed line, red arrow).

The vital facts of above discussion are summarised in table 3.5.1., which suggest that during each positive IOD event phase, suppressed phase of atmospheric convection develops prior to the appearance of substantial negative SST anomaly of the eastern box of the DMI every time as displayed in table 3.5.1. During this suppressed phase over the eastern tropical Indian Ocean the atmospheric convections

shifts to the western part initially and then later it is disappeared from the western part as well and the entire equatorial Indian Ocean suffers from dry atmospheric phase as displayed in **figure** 3.5.19 and 3.5.20 (d) to (f). The newly developed index, as the difference between OLR values of eastern and western box of DMI (OLR east – OLR west) also displays the similar characteristics in **figure** 3.5.19 and 3.5.20 (a) to (c) (black line), where it initiates its progress toward positive values prior to the appearance of substantial negative values of SSTA in the eastern box of DMI. Later, within two to three weeks of time strong DMI are developed with values above 1 STD as displayed in table 3.5.1 and **figures** 3.5.19 and 3.5.20 (a) to (c) (red line).

### **Summary**

The atmospheric deep convective episodes developed over the study region can consecutively trigger the “SETIO cyclone” which has destructive consequences on the southern Sumatra upwelling favourable winds. Moreover, it can trigger series of WWB episodes over the eastern equatorial Indian Ocean. This sub-section suggests that the suppressed phase of atmospheric convection over the SETIO region arrive prior to the appearance of the negative SSTA of the region, which also comprises the eastern box of the DMI. This suppressed atmospheric convection phase allows strengthening of the seasonal “south easterly” along the southern Sumatra coastline and consecutively the coastal upwelling process is initiated and sustained for a considerable time in the region which further responsible for the development of negative SSTA in the region. This brief analysis creates doubts on the previous claims that suppressed convection over the study region during pIOD phases is an aftermath to the negative SST anomalies. To further verify the claims made in this subsection, a lead-lag correlation analysis between tropical convection and SST anomalies of the regions should be attempted as part of future studies. Moreover, the coupled climate modelling studies on this scenario will precisely evaluate these claims (aftermath or precursor relation between convection and SSTA), which I will attempt in my future role (or anyone else).

### 3.5.5 Composite view of all the SETIO cyclones

The crucial role of the “SETIO cyclones”, consecutively triggered during the “bi-weekly” mode deep convective events over the study region, is explored in previous section 3.5.1 and 3.5.2 using event analysis method. The event analysis of the previous sections assessed the atmospheric conditions and surface circulation of nine different years during boreal summer-fall period. Though the question is, does every year of the study period (1988-2016) can be characterised by these events. To answer this question, I prepared a composite analysis of the entire study period 1988-2016 in this section.

#### (a) Composite statistics

As per the discussion in section 3.4.3c, each “SETIO cyclone” is triggered during the atmospheric “bi-weekly” mode deep convective episodes and according to discussion in section 3.5.1 the suppressed phase of atmospheric convection and absence of the “SETIO cyclone” is the suitable conditions for the southern Java-Sumatra coastal upwelling to thrive. To visualise the difference between atmospheric convective conditions over the study region during positive phase of the IOD events and during neutral phase of the IOD, I prepared time average maps of OLR values. **Figure 3.5.21a** displays the distribution of the OLR values over the tropical Indian Ocean average during the boreal summer-fall of 25 neutral IOD event years in the study period (1988-2016) and **figure 3.5.21b** displays the distribution of the OLR values over the tropical Indian Ocean average during the boreal summer-fall of three pIOD event years in the study period (1994, 1997 and 2006). The red box in **figure 3.5.21 a** and **b** indicate the study are SETIO ( $80^{\circ}$ - $100^{\circ}$ E,  $Eq$ - $10^{\circ}$ S).

Strong presence of atmospheric convection is evident in **figure 3.5.21a** over the study region, which suggests the higher convective atmosphere during average neutral years. While, suppressed phase of atmospheric convection is evident **figure 3.5.21b**, which suggests the higher dryer atmospheric conditions during positive IOD event years. The convective atmosphere can trigger “SETIO cyclones” in the study region while dry atmospheric conditions cannot trigger.

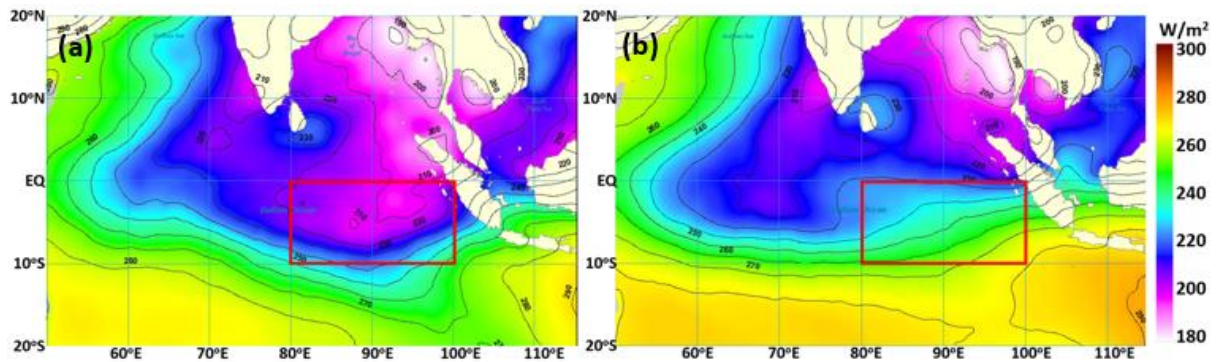


**Figure 3.5.21:** Season averaged OLR values for boreal summer-fall over tropical Indian Ocean. Panel (a) displays OLR values for June to September of neutral 25 years and (b) displays OLR values for June to September of three strong pIOD years.

The prime motive here is to identify the presence of “SETIO cyclone” during boreal summer-fall of each year in the study period (1988-2016). I have analysed daily maps of wind streamline, wind vectors and sea level pressure to visually identify such a cyclonic circulation, during the mature phase of the “bi-weekly” mode deep convective events during the boreal summer-fall of each year in the study period. To considered it as the “SETIO cyclone”, the surface circulation of the study area has to fulfil the following criteria; the synoptic scale cyclonic circulation which is triggered during the mature stage of the deep convective events, the entire synoptic scale coverage is within the study area (the SETIO) and fully developed centre of low pressure.

I recorded total 162 synoptic scale cyclonic circulation by visual interpretation of wind streamline, wind vector and sea level pressure maps, which can be characterised as the “SETIO cyclone”. It is difficult to display all the recorded events; hence, I prepared a table which displays vital characteristics of the recorded “SETIO cyclones”, which includes dates on which they are recorded, locations of the centre and approximate synoptic coverage (in kms). Table 3.5.2 displays all the cyclonic circulation recorded during the boreal summer-fall of 1988 to 2016, they are total 162 events, where events written in bold letters indicates events recorded during positive Indian Ocean dipole event years. Each event has more than 1000 kms of coverage as evident in table 3.5.2, and location of centre of the “SETIO cyclone” in table 3.5.2 indicates entire coverage is within the study region.

**Table 3.5.2:** Displays detected cyclonic circulation in lower atmosphere in daily wind fields maps triggered from Rossby wave response during the convective events within the SETIO.

Date	Location	Extent (km)	Date	Location	Extent (km)	Date	Location	Extent (km)
3-Jul-88	88E/5S	1150	6-Jun-93	89E/6S	1200	10-Jun-99	96E/3S	1050
9-Aug-88	87E/4S	1700	1-Jul-93	93E/4S	1050	15-Jun-99	91E/3S	1200
25-Sep-88	97E/1N	1400	19-Jul-93	99E/1S	1200	4-Jul-99	93E/3S	1750
3-Jun-89	95E/8S	1800	29-Jul-93	95E/5S	1350	25-Jul-99	96E/3S	1150
5-Jul-89	88E/7S	1050	12-Sep-93	86E/2S	1600	26-Aug-99	91E/1S	1660
7-Jul-89	100E/4S	1200	27-Sep-93	96E/2S	1450	28-Sep-99	97E/2S	1400
14-Jul-89	94E/9S	1750	<b>8-Jun-94</b>	<b>86E/4S</b>	400	4-Jun-00	94E/4S	1200
14-Aug-89	92E/6S	1150	6-Jun-95	91E/2S	1050	20-Jun-00	90E/5S	1800
26-Aug-89	95E/2S	1660	20-Jun-95	97E/3S	1200	3-Jul-00	94E/8S	2100
11-Sep-89	96E/2S	900	5-Jul-95	97E/6S	1750	29-Jul-00	86E/4S	1100
19-Sep-89	84E/2S	1750	25-Jul-95	96E/6S	1150	9-Aug-00	86E/1S	1250
6-Jun-90	92E/3S	1150	17-Aug-95	95E/2S	1660	21-Aug-00	92E/1S	1050
21-Jun-90	97E/1S	1200	19-Sep-95	96E/1S	1800	20-Sep-00	92E/4S	1200
14-Jul-90	92E/7S	1050	25-Sep-95	97E/3S	1050	6-Jun-01	94E/6S	1050
3-Aug-90	98E/9S	1200	10-Jun-96	96E/4S	1200	26-Jun-01	92E/7S	1200
23-Aug-90	93E/2S	1350	8-Jul-96	93E/4S	1150	26-Jul-01	95E/7S	1150
4-Sep-90	97E/3S	1600	14-Aug-96	96E/2S	1050	4-Aug-01	92E/4S	1350
22-Sep-90	94E/3S	1450	28-Aug-96	100E/6S	1400	4-Sep-01	90E/3S	1600
5-Jun-91	95E/4S	1200	9-Sep-96	101E/5S	1750	16-Sep-01	97E/2S	850
27-Jun-91	88E/3S	1800	29-Sep-96	93E/1S	1100	27-Sep-01	98E/2S	1050
22-Jul-91	96E/3S	2100	<b>20-Jul-97</b>	<b>99E/2N</b>	350	8-Jun-02	96E/2S	1400
12-Sep-91	98E/1N	1100	4-Jun-98	98E/3S	1800	24-Jun-02	88E/2S	1800
23-Sep-91	91E/1N	1800	16-Jun-98	101E/8S	1050	6-Jul-02	97E/5S	1050
6-Jun-92	99E/4S	1050	18-Jul-98	92E/3S	1200	17-Jul-02	96E/9S	1200
17-Jun-92	106E/8S	1200	8-Aug-98	94E/3S	1150	1-Aug-02	92E/4S	1750
10-Jul-92	88E/5S	1150	20-Aug-98	90E/5S	1700	24-Aug-02	98E/1S	1150
2-Aug-92	91E/2S	1050	22-Sep-98	92E/8S	1400	3-Sep-02	96E/0N	1150
14-Aug-92	94E/0N	1400				29-Sep-02	88E/1N	1050
26-Aug-92	101E/4S	1750						
25-Sep-92	88E/3S	1150						
Date	Location	Extent (km)	Date	Location	Extent (km)	Date	Location	Extent (km)
2-Jul-03	97E/0N	600	5-Jun-09	100E/6S	1750	5-Jun-14	98E/4S	1800
17-Aug-03	98E/3S	1050	25-Jun-09	96E/6S	1150	15-Jun-14	94E/3S	1050
27-Sep-03	96E/2S	1400	4-Aug-09	97E/3S	1200	24-Jun-14	101E/6S	1200
5-Jun-04	97E/2S	900	16-Aug-09	86E/4S	1050	5-Jul-14	94E/2S	1150
3-Jul-04	96E/4S	1750	17-Sep-09	96E/4S	1200	13-Jul-14	96E/8S	1050
16-Jul-04	96E/6S	1150	7-Jun-10	95E/8S	1350	29-Jul-14	88E/5S	1400
24-Jul-04	93E/4S	1660	24-Jun-10	92E/4S	1600	5-Aug-14	91E/6S	1750
24-Aug-04	98E/3S	950	2-Jul-10	91E/5S	1800	22-Aug-14	100E/4S	1200
24-Sep-04	88E/6S	1200	17-Jul-10	92E/6S	2100	24-Sep-14	95E/3S	1050
17-Jun-05	103E/7S	1750	16-Aug-10	90E/3S	1100	12-Jun-15	96E/2S	1200
13-Jul-05	99E/3S	1150	23-Aug-10	92E/9.5S	1800	17-Jul-15	94E/3S	1350
19-Aug-05	96E/4S	1200	6-Sep-10	93E/2S	1050	17-Aug-15	88E/5S	1600
27-Aug-05	98E/5S	1050	22-Sep-10	96E/4S	1200	28-Aug-15	94E/2N	1450
5-Sep-05	88E/3S	1200	5-Jun-11	92E/4S	1400	1-Sep-15	94E/2S	1200
28-Sep-05	95E/3S	1350	28-Jun-11	91E/6S	1550	24-Sep-15	96E/8S	1050
<b>21-Jun-06</b>	<b>94E/1S</b>	800	14-Jul-11	94E/3S	800	5-Jun-16	94E/8S	1200
<b>7-Jul-06</b>	<b>84E/3S</b>	600	14-Aug-11	92E/4S	1200	20-Jun-16	94E/8S	1350
16-Jun-07	100E/4S	1200	28-Sep-11	91E/5S	950	12-Jul-16	92/5S	1550
21-Jul-07	93E/7S	1150	5-Jun-12	102E/5S	1150	22-Jul-16	94E/6S	1350
29-Jul-07	98E/4S	1050	7-Jul-12	90E/3S	1050	12-Aug-16	93E/5S	1600
20-Aug-07	98E/0N	1400	20-Jul-12	97E/2N	1200	26-Aug-16	96E/8S	1450
19-Sep-07	98E/0N	1550	16-Aug-12	97E/2S	400	5-Sep-16	91E/4S	1200
17-Jul-08	90E/4S	800	11-Jun-13	100E/5S	1200	12-Sep-16	102E/7S	1800
29-Aug-08	96E/0N	1200	8-Jul-13	101E/5S	1050	27-Sep-16	99E/7S	1700
			7-Aug-13	92E/6S	1200			
			28-Aug-13	102E/6S	1350			
			7-Sep-13	96E/4S	1550			

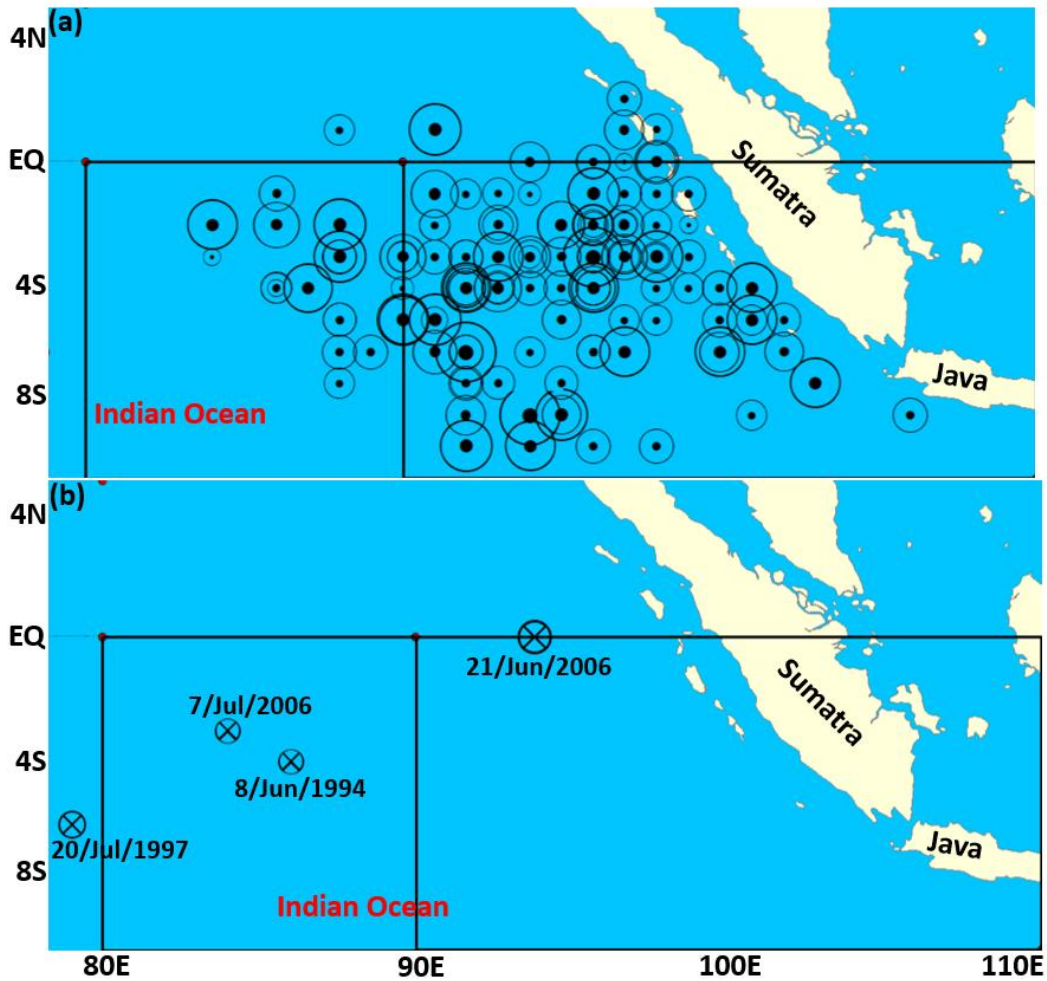


**Figure 3.5.22:** Location of cyclonic circulation triggered from atmospheric Rossby waves during “bi-weekly” convective event in the study region during June to September of study period (1988-2016). Panel (a) displays locations all event of 1988 to 2016 (b) displays locations of events during pIOD years 1994, 1997 and 2006.

**Table 3.5.3:** Displays summary of values of table 1 and **figure 4**.

Total events	162 (28 years)
Events during active pIOD years	5 (3 years)
Events in other years	158 (25 years)
Events per season	7 (6.52)

The location centre of the cyclonic circulation (displayed in table 3.5.2) is also displayed in map form in **figure 3.5.22a** for visual examination. The map in **figure 3.5.22a** reveals the strong presence of “SETIO cyclones” in the eastern box of the DMI (90°-110°E and Eq-10°S) and they are rarely developed outside of this box. With

synoptic scale coverage and their centre within the eastern box of DMI indicates that each of these “SETIO cyclone” can affect the surface circulation of the study region (**figure 3.5.22**, table 3.5.2). They can trigger the eastern equatorial “westerly wind burst (WWB)” events as northern branch of the “SETIO cyclone” and they can reverse the seasonal “south-easterly” along the southern Sumatra coastline as eastern branch of the cyclonic circulation (as discussed in section 3.4.3d). According to **figure 3.5.22b** the centre of “SETIO cyclones” triggered during positive phase of IOD events are developed far from the southern Sumatra coastline and hence their synoptic coverage cannot reach to the southern Sumatra coastline and cannot alter the season “south easterly” of the region.

The summary statistics of table 3.5.2 and **figure 3.5.22** is prepared in table 3.5.3, which indicates that total 162 “SETIO cyclones” are triggered during the study period of 28 years (1988-2016). If weak or far developed “SETIO cyclones” triggered during pIOD events of 1994, 1997 and 2006 are avoided then, statistics suggest that total 158 “SETIO cyclones” are triggered during the neutral IOD phases of 25 years. Hence, these statistics suggests that approximately seven “SETIO cyclones” are triggered during the boreal summer of the any particular year. According to discussion in section 3.5.4c, the “SETIO cyclone” and related altered surface circulation has a lifetime of 8-10 days, hence seven “SETIO cyclones” can alter the surface circulation of the region for 50-60 days during the season. The period from 1st June to 30th September is characterised as boreal summer-fall season in this study which has typically 122 days of life. During 122 days of life, “SETIO cyclones” alter the surface circulation for 50-60 days which is almost half of the season. Hence, half of the season suffers from the altered surface circulation, which has devastating consequences on the Java-Sumatra coastal upwelling system (as discussed in section 3.5.1 and 3.5.2). The other half of the season is not available straight forward and it is available in the form of smaller gaps of a week or two between consecutive “SETIO cyclone” which is not the sufficient period for the coastal upwelling to thrive in the region.

### (b) Interannual statistics

According to table 3.5.2, number of “SETIO cyclone” triggered during each year is not exactly same; hence their percentage presence in the season of 122 days is also not identical. To visualise the statistics at interannual time scale, I prepared a bar plot in **figure 3.5.23**, which displays the number of “SETIO cyclone” triggered during boreal summer-fall of each individual year in the study period. The bar plot of **figure 3.5.23** confirms the presence of 5 to 9 “SETIO cyclones” during the boreal summer of the neutral IOD event years. This number drops during positive phase of the IOD event years up to 1-3 only (as marked by arrow in **figure 3.5.23**).

As mentioned above the “SETIO cyclones” are triggered during the atmospheric deep convective phase. Hence, to visualise the statistical presence of deep atmospheric convection over the study region during boreal summer-fall of each year at interannual time scale I calculated the statistical presence of the deep convective events. I prepared an area average daily time series of OLR anomaly (OLRA) over the study region for the entire study period (1988-2016). The deep convective event over the study region can be identified as the OLRA values below  $-10 \text{ W/m}^2$ . Hence, the days in the season with OLRA values below  $-10 \text{ W/m}^2$  are identified and calculated as percentage compare to 122 days (length of the season), where 122 days hold 100 percent value. The derived presence of deep convective event in the boreal summer-fall of each in the form of percentage is displayed in a bar plot in **figure 3.5.24a**.

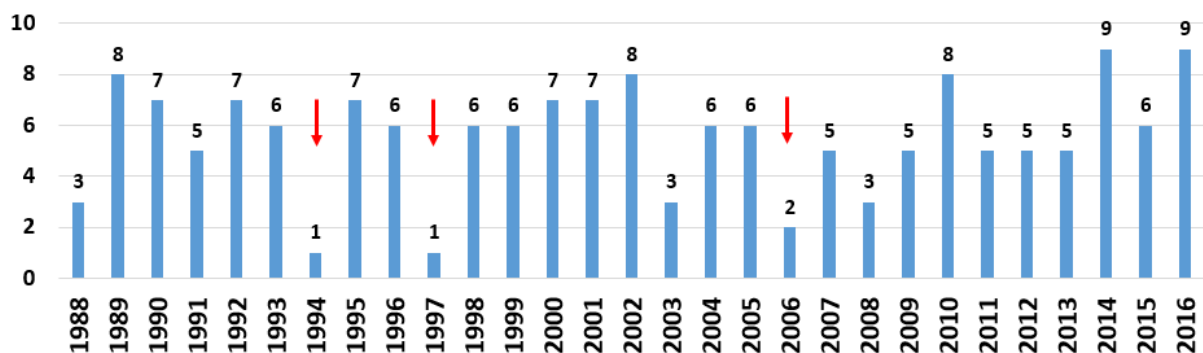


**Figure 3.5.23:** Number of “SETIO cyclones” recorded during the boreal summer-fall of each year (data adopted from table 3.5.2). Red arrows indicate positive Indian Ocean Dipole event years.

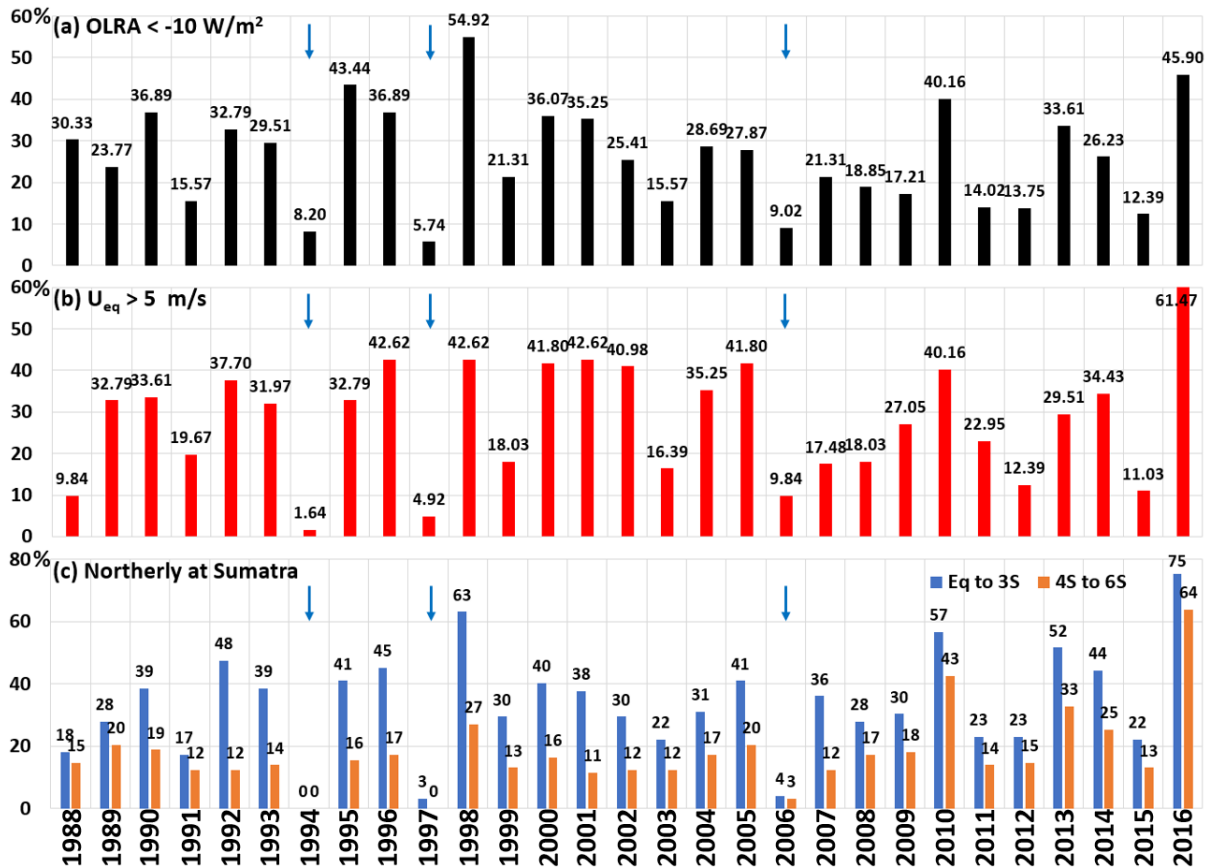


**Figure 3.5.24:** Seasonal presence of different values in percentage from June to September. Panel (a) displays presence of OLR anomaly values below  $-10$  ( $W/m^2$ ) averaged over  $80^\circ$ - $100^\circ E$  and  $2^\circ N$ - $10^\circ S$ , (b) displays presence of zonal wind speed values above  $5$  ( $m/s$ ) averaged over  $70^\circ$ - $90^\circ E$  and  $1^\circ N$ - $1^\circ S$ , (c) displays presence of northerly with values above  $3$  ( $m/s$ ) averaged over  $97^\circ$ - $102^\circ E$  and  $00^\circ N$ - $3^\circ S$  (blue bars) and  $100^\circ$ - $104^\circ E$  and  $4^\circ S$ - $6^\circ S$  (orange bars). Blue arrow indicates positive Indian Ocean Dipole events years.

The deep convective events can trigger “SETIO cyclone”, which consecutively triggers the eastern equatorial “westerly wind burst (WWB)” events as northern branch of the “SETIO cyclone” and they can reverse the seasonal “south-easterly” along the southern Sumatra coastline as eastern branch of the cyclonic circulation (as discussed in section 3.4.3d). Hence, to visualise the presence of WWB events at interannual time scale, the time series of area average zonal wind speed is derived and days with zonal wind speed values above  $5$   $m/s$  is calculated during boreal summer-fall of every year. This derived number of days with higher zonal wind speed during each season, is displayed in percentage form compare to 122 days in **figure 3.5.24b**.

Likewise, to visualise the presence of reversed winds along the southern Sumatra coastline at interannual time scale, the time series of area average wind direction is derived and days with northerly winds in the region is calculated during boreal summer-fall of every year. This derived number of days with northerly winds during each season, is displayed in percentage form compare to 122 days in **figure 3.5.24b**. As discussed in section 3.4.3d, southern most locations of the southern Sumatra coastline are less affected by “SETIO cyclones” compare to the northern locations; hence, presence percentage of northerly winds are derived independently for locations Eq to 3°S (blue bars in **figure 3.5.24c**) and for 4°S to 6°S (orange bars in **figure 3.5.24c**).

Strong presence of the atmospheric deep convective phase is evident during boreal summer-fall of the most years in the study period in **figure 3.5.24a**. The bar plot of **figure 3.5.24a** confirms the presence of deep convective atmosphere for 20% to 60% time of the season during the boreal summer of the neutral IOD event years. While, during pIOD events years this presence is declined to 5% to 15% (marked arrows, **figure 3.5.24a**).

Presence of the higher zonal wind speed is evident during boreal summer-fall of the most years in the study period in **figure 3.5.24b**. As per the discussion in section 3.5.3c convective episode has longer lifetime than consecutively triggered abrupt wind events and “SETIO cyclones”. Hence, in the bar plot of **figure 3.5.24a** the eastern equatorial “westerlies” mark their presence with 20% to 50% time during the boreal summer-fall of the neutral IOD event years. While, during pIOD events years this presence is declined to 2% to 10% (marked arrows, **figure 3.5.24b**). Likewise, the northerly winds marked their presence in the southern Sumatra coastal region during each season with range of 20-60% at location Eq-3°S (**figure 3.5.24c**, blue bars) and 15-30% presence at locations 3°S-6°S (**figure 3.5.24c**, orange bars). During positive IOD event years these presence declines to 0-5% only (**figure 3.5.24c**, marked arrows).

Substantial difference between presence of northerly winds between location Eq-3°S and 3°S-6°S in **figure 3.5.24c** in a single season is crucial for the southern Java coastal upwelling to develop in the season, because this is the time when “northerly winds persist at locations Eq-3°S, while “southerly” winds persist at locations

4°S to 6°S which consecutively develops sufficient precondition so that the full upwelling conditions can thrive along the southern Java coastline.

### **Summary**

This sub-section statistically confirms the presence of the “SETIO cyclones” in the study region (the SETIO) during boreal summer-fall of most years in the study period of 28 years. (1988-2016). The destructive effects of the “SETIO cyclones” on the southern Java-Sumatra upwelling region, mainly the reversal of season “south easterly” along the southern Sumatra coastline and the series of WWB episodes over the eastern equatorial Indian Ocean, are also confirmed for year. The “SETIO cyclone” and their effects are remarkably absent during strong pIOD event years. This all discussion confirms the dominance of the convectively triggered “SETIO cyclone” on one of the most important coupled climatic mode of the Indian Ocean called the Indian Ocean Dipole events.

## CHAPTER 4: SUMMARY AND CONCLUSION

This study aims to explore the unexplored physical oceanographic and climatic processes over the study region, which actively dominate the ocean-atmosphere coupled system of the southern equatorial Indian Ocean and controls the most important climatic mode of the Indian Ocean the IOD. This study intensively analyses the oceanic process of the southern Java-Sumatra coastal region during boreal summer-fall of 1998-2016, as this region is claimed as the region of strong coastal upwelling during boreal summer-fall in several previous studies though related processes are complex in understanding.

In the beginning, this study noted that the seasonal upwelling favourable winds along the southern Java coastline are more frequent than southern Sumatra coastline at interannual time scale. The SST anomalies along the southern Java-Sumatra coastline is systematically examined, which reveals that though upwelling favourable winds predominate in the southern coastal Java region it cannot exhibit negative SST anomalies in all the season of the study year. The careful examination of the SST anomaly suggests the north-eastward progress of the negative SST anomalies during the strong positive IOD event years, where negative SST anomalies at the southern Java coastline leads the progress as it is the onset location of negative SST anomalies.

The SST anomalies uncover very complex signature of the SST in the coastal region along two adjacent coastlines of the southern Java-Sumatra. These adjacent coastlines of southern Java and southwest Sumatra are hypothetical anticipated to develop a strong surface cooling signature (-ve SSTA) through coastal upwelling process under the influence of season "south easterly" winds (coast parallel winds) during boreal summer-fall every year. Though the sea surface temperature (SST) data of last three decades of this region exhibits very strange signature, where surface cooling signature (during boreal summer) is limited to rare instances, which is matter of study from a long time. For example, during certain years both coastlines do not exhibit negative SST anomaly during the entire boreal summer-fall, during certain years only the southern Java coastline exhibit negative SST anomaly in the season, while in certain years both coastlines as a single system exhibits strong negative SST anomalies (known as positive IOD phase).

The thorough analysis of the local wind along the southern Java-Sumatra coastline as local forcing and the zonal winds over the equatorial Indian Ocean as remoter forcing is performed, which reveals the strong interannual variation of the zonal winds of the eastern equatorial Indian Ocean along with the “south easterly” of the southern Sumatra coastal region with the covarying nature.

The wavelet analysis of the zonal equatorial winds and atmospheric convection of the study region discovers the existence of high frequency “bi-weekly” mode intraseasonal atmospheric oscillations in the study region (the SETIO) during boreal summer-fall. The synoptic structure of the atmospheric deep convective events is demonstrated, which explains the maintenance mechanism of the “bi-weekly” mode atmospheric oscillations. The synoptic structure of the deep convective events uncovers consecutively triggered anomalous cyclonic circulation in the lower atmosphere of the study region during the phase of the atmospheric convective event. The anomalous cyclonic circulation is triggered by the atmospheric Rossby wave response developed from the atmospheric convective heating. This synoptic scale anomalous cyclonic circulation of the region is named the “SETIO cyclone” in this section. It is demonstrated in this study that, the strong equatorial “westerly” events of the eastern equatorial Indian Ocean and reversal of seasonal “south-easterlies” along the southern Sumatra coastline are triggered from the “SETIO cyclone”. Consecutively triggered “westerly” events, at the eastern equatorial Indian Ocean, have sufficient wind speed and zonal coverage that it can be considered as the WWBs of the Indian Ocean. The wind reversal along the south Sumatra coastline, consecutively triggered from the “SETIO cyclones”, is not noticed in any previous studies and they are discovered in this study.

The series of “SETIO cyclones” during boreal summer-fall triggers series of WWB events over the eastern equatorial Indian Ocean. The presence of WWB is known in the eastern equatorial Indian Ocean for a long time, and it was claimed in a number of previous studies that these intraseasonal WWB episodes deepen the thermocline of the eastern equatorial Indian Ocean and along the southern Java-Sumatra coastline by triggering downwelling Kelvin waves. Though, no previous studies can precisely claim the mechanism responsible for the trigger of these WWB episodes. This study explains that the “SETIO cyclone” triggers the WWB episode

over the eastern equatorial Indian Ocean as the northern branch of the cyclonic circulation over the SETIO region. The actual effect of downwelling Kelvin waves on the depth of thermocline is still under speculation as this region suffers from the lack of high temporal resolution subsurface data.

The event analysis explores the role “SETIO Cyclones” in the intraseasonal variation of the seasonal “south easterly” winds of the southern Java-Sumatra coastal region and it confirms that the “SETIO cyclones” profoundly affect the seasonal winds of the region. During the active phase of the “SETIO cyclones” the seasonal “south easterly” of the southern coastal Sumatra completely reverse their direction and becomes “north westerly”, while the seasonal “south easterly” of the southern coastal Java remain unaltered during any “SETIO cyclone” episode. As a result, the strong coast parallel wind stress cannot develop in the southern Sumatra coastal region during the most season of the study period (1988-2016), while the seasonal coast parallel winds along the southern Java coastline are persistently strong during most seasons. The suppressed phase of atmospheric convection over the study region followed by the absence of “SETIO cyclone” can be considered as “the atmospheric window” for the seasonal “south easterly” winds to thrive along the southern Sumatra coastline. Consecutively strong coast parallel wind stress can be developed along the southern Sumatra coastline only during suppressed atmospheric convection phase over the study region.

This situation discussed above uncovers very complex settings of surface winds along two adjacent coastlines of the southern Java-Sumatra region. A simple the theory of coastal upwelling along the finite coast is used in this study to explore the effects of complex surface wind forcing along the Java-Sumatra coastline on the oceanic upper layer. The theory examines the response of the surface mixed layer and the thermocline to the complex and highly varying surface wind conditions of the region by treating them as individual segments of the single coastline. The theory uncovers the precise situations when the turbulent entrainment of the cold thermocline water into the surface mixed layer can happen. The theory of coastal upwelling at a finite length coast divides the longer coastline in segments and suggest the crucial role of precursor segment (in Kelvin wave propagation direction) in the development of full upwelling conditions at a certain segment of the coastline. It suggests that full

upwelling conditions cannot develop at a certain segment of the coast on its own with its local strong coast parallel wind conditions, and it must require sufficient coast parallel winds at precursor locations as well, which sets up preconditioning for full upwelling conditions at the next location (in Kelvin wave propagation direction). This hypothetical explanation suggests that the local strong coast parallel winds along the southern Java coastline is not sufficient to develop full upwelling conditions in the region and it requires preconditioning from the southern Sumatra coastline.

There are three different atmospheric conditions can be developed over the study region which reveals three different weather mechanisms for the ocean response in the Java-Sumatra upwelling region. They can be considered IOD phases pre-cursor atmospheric signatures.

The first atmospheric condition can be characterised as, the presence of strong atmospheric convective aggregation over the study region throughout the season, which consecutively triggers series of “bi-weekly” mode convective episode and series of the “SETIO cyclone” without any substantially temporal gap (the atmospheric window). The series of “SETIO cyclones” develops “north westerly” winds along the southern Sumatra coastline. Hence, there is no “atmospheric window” during which the seasonal “south easterly” can develop. As a result, during this atmospheric condition, the strong coast parallel winds thrive solely along the southern Java coastline, and the entire southern Sumatra coastline suffers lack of coast parallel winds. In this situation, despite the presence of coastal parallel winds along the southern Java coastline, the region cannot reach to full upwelling conditions due to lack of sufficient preconditioning at southern Sumatra locations. These atmospheric conditions are developed during the negative phase of the IOD events. Consecutively, under the influence of series of “SETIO cyclones” and “north westerly” winds the south equatorial counter current (SECC; Schott et al., 2009) is intensified which brings surface equatorial warm water in the southern Sumatra coastal region through southward advection, which may extend up to southern Java coastal region. As a result, surface warm water predominates in the entire southern Sumatra and Java coastal region in the season, which exhibits positive the SST anomaly in the region.

The second atmospheric condition is the presence of “the atmospheric window” over the study region for a substantial time (for example for a month) in the season,

during which the seasonal “south easterly” winds can develop along the southern Sumatra coastline. As a result, the strong coast parallel winds are developed along the southern Java coastline with extended coverage up to the southern Sumatra coastline during the “atmospheric window”. Hence, the southern Sumatra coastline can provide sufficient preconditioning and the full upwelling conditions can be developed along the southern Java coastline. These atmospheric conditions are developed during a neutral phase of IOD events, during which the southern coastal Java exhibits strong surface cooling signature, developed from the strong coastal upwelling and consecutively triggered the south Java current (SJC; Schott *et al.*, 2009)

The third atmospheric condition is, the suppressed phase of atmospheric convection over the study region prevails throughout the season followed by the absence of “SETIO cyclone” in the season; hence, the entire season is a big “atmospheric window”. During this atmospheric condition, strong coast parallel winds are developed along both the adjacent coastline of the southern Java-Sumatra coastal region in the season. Hence, rarely developed the strong coast parallel winds along the entire southern Sumatra coastline intensify upwelling conditions at each segment of the coastline. Consecutively, under the influence of strong cumulative upwelling effect at precursor locations (at location 1°S to 4°S of the southern Sumatra coastline), the locations at southernmost end of the southern Sumatra coastline (5°S and 6°S) and the entire southern Java coastline (7°S to 10°S) exhibit strongest upwelling conditions, which successively triggers the strongest surface cooling at the locations 5°S to 6°S. These atmospheric conditions are developed during a positive phase of IOD events.

Locations 1°S to 3°S along the Southern Sumatra coastline (**figure 3.5.11**) never reach to the full upwelling conditions in any season of any year. The primary reason behind this situation is weaker coast parallel winds in the region along with weak or no “easterlies” at the eastern equatorial Indian Ocean which supports the eastern equatorial upwelling. Though, the negative SST anomalies are developed in these northern locations during the strong positive phase of the IOD events, which are the results from the north-eastward progress of strong negative SST anomalies developed at southern Java locations (7°S to 10°S) and Southern Sumatra locations (5°S and 6°S) in the region. The north-eastward progress of the negative SST

anomalies in the region from southern locations can be characterised by the horizontal advection of cooler upwelled water.

The mechanism of horizontal “north-eastwards” progress of the negative SST anomalies is explained in detail in Kämpf and Kavi, 2018 (**figure 6a**). They suggested that the rarely developed coastal upwelling along the southern Sumatra coastline consecutively triggers another upwelling jet in the region transient to the South Java Current (SJC) (Sprintall *et al*, 1999) and they called it South East Sumatra Current (SESC). This rarely triggered SESC interacts with the south equatorial current (or south equatorial counter current, SECC; Schott *et al.*, 2009) in the region and develops strong cold-water wedge extending westward in the eastern box of IOD events (see **figure 5c** and **6a** in Kämpf and Kavi, 2018). As a result, the growth of rarely developed full upwelling conditions at both adjacent coastlines of the southern Java-Sumatra triggers strong surface cooling in the region, and north-eastward progression of the upwelled surface cold water develops strong surface cooling over the entire eastern box of the DMI.

Previous studies suggested that, once the substantial negative SST anomaly is developed in the eastern box of the DMI, it alters the air-sea coupling of the region and consecutively suppresses the convection of the region which cannot be restored by itself. Though, this study re-establishes the dominant role of the atmospheric convection over the study region and suggests that the suppressed phase of atmospheric convection over the SETIO region arrive prior to the appearance of the negative SSTA of the eastern box of the DMI. This suppressed atmospheric convection phase creates the “atmospheric window” which further allows the seasonal “south easterly” to grow along the southern Sumatra coastline and consecutively the coastal upwelling is triggered in the region which further develops surface cooling in the region. Hence, it suggests that the suppressed phase of atmospheric convection over the eastern box of the DMI is not the aftermath of the negative SST anomaly of the region, but it is the precursor of them.

Moreover, the examples of the aborted positive IOD events also confirm the dominance of the atmospheric convection in the SETIO region. During aborted pIOD events, abruptly developed atmospheric deep convective phase over the study region destroys the coast parallel “south easterly” winds in the southern Sumatra coastal

region by setting up “SETIO cyclone” over the study region and the “atmospheric window” is withdrawn. Consecutively, previously developed full upwelling conditions along the southern Sumatra coastline is withdrawn and surface cooling in the region is suspended. The withdrawal of upwelling in the region also suspend the north-eastward advection of cold water by terminating the SESC. Although, the coast parallel seasonal winds along the southern Java coastline remains unaltered during any atmospheric conditions, as a result, surface cooling signature prevails with the presence of SJC in the region till the full upwelling conditions.

This study establishes the dominance of the atmospheric convective variability over the SETIO region in the IOD mode air-sea coupling. It is interesting to see in future that, is this atmospheric convective oscillation over the SETIO region and the “SETIO cyclones” are present in the climate models of the region. The “SETIO cyclones” are topographically trapped on the eastern side from the “Barisan Mountains” range; hence, it is also interesting to visualise the growth of the “SETIO cyclones” without eastern edge blockade in the climate models setup.

The SETIO region is characterised by the complex subsurface stratification, with the presence of the salinity stratified sub surface barrier layer and previous modelling studies suggest that the barrier layer can act as a blockade in the upwelling process. Though the southern Java-Sumatra coastal region suffers from the scarcity of the high temporal resolution subsurface observation and this is the reason why this study ignored the effects of the barrier layer. A couple of permanent mooring and the high-density ARGO network in the region will help the scientific community to understand sub-surface processes precisely.

The 8-20 days filtered time series of the OLR anomaly, which represents the “bi-weekly mode” of convective oscillations, along with zonal wind speed values averaged over the eastern equatorial Indian Ocean region ( $70^{\circ}$ - $90^{\circ}$  E,  $5^{\circ}$ N- $5^{\circ}$ S) at the similar filtered range is displayed in **figures of Appendix A** as the composite plot.

## REFERENCES

- Abram, N., Gagan, M., Cole, J., Hantoro, W.S., Mudelesee, M. (2008). Recent intensification of tropical climate variability in the Indian Ocean. *Nature Geosci* 1, 849–853. <https://doi.org/10.1038/ngeo357>
- Adames, Á. F., Wallace, J. M., & Monteiro, J. M. (2016). Seasonality of the Structure and Propagation Characteristics of the MJO. *J. Atmos. Sci.*, 73, 3511-3526. <https://doi.org/10.1175/JAS-D-15-0232.1>
- Annamalai, H., Murtugudde, R., Potemra, J., Xie, S. P., Liu, P., & Wang, B. (2003). Coupled dynamics over the Indian Ocean: Spring initiation of the zonal mode. *Deep-Sea Res. II: Tropical Studies in Oceanography*, 50(12-13), 2305-2330. [https://doi.org/10.1016/s0967-0645\(03\)00058-4](https://doi.org/10.1016/s0967-0645(03)00058-4)
- Ashok, K., Guan, Z., Yamagata, T. (2001). Impact of the Indian Ocean dipole on the relationship between the Indian monsoon rainfall and ENSO. 28, 23, 4499-4502. <https://doi.org/10.1029/2001GL013294>
- Ashok, K., Guan, Z., & Yamagata, T. (2003). A look at the relationship between the ENSO and the Indian Ocean dipole. *Journal of the Meteorological Society of Japan*. Ser. II, 81(1), 41-56.
- Ashok, K., Guan, Z., Yamagata, T. (2003). Influence of the Indian Ocean Dipole on the Australian winter rainfall. *Geophys. Res. Lett.* 30, 1821. <https://doi.org/10.1029/2003GL017926>
- Ashok, K., Guan, Z., Saji, N. H., Yamagata, T. (2004). Individual and combined influences of ENSO and the Indian Ocean Dipole on the Indian summer monsoon. *J. Clim.* 17, 3141–3155. [https://doi.org/10.1175/1520-0442\(2004\)017%3C3141:IACIOE%3E2.0.CO;2](https://doi.org/10.1175/1520-0442(2004)017%3C3141:IACIOE%3E2.0.CO;2)
- Atlas, R., Hoffman, R.N., Ardizzone, J., Leidner, S.M., Jusem, J.C., Smith, D.K., & Gombos, D. (2011). A Cross-calibrated, Multiplatform Ocean Surface Wind Velocity Product for Meteorological and Oceanographic Applications. *Bull. Amer. Meteor. Soc.*, 92, 157-174. <https://doi.org/10.1175/2010BAMS2946.1>
- Bakun, A. (1973). Coastal upwelling indices, west coast of North America, 1946-71.
- Barnston, A.G., Tippett M.K., L'Heureux M.L., Li S., & DeWitt D.G. (2012). Skill of Real-Time Seasonal ENSO Model Predictions during 2002–11: Is Our Capability Increasing? *Bull. Amer. Meteor. Soc.*, 93, 631–651, <https://doi.org/10.1175/BAMS-D-11-00111.1>
- Behera, S. K., Krishnan, R., & Yamagata, T. (1999). Unusual ocean-atmosphere conditions in the tropical Indian Ocean during 1994. *Geophysical Research Letters*, 26(19), 3001-3004.

- Behera, S. K., & Yamagata, T. (2003). Impact of the Indian Ocean Dipole on the Southern Oscillation. *J. Meteorol. Soc. Jpn.*, 81, 169-177.  
<https://doi.org/10.2151/jmsj.81.169>
- Behera, S. K., Luo, J.J., Yamagata, T. (2008), Unusual IOD event of 2007, *Geophys. Res. Lett.*, 35, L14S11, <https://doi.org/10.1029/2008GL034122>
- Bjerknes, J., (1969). Atmospheric Teleconnections from the equatorial Pacific. *Mon. Wea. Rev.*, 97, 163–172, [https://doi.org/10.1175/1520-0493\(1969\)097<0163:ATFTEP>2.3](https://doi.org/10.1175/1520-0493(1969)097<0163:ATFTEP>2.3).
- Black, E., Slingo, J., Sperber, K. R. (2003). An observational study of the relationship between excessively strong short rains in coastal East Africa and Indian Ocean SST. *Monthly Weather Review*, 131(1), 74-94.  
[https://doi.org/10.1175/1520-0493\(2003\)131%3C0074:AOSOTR%3E2.0.CO;2](https://doi.org/10.1175/1520-0493(2003)131%3C0074:AOSOTR%3E2.0.CO;2)
- Black, E. (2005). The relationship between Indian Ocean sea–surface temperature and East African rainfall. *Philosophical Transactions of the Royal Society A: Mathematical, Physical and Engineering Sciences*, 363(1826), 43-47.  
<https://doi.org/10.1007/s002270050586>
- Bosc, C., Delcroix, T. (2008). Observed equatorial Rossby waves and ENSO-related warm water volume changes in the equatorial Pacific Ocean, *J. Geophys. Res.*, 113, C06003, <https://doi.org/10.1029/2007JC004613>
- Boulangier, J.P., Cravatte, S., Menkes, C. (2003). Reflected and locally wind-forced interannual equatorial Kelvin waves in the western Pacific Ocean, *J. Geophys. Res.*, 108, 3311, <https://doi.org/10.1029/2002JC001760>
- Bunge, L., Clarke A.J. (2014). On the Warm Water Volume and Its Changing Relationship with ENSO. *J. Phys. Oceanogr.*, 44, 1372–1385,  
<https://doi.org/10.1175/JPO-D-13-062.1>
- Burns, J. M., B. Subrahmanyam, E., Nyadjro, S., Murty V. S. N. (2016). Tropical cyclone activity over the Southwest Tropical Indian Ocean, *J. Geophys. Res. Oceans*, 121, 6389–6402, <https://doi.org/10.1002/2016JC011992>
- Cai, W., Shi, G., Cowan, T., Bi, D., Ribbe, J. (2005), The response of the Southern Annular Mode, the East Australian Current, and the southern mid-latitude ocean circulation to global warming, *Geophys. Res. Lett.*, 32, L23706,  
<https://doi.org/10.1029/2005GL024701>
- Cai, W., Hendon, H.H., Meyers, G. (2005). Indian Ocean Dipole like Variability in the CSIRO Mark 3 Coupled Climate Model. *J. Climate*, 18, 1449–1468,  
<https://doi.org/10.1175/JCLI3332.1>
- Cai, W., Pan, A., Roemmich, D., Cowan, T., & Guo, X. (2009). Argo profiles a rare occurrence of three consecutive positive Indian Ocean Dipole events, 2006-2008. *Geophys. Res. Lett.*, 36, L08701.  
<https://doi.org/10.1029/2008GL037038>

- Cai, W., Sullivan, A., Cowan, T., Ribbe, J., Shi, G. (2011). Simulation of the Indian Ocean Dipole: A relevant criterion for selecting models for climate projections. *Geophysical Research Letters*, 38(3). <https://doi.org/10.1029/2010GL046242>
- Cane, M., Zebiak, S., Dolan, S. (1986). Experimental forecasts of El Niño. *Nature* 321, 827–832. <https://doi.org/10.1038/321827a0>
- Carr M. E. (2001). Estimation of potential productivity in Eastern Boundary Currents using remote sensing. *DSR II: Top Stu in Oce*, 49, 1-3, 59-80. [https://doi.org/10.1016/S0967-0645\(01\)00094-7](https://doi.org/10.1016/S0967-0645(01)00094-7)
- Carr, M.E., Strub, P. T., Thomas, A. C., Blanco, J. L. (2002). Evolution of 1996–1999 La Niña and El Niño conditions off the western coast of South America: A remote sensing perspective, *J. Geophys. Res.*, 107 (C12), 3236, <https://doi.org/10.1029/2001JC001183>.
- Carr, M.E. (2003). Simulation of carbon pathways in the planktonic ecosystem off Peru during the 1997 - 1998 El Niño and La Niña, *J. Geophys. Res.*, 108, 3380, <https://doi.org/10.1029/1999JC000064>.
- Chan, S. C., Behera, S. K., Yamagata, T. (2008). Indian Ocean dipole influence on South American rainfall. *Geophysical Research Letters*, 35(14). <https://doi.org/10.1029/2008GL034204>
- Chatterjee, P., & Goswami, B. N. (2004). Structure, genesis and scale selection of the tropical quasi-biweekly mode. *Quarterly Journal of the Royal Meteorological Society*, 130(599), 1171-1194. <https://doi.org/10.1256/qj.03.133>
- Chen, T. C., & Chen, J.M. (1993). The 10-20-day mode of the 1979 Indian Monsoon: Its Relationship with the time variation of Monsoon Rainfall. *Monthly Weather Review*, 121, 2465-2482.
- Chen, G., Han, W., Li, Y., Wang, D., & Shinoda, T. (2015). Intraseasonal variability of upwelling in the equatorial Eastern Indian Ocean. *Journal of Geophysical Research: Oceans*, 120(11), 7598-7615. <https://doi.org/10.1002/2015JC011223>
- Chen, G., Han, W., Li, Y., and Wang, D. (2016). Interannual Variability of Equatorial Eastern Indian Ocean Upwelling: Local versus Remote Forcing. *J. Phys. Oceanogr.*, 46, 789-807. <https://doi.org/10.1175/JPO-D-15-0117.1>
- Chen, G., Han, W., Li, Y., McPhaden, M.J., Chen, J., Wang, W., and Wang, D. (2017). Strong Intraseasonal Variability of Meridional Currents near 5°N in the Eastern Indian Ocean: Characteristics and Causes. *J. Phys. Oceanogr.*, 47, 979-998. <https://doi.org/10.1175/JPO-D-16-0250.1>
- Chen, S.S., Houze, R.A., Mapes, B.E. (1996) Multiscale Variability of Deep Convection in Relation to Large-Scale Circulation in TOGA COARE. *J. Atmos.*

Sci., 53, 1380–1409, [https://doi.org/10.1175/1520-0469\(1996\)053<1380:MVODCI>2.0.CO;2](https://doi.org/10.1175/1520-0469(1996)053<1380:MVODCI>2.0.CO;2)

- Chiodi, A.M., Harrison, D.E. (2013). El Niño Impacts on Seasonal U.S. Atmospheric Circulation, Temperature, and Precipitation Anomalies: The OLR-Event Perspective. *J. Climate*, 26, 822–837, <https://doi.org/10.1175/JCLI-D-12-00097.1>
- Clarke, A. J., Van Gorder, S. (2003). Improving El Niño prediction using a space-time integration of Indo-Pacific winds and equatorial Pacific upper ocean heat content. *Geophysical research letters*, 30(7). <https://doi.org/10.1029/2002GL016673>
- Cronin, M. F., & McPhaden, M. J. (2002). Barrier layer formation during westerly wind bursts. *Journal of Geophysical Research: Oceans*, 107(C12), SRF 21-21-SRF 21-12. <https://doi.org/10.1029/2001JC001171>
- Delman, A. S., Sprintall, J., McClean, J. L., & Talley, L. D. (2016). Anomalous Java cooling at the initiation of positive Indian Ocean Dipole events. *Journal of Geophysical Research: Oceans*, 121(8), 5805-5824. <https://doi.org/10.1002/2016jc011635>
- Du, Y., T. Qu, G. Meyers, Y. Masumoto, and H. Sasaki (2005), Seasonal heat budget in the mixed layer of the south-eastern tropical Indian Ocean in a global GCM, *J. Geophys. Res.*, 110, C04012, doi:10.1029/2004JC002845.
- Du, Y., Qu, T., & Meyers G. (2008). Interannual Variability of Sea Surface Temperature off Java and Sumatra in a Global GCM. *J. Climate*, 21, 2451-2465. <https://doi.org/10.1175/2007JCLI1753.1>
- Du, Y., Liu, K., Zhuang, W., & Yu, W.D. (2012). The Kelvin wave processes in the equatorial Indian Ocean during the 2006–2008 IOD events. *Atmos. Oceanic Sci. Lett.*, 5, 324-328.
- Du, Y., Cai, W., & Wu, Y. (2013). A New Type of the Indian Ocean Dipole since the Mid-1970s. *J. Climate*, 26, 959-972. <https://doi.org/10.1175/JCLI-D-12-00047.1>
- Duan, Y., Liu, L., Han, G., Liu, H., Yu, W., Yang, G., Wang, H., Wan, H., Liu, Y., Waheed, Z & H. (2016). Anomalous behaviours of Wyrтки Jets in the equatorial Indian Ocean during 2013. *Sci Rep*, 6, 29688. <https://doi.org/10.1038/srep29688>
- Endo, S., & Tozuka, T. (2015). Two flavours of the Indian Ocean Dipole. *Climate Dynamics*, 46(11-12), 3371-3385. <https://doi.org/10.1007/s00382-015-2773-0>
- Felton, C. S., Subrahmanyam, B., Murty, V. S. N., & Shriver, J. F. (2014). Estimation of the barrier layer thickness in the Indian Ocean using Aquarius Salinity. *Journal of Geophysical Research: Oceans*, 119(7), 4200-4213. <https://doi.org/10.1002/2013JC009759>

- Feng, M., Meyers, G., & Wijffels, S. (2001). Interannual Upper Ocean Variability in the Tropical Indian Ocean. *Geophysical Research Letters*, 28(21), 4151-4154. <https://doi.org/10.1029/2001GL013475>
- Feng, M., & Wijffels, S. (2002). Intraseasonal variability in the South Equatorial Current of the east Indian Ocean. *Journal of physical oceanography*, 32(1), 265-277. [https://doi.org/10.1175/1520-0485\(2002\)032%3C0265:IVITSE%3E2.0.CO;2](https://doi.org/10.1175/1520-0485(2002)032%3C0265:IVITSE%3E2.0.CO;2)
- Feng, M., & Meyers, G. (2003). Interannual variability in the tropical Indian Ocean: a two-year timescale of Indian Ocean Dipole. *Deep Sea Research Part II: Topical Studies in Oceanography*, 50(12-13), 2263-2284. [https://doi.org/10.1016/S0967-0645\(03\)00056-0](https://doi.org/10.1016/S0967-0645(03)00056-0)
- Graham, N. E., & Barnett, T. P. (1987). Sea Surface Temperature, Surface Wind Divergence, and Convection over Tropical Oceans. *Science*, 238(4827), 657-659. <https://doi.org/10.1126/science.238.4827.657>
- Greenland D., Goodin, D. G., Smith, R. C. (2003). *Climate Variability and Ecosystem Response in Long-Term Ecological Research Sites* (book), ISBN: 9780195150599.
- Godfrey, J. S., Lindstrom, E. J. (1989). The heat budget of the equatorial western Pacific surface mixed layer. *Journal of Geophysical Research: Oceans*, 94(C6), 8007-8017. <https://doi.org/10.1029/JC094iC06p08007>.
- Harrison D. E. (1984). The Appearance of Sustained Equatorial Surface Westerlies During the 1982 Pacific Warm Event. *Science*, 224, 4653, 1099-1102. <https://doi.org/10.1126/science.224.4653.1099>
- Harrison, D. E., & Giese, B. S. (1988). Remote westerly wind forcing of the eastern equatorial Pacific; Some model results. *GRL*, 15, 8, 804-807. <https://doi.org/10.1029/GL015i008p00804>
- Harrison, D. E., & Giese, B. S. (1991). Episodes of surface westerly winds as observed from islands in the western tropical Pacific, *J. Geophys. Res.*, 96(S01), 3221– 3237, <https://doi.org/10.1029/90JC01775>
- Harrison, D. E., & Vecchi, G. A. (1997). Westerly Wind Events in the Tropical Pacific 1986–95. *Journal of Climate*, 10, 3131-3156. [https://doi.org/10.1175/1520-0442\(1997\)010%3C3131:WWEITT%3E2.0.CO;2](https://doi.org/10.1175/1520-0442(1997)010%3C3131:WWEITT%3E2.0.CO;2)
- Hartten, L. M. (1996). Synoptic settings of westerly wind bursts. *Journal of Geophysical Research: Atmospheres*, 101(D12), 16997-17019. <https://doi.org/10.1029/96JD00030>
- Hayes, S.P., McPhaden M.J., Wallace, J.M. (1989). The Influence of Sea-Surface Temperature on Surface Wind in the Eastern Equatorial Pacific: Weekly to Monthly Variability. *J. Climate*, 2, 1500–1506, <https://doi.org/10.1175/1520->

[0442\(1989\)002<1500:TIOSST>2.0.CO;2](https://doi.org/10.1007/s00382-015-2525-1)

- Henley, B.J., Gergis, J., Karoly, D.J. (2015). A Tripole Index for the Interdecadal Pacific Oscillation. *Clim Dyn* 45, 11-12, 3077 - 3090.  
<https://doi.org/10.1007/s00382-015-2525-1>
- Hoffman, R. N., Leidner, M., Henderson, J. M., Atlas, R., Ardizzone, J. V., and Bloom, S. C. (2003). A two-dimensional variational analysis method for NSCAT ambiguity removal: methodology, sensitivity, and tuning. *J. Atmos. Oceanic Technol.*, 20, 585-605. [https://doi.org/10.1175/1520-0426\(2003\)20<585:ATDVAM>2.0.CO;2](https://doi.org/10.1175/1520-0426(2003)20<585:ATDVAM>2.0.CO;2)
- Holmes, R. M., McGregor, S., Santoso, A., & England, M. H. (2018). Contribution of tropical instability waves to ENSO irregularity. *Climate Dynamics*, 52, 1837-1855. <https://doi.org/10.1007/s00382-018-4217-0>
- Holte, J., Talley, L.D., Gilson, J., & Roemmich, D. (2017). An Argo mixed layer climatology and database, *Geophysical. Research. Lett.*, 44(11), 5618-5626.  
<https://doi.org/10.1002/2017GL073426>
- Hong, C., Li, T., LinHo, & Kug, J. (2008a). Asymmetry of the Indian Ocean Dipole. Part I: Observational Analysis. *J. Climate*, 21, 4834-4848.  
<https://doi.org/10.1175/2008JCLI2222.1>
- Hong, C., Li, T., & Luo, J. (2008). Asymmetry of the Indian Ocean Dipole. Part II: Model Diagnosis. *J. Climate*, 21, 4849-4858.  
<https://doi.org/10.1175/2008JCLI2223.1>
- Horii, T., Ueki, I., Hanawa, K. (2012). Breakdown of ENSO predictors in the 2000s: Decadal changes of recharge/discharge-SST phase relation and atmospheric intraseasonal forcing. *Geophys. Res. Lett.*, 39, L10707,  
<https://doi.org/10.1029/2012GL051740>
- Huang, B., Kinter, J.L. (2002). Interannual variability in the tropical Indian ocean. *J. Geophys. Res.*, 107. <https://doi.org/10.1029/2001JC001278>
- Iskandar, I., Mardiansyah, W., Masumoto, Y., and Yamagata, T. (2005). Intraseasonal Kelvin waves along the southern coast of Sumatra and Java, *J. Geophys. Res.*, 110, C04013. <https://doi.org/10.1029/2004JC002508>
- Iskandar, I., Tozuka, T., Sasaki, H., Masumoto, Y., and Yamagata, T. (2006). Intraseasonal variations of surface and subsurface currents off Java as simulated in a high-resolution ocean general circulation model, *J. Geophys. Res.*, 111, C12015. <https://doi.org/10.1029/2006JC003486>
- Izumo, T., Vialard, J., Lengaigne, M., de Boyer Montegut, C., Behera, S. K., Luo, J. J., Yamagata, T. (2010). Influence of the state of the Indian Ocean Dipole on the following year's El Niño. *Nature Geoscience*, 3(3), 168.  
<https://doi.org/10.1038/ngeo760>

- Joseph, S., Wallcraft, A. J., Jensen, T. G., Ravichandran, M., Shenoi, S. S. C., & Nayak, S. (2012). Weakening of spring Wyrтки jets in the Indian Ocean during 2006-2011, *J. Geophys. Res.*, 117, C04012. <https://doi.org/10.1029/2011JC007581>
- Jin, F. (1997). An Equatorial Ocean Recharge Paradigm for ENSO. Part I: Conceptual Model. *J. Atmos. Sci.*, 54, 811–829, [https://doi.org/10.1175/1520-0469\(1997\)054](https://doi.org/10.1175/1520-0469(1997)054)
- Jin, F. (1997). An Equatorial Ocean Recharge Paradigm for ENSO. Part II: A Stripped-Down Coupled Model. *J. Atmos. Sci.*, 54, 830–847, [https://doi.org/10.1175/1520-0469\(1997\)054](https://doi.org/10.1175/1520-0469(1997)054)
- Kämpf, J., Doubell, M., Griffin, D., Matthews, R. L., & Ward, T. M. (2004). Evidence of a large seasonal coastal upwelling system along the southern shelf of Australia. *Geophysical Research Letters*, 31(9). <https://doi.org/10.1029/2003GL019221>
- Kämpf, J. (2012). Lee effects of localized upwelling in a shelf-break canyon. *Cont. Shelf Res.*, 42, 78-88. <https://doi.org/10.1016/j.csr.2012.05.005>
- Kämpf, J., & Chapman, P. (2016). Upwelling Systems of the World. *Springer, Cham*. <https://doi.org/10.1007/978-3-319-42524-5>
- Kämpf, J., & Kavi, A. (2018). SST variability in the eastern intertropical Indian Ocean – On the search for trigger mechanisms of IOD events. *Deep Sea Research Part II: Topical Studies in Oceanography*, 166, 66-74. <https://doi.org/10.1016/j.dsr2.2018.11.010>
- Keen, R. A. (1982). Equatorial westerlies and the Southern Oscillation. In: Proceedings of US TOGA Western Pacific Air-sea Interaction Workshop, 16-18 September, Honolulu, Hawaii.
- Keen, R.A. (1982). The Role of Cross-Equatorial Tropical Cyclone Pairs in the Southern Oscillation. *Mon. Wea. Rev.*, 110, 1405–1416, [https://doi.org/10.1175/1520-0493\(1982\)110](https://doi.org/10.1175/1520-0493(1982)110)
- Kikuchi, K., & Wang, B. (2009). Global Perspective of the Quasi-Biweekly Oscillation. *J. Climate*, 22, 1340-1359. <https://doi.org/10.1175/2008JCLI2368.1>
- Kim, S. T., Yu, J.Y., and Lu, M.M. (2012). The distinct behaviours of Pacific and Indian Ocean warm pool properties on seasonal and interannual time scales. *J. Geophys. Res.*, 117, D05128. <https://doi.org/10.1029/2011JD016557>
- Kim, H. M., Webster, P. J., Curry, J. A., Toma, V. E. (2012). Asian summer monsoon prediction in ECMWF System 4 and NCEP CFSv2 retrospective seasonal forecasts. *Climate dynamics*, 39(12), 2975-2991. <https://doi.org/10.1007/s00382-012-1470-5>

- Kripalani, R. H., Oh, J. H., Chaudhari, H. S. (2010). Delayed influence of the Indian Ocean Dipole mode on the East Asia–West Pacific monsoon: possible mechanism. *International Journal of Climatology: A Journal of the Royal Meteorological Society*, 30(2), 197-209. <https://doi.org/10.1002/joc.1890>
- Krishnamurthy, V., & Kirtman, B. P. (2003). Variability of the Indian Ocean: Relation to monsoon and ENSO. *Quarterly Journal of the Royal Meteorological Society*, 129(590), 1623-1646. <https://doi.org/10.1256/qj.01.166>
- Ladage, S., Gaedicke, C., Barckhausen, U., Heyde, I., Weinrebe, W., Flueh, E. R., Krabbenhoft, A., Kopp, H., Fajar, S., and Djajadihardja, Y. (2006). Bathymetric survey images structure off Sumatra. *Eos Trans. AGU*, 87(17), 165-168. <https://doi.org/10.1029/2006EO170001>
- Lau, N., Nath, M.J. (2004). Coupled GCM Simulation of Atmosphere–Ocean Variability Associated with Zonally Asymmetric SST Changes in the Tropical Indian Ocean. *J. Climate*, 17, 245–265, [https://doi.org/10.1175/1520-0442\(2004\)017<0245:CGSOAV>2.0.CO;2](https://doi.org/10.1175/1520-0442(2004)017<0245:CGSOAV>2.0.CO;2)
- Lee, H.T. (2014). Climate Algorithm Theoretical Basis Document (C-ATBD), Outgoing Longwave Radiation (OLR) - Daily. NOAA's Climate Data Record (CDR) Program, *CDRP-ATBD-0526*, 46 pp.
- Lee, H.T., Schreck, C. J., Knapp, K. R. (2014). Generation of the Daily OLR Climate Data Record. *2014 EUMETSAT Meteorological Satellite Conference*, 22-26 September 2014, Geneva, Switzerland.
- Lee, S.S., & Wang, B. (2015). Regional boreal summer intraseasonal oscillation over Indian Ocean and Western Pacific: comparison and predictability study. *Climate Dynamics*, 46(7-8), 2213-2229. <https://doi.org/10.1007/s00382-015-2698-7>
- Lengaigne, M., Guilyardi, E., Boulanger, JP., Menkes, C., Delecluse, P., Inness, P., Cole, J., Slingo, J. (2004). Triggering of El Nino by westerly wind events in a coupled general circulation model. *Climate Dynamics*, 23(6), 601-620. <https://doi.org/10.1007/s00382-004-0457-2>
- Li, T., Zhang, Y., Lu, E., Wang, D. (2002). Relative role of dynamic and thermodynamic processes in the development of the Indian Ocean dipole: An OGCM diagnosis, *Geophys. Res. Lett.*, 29 (23), 2110, <https://doi.org/10.1029/2002GL015789>
- Li, T., Wang, B., Chang, C., Zhang, Y. (2003). A Theory for the Indian Ocean Dipole–Zonal Mode. *J. Atmos. Sci.*, 60, 2119–2135, [https://doi.org/10.1175/1520-0469\(2003\)060<2119:ATFTIO>2.0.CO;2](https://doi.org/10.1175/1520-0469(2003)060<2119:ATFTIO>2.0.CO;2)
- Li, H., Xu, F., Zhou, W., Wang, D., Wright, J. S., Liu, Z., and Lin, Y. (2017). Development of a global gridded Argo data set with Barnes successive corrections. *J. Geophys. Res. Oceans*, 122, 866-889.

<https://doi.org/10.1002/2016JC012285>

- Li, Z., Cai, W., & Lin, X. (2016). Dynamics of changing impacts of tropical Indo-Pacific variability on Indian and Australian rainfall. *Sci Rep*, 6, 31767. <https://doi.org/10.1038/srep31767>
- Lian, T., Chen, D., Tang, Y., Liu, X., Feng, J., & Zhou, L. (2018). Linkage between westerly wind bursts and tropical cyclones. *Geophysical Research Letters*, 45, 11431-11438. <https://doi.org/10.1029/2018GL079745>
- Lin, X., Johnson, R.H. (1996). Heating, Moistening, and Rainfall over the Western Pacific Warm Pool during TOGA COARE. *J. Atmos. Sci.*, 53, 3367–3383, [https://doi.org/10.1175/1520-0469\(1996\)053<3367:HMAROT>2.0.CO;2](https://doi.org/10.1175/1520-0469(1996)053<3367:HMAROT>2.0.CO;2)
- Luo, J. J., Behera, S., Masumoto, Y., Sakuma, H., Yamagata, T. (2008). Successful prediction of the consecutive IOD in 2006 and 2007. *Geophysical Research Letters*, 35(14). <https://doi.org/10.1029/2007GL032793>
- Luther D. S., Harrison D. E., Knox R. A. (1983). Zonal Winds in the Central Equatorial Pacific and El Niño. *Science*, 222, 4621, 327-330. <https://doi.org/10.1126/science.222.4621.327>
- Wheeler, M.C., & Hendon, H. H. (2004). An All-Season Real-Time Multivariate MJO Index: Development of an Index for Monitoring and Prediction. *Mon. Wea. Rev.*, 132, 1917-1932. [https://doi.org/10.1175/1520-0493\(2004\)132<1917:AARMMI>2.0.CO;2](https://doi.org/10.1175/1520-0493(2004)132<1917:AARMMI>2.0.CO;2)
- Madden, R. A., & Julian, P. R. (1971). Detection of a 40-50 Day Oscillation in the Zonal Wind in the Tropical Pacific. *J. Atmos. Sci.*, 28, 702-708. [https://doi.org/10.1175/1520-0469\(1971\)028<0702:DOADOI>2.0.CO;2](https://doi.org/10.1175/1520-0469(1971)028<0702:DOADOI>2.0.CO;2)
- Madden, R. A., & Julian, P. R. (1972). Description of Global-Scale Circulation Cells in the Tropics with a 40-50 Day Period. *J. Atmos. Sci.*, 29, 1109-1123. [https://doi.org/10.1175/1520-0469\(1972\)029<1109:DOGSCC>2.0.CO;2](https://doi.org/10.1175/1520-0469(1972)029<1109:DOGSCC>2.0.CO;2)
- Madden, R. A., & Julian, P. R. (1994). Observations of the 40–50-Day Tropical Oscillation - A Review. *Mon. Wea. Rev.*, 122, 814-837. [https://doi.org/10.1175/1520-0493\(1994\)122<0814:OOTDTO>2.0.CO;2](https://doi.org/10.1175/1520-0493(1994)122<0814:OOTDTO>2.0.CO;2)
- Mantua, N.J., Hare, S.R. (2002). The Pacific Decadal Oscillation. *Journal of Oceanography* 58, 35 - 44. <https://doi.org/10.1023/A:1015820616384>
- Masson, S., Delecluse, P., Boulanger, J.P., and Menkes, C. (2002). A model study of the seasonal variability and formation mechanisms of the barrier layer in the eastern equatorial Indian Ocean. *J. Geophys. Res.*, 107(C12), 8017. <https://doi.org/10.1029/2001JC000832>
- Masson, S., Boulanger, J.-P., Menkes, C., Delecluse, P., and Yamagata, T. (2004). Impact of salinity on the 1997 Indian Ocean dipole event in a numerical

- experiment. *J. Geophys. Res.*, 109, C02002.  
<https://doi.org/10.1029/2003JC001807>
- Masumoto, Y., Hase, H., Kuroda, Y., Matsuura, H., and Takeuchi, K. (2005). Intraseasonal variability in the upper layer currents observed in the eastern equatorial Indian Ocean. *Geophys. Res. Lett.*, 32, L02607.  
<https://doi.org/10.1029/2004GL021896>
- McBride, J.L., Davidson, N.E., Puri, K., Tyrell, G.C. (1995). The Flow during TOGA COARE as Diagnosed by the BMRC Tropical Analysis and Prediction System. *Mon. Wea. Rev.*, 123, 717–736, [https://doi.org/10.1175/1520-0493\(1995\)123](https://doi.org/10.1175/1520-0493(1995)123)
- McGregor, S., Timmermann, A., Jin, F.F., Kessler, W.S. (2016). Charging El Niño with off-equatorial westerly wind events. *Clim Dyn*, 47, 3-4, 1111-1125.  
<https://doi.org/10.1007/s00382-015-2891-8>
- McGregor, S., Gupta, A. S., Dommenges, D., Lee, T., McPhaden, M. J., & Kessler, W. S. (2017). Factors influencing the skill of synthesized satellite wind products in the tropical Pacific. *Journal of Geophysical Research: Oceans*, 18, 1072–1089. <https://doi.org/10.1002/2016JC012340>
- McPhaden, M. J., Freitag, H. P., Hayes, S. P., Taft, B. A., Chen, Z., Wyrki, K. (1988), The response of the equatorial Pacific Ocean to a westerly wind burst in May 1986, *J. Geophys. Res.*, 93(C9), 10589– 10603,  
<https://doi.org/10.1029/JC093iC09p10589>
- McPhaden, M. J., Bahr, F., Du Penhoat, Y., Firing, E., Hayes, S. P., Niiler, P. P., Richardson, P. L., and Toole, J. M. (1992). The response of the western equatorial Pacific Ocean to westerly wind bursts during November 1989 to January 1990. *J. Geophys. Res.*, 97(C9), 14289-14303.  
<https://doi.org/10.1029/92JC01197>
- McPhaden, M.J., Meyers, G. K., Masumoto, A. Y., Murty, V.S., Ravichandran, M. F., Vialard, S. J., Yu, L., & Yu, W. (2009). RAMA: The Research Moored Array for African-Asian-Australian Monsoon Analysis and Prediction\*. *Bull. Amer. Meteor. Soc.*, 90, 459-480. <https://doi.org/10.1175/2008BAMS2608.1>
- McPhaden, M. J., Zhang, X. (2009). Asymmetry in zonal phase propagation of ENSO sea surface temperature anomalies. *Geophys. Res. Lett.*, 36, L13703,  
<https://doi.org/10.1029/2009GL038774>
- McPhaden, M. J. (2012). A 21st century shift in the relationship between ENSO SST and warm water volume anomalies. *Geophys. Res. Lett.*, 39, L09706,  
<https://doi.org/10.1029/2012GL051826>
- McPhaden, M. J., Wang, Y., Ravichandran, M. (2015). Volume transports of the Wyrki jets and their relationship to the Indian Ocean Dipole. *J. Geophys. Res. Oceans*, 120, 5302-5317. <https://doi.org/10.1002/2015JC010901>
- Meehl, G. A. (1987). The Annual Cycle and Interannual Variability in the Tropical

- Pacific and Indian Ocean Region. *Monthly Weather Review*, 115, 27-50.  
[https://doi.org/10.1175/1520-0493\(1987\)115%3C0027:TACAIV%3E2.0.CO;2](https://doi.org/10.1175/1520-0493(1987)115%3C0027:TACAIV%3E2.0.CO;2)
- Meinen, C.S., McPhaden, M.J. (2000). Observations of Warm Water Volume Changes in the Equatorial Pacific and Their Relationship to El Niño and La Niña. *J. Climate*, 13, 3551–3559, [https://doi.org/10.1175/1520-0442\(2000\)013](https://doi.org/10.1175/1520-0442(2000)013)
- Meinen, C.S., McPhaden, M.J. (2001). Interannual Variability in Warm Water Volume Transports in the Equatorial Pacific during 1993–99. *J. Phys. Oceanogr.*, 31, 1324–1345, [https://doi.org/10.1175/1520-0485\(2001\)031](https://doi.org/10.1175/1520-0485(2001)031)
- Mears, C. A., Scott, J., Wentz, F. J., Ricciardulli, L., Leidner, S. M., Hoffman, R., & Atlas, R. (2019). A Near-Real-Time Version of the Cross-Calibrated Multiplatform (CCMP) Ocean Surface Wind Velocity Data Set. *Journal of Geophysical Research: Oceans*, 124(10), 6997-7010.  
<https://doi.org/10.1029/2019JC015367>
- Meyers, G. (1996). Variation of Indonesian throughflow and the El Niño-Southern Oscillation. *J. Geophys. Res.*, 101(C5), 12255-12263.  
<https://doi.org/10.1029/95JC03729>
- Meyers, G., McIntosh, P., Pigot, L., & Pook, M. (2007). The Years of El Niño, La Niña, and Interactions with the Tropical Indian Ocean. *J. Climate*, 20, 2872-2880. <https://doi.org/10.1175/JCLI4152.1>
- Moteki, Q., Katsumata, M., Yoneyama, K., Ando, K., & Hasegawa, T. (2018). Drastic thickening of the barrier layer off the western coast of Sumatra due to the Madden-Julian oscillation passage during the Pre-Years of the Maritime Continent campaign. *Prog Earth Planet Sci* (2018) 5: 35.  
<https://doi.org/10.1186/s40645-018-0190-9>
- Moum, J. N., de Szoeke, S. P., Smyth, W. D., Edson, J. B., DeWitt, H. L., Moulin, A. J., Thompson, E.J., Zappa, C.J., Rutledge, S.A., Johnson, R.H., Fairall, C.W. (2014). Air–Sea Interactions from Westerly Wind Bursts During the November 2011 MJO in the Indian Ocean. *Bull. Amer. Meteor. Soc.*, 95, 1185-1199.  
<https://doi.org/10.1175/BAMS-D-12-00225.1>
- Murtugudde, R., McCreary Jr, J. P., Busalacchi, A. J. (2000). Oceanic processes associated with anomalous events in the Indian Ocean with relevance to 1997–1998. *Journal of Geophysical Research: Oceans*, 105(C2), 3295-3306.  
<https://doi.org/10.1029/1999JC900294>
- Nagura, M., & McPhaden, M. J. (2012). The dynamics of wind-driven intraseasonal variability in the equatorial Indian Ocean. *J. Geophys. Res.*, 117, C02001.  
<https://doi.org/10.1029/2011JC007405>
- Newman, M., Alexander M.A., Ault T.R., Cobb K.M., Deser C., Lorenzo E. Di, Mantua N.J., Miller A.J., Minobe S., Nakamura H., Schneider N., Vimont D.J., Phillips A.S., Scott J.D., Smith, C.A. (2016). The Pacific Decadal Oscillation,

- Revisited. *J. Climate*, 29, 4399-4427, <https://doi.org/10.1175/JCLI-D-15-0508.1>
- Neske, S., & McGregor, S. (2018). Understanding the warm water volume precursor of ENSO events and its interdecadal variation. *Geophys. Res. Lett.*, 45, 1577-1585. <https://doi.org/10.1002/2017GL076439>
- Ng, B., & Cai, W. (2016). Present-day zonal wind influences projected Indian Ocean Dipole skewness. *Geophys. Res. Lett.*, 43, 11392-11399. <https://doi.org/10.1002/2016GL071208>
- Ng, B., Cai, W., Walsh, K. (2014). The role of the SST-thermocline relationship in Indian Ocean Dipole skewness and its response to global warming. *Sci Rep*, 4, 6034. <https://doi.org/10.1038/srep06034>
- Ng, B., Cai, W., Walsh, K., Santoso, A. (2015). Nonlinear processes reinforce extreme Indian Ocean Dipole events. *Sci Rep*, 5, 11697. <https://doi.org/10.1038/srep11697>
- O'Neill, L. W., Haack, T., Durland, T. (2015). Estimation of Time-Averaged Surface Divergence and Vorticity from Satellite Ocean Vector Winds. *J. Climate*, 28, 7596-7620. <https://doi.org/10.1175/JCLI-D-15-0119.1>
- Potemra, J. T., Hacker, P. W., Melnichenko, O., Maximenko, N. (2016). Satellite estimate of freshwater exchange between the Indonesian Seas and the Indian Ocean via the Sunda Strait. *J. Geophys. Res. Oceans*, 121, 5098-5111. <https://doi.org/10.1002/2015JC011618>
- Power, S., Casey, T., Folland, C. (1999). Inter-decadal modulation of the impact of ENSO on Australia. *Climate Dynamics*, 15, 319. <https://doi.org/10.1007/s003820050284>
- Qiu, B., Mao, M., Kashino, Y. (1999). Intraseasonal variability in the Indo-Pacific throughflow and the regions surrounding the Indonesian Seas. *Journal of Physical Oceanography*, 29(7), 1599-1618. [https://doi.org/10.1175/1520-0485\(1999\)029%3C1599:IVITIP%3E2.0.CO;2](https://doi.org/10.1175/1520-0485(1999)029%3C1599:IVITIP%3E2.0.CO;2)
- Qiu, Y., Cai, W., Li, L., and Guo, X. (2012). Argo profiles variability of barrier layer in the tropical Indian Ocean and its relationship with the Indian Ocean Dipole. *Geophys. Res. Lett.*, 39, L08605. <https://doi.org/10.1029/2012GL051441>
- Qu, T., & Meyers, G. (2005). Seasonal variation of barrier layer in the south-eastern tropical Indian Ocean. *J. Geophys. Res.*, 110, C11003. <https://doi.org/10.1029/2004JC002816>
- Knox, R.A. (1976). On a long series of measurements of Indian Ocean equatorial currents near Addu Atoll. *Deep-Sea Research*, 23(3), 211-221. [https://doi.org/10.1016/0011-7471\(76\)91325-5](https://doi.org/10.1016/0011-7471(76)91325-5)
- Rao, S. A. (2004). Abrupt termination of Indian Ocean dipole events in response to

- intraseasonal disturbances. *Geophysical Research Letters*, 31(19).  
<https://doi.org/10.1029/2004GL020842>
- Rao, S.A., Luo, J.J., Behera, S.K., Yamagata, T. (2008). Generation and termination of Indian Ocean dipole events in 2003, 2006 and 2007. *Climate Dynamics*, 33(6), 751-767. <https://doi.org/10.1007/s00382-008-0498-z>
- Rao, S. A., Behera, S. K., Masumoto, Y., Yamagata, T. (2002). Interannual subsurface variability in the tropical Indian Ocean with a special emphasis on the Indian Ocean Dipole. *Deep-Sea Res Part II: Topical studies in Oceanography*, 49(7-8), 1549-1572. [https://doi.org/10.1016/S0967-0645\(01\)00158-8](https://doi.org/10.1016/S0967-0645(01)00158-8)
- Reynolds, R.W., Smith, T.M., Liu, C., Chelton, D.B., Casey, K.S., Schlax, M.G. (2007). Daily High-Resolution-Blended Analyses for Sea Surface Temperature. *J. Climate*, 20, 5473-5496.  
<https://doi.org/10.1175/2007JCLI1824.1>
- Risien, C. M., Chelton, D. B. (2008). A Global Climatology of Surface Wind and Wind Stress Fields from Eight Years of QuikSCAT Scatterometer Data. *J. Phys. Oceanogr.*, 38, 2379–2413. <https://doi.org/10.1175/2008JPO3881.1>
- Santoso, A., Hendon, H., Watkins, A., Power, S., Dommenges, D., England, M.H., Frankcombe, L., Holbrook, N.J., Holmes, R., Hope, P., Lim, E., Luo, J., McGregor, S., Neske, S., Nguyen, H., Pepler, A., Rashid, H., Gupta, A.S., Taschetto, A.S., Wang, G., Abellán, E., Sullivan, A., Huguenin, M.F., Gamble, F., Delage, F. (2019). Dynamics and Predictability of El Niño–Southern Oscillation: An Australian Perspective on Progress and Challenges. *Bull. Amer. Meteor. Soc.*, 100, 403–420. <https://doi.org/10.1175/BAMS-D-18-0057.1>
- Saji, N. H., Goswami, B. N., Vinayachandran, P. N., and Yamagata, T. (1999). A dipole mode in the tropical Indian Ocean. *Nature*, 401, 360-363.  
<https://doi.org/10.1038/43854>
- Saji, N. H., and Yamagata, T. (2003). Possible impacts of Indian Ocean Dipole Mode events on global climate. *Clim. Res.*, 25, 151-169.  
<https://doi.org/10.3354/cr025151>
- Schott, F. A., & McCreary, J. P. (2001). The monsoon circulation Indian Ocean. *Progress in Oceanography*, 51(1), 1-123. [https://doi.org/10.1016/S0079-6611\(01\)00083-0](https://doi.org/10.1016/S0079-6611(01)00083-0)
- Schott, F. A., Xie, S.P., McCreary, J. P. (2009). Indian Ocean circulation and climate variability. *Reviews of Geophysics*, 47(1).  
<https://doi.org/10.1029/2007RG000245>
- Seiki, A., & Takayabu, Y. N. (2007). Westerly Wind Bursts and Their Relationship with Intraseasonal Variations and ENSO. Part I: Statistics. *Mon. Wea. Rev.*, 135, 3325-3345. <https://doi.org/10.1175/MWR3477.1>

- Senan, R., Sengupta, D., and Goswami, B. N. (2003). Intraseasonal “monsoon jets” in the equatorial Indian Ocean. *Geophys. Res. Lett.*, 30, 1750.  
<https://doi.org/10.1029/2003GL017583>
- Sengupta, D., Senan, R., Goswami, B. N., Vialard, J. (2007). Intraseasonal Variability of Equatorial Indian Ocean Zonal Currents. *J. Climate*, 20, 3036-3055. <https://doi.org/10.1175/JCLI4166.1>
- Shankar, D., Vinayachandran, P.N., Unnikrishnan, A.S. (2002). The monsoon currents in the north Indian Ocean. *Progress in Oceanography*, 52, 1, 63-120.  
[https://doi.org/10.1016/S0079-6611\(02\)00024-1](https://doi.org/10.1016/S0079-6611(02)00024-1).
- Shinoda, T., Hendon H. H., Alexander M. A. (2004). Surface and subsurface dipole variability in the Indian Ocean and its relationship with ENSO. DSR I: Oce Res Papers, Volume 51, Issue 5, May 2004, Pages 619-635,  
<https://doi.org/10.1016/j.dsr.2004.01.005>
- Shukla, R. P. (2014). The dominant intraseasonal mode of intraseasonal South Asian summer monsoon. *J. Geophys. Res. Atmos.*, 119, 635-651.  
<https://doi.org/10.1002/2013JD020335>
- Smith, R. L., Huyer, A., Godfrey, J. S., & Church, J. A. (1991). The Leeuwin current off western Australia, 1986–1987. *Journal of Physical Oceanography*, 21(2), 323-345.
- Sprintall, J., & Tomczak, M. (1992). Evidence of the barrier layer in the surface layer of the tropics. *J. Geophys. Res.*, 97(C5), 7305-7316.  
<https://doi.org/10.1029/92JC00407>
- Sprintall, J., Gordon, A. L., Murtugudde, R., Susanto, R. D. (2000). A semi-annual Indian Ocean forced Kelvin wave observed in the Indonesian seas in May 1997. *J. Geophys. Res.*, 105(C7), 17217-17230.  
<https://doi.org/10.1029/2000JC900065>
- Sprintall, J., Wijffels, S. E., Molcard, R., Jaya, I. (2009). Direct estimates of the Indonesian Throughflow entering the Indian Ocean: 2004-2006. *J. Geophys. Res.*, 114, C07001. <https://doi.org/10.1029/2008JC005257>
- Sprintall, J., & Révelard, A. (2014). The Indonesian throughflow response to Indo-Pacific climate variability. *J. Geophys. Res. Oceans*, 119, 1161-1175.  
<https://doi.org/10.1002/2013JC009533>
- Sui, C., Lau K. (1992). Multiscale Phenomena in the Tropical Atmosphere over the Western Pacific. *Mon. Wea. Rev.*, 120, 407–430,  
[https://doi.org/10.1175/1520-0493\(1992\)120](https://doi.org/10.1175/1520-0493(1992)120)
- Susanto, R. D., Gordon, A. L., Sprintall, J., Herunadi, B. (2000). Intraseasonal variability and tides in Makassar Strait. *Geophysical Research Letters*, 27(10), 1499-1502. <https://doi.org/10.1029/2000GL011414>

- Susanto, R. D., Gordon, A.L., Zheng, Q. (2001). Upwelling along the coasts of Java and Sumatra and its relation to ENSO. *Geophysical Research Letters*, 28(8), 1599-1602. <https://doi.org/10.1029/2000GL011844>
- Tomczak, Matthias, and Daniel GB Large. "Optimum multiparameter analysis of mixing in the thermocline of the eastern Indian Ocean." *Journal of Geophysical Research: Oceans* 94, no. C11 (1989): 16141-16149.
- Tomczak, M., & Godfrey, J. S. (2003). *Regional Oceanography: An Introduction, 2nd edn.*, Elsevier. ISBN: 9781483287614
- Tomczak, M., & Godfrey, J. S. (2013). *Regional oceanography: an introduction.* Elsevier
- Ummenhofer, C. C., Sen Gupta, A., England, M. H., Reason, C. J. (2009). Contributions of Indian Ocean sea surface temperatures to enhanced East African rainfall. *Journal of Climate*, 22(4), 993-1013. <https://doi.org/10.1175/2008JCLI2493.1>
- Varela, R., Santos, F., Gómez-Gesteira, M., Álvarez, I., Costoya, X., Días J.M. (2016). Influence of Coastal Upwelling on SST Trends along the South Coast of Java. *PLoS ONE* 11(9): e0162122. <https://doi.org/10.1371/journal.pone.0162122>
- Vecchi, G. A., & Harrison, D. E. (2000). Tropical Pacific Sea Surface Temperature Anomalies, El Niño, and Equatorial Westerly Wind Events. *J. Climate*, 13, 1814-1830. [https://doi.org/10.1175/1520-0442\(2000\)013<1814:TPSSTA>2.0.CO;2](https://doi.org/10.1175/1520-0442(2000)013<1814:TPSSTA>2.0.CO;2)
- Vinayachandran, P. N., & Shetye, S.R. (1991). The warm pool in the Indian Ocean. *Proc. Indian Acad Sci. (Earth Planet Sci)*, 100, 165-175. <https://doi.org/10.1007/BF02839431>
- Vinayachandran, P. N., Saji, N. H., Yamagata, T. (1999). Response of the equatorial Indian Ocean to an unusual wind event during 1994. *Geophysical Research Letters*, 26(11), 1613-1616. <https://doi.org/10.1029/1999GL900179>
- Vinayachandran, P. N., S., I., Yamagata, T. (2002). Indian Ocean dipole mode events in an ocean general circulation model. *Deep Sea Research Part II*, 49, 1573-1596.
- Vinayachandran, P.N., Francis, P.A., Rao, S.A. (2009). Indian Ocean Dipole: processes and impacts. *Current Trends in Science (Platinum Jubilee Special Publication)*. Indian Academy of Sciences, 569-589.
- Webster, P. J., Lukas, R. (1992). TOGA COARE: The coupled ocean-atmosphere response experiment. *Bulletin of the American Meteorological Society*, 73(9), 1377-1416. [https://doi.org/10.1175/1520-0477\(1992\)073%3C1377:TCTCOR%3E2.0.CO;2](https://doi.org/10.1175/1520-0477(1992)073%3C1377:TCTCOR%3E2.0.CO;2)

- Webster, P.J., Moore, A.M., Loschnigg, J.P., Leben, R.R. (1999). Coupled ocean-atmosphere dynamics in the Indian Ocean during 1997-98. *Nature*, 401, 356-360. <https://doi.org/10.1038/43848>
- Weller, E., & Cai, W. (2014). Meridional variability of atmospheric convection associated with the Indian Ocean Dipole Mode. *Scientific reports*, 4, 3590. <https://doi.org/10.1038/srep03590>
- Wen, M., & Zhang, R. (2008). Quasi-Biweekly Oscillation of the Convection around Sumatra and Low-Level Tropical Circulation in Boreal Spring. *Mon. Wea. Rev.*, 136, 189-205. <https://doi.org/10.1175/2007MWR1991.1>
- Wentz, F.J., Scott, J., Hoffman, R., Leidner, M., Atlas, R., Ardizzone, J. (2015). Remote Sensing Systems Cross-Calibrated Multi-Platform (CCMP) 6-hourly ocean vector wind analysis product on 0.25 deg grid, Version 2.0. Available online at [www.remss.com/measurements/ccmp](http://www.remss.com/measurements/ccmp).
- Wijffels, S., & Meyers, G. (2004). An intersection of oceanic waveguides - Variability in the Indonesian Throughflow region. *J. Phys. Oceanogr.*, 34, 1232–1253. [https://doi.org/10.1175/1520-0485\(2004\)034<1232:AIOOWV>2.0.CO;2](https://doi.org/10.1175/1520-0485(2004)034<1232:AIOOWV>2.0.CO;2)
- Wyrtki, K. (1962). The upwelling in the region between Java and Australia during the south-east monsoon. *Aust. J. Mar. Freshwater Res.*, 13(3), 217-225. <https://doi.org/10.1071/MF9620217>
- Wyrtki, K. (1973). An Equatorial Jet in the Indian Ocean. *Science*, 181, 4096, 262-264. <https://doi.org/10.1126/science.181.4096.262>.
- Wyrtki, K. (1975). El Niño—The Dynamic Response of the Equatorial Pacific Ocean to Atmospheric Forcing. *J. Phys. Oceanogr.*, 5, 572–584, [https://doi.org/10.1175/1520-0485\(1975\)005](https://doi.org/10.1175/1520-0485(1975)005).
- Wyrtki, K. (1978). Monitoring the strength of equatorial currents from XBT sections and sea level. *Journal of Geophysical Research: Oceans*, 83(C4), 1935-1940.
- Wyrtki, K. (1985). Water displacements in the Pacific and the genesis of El Niño cycles, *J. Geophys. Res.*, 90( C4), 7129– 7132. <https://doi.org/10.1029/JC090iC04p07129>.
- Xie, S. P., Annamalai, H., Schott, F. A., McCreary Jr, J. P. (2002). Structure and mechanisms of South Indian Ocean climate variability. *Journal of Climate*, 15(8), 864-878. [https://doi.org/10.1175/1520-0442\(2002\)015%3C0864:SAMOSI%3E2.0.CO;2](https://doi.org/10.1175/1520-0442(2002)015%3C0864:SAMOSI%3E2.0.CO;2)
- Xie, S., Hu, K., Hafner, J., Tokinaga, H., Du, Y., Huang, G., Sampe, T., (2009). Indian Ocean Capacitor Effect on Indo-Western Pacific Climate during the Summer following El Niño. *J. Climate*, 22, 730–747,

<https://doi.org/10.1175/2008JCLI2544.1>

- Yamagata, T., Behera, S. K., Luo, J. J., Masson, S., Jury, M. R., and Rao, S. A. (2004). Coupled Ocean-Atmosphere Variability in the Tropical Indian Ocean. *In Earth's Climate* (eds C. Wang, S. Xie and J. Carton). <https://doi.org/10.1029/147GM12>
- Yamagata, T., Behera, S. K., Luo, J. J., Masson, S., Jury, M. R., & Rao, S. A. (2004). Coupled ocean-atmosphere variability in the tropical Indian Ocean. *Earth's Climate: The Ocean-Atmosphere Interaction*, Geophys. Monogr, 147, 189-212.
- Yan, D., Kai, L., Wei, Z., & Wei-Dong, Y. (2015). The Kelvin Wave Processes in the Equatorial Indian Ocean during the 2006-2008 IOD Events. *Atmospheric and Oceanic Science Letters*, 5(4), 324-328. <https://doi.org/10.1080/16742834.2012.11447007>
- Yuan, Y., Yang, H., Zhou, W., Li, C. (2008). Influences of the Indian Ocean dipole on the Asian summer monsoon in the following year. *International Journal of Climatology: A Journal of the Royal Meteorological Society*, 28(14), 1849-1859. <https://doi.org/10.1002/joc.1678>
- Zhang, C. (1996). Atmospheric intraseasonal variability at the surface in the tropical western Pacific Ocean. *J. Atmos. Sci*, 53, 739–758. [https://doi.org/10.1175/1520-0469\(1996\)053%3C0739:AIVATS%3E2.0.CO;2](https://doi.org/10.1175/1520-0469(1996)053%3C0739:AIVATS%3E2.0.CO;2)
- Zhang, C. (2005). Madden-Julian Oscillation. *Rev. Geophys.*, 43, RG2003. <https://doi.org/10.1029/2004RG000158>
- Zhang, Q., Hou, Y., Qi, Q., Bai, X. (2009). Variations in the eastern Indian Ocean warm pool and its relation to the dipole in the tropical Indian Ocean. *Chin. J. Ocean. Limnol.* 27, 640. <https://doi.org/10.1007/s00343-009-9148-5>.
- Zhang, Y., Du, Y., & Qu, T. (2016). A sea surface salinity dipole mode in the tropical Indian Ocean. *Climate Dynamics*, 47(7-8), 2573-2585. <https://doi.org/10.1007/s00382-016-2984-z>
- Zheng, X., Xie, S., Vecchi, G.A., Liu, Q., Hafner, J. (2010). Indian Ocean Dipole Response to Global Warming: Analysis of Ocean-Atmospheric Feedbacks in a Coupled Model. *J. Climate*, 23, 1240–1253, <https://doi.org/10.1175/2009JCLI3326.1>
- Zhong, A., Hendon, H.H., Alves, O. (2005). Indian Ocean Variability and Its Association with ENSO in a Global Coupled Model. *J. Climate*, 18, 3634 - 3649, <https://doi.org/10.1175/JCLI3493.1>
- Zubair, L., Rao, S. A., Yamagata, T. (2003). Modulation of Sri Lankan *Maha* rainfall by the Indian Ocean Dipole, *Geophys. Res. Lett.*, 30, 1063, <https://doi.org/10.1029/2002GL015639>.

# APPENDICES

## Appendix A

The 8-20 days filtered time series of the OLR anomaly, which represents the “bi-weekly mode” of convective oscillations, along with zonal wind speed values averaged over the eastern equatorial Indian Ocean region (70°-90 ° E, 5°N-5°S) at similar filtered range are displayed in **figures A1** as the composite plot.

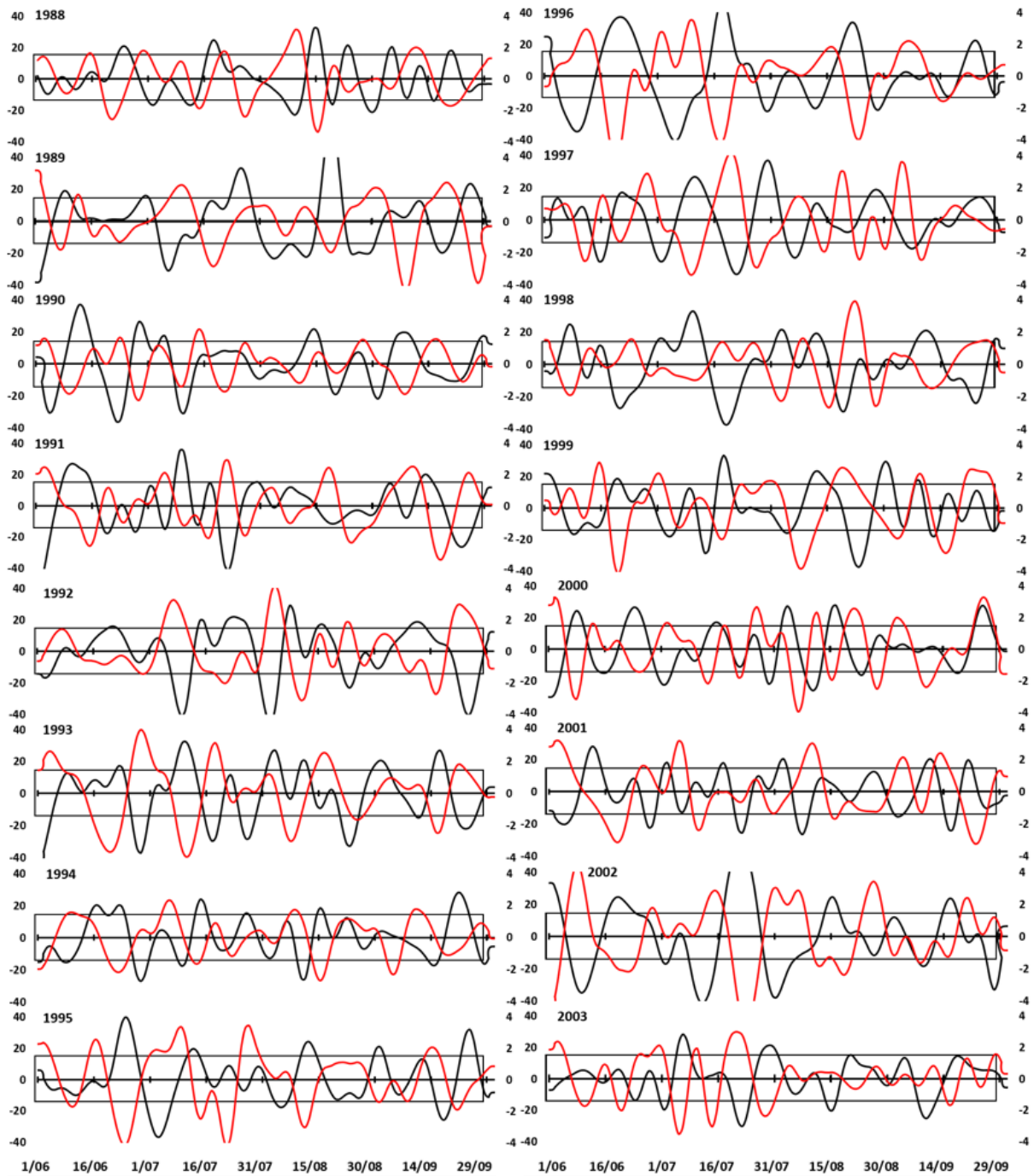


**Figure A1:** The 8-20 days filtered time series of the OLR anomaly average over the study region along with the zonal wind speed average over the eastern equatorial Indian Ocean filtered at similar temporal range are displayed during June to September of 1988-2004.

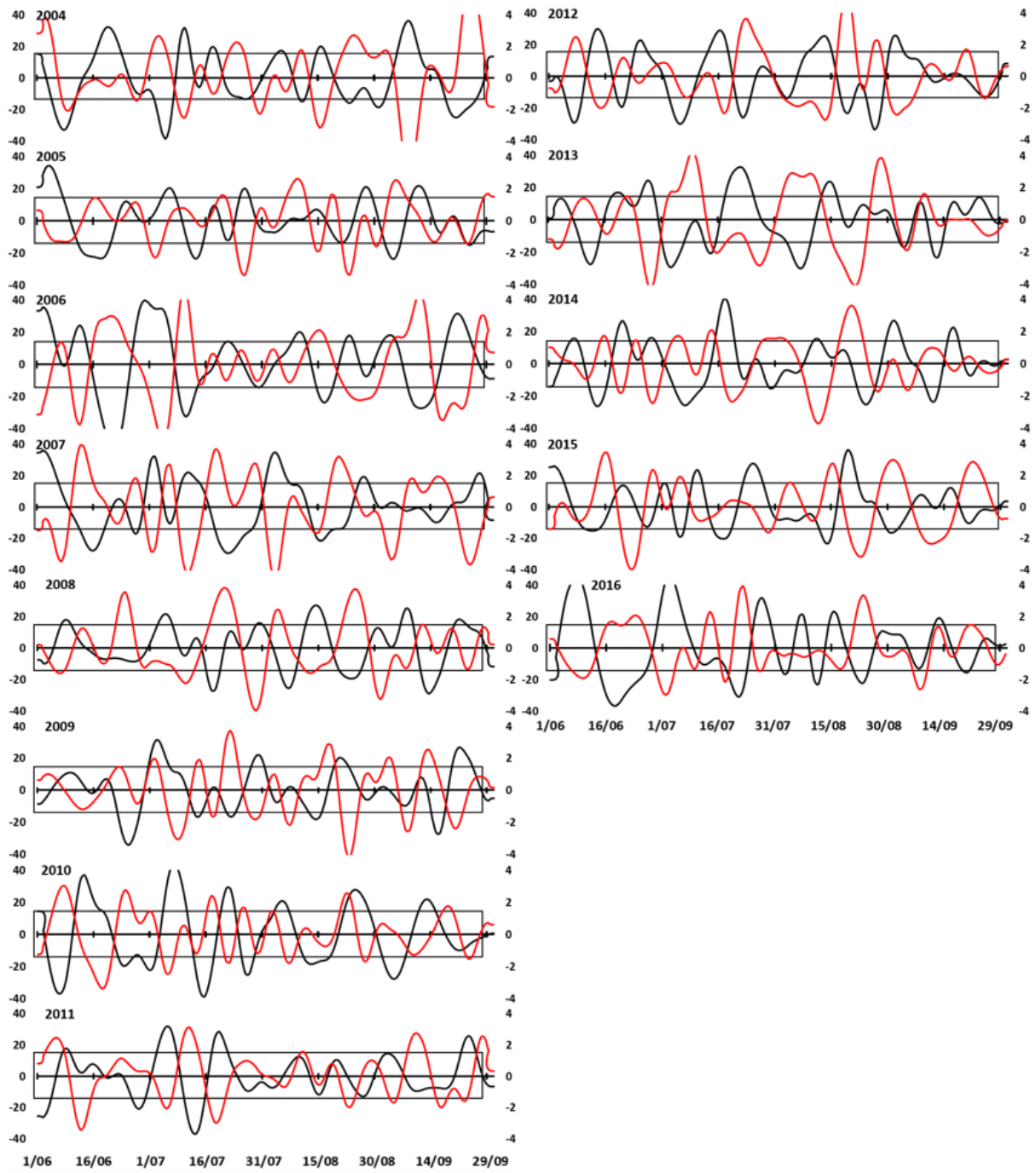


**Figure A1:** (continued) for 2004 to 2006

## Appendix B

The actual (unfiltered) time series of the OLR anomaly along with zonal wind speed values averaged over the eastern equatorial Indian Ocean region ( $70^{\circ}$ - $90^{\circ}$  E,  $5^{\circ}$ N- $5^{\circ}$ S) at similar filtered range are displayed in **figures A2** as the composite plot.

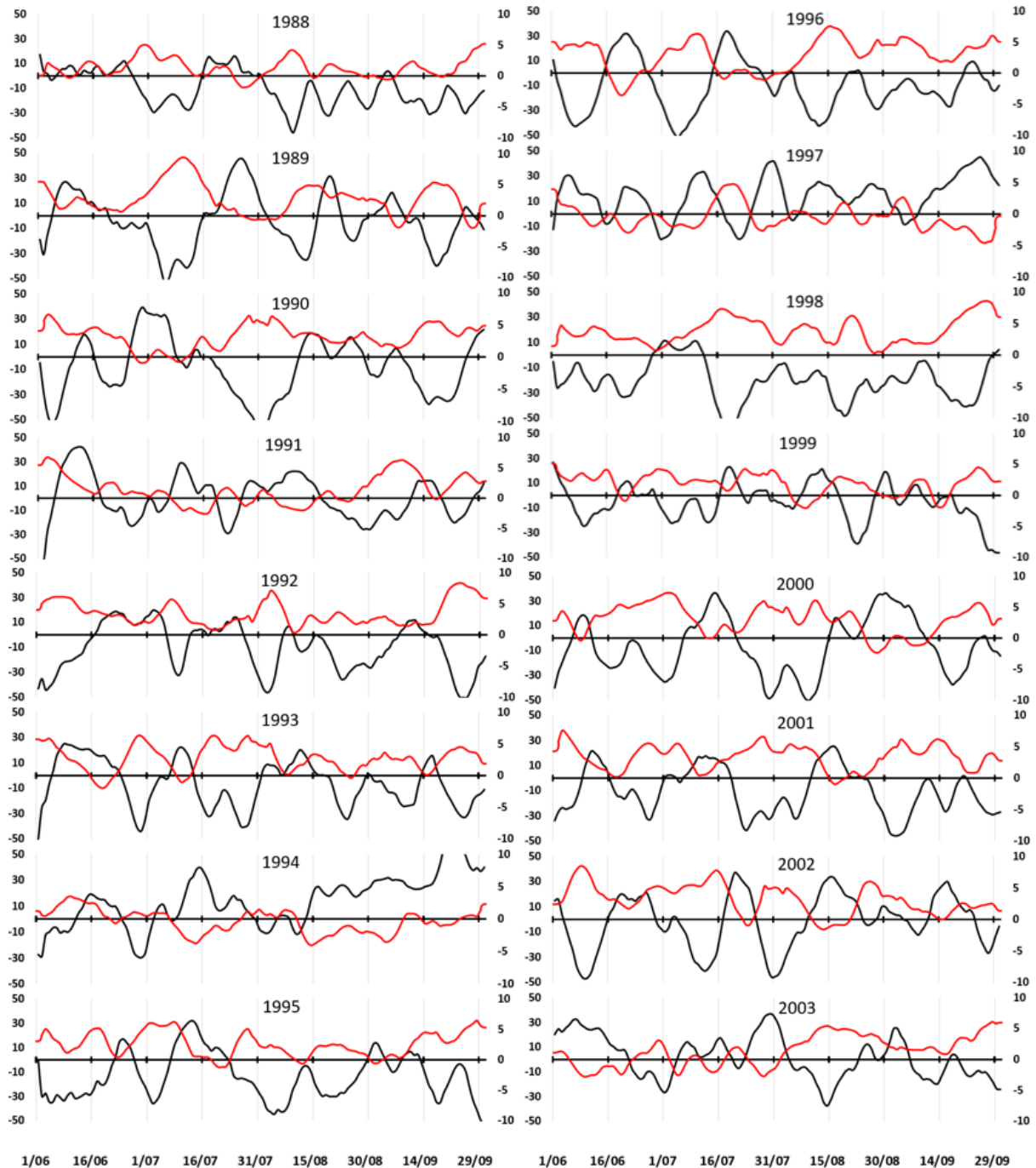


**Figure A2:** Unfiltered time series of the OLR anomaly average over the study region along with zonal wind speed values averaged over the eastern equatorial Indian Ocean region ( $70^{\circ}$ - $90^{\circ}$  E,  $5^{\circ}$ N- $5^{\circ}$ S) are displayed during June to September of 1988-2004.

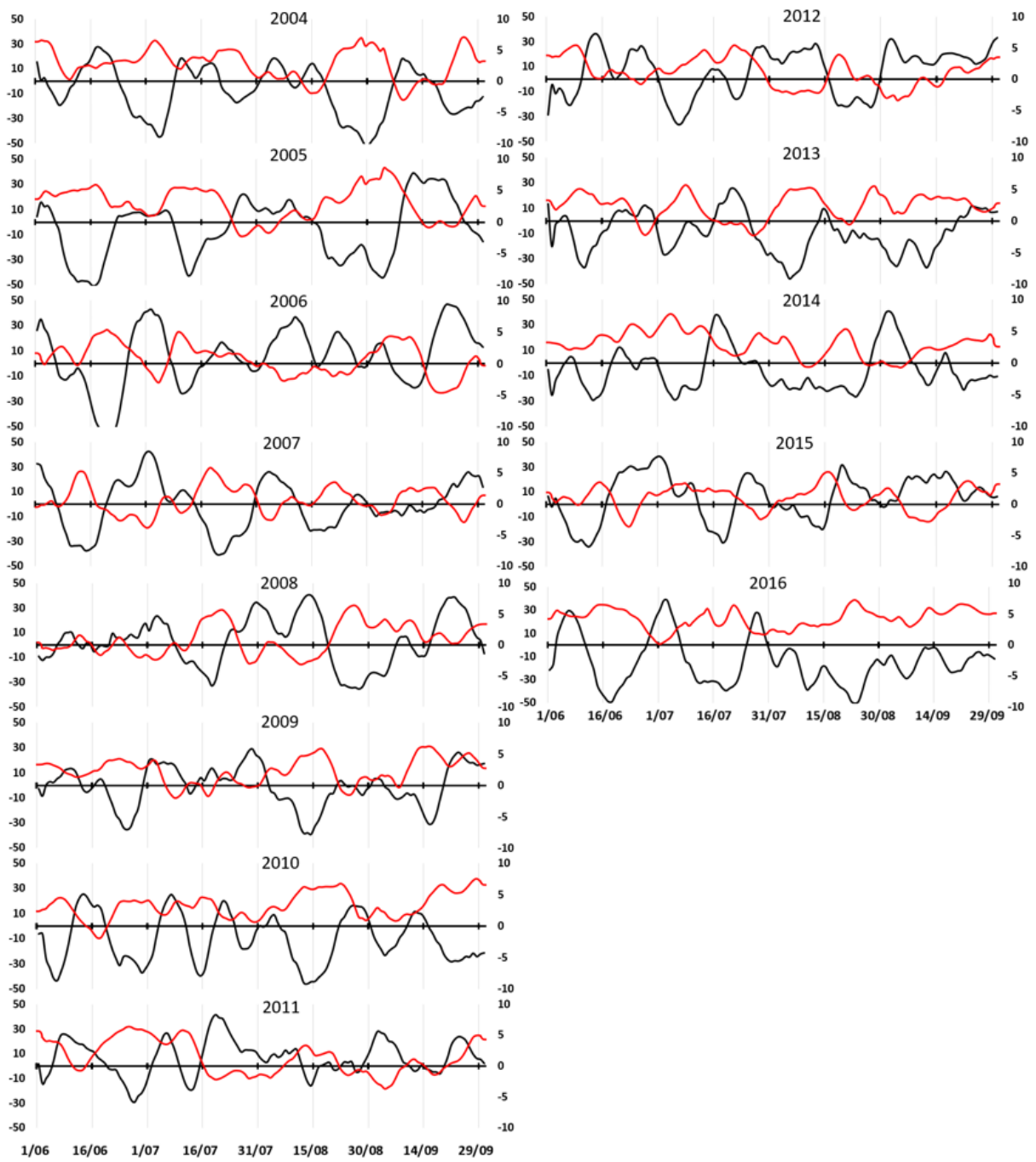


**Figure A2:** (continued) for 2004 to 2006

## Appendix C

The 8-20 days filtered time series of the OLR anomaly, which represents the “bi-weekly mode” of convective oscillations, along with meridional wind speed values averaged over the southern Sumatra coastal region (97°-103° E, 2°N-5°S) at similar filtered range are displayed in **figures A2** as the composite plot.

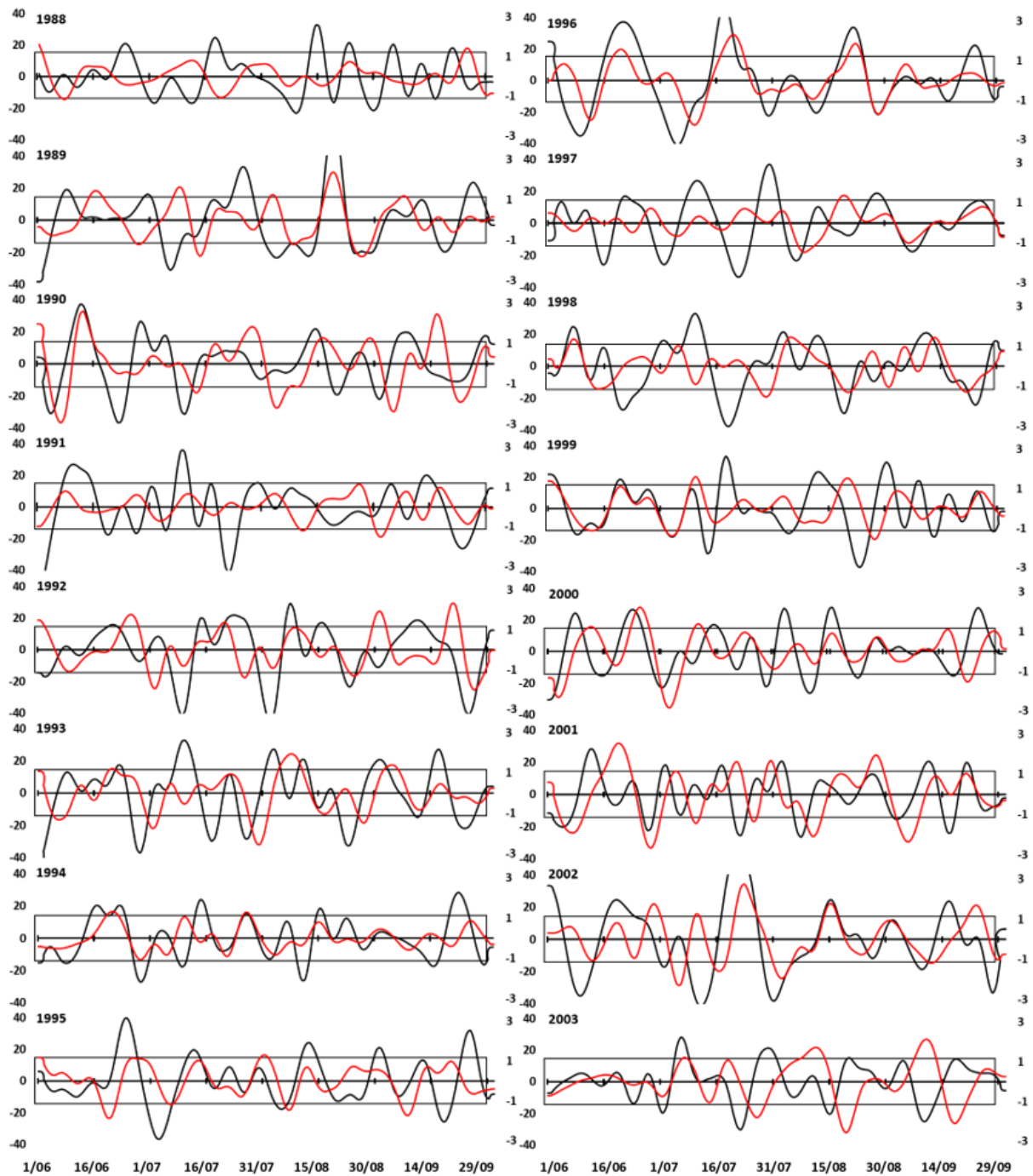


**Figure A3:** The 8-20 days filtered time series of the OLR anomaly average over the study region along with the meridional wind speed values averaged over the southern

Sumatra coastal region filtered at similar temporal range, are displayed during June to September of 1988-2004.

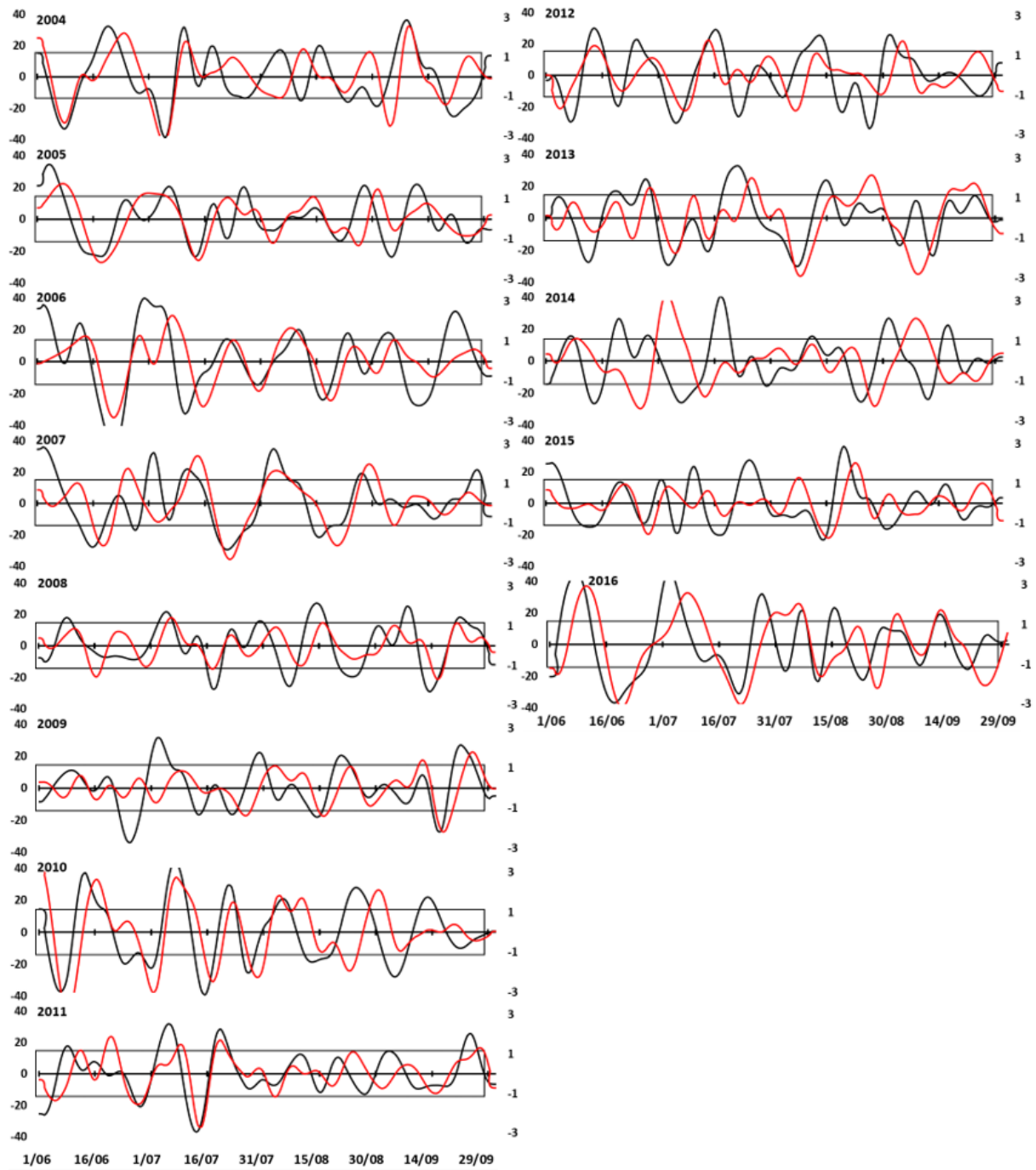


**Figure A3:** (continued) for 2004 to 2006

## Appendix D

The actual (unfiltered) time series of the OLR anomaly along with meridional wind speed values averaged over the southern Sumatra coastal region (97°-103° E, 2°N-5°S) are displayed in **figures A2** as the composite plot.

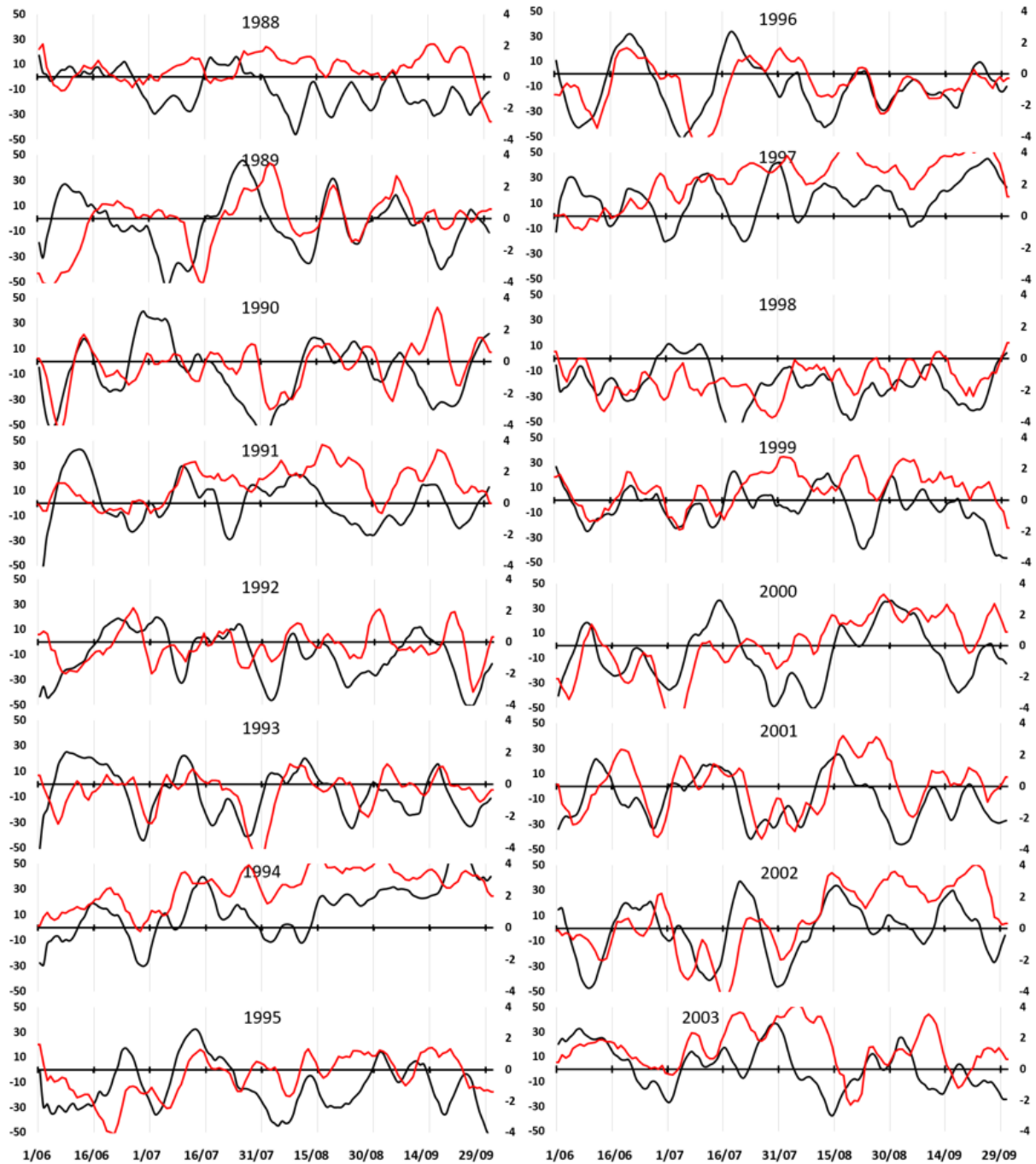


**Figure A4:** Unfiltered time series of the OLR anomaly average over the study region along with meridional wind speed values averaged over the southern Sumatra coastal region (97°-103° E, 2°N-5°S) are displayed during June to September of 1988-2004.

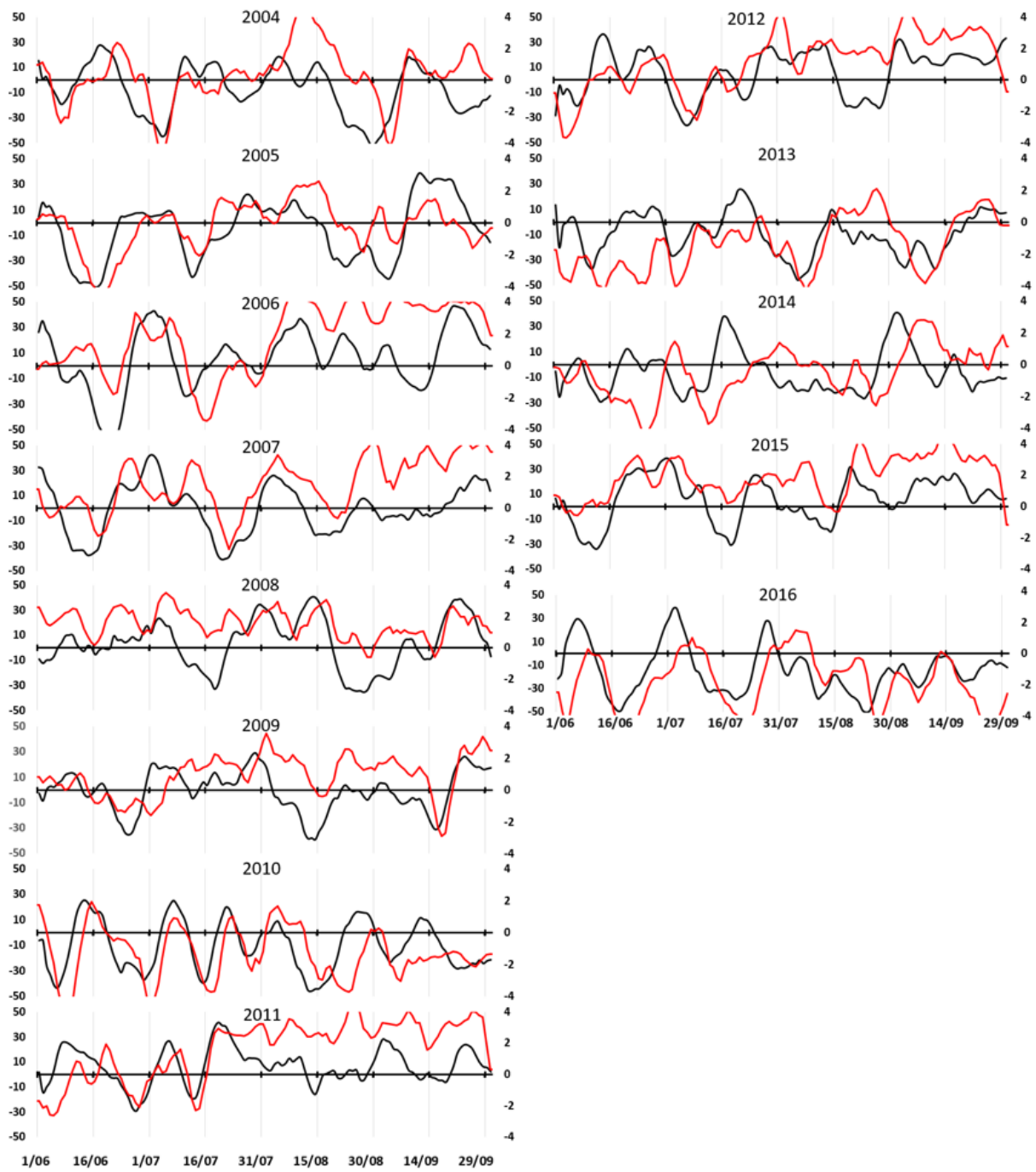


**Figure A3:** (continued) for 2004 to 2006